Novel Preparative Routes to Nanostructured Materials for Fuel Cell Applications

John Beresford Lowe

University of St Andrews

This thesis is submitted in partial fulfilment for the degree of PhD at the University of St Andrews

November 2014

Dedicated to the memory of my mother Olivia and brother William.

May this thesis prove to be an inspiration to my beautiful daughters Jennifer and Elizabeth in years to come.

Declaration

1. Candidate's declarations:

I, John Beresford Lowe hereby certify that this thesis, which is approximately 63 000 words in length, has been written by me, and that it is the record of work carried out by me, or principally by myself in collaboration with others as acknowledged, and that it has not been submitted in any previous application for a higher degree.

I was admitted as a research student in November 2010 and as a candidate for the degree of PhD in November 2011; the higher study for which this is a record was carried out in the University of St Andrews between 2010 and 2014.

Date 26th November 2014 signature of candidate .....

2. Supervisor's declaration:

I hereby certify that the candidate has fulfilled the conditions of the Resolution and Regulations appropriate for the degree of PhD in the University of St Andrews and that the candidate is qualified to submit this thesis in application for that degree.

Date 26th November 2014 signature of supervisor .....

3. Permission for publication: (to be signed by both candidate and supervisor)

In submitting this thesis to the University of St Andrews I understand that I am giving permission for it to be made available for use in accordance with the regulations of the University Library for the time being in force, subject to any copyright vested in the work not being affected thereby. I also understand that the title and the abstract will be published, and that a copy of the work may be made and supplied to any bona fide library or research worker, that my thesis will be electronically accessible for personal or research use unless exempt by award of an embargo as requested below, and that the library has the right to migrate my thesis into new electronic forms as required to ensure continued access to the thesis. I have obtained any third-party copyright permissions that may be required in order to allow such access and migration, or have requested the appropriate embargo below.

The following is an agreed request by candidate and supervisor regarding the publication of this thesis:

PRINTED COPY

Embargo on all of the print copy for a period of three years (maximum five) on the following ground(s):

Publication would be commercially damaging to the researcher, or to the supervisor, or the University

Publication would preclude future publication

Supporting statement for printed embargo request:

The work contained in this thesis is confidential. The thesis refers to a technique described in the PhD thesis of a previous student (Troy Dougherty) which is itself embargoed in both electronic and print forms and is the subject of a patent application which is currently being prepared by the University of St Andrews. Publication of this thesis would invalidate this patent. In addition, the current thesis contains work which it is intended to publish in international journal articles. Prior publication of the thesis may invalidate such articles.

ELECTRONIC COPY

Embargo on all of the electronic copy for a period of three years (maximum five) on the following ground(s):

Publication would be commercially damaging to the researcher, or to the supervisor, or the University

Publication would preclude future publication

Supporting statement for electronic embargo request:

The work contained in this thesis is confidential. The thesis refers to a technique described in the PhD thesis of a previous student (Troy Dougherty) which is itself embargoed in both electronic and print forms and is the subject of a patent application which is currently being prepared by the University of St Andrews. Publication of this thesis would invalidate this patent. In addition, the current thesis contains work which it is intended to publish in international journal articles. Prior publication of the thesis may invalidate such articles.

Date 26th November 2014 signature of candidate .....

Date 26th November 2014 signature of supervisor .....

Acknowledgement

My sincerest gratitude is extended to all persons from the chemistry department at the University of St-Andrews who have shown a willingness and courtesy throughout my tenure.

I would like to thank my fellow group especially Juan Carlos and Toby for their daily enthusiasm and banter.

Special mention should also be made regarding the technical support staff. I am especially grateful to Julie Nairn and Ross Blakely who have helped in sample preparation and microscopy respectively, Derek Waddell for XRD help and Sylvia Williamson for her continuing analytical support.

I would also like to take this opportunity to thank Helmut Gnägi of Diatome Ltd. for the invaluable help in sample preparations, the EPSRC National Solid-state NMR Service at Durham, UK including Dr D.C. Apperley and colleagues from the solid state NMR service at St Andrews for ^{29}Si MAS-NMR.

Appreciation is also expressed to the School of Chemistry, University of St Andrews for PhD funding of this research and the opportunity to further my knowledge and understanding.

Finally, my greatest appreciation and sincerest gratitude is reserved for my supervisor Richard Baker for guidance and patience despite my opportunistic salvo of questions whenever we meet.

Abstract

Nanostructured materials with high specific surface areas and high pore volumes are of interest for applications in solid oxide fuel cells (SOFCs). This study describes the use of novel preparative methods for obtaining nanostructured samarium-doped ceria (SDC) with a view to its application as an anode material in SOFCs.

The strategy employed in this work was based on the nanocasting concept. Template materials with a polymer, carbon or silica framework are first obtained using a self-assembly process. These materials have long range networks of ordered mesopore channels and so act as templating moulds. From a three step procedure of precursor impregnation, *in-situ* formation of SDC by calcination and template removal, SDC with the inverse pore structure of the template is created. Novel methods for producing such SDC materials were applied and the products evaluated.

As silica templates have wide ranging applications involving exposure to high temperatures -not least in nanocasting- it was desirable to understand the thermal stability of these materials over a range of temperatures. A systematic study was conducted on three representative silica templates. An inherent problem in nanocasting from silica templates is retention of residual silica after the template removal step. A detailed investigation into these alternative wet chemistry procedures was undertaken. To circumvent the silica problem completely, a number of alternative templates made of mesoporous carbon were considered. A range of ordered mesoporous carbons were prepared and evaluated as templates.

To provide a comparator for the ordered SDC materials, a simple combustion method was used to prepare an SDC product without the influence of a structure directing template.

The techniques of TEM, SEM-EDX, UV–Vis spectroscopy, MAS-NMR, PXRD and gas physisorption were used to characterise the physical and chemical properties of the products in the bulk and at the nanoscale.

Contents

List of Abbreviations and Acronyms

Common Terms:

EISA	**Evaporative Induced Self Assembly**
EO	**Poly[ethylene oxide]**
IWIT	**Incipient Wetness Impregnation Technique**
OMC	**Ordered Mesoporous Carbon**
OMP	**Ordered Mesoporous Polymer**
OMS	**Ordered Mesoporous Silica**
PO	**Poly[propylene oxide]**
PSD	**Pore Size Distribution**
SDC	**Samarium Doped Ceria**
SSA	**Specific Surface Area**
VI	**Vacuum Impregnation**

Template Acronyms

FDU-12	**Fudan University, Cubic Structure, Silica Framework**
FDU-14	**Fudan University, Cubic Structure, Carbon Framework**
FDU-15	**Fudan University, Hexagonal Structure, Carbon Framework**
FDU-16	**Fudan University, Cubic Structure, Carbon Framework**
KIT-6	**Korea Advanced Institute of Science and Technology, Bi-continuous Structure, Silica Framework**
SBA-15	**Santa-Barbara Amorphous (Univ. of California), Hexagonal Structure, Silica Framework**

Sample Nomenclature

Materials have been classified according to their stage in synthesis and the major variable in their production, this forms the sequence

[Template]-[Pyrolysis]-[Property]-[Impregnation Technique]-[Stage of Synthesis]-[Other]

For Example: FDU-14-500-FUN-IWIT-FP-200/400 would represent a final product made from an FDU-14 carbon template synthesised at 500°C then functionalised with nitric acid before being impregnated with SDC nitrate precursor using an incipient wetness impregnation technique which was converted to the SDC oxide under 200 and 400°C thermal exposure.

Nomenclature Variables

[Template]:	**As per template acronyms**
[Pyrolysis Temperature]:	**[Blank] Represents standard preparation**
	[XXX] Represents XXX°C thermal treatment
	[2/400] 2 stage thermal treatment.
[Property]:	**[FUN] If the material was functionalised**
	[MONO] Monolith structure
[Impregnation Technique]:	**[IWIT] Incipient wetness impregnation technique**
	[VI] Vacuum impregnation
[Stage of Synthesis]:	**[IT] An intermediate stage after template impregnation and before calcination**
	[FP] SDC oxide final product
[Other]:	**[B4C] Before Carbon Removal at 400°C**
	[OC] Open Container Calcination
	[CC] Closed Container Calcination
	[LB] Large Boat
	[SB] Small Boat

List of Chemical Reagents Used:

1,1,3,3-tetramethyldisilazane	**TMDS**
(3-Aminopropyl)trimethoxysilane	**APTS**
Ammonium Hydrogen Fluoride	**ammonium bifluoride**
n-butanol	**1-butanol**
$Ce(NO_3)_3.6H_2O$	**cerium nitrate**
1,2-dihydroxybenzene	**Catechol**
Distilled H_2O	**prepared inter-departmental**
Ethanol	**EtOH**
Hexamethylenetetramine	**hexamine**
Hydrochloric acid	**HCl**

Phenol	
Potassium Chloride	**KCl**
Pluronic® P123	**tri-block copolymer**
Pluronic® F127	**tri-block copolymer**
Resorcinol	
$Sm(NO_3)_3.6H_2O$	**samarium nitrate**
Sodium Hydroxide (Pellet)	**NaOH prepared as solution**
Tetraethylorthosilicate	**TEOS**
1,3,5-triisopropylbenzene	**(TIPB)**
Trimethylbenzene	**Mesitylene (TMB)**

Instrumental Techniques and Apparatus:

BET analysis	**Brunauer, Emmett, Teller: an analysis model used in determination of surface area by gas adsorption.**
BJH analysis	**Barrett, Joyner and Halenda: an analysis model used in determination of average pore width and distribution.**
t-plot	**de Boer t-plot: an analysis model used in determination of micropores by gas adsorption**
DDP	**Digital Diffraction Pattern**
EDX or EDS	**Energy-dispersive X-ray spectroscopy**
FFT	**Fast Fourier Transform**
HRTEM	**High Resolution Transmission Electron Microscopy**
SAXS	**Small Angle X-Ray Diffraction Analysis**
SEM	**Scanning Electron Microscopy**
TEM	**Transmission Electron Microscopy**
UV-Vis	**Ultraviolet-Visible Spectroscopy**
PXRD	**Powder X-Ray Diffraction Analysis**

Chapter 1

Introduction

In the coming decades, a major challenge for mankind is one of energy availability and climatic change[1]. With worldwide demands for energy ever increasing[2], a point of use energy conversion unit that is both efficient and negligible in emissions would be desirable. Solid oxide fuel cells (SOFCs) are viewed as one such technology that will play a part in helping to meet these requirements. SOFCs are an electrochemical means to generate electricity in much the same way as a battery but fundamentally differ in that the generated electricity is not from a stored chemical resource but externally fuelled. This has an advantage that the SOFC can theoretically work continuously so long as fuel is supplied. Some of the advantages in moving to this technology include low emissions, high efficiency compared with mechanical alternatives and potentially multi-fuel compatibility. They can be utilised as a hybrid technology finding place with both solar and wind and capable of working with existing hydrocarbon fuels. Serious efforts are being made to wean ourselves from a hydrocarbon addiction which will involve different sectors of society, promising a technological, political and societal seismic shift in energy usage. One such direction is combining the intermittent and often variable energy of the renewables sector into a hydrogen economy. This phrase is often used to refer to the storage of excess energy in the form of hydrogen with the view to using it at a more convenient time. This strategy is fundamentally linked with the renewable sector as energy production from renewable is often intermittent and unsynchronised from that of human consumption. SOFCs are an ideal fit with this technology in that the hydrogen can be converted back to useful energy with great efficiencies of over 80% when used in combined heat and power applications[3].

1.1 Fuel Cells Types

Fuel Cells and their development are in an extensive and rapid state of flux. There are many types of fuel cell design with each having practical limitations due to their associated chemical or physical attributes. Fuel cells are differentiated according to their operating temperature, efficiency, applications and costs. They are classified according to the choice of fuel and electrolyte into 6 major groups[4]. These are presented in Table 1-1 along with their main benefits and limitations and are: alkaline fuel cell (AFC), direct methanol fuel cell

(DMFC), molten carbonate fuel cell (MCFC), phosphoric acid fuel cell (PAFC), proton exchange membrane (PEMFC) and solid oxide fuel cell (SOFC). As viewed from the table, the variety of fuel cells will naturally dictate specific areas of application. For example PEMFCs are available commercially from Horizon Fuel Cell Technologies and being utilised as vehicular power plants[5]. DMFCs available commercially from MTImicro are perceived as being battery replacements for mobile electronic devices[6]. SOFCs because of their higher operating temperatures have end applications in combined heat and power and as large auxiliary power units.[8]

Table 1-1: Variety of fuel cells and selected properties

Fuel Cell Type	Electrolyte	Operating Temperature (°C)	Fuel	Limitations	Benefits
AFC	KOH	50-200	H_2, N_2H_4	Sensitive to impurities	Inexpensive materials
DMFC	Polymer	60-200	CH_3OH	Possible permeation of methanol	No methanol reforming required
MCFC	(Li or Na) carbonate	600-700	H_2, CH_4, CO, natural gas	Corrosion (from electrolyte)	Resistance to impurities
PAFC	H_3PO_4	160-210	H_2, CH_4, CO, CH_3OH	Corrosion (from electrolyte)	Combined heat and power efficiency of 80%
PEMFC	Polymer membrane	50-100	H_2, CH_3OH	Sensitive to impurities	Low operating temperature
SOFC	YSZ, GDC, SDC	600-1000	H_2, CH_4, CO, natural gas	Start Up Time	Combined heat and power efficiency of 80%

Although the maximum operating voltage of a fuel cell is approximately 1 V when placed under load, these cells are modular and can be stacked together to increase power density. This can be achieved by stacking in series or in parallel therefore allowing the power output to be controlled in terms of current or voltage.

1.2 Fuel Cell Operation

Fuel cells have four common components in their construction. These are, two electrodes (anode and cathode), an electrolyte and an interconnect between the anode and cathode allowing current to flow. Figure 1-1 is a schematic of a typical SOFC showing these components. In this diagram, which is not to scale, the anode is represented as a thick layer in relation to the electrolyte and cathode. Often the design is to have either one of the electrodes or the electrolyte function as a physical support through thickness of construction. This allows the other two components to be constructed in thinner dimensions. Often though, the electrolyte is maintained as thin as possible for reasons of minimising the travelling distance of oxygen ions and electrolyte resistance. Using the anode as the support is the more common practice[7] as they allow an opportunity to increase the size of the 3-phase boundary (described later- section 1.4).

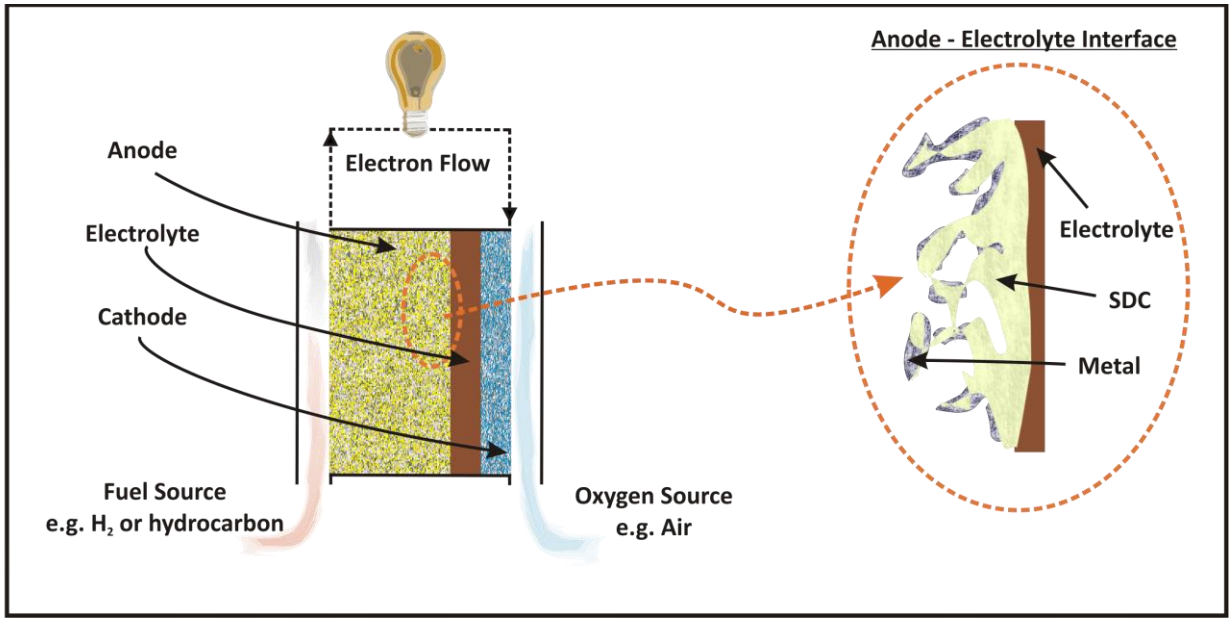

Figure 1-1: Schematic of a solid oxide fuel cell

The fuel cell in Figure 1-1 combines three separate functions. In the first of these functions, air is passed through an electrode chamber (the cathode) where oxygen from the air is charged with electrons to form oxygen ions. Next, the oxygen ions flow to the other electrode (the anode) where it reacts with a fuel gas such as hydrogen or alternatively natural gas or syngas. These reactions are represented in the equations 1, 2 and 3.

Cathode	$O_2 + 4e^- \rightarrow 2O^{2-}$	***Eqn. 1***
Anode	$2H_2 + 2O^{2-} \rightarrow 4e^- + 2H_2O$	***Eqn. 2***
Overall	$O_2 + 2\,H_2 \rightarrow 2H_2O$	***Eqn. 3***

The transport occurs through the electrolyte as oxygen vacancies exist within the crystal lattice as empty crystallographic positions which the anions can travel spontaneously down their concentration gradient by diffusion. This is because the electrolyte has been deliberately manufactured to have oxygen vacancies by way of crystal lattice defects but with poor electrical conductivity, thus negating a short circuit from occurring. When the oxygen ion has crossed the electrolyte it will combine with the fuel source (hydrogen) at the interface with the anode in an electrochemical reaction. The end product of the reaction is a water molecule (H_2O). Left over from this chemical recombination are the excess electrons from the charged oxygen ion. As electrons are consumed at the anode and generated at the cathode, this differential allows an electronic current to flow. As the electrolyte is impervious to electrons, the only way it can be achieved is by completing a wire pathway - effectively an electrical circuit. An electron travelling along a wire is the definition of electronic current, the sustainable generation of which can be used as a useful source of energy.

1.3 Solid Oxide Fuel Cell Design Considerations and Limitations

SOFCs have been in constant development including some high profile commercial applications. Several bluechip companies such as Google inc, AT&T, E-bay and Fed-Ex have installed modular stack design systems-as developed by BloomEnergy [8]. This implies that the technology is robust and the electrical generation is both cost effective and competitive now or likely to be in the near future. In regards the latter statement, the US department of Energy via SECA (Solid State Energy Conversion Alliance) is actively pursuing SOFC advancement in respect to cost parameters under the caveats of power densities[9]. Part of this costing analysis considers current technology and usage of rare earth materials including ceria and samarium. The study highlighted the need for consideration of the availability of such rare earth elements when manufacturing SOFCs on a commercial scale[10]. Apart from the cost of raw materials, the considerations of fuel cell design includes taking into account factors such as degradation (primarily from corrosion) which is a limitation on the practical life of a fuel cell. The components of the cell must be chemically stable so that internal component interaction is avoided. Also, these components should have similar thermal expansions so that thermal stresses and cracks and-or delamination are avoided in operational cycling or in manufacture. Other important properties include

high strength, durability, ease and low cost of fabrication [11]. Therefore, lowering the operating temperature of SOFCs to the intermediate range (500–750°C) and even lower, if possible, has become a major research goal. The reason for this is that high operating temperatures (~1000°C) require materials to be specifically attuned to withstand such harsh chemically and physically aggressive operational conditions, limiting the commercial development of SOFCs and maintaining higher costs of production[12]. Often commercial manufacturers prepare SOFCs by spray, screen print and tape casting methods[13] allowing for thin SOFC cells to be formed which can then be stacked to enable a combination of the power produced from each individual cell into a more meaningful power output. The manufacturing process produces thin components and often structural support will be required in one of these to give the cell mechanical strength. Electrolyte-supported cells are the simplest to fabricate, but thick electrolytes limit the performance due to their high resistance, particularly at temperatures below 800°C. Due to manufacturing difficulties of applying dense films at low temperatures to electrolytes, often the anode is supported by way of a cermet (ceramic –metallic composite)[14]. Mechanical stability is required in any cell design but it is also desirable to minimise the thickness of the electrolyte as SOFCs are sensitive to electrolyte thickness. This is because the thinner the electrolyte, the smaller the resistance to the flux of ions. Typically this equates to a compromise with membranes being produced in the 10 to 15 µm range. Recent research, however has been investigating 100 nm structures that not only perform in laboratory conditions but are able to be scaled to an extent of making them viable for mass production[15]. For these reasons, SDC materials synthesised with specific properties in mind such as high surface area, ordered mesoporosity, high mesopore volume and crystallinity should be able to meet or exceed the demands required for the anode section of a SOFC.

1.4 Rare-earth Doped Ceria as an Anode Material

The anode component for SOFCs has evolved over the years with Tarancon et al[12] reporting a porous platinum material in 1965 and Ni-ZrO_2 cermet in 1975. A common material at present -amongst others- is Ni-ZrO_2 cermet of approximately 150 µm thickness which is used in tubular designed SOFCs. One of the major advantage of SOFCs is the ability to be fuel flexible, however in order to maintain this advantage while trying to overcome the obstacle of high operating temperatures, an anode material with high catalytic activity at lower operating temperature is required [12]. For this reason, much research is being

undertaken with anode materials. This has involved the study of a variety of materials including a tri-metal $Fe_xCo_{0.5-x}Ni_{0.5}/Sm_{0.2}Ce_{0.8}O_{1.9}$. [16] Since 1964 when Mobius and Rohland [17] demonstrated ceria as an anode in a SOFC, much effort has been devoted to the development of ceria as an anode material helped by the fact that CeO_2 is less susceptible to sulphur poisoning as occurs with Ni in a Ni/YSZ anode[18]. Many ceria-alkaline-earth and rare-earth oxides have been investigated such as gadolina, Ni-samaria[19], in relation to their structures, electrical conductivity, and reducibility. Samarium and gadolinium-doped ceria samples exhibited the highest electrical conductivity in ceria-based oxides because of the close ionic radii of Sm^{3+} and Gd^{3+} to that of Ce^{4+}[20].

Design considerations for the anode material apart from chemical constitution are the physical properties. Apart from the benefit of the large reaction potential from having high surface area materials, high porosity is also desired to allow the flow of fuel and exhaust emissions in and out of the anode. Further requirements of the anode material are to allow electron passage – conductivity, otherwise the fuel cell would be inefficient and so a continuously interconnected structure would be ideal. There is a requirement to be catalytically active to the breakdown of the fuel source, stability to thermal cycling at temperatures anywhere from 500 to 1000°C and resistance to potential poisons such as carbon coking. So a strong crystalline structure would be desired. The combination of these requirements often creates a material that needs to handle simultaneously the chemical reaction in respect to fuel and exhaust gases, the oxygen ion transfer as well as electron transport. The area where this occurs is known as the three phase boundary. This is shown pictorially from the inset in Figure 1-1 and depicts an expanded area of the anode interface. This particular three phase model has a metal coating with the SDC material and serves to highlight the importance of a continuous and open framework to allow continuity of the ions and electrons as well as space for gases to move freely.

1.5 Catalysis

Catalysis is undoubtedly a very important area of chemistry and is fundamental to the production of fuels and plastics. In particular heterogeneous catalysis is an important application for solid metal oxides. An example of ceria used as a catalyst is in the formation of ketones by the condensation of two carboxylic acids or an acid and aldehyde[21]. In this particular example, the ceria is supported on an Al_2O_3 structure. Ceria also plays an extensive role in three-way automotive catalysts[22] due to the ability to store

oxygen[23]when in excess from the exhaust gas stream and with association of other catalysts[24], reduction of NO_x, oxidation of CO and oxidation of unburnt hydrocarbons occurs. Such supporting structures play a significant role in the development of any catalyst. Other fundamental characteristics of catalysts that are just as important include factors such as high specific surface area, surface structure, chemical impurities and structural impurities[25]. Chemical impurities - wanted or otherwise- can have either a positive or negative impact on catalytic activity through promotion or poisoning respectively[26]. Allied to the promotion effect, a technique of alloying (doping) by way of deliberate addition of another metal or oxide can be utilised to change properties which are several and are dependent on the nature of the solvent and solute atoms. For this reason, it is of interest to develop and characterise SDC as well as native ceria in terms of producing a high porosity and surface area product that is self-supporting with minimal parasitic elements such as silicon, fluorine etc. and stable to operational temperatures. The materials synthesised in this research may therefore have a secondary role as catalysts.

1.6 Mesoporous Structures

Doped ceria with nanoporous structures are desirable materials for a variety of applications including anode materials for solid oxide fuel cells. Several directions have been followed in an attempt to achieve them. Popular amongst these methods are self-assembly strategies which are similar to the silica and carbon template methods. While these methods successfully create ceria with ordered pore structures using organic amphiphiles, the material is amorphous in nature due to the low temperature synthesis requirement. Conversion of the amorphous material into a crystalline state is achieved using thermal treatment but at the cost of structural integrity with a loss of pore structure unless remedial action is undertaken to prevent this[27]. To successfully convert a cerium precursor –usually in the nitrate form- into a crystallised oxide, high temperatures are desired. Confinement within a framework would help achieve this while maintaining a partition between the growing crystals. An ideal framework is found in ordered mesoporous templates where the walls provide the necessary scaffolding and the pores provide the necessary space for crystal growth. Removal of the original scaffold material would reveal a 3-D porous structure that was the inverse structure of the original template.

1.6.1 *Self-Assembly Techniques*

The formation of an ordered structure can be achieved through molecular interactions in a technique described as self-assembly. The various stages of this are depicted in Figure 1-2.

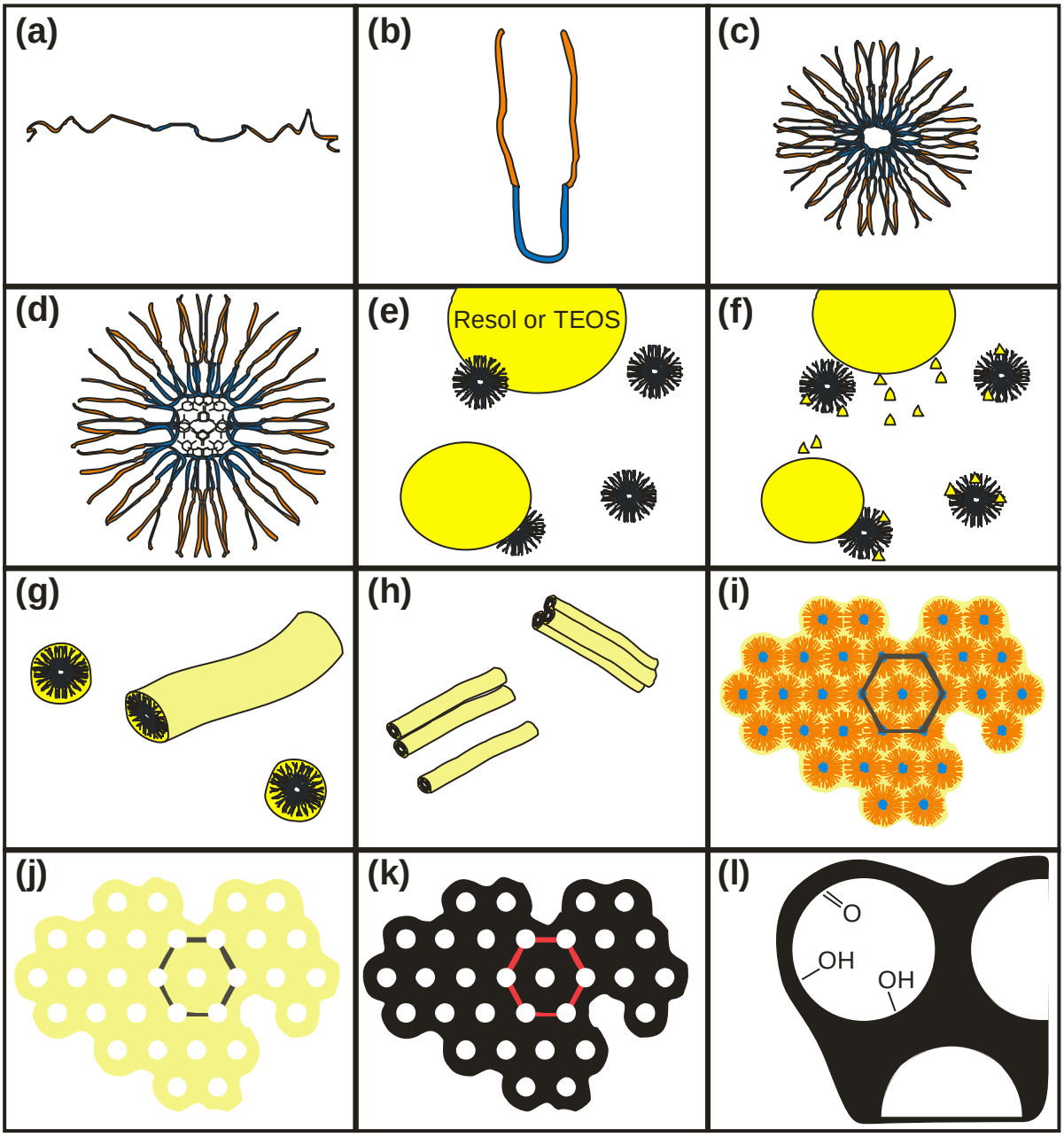

Figure 1-2: Pictorial representation of the various stages of template self-assembly.

This technique is the basis of the carbon and silica template formation and is often referred to as a soft template method.

(a) A copolymer is selected. In this instance it is a tri-block co-polymer where the middle block is a hydrophobic section and the two outer blocks are hydrophilic. These blocks can vary in molecular weight. Two common tri-block co-polymers commercially available are Pluronic P123 ($PEO_{20}PPO_{70}PEO_{20}$) and Pluronic F127($PEO_{106}PPO_{70}PEO_{106}$)

(b) The hydrophobic component will be repelled in a polar solvent such as water. The hydrophilic ends will try and coalesce.

(c) As these tri-block copolymers move around in solution, the hydrophobic parts will come together as they minimise the repelling force of the polar water molecules. This will over a period time create spherical clusters (micelles) of these copolymers with the hydrophilic blocks being on the outer perimeter.

(d) If a swelling reagent is used, it will centre itself within the triblock cluster allowing the hydrophobic part to relax and expand. This will create larger pores once the micelle is removed.

(e) A reagent that will interact with the hydrophilic component of the micelle is added, this is often tetraethylorthosilicate for a silica framework or resol polymer for a carbon based framework.

(f) The loading of the reagents within the micelle increases and leads to a spontaneous formation of a framework

(g) Depending on the concentration and molecular weight of the tri-block copolymer, different structural formations can occur. Rod like structures are shown here.

(h) These rods will start to coalesce with each other as weak hydrogen or Wan der Vaal bonding occurs between the reagents and will start to build up a multi-dimensional structure with regular and repeat (rod) units.

(i) The self-assembly nature of the synthesis will produce a structure of repeat unit cell, several of which have been synthesised. A hexagonal structure is shown however, others have been successfully prepared such as 3-d cubic, 3-d hexagonal etc. To consolidate the structure by way of forming strong covalent bonds, a thermo-polymerisation or hydrothermal is performed.

(j) Having a strong covalently bonded framework between the silica atoms or resol polymers, allows the micelles to be removed thereby creating a regular array of pore channels. This is achieved through heating.

(k) With polymer based frameworks, conversion to a more carbonaceous framework will occur as a function of higher thermal exposure.

(l) Within the pore channels the surface of the self-assembled product (template) will contact organic moieties which are important in determining the hydrophilic nature of the pore channel.

1.6.2 *Structure of Framework*

Since the first synthesis of mesostructures using nanocasting techniques that developed silica structures such as MCM-41 [28] FDU-1[29], three types – namely- SBA-15, KIT-6 and FDU-12, have found favour amongst material scientists. Each of these hard templates represents different structures that can be utilised in a range of techniques and as they have been used extensively in research it allows for cross comparison of results. The key properties of the three templates used are summarised in **Table 1-2**.

SBA-15 is one-dimensional hexagonal (*p6mm*) mesosporous silica with microporous walls[30] and has received a lot of attention over the past two decades. As such its synthesis has been developed to an extent that pore size and associated wall thickness control using different synthetic pathways has been developed and understood. Surface area would be within the range of 630 and 1040 m^2g^{-1} as dictated by experimental conditions.

Kit-6 is a 3-dimensional cubic (*Ia3d*) mesoporous silica with a surface area of approximately 800 m^2g^{-1}. This structure is bi-continuous, containing two enantiomeric pore systems, separated by a minimal surface composed of silica. The pore entrance range can be influenced and controlled by manipulating synthesis conditions.[31]

FDU-12 is a cubic (*Fm-3m*) mesoporous silica that has a cavity range of between 10 and 12.3 nm with a pore entrance of between 4 and 9 nm[32]. This pore entrance range can also be influenced and controlled by manipulating synthesis conditions[33]. In order to verify the synthesis of these products, gas physisorption, low angle XRD and TEM analysis would be routinely performed.

Table 1-2: A summary of the key properties of the mesoporous silica templates utilised**.**

Template	**Structure**	**Description**	**Pore Size* (nm)**	**Pore Volume* (cm^3g^{-1})**	**Pore Entrance* (nm)**	**Surface Area m^2g^{-1}**
SBA -15	*p6mm*	2-D Hexagonal (channel like pore structure)	8.9	1.17		780
Kit -6	*Ia3d*	3D Hexagonal	8.5	1.05		800
FDU -12	*Fm-3m*	3D Pore System	12.3	0.78	8.9	300

* Estimated pore size based on conditions of preparation [34]

Mesoporous solids, especially those with an ordered pore structure, possess unusual and interesting properties including very high specific surface areas, chemical and thermal stability in many environments, interconnected pore structures and uniform pore size and

shape which, furthermore, can be predetermined to a large extent by modification of the preparation parameters.

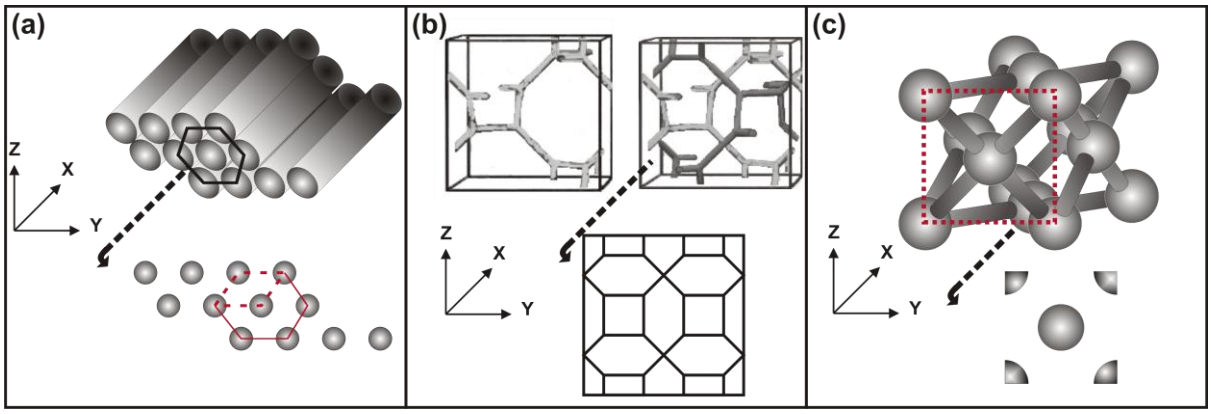

Figure 1-3: Pictorial representation of (a) SBA-15 (b) KIT-6, (c) FDU-12. Only the pore structures are shown, the surrounding pore walls are removed for clarity. The pore size and spacing's are not to scale. Front elevation highlights the [100] lattice direction and unit cell.

As a consequence, this group of materials is in demand for a wide range of current and potential applications. The most widely studied group of ordered mesoporous materials are those consisting of amorphous silica but with ordered pore structures. These are typically prepared by the self-assembly of surfactant-based micelles in the presence of a silica source such as tetraethoxysilane and subsequent removal of the organics to leave the mesoporous silica. Although these products are not crystalline in the conventional sense, the periodically-repeating pore structures can be assigned unit cells and space groups. An extensive family of these Ordered Mesoporous Silicas (OMSs) has been reported and features a wide range of pore structure symmetries including hexagonal *p6mm* (MCM-41[35], SBA-15[28], SBA-3[36]), cubic *Ia3d* (MCM-48[37], KIT-6[31b], FDU-5[38]), cubic *Im3m* (SBA-16[39]) and cubic *Fm-3m* (FDU-12[40]). The pore structures of the three representative materials chosen for the current study – SBA-15, KIT-6 and FDU-12 – are presented in Figure 1-3[41]. OMS materials are under consideration for many fields of application such as heterogeneous catalysis[42], gas adsorption[43] (including hydrogen storage[44]), drug delivery[45] and molecular separation[37]. Depending on the application, the OMS may require further chemical modification. The pore surfaces may be functionalised by post-synthesis grafting[43, 45b, 46] or by addition of the desired functional groups during the initial self-assembly process[45b]. Furthermore, a second solid phase may be impregnated into the pores, for example, to provide active catalytic sites[47]. In a very fruitful development, this process can be taken one step further. The OMS can be used as a mould into which the precursor of a different solid phase is introduced, often by impregnation of a solution. The second phase is then formed within the pore structure of the OMS, usually by calcination,

and finally the original OMS is removed by dissolution to leave an inverse ordered mesoporous structure comprised of the second material. This process is known as hard templating or nanocasting[48].

This group of techniques has been used to create a series of novel ordered mesoporous materials, often crystalline, including metal oxides[49], metal sulphides[50] and polymers[51] which exhibit the novel properties – such as high specific surface area – seen in the parent OMS. Fundamental to this methodology is the OMS itself, which must possess sufficient chemical and thermal stability to survive the first steps of the nanocasting process without losing its pore structure. For some preparations these factors may make hard templating difficult. For example, the preparation of mesoporous semiconductor materials is problematic because of their high crystal growth temperature[52].

1.6.3 *Carbon and Polymer Frameworks*

As an extension to silica based ordered mesoporous materials, a new range of OMMs have been developed where the silica framework has been replaced with an organic equivalent. In substituting the tetravalent silicon within such frameworks, carbon would be a logical alternative however practical limitations have for many years curtailed the development of useful materials until recently and is further explained in Chapter 8. Although many methods have been published recently showing tantalising formations of OMS analogues in carbon (and polymer structures), many methods are unfortunately impracticable due to low yield of quality product. For the purposes of this study, three structures were chosen namely: FDU-14, FDU-15 and FDU-16. This was because of similarities with the silica structures utilised, their abilities to be synthesised in meaningful quantities and transition properties from polymer to carbon framework.

1.7 Hard Template Replication (Nanocasting)

The conversion of metal nitrates to the associated oxide is an important aspect of any nanocasting process. Typical inverse structure from nanocast materials using (a) FDU-14, (b) FDU-15 and (c) FDU-16 are shown in Figure 1-4. Understandably it has received much attention with factors such as loading amounts through multiple impregnations, thermal conditions and the combination of precursor solvent and reagents[53].

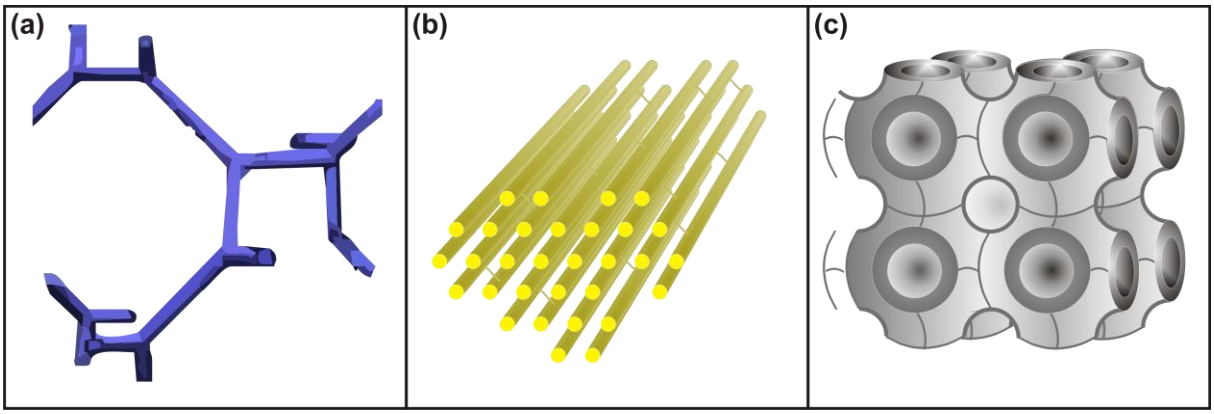

Figure 1-4: Pictorial representations of the inverse structure derived from nanocasting of (a) FDU-14 as a single pore channel, (b) FDU-15 and (c) FDU-16.

One particular variable that was researched by Sun and co-workers[54] involved an extensive study into the effect of nitrate conversion in a confined environment. Referred to as a container effect, it investigates the influence a confined volume has as opposed to calcination temperature. This study has revealed that crystallinity of product is mainly determined by container volume and not by calcination temperature. A major factor in the controlled conversion is the delayed water evaporation of the reagents to a higher temperature. For this reason the 200°C temperature is thought to be a critical temperature in cerium nitrate conversion to a highly crystallised oxide. Figure 1-5 outlines the various possibilities when impregnating materials. Three outcomes can occur which are (a) underfill, (c) ideal fill and (e) overfill. This fill refers to the amount of a liquid precursor that has entered into the pore system of an ordered mesoporous template. If not enough liquid has entered then the consequence is that the crystallised (oxidised) material will not bind with neighbouring pore channels by way of open micropores that are present between walls thus creating nanobridges or if grossly underfilled then some pore channels may not even be filled. This will lead to a series of individual rods or spheres being formed (b) as related to the template structure. If an ideal amount of precursor is present in the pore structure then a good inverse replication will occur (d). If too much liquid is present then it will spill over and create unwanted joining at pore entrances or worse still, completely engulf the template making a large disordered particle (f).

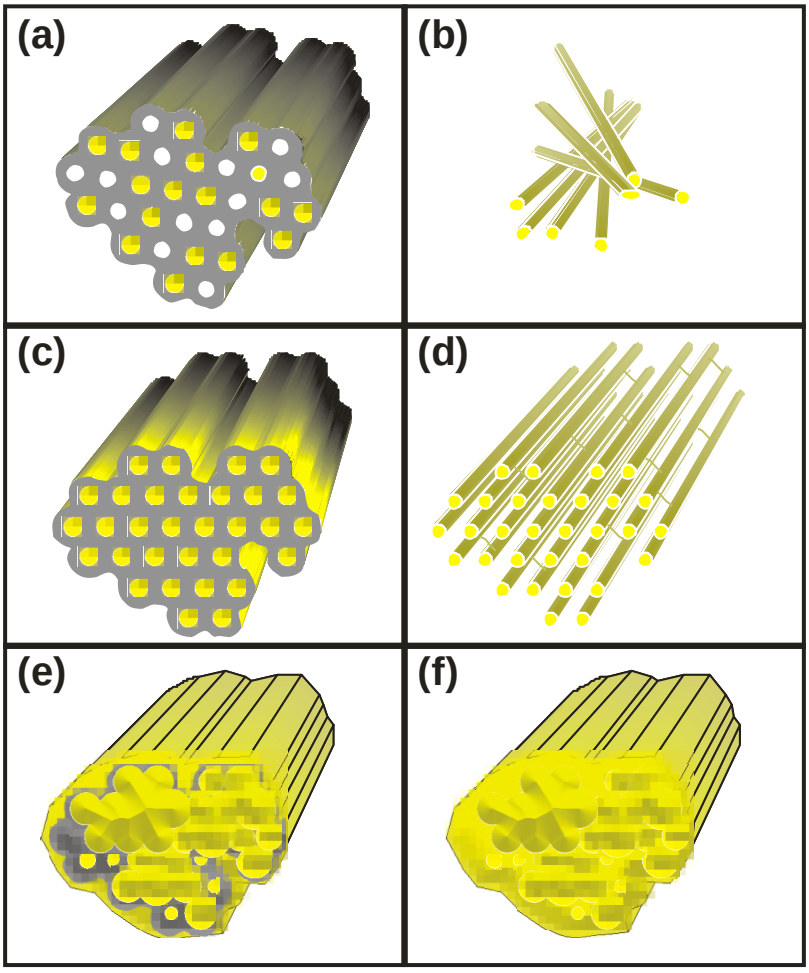

Figure 1-5: Stages of Impregnation (a) Partially impregnated template (b) Template removal generates singular rods (c) Ideally impregnated template (d) Inverse structure after template removal of ideally impregnated template. (e) Excessively impregnated template (f) Template removal after excessive impregnation.

1.8 Silica Hard Template Removal

One of the consequences of using silica as a hard template is that it has to be removed in order to reveal the nanocast oxide. Removal is often difficult as careful selection of reagent has to be considered. It has been widely reported in literature that silica is removed from template products by a wet chemical method, namely dissolving the silica in hydrofluoric acid (HF) or NaOH solution. For example, HF will dissolve SiO_2 but not silicon so it is possible to etch the SiO_2 with extreme selectivity to silicon. HF etching is by far the more aggressive technique and is commonly associated with silicon crystal and SiO_2 passivation etching in semiconductor and associated industries due to the precision of etch that can be achieved. However, given the extremely hazardous nature of this substance, NaOH is often used as an alternative when dissolving silica templates. It was realised previously within the Baker group that the removal of silica when producing template material, was often incomplete

particularly for ceria based oxides and that residual silica was present on nanocast materials despite several NaOH washes[56]. No quantitative mention of the residual silica has been found in the literature although some publications do refer to it qualitatively[57].

In order to make as pure a final product as possible, it would be ideal if no silica was present as this can in some instances poison its function as a catalyst or anode material due to its high mobility and propensity to act as an insulator even at low concentrations[58]. Likewise substituting the silicon with other elements such as fluorine may change the nature of the catalyst for better or worse depending on what the catalytic process involves. Any removal technique developed would need to avoid altering or dissolving the cerium oxide or SDC final product[48a].

Due to the known difficulties in achieving complete silica removal using wet chemical dissolution, a strategy to coat the wall matrix of the template with different terminal groups was deliberated. Two group terminations of methyl and amine were considered on the basis of being organic and therefore removed easily by thermal treatment. By having this intermediate group, it was proposed that the geminal Si-O-Ce species formed from the precursor-calcination conversion of the associated nitrates might be avoided. More specifically, the choice of methyl or amine termination is further complicated by the assortment of reagents available. A selection of which are highlighted in Figure 1-6. This choice is extensive, ranging from alkoxysilanes, chlorosilanes, disilazanes, organolithium and Grignard reagents – all of which have been reported as successfully functionalising silica materials. Even within each of these material types, there are subset considerations based on the stereo chemical implications for example triphenylchlorosilane, Figure 1-6 (d), is bulky on a molecular scale, and will influence the degree of surface coverage or even the specific placement within the silica channels to the extent that micropores and mesopores can be selectively modified or blocked.

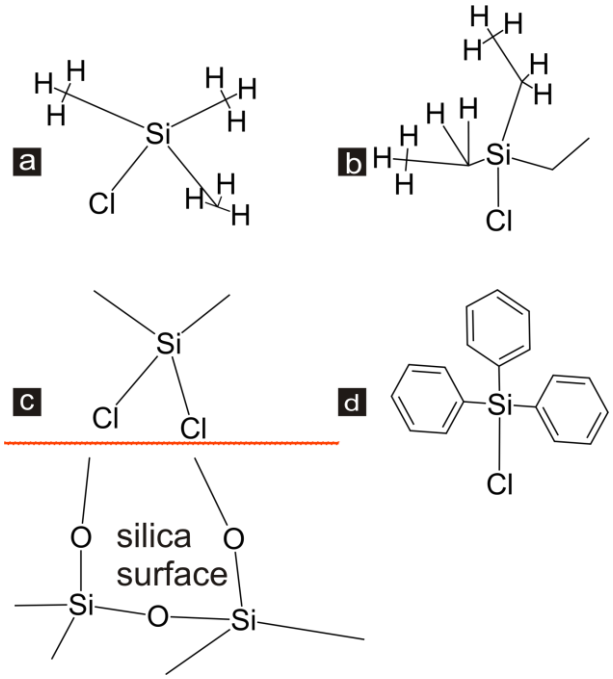

Figure 1-6: Different functionalising reagents (a) trimethylchlorosilane (b) triethylchlorosilane (c) dimethyldichlorosilane (d) triphenylchlorosilane.

The technique was found to be fraught with difficulties with great care required to avoid moisture. The procedure was susceptible to water interference such that use of anhydrous materials and drying of glassware and associated equipment was necessary in order to avoid self-condensation of the reagent.

In light of this review, objectives for this study were to develop facile methods in the production of samarium-doped ceria and gain a deeper understanding of the synthesis mechanisms through characterisation of materials. Specifically, the aim is to create materials with unique 3-dimensional structures that exhibit crystalline wall structures which are strong enough to withstand sintering effects of temperature. It is also desirable to maximise the porosity for reasons of mass gas transport and as a potential means to hold other catalytically active metals. To achieve maximum porosity, a crystalline network with highly ordered arrays of mesopores would be desired. This will hopefully create SDC materials with high mesoporous volumes beyond 0.3 cm^3g^{-1} and specific surface areas in the 150 m^2g^{-1} range. It is also hoped that these materials can be synthesised easily, in high purity and with potential for mass production.

Chapter 2

Analytical Techniques

2.1 Instrumentation

2.1.1 *Electron Microscopy*

The development and use of the microscope has proven to be fundamental in scientific research with the early use of microscopy based on light and glass optics to obtain the desired magnifications. The obvious advantage of using light is that magnified images are directly viewable to the observer. However, it was quickly realised that a limiting factor was one of resolution and it was not until the early twentieth century that electron radiation was utilised to improve and overcome the resolution limitations.

The fundamental limit to resolution in a system is determined by the diffraction resolution which in turn is limited by the wavelength of the imaging radiation. In practice aberrations and distortions limit the resolution of a microscope system. As an optical system uses light which can be described as particles with wave-light properties, fundamental physics states that the particles will have diffraction and interference and the passage through any aperture will create a spherical wavefront, Figure 2-1 A. Secondly, a source of light cannot be focused to a single point because of these effects of diffraction and interference and so the point achieved will be formed of concentric surrounding rings of decreasing intensity which is referred to as an Airy disk and shown diagrammatically in Figure 2-1 B.

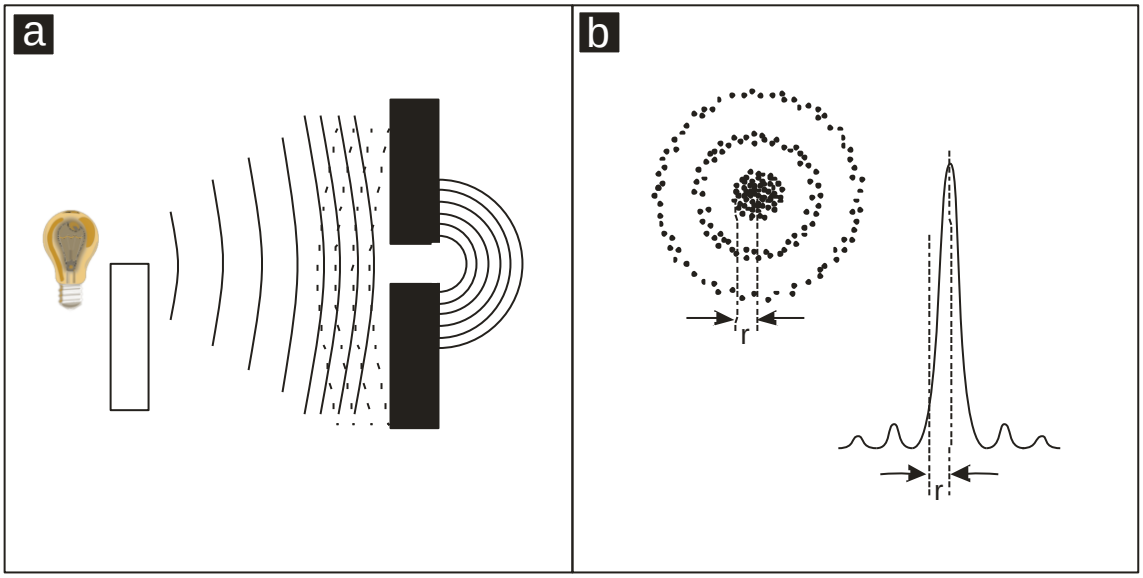

Figure 2-1: (a) The particle and wave duality of light dictates that any point source will be subject to interference and diffraction when impeded by an object such as a lens. (b) Representation of an Airy disk. The Intensity waveform and map showing the concentric circles of diminishing intensity with (**r**) representing the radius of the central disk which defines the resolution.

Using these principles of Airy resolution and wavelength, the Abbe equation (Eqn. 4) can be applied to determine the resolution (d).

$$d = \lambda / 2 n \sin \alpha \qquad \textit{Eqn. 4}$$

λ = wavelength

n = refraction index (of medium between lens and point source)

α = half aperture in radians

This equation can be simplified as:

$$d = \lambda / 2NA$$

(n sin α) is referred to as numerical aperture (NA)

$$d = 0.61\lambda / NA \qquad \textit{Eqn. 5}$$

The value 0.61 is calculated from the consideration of the Airy disk. It is not an absolute value and is based on an air medium. It is a value derived by considering the peak to trough values of the first order ring in the Airy disk (Figure 2-1).

This can be further expressed as:

$$d = 1.22\lambda / (NA(Obj) + NA(cond)) \qquad \textit{Eqn. 6}$$

Therefore, in light microscopy, a mid-range wavelength using a tungsten light source centred around 550 nm -which is a typical light source- will mean that in practical terms the absolute resolution is approximately 0.2 micrometres.

When these principles are applied to electron radiation then according to the De Broglie equation:

$$\lambda = h/mv \qquad \textit{Eqn. 7}$$

λ = wavelength

h = Planck's constant

m = mass of particle

v = velocity of particle

As eV (electron Volt) can be expressed by the classical physics equation:

$$eV = \frac{1}{2}mv^2 \qquad \textit{Eqn. 8}$$

Substitution into the equation can be expressed as ***Eqn. 9***

$$\lambda = \frac{1.23\text{nm}}{V^{\frac{1}{2}}}$$

Substitution of the Abbe equation (Eqn. 4) into the modified De Broglie equation (Eqn. 9) can be used to determine the resolution (Eqn. 10) for transmission electron microscopy (TEM) with the assumption that for very small angles, sin α approximates to α and n (refractive index) approximates to 1:

$$d = \frac{0.753}{\alpha V^{\frac{1}{2}}} \qquad \textit{Eqn. 10}$$

d = resolution (nm)

α = half aperture

V = accelerating voltage

Therefore the theoretical resolution of a 200kV TEM would equate to 0.12 nm

2.1.1.1 Transmission Electron Microscopy (TEM)

Since the first design of a transmission electron microscope by Ruska and Knoll in 1931[59], a steady improvement in the resolution has occurred over the decades. Despite the incremental improvements, the basic components of the microscope have not changed and include five major components. These are: column for the generation and control of electrons, a high vacuum system, control electronics, software integration and a viewing platform. The limitation of resolution is due to spherical aberration, chromatic aberration and astigmatism but with the introduction of aberration-corrected electron lenses, both the spatial resolution and the image quality in transmission electron microscopy have been improved such that atomic scale imaging has become a reality[60].

The diagram shown in Figure 2-2 details the layout of the TEM used and gives an indication of the size of the instrument and the main working components. As mentioned, the instrument relies on the control of an electron beam and the diagram highlights just how much lens control is required.

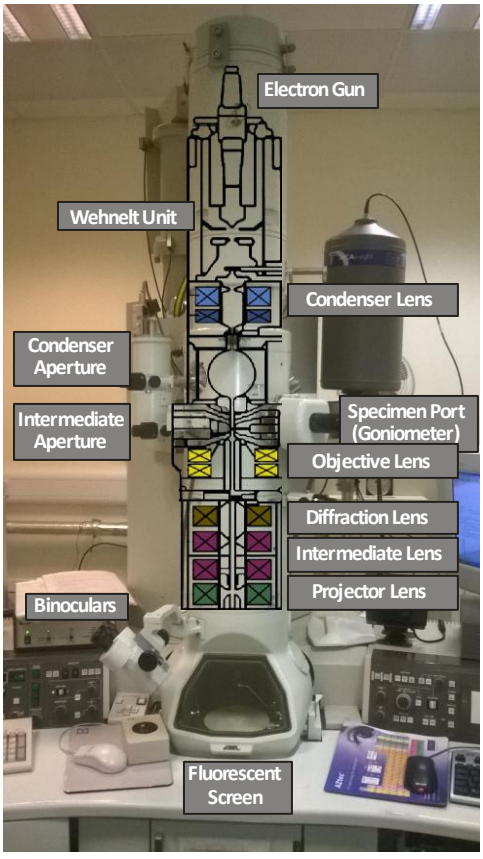

Figure 2-2: The components of a JEOL JEM 2011 transmission electron microscope.

The TEM in contrast to light microscopes uses a beam of electrons in place of a beam of light. The electron beam source is produced by heating a filament (typically W or LaB_6) and accelerating the electron emissions using voltages ranging from 60 to 200 kV. As these

electrons are negatively charged particles they can be controlled using electromagnets. By varying the strength of these lenses using software control, the magnification of the formed image can be changed. Also, collision with charged molecules of air will interact and deflect electrons creating beam distortion therefore the beam path of the microscope must be evacuated of air. As electron beams are invisible to the eye, the images they form are revealed on a fluorescent screen and can be photographed or recorded using a digital CCD camera.

- **Sample Preparation**

One limitation of TEM is that the specimen must be extremely thin for the electrons to pass through it and create an image, so careful preparation is required. Different techniques have been developed but the simplest and most efficient method is to catch small micron sized particles by way of swiping through a suspension in solvent medium. This is the main method of preparation employed in this study. However ultra-thin sections of approximately 100 nm thick were prepared using an ultra-microtome. This is a technique usually employed in the preparation of ultra-thin sections of biological samples. However, these samples have little contrast and often they must be stained with electron-absorbing heavy metal salts to provide this necessary contrast. With the preparation method presented here, the material should require no further treatment with the expectation that cross sectional information of the 3 dimensional structures could be obtained.

- **Digital Diffraction Pattern**

In conjunction with TEM, digital diffraction patterns (DDPs) were generated as a method of analysing structures for mesopore ***d***-spacings and pore formation. If the object of interest has a similar periodicity to the diffraction beam wavelength then the generated peaks would become smeared out (broadened). This is an effect referred to as Scherrer broadening. Electron diffraction as a technique has therefore an advantage over X-ray diffraction in the nm range. With electrons being smaller in wavelength in comparison with X-rays, better resolution of ordered spacing present in mesoporous materials should be possible. If short range periodicity of structure was present as often occurs in amorphous solids such as ordered mesoporous silica or carbon, then the periodicity can act as a diffraction grating, scattering electrons in a predictable manner. This will give rise to sharp spots at distances inversely proportional to the lattice spacing and so working back from the observed diffraction pattern, information can be gained regarding ***d***-spacing. Two techniques are available in transmission electron microscopy to generate such patterns and

are known as digital diffraction and selected area electron diffraction (SAED). The digital diffraction method is a mathematical interpretation using a discrete Fourier transformation (DFT) which generates a DDP. This DFT is a mathematical function to convert the observed electron frequency into a discrete point and is computed by the application of an algorithm known as a Fast Fourier Transformation. As the DDP is a calculated pattern, it has an advantage over the affiliated SAED technique of a low intensity (000) Miller index spot from the un-diffracted beam allowing ***d***-spacings to be better resolved.

2.1.1.2 Scanning Electron Microscopy (SEM)

SEM is primarily a method for obtaining structural and morphological information through interaction of an incident electron beam with a sample. An electron beam of a single energy is generated thermionically or by field emission. These generated electrons are controlled using a series of electromagnetic lenses such that they are collimated and focused under vacuum conditions into a single beam. By controlling electrons into a fine streaming beam under vacuum conditions they can be made to travel (accelerated) in a linear column until they come in contact with any substance. This contact is occurring on the atomic scale and statistically the majority of collisions will be with the outer shell electrons of the atom(s) being bombarded whereby these valence electrons are ejected as secondary electrons.

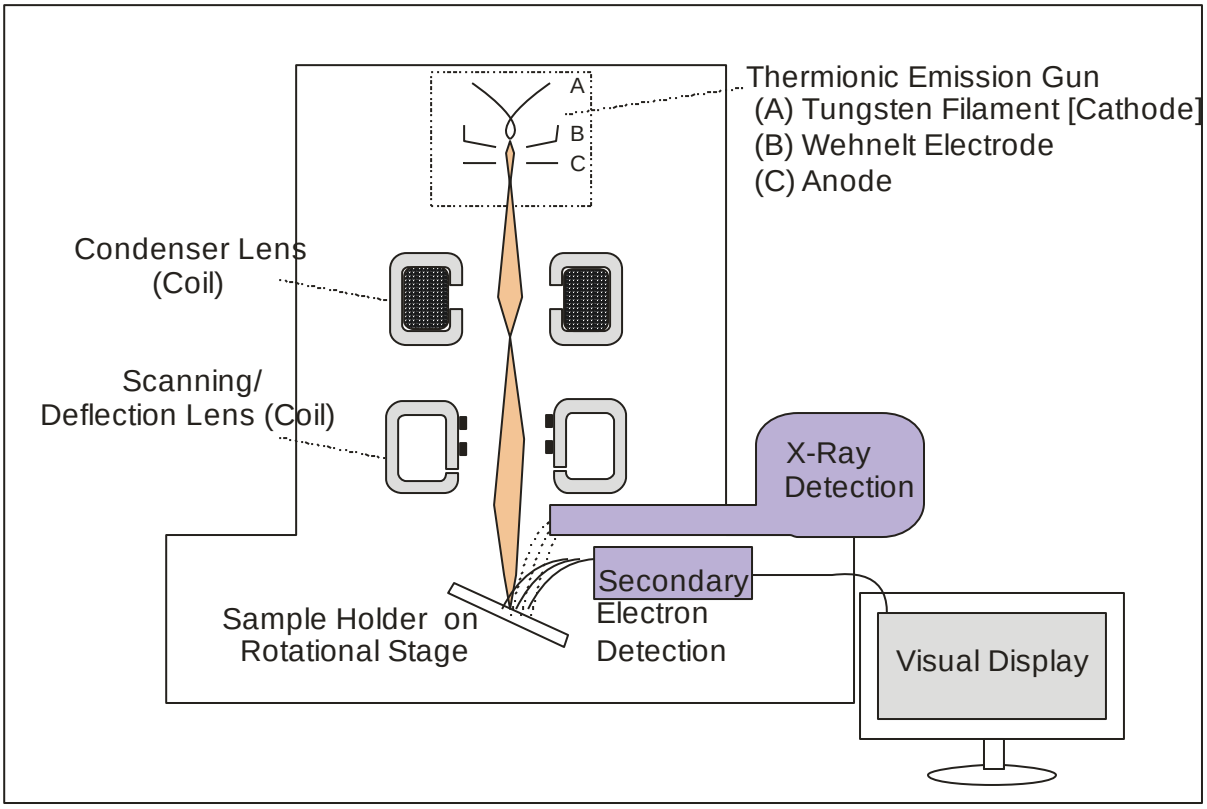

Figure 2-3: Schematic of basic SEM construction showing electron beam formation.

As materials have a 3 dimensional profile and the incident electrons have an associated energy, they can penetrate into the material as a factor of beam energy, however by having a selective energy of incident beam, a balance can be struck between depth of diffusion whereby energy is internally dissipated and a detectable number of secondary electrons are liberated (Figure 2-4). As it is the detection of these escaped secondary electrons this technique will constitute a surface profile and can be converted into a visual image (Figure 2-3).

2.1.2 *Energy Dispersive X-Ray Spectroscopy (EDX or EDS)*

EDX is a non-destructive analytical tool that has advantages of allowing very quick elemental analysis of solid samples. An EDX spectrometer can be added to a TEM or SEM system. The interaction of the monochromated electron beam in these instruments generates X-rays whose frequencies are characteristic of the elements present in the sample.

The displacement of elemental electrons from the atomic interaction with the electron beam generates characteristic X-rays from the excitation and relaxation of shell electrons. This allows for semi-quantitative and qualitative elemental analysis as each X-ray emitted is dependent on discrete energy levels with the shell characteristic associated with each element. A spectrum of K, L and M lines generated from the K, L and M shells respectively will be generated with heavier elements emitting X-rays of higher energy. As the spectral lines have an associated intensity which is proportional to elemental concentration and by comparing against a known standard, quantitative analysis can be performed. EDX is however limited by not being able to detect elements lighter than beryllium and quantitatively by the background noise of X-rays generated by deceleration of the primary electron source.

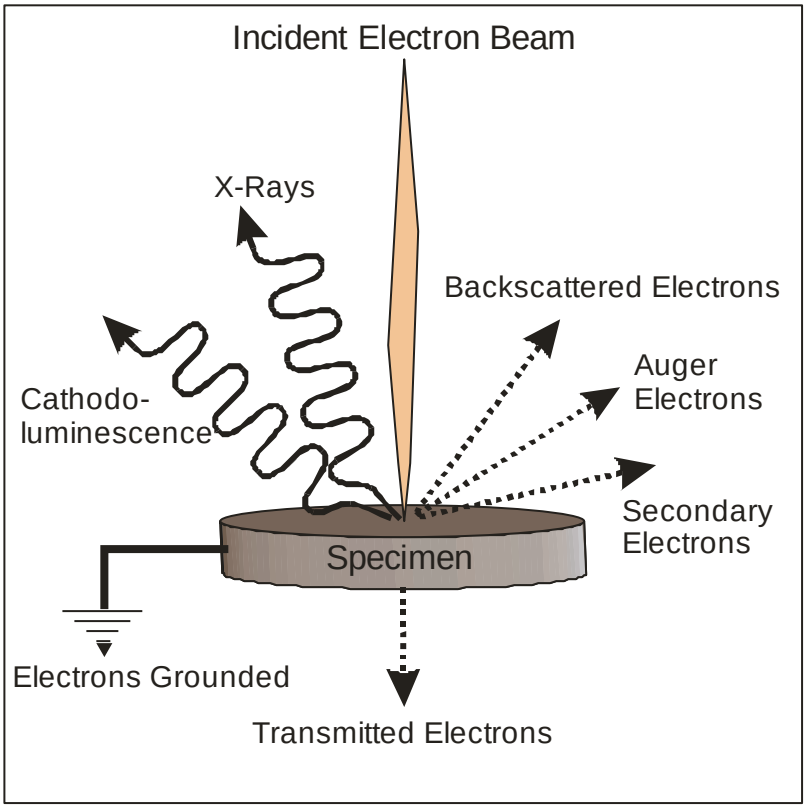

Figure 2-4: Emission of various electromagnetic waves and electrons from the electron beam- specimen interaction.

2.1.3 *Gas Sorption*

Two common techniques available for surface and porosity characterisation involve chemisorption or physisorption analysis. The first technique, chemisorption analysis is an important tool in catalysis characterisation. It is a useful technique to characterise materials in respect to metal dispersion, the active metal surface area and associated size, surface acidity etc. Chemisorption as defined by IUPAC "Adsorption which results from chemical bond formation (strong interaction) between the adsorbent and the adsorbate in a monolayer on the surface"[61] is however fundamentally different from physisorption.

Physisorption analysis is a related technique but does not involve strong (chemical bond) interactions but instead measures the weaker interaction involving van der Waal forces and therefore exploits the physical changes when a gas condenses through the stages of monolayer, multi-layer and liquid condensate formation. Solid materials that enclose a pore system are difficult to analyse in a non-destructive method but by using the physical phenomenon of gas adsorption it is possible to learn about the pore characteristics of a material in just such a manner. By carefully controlling the gas uptake and monitoring it relative to pressure, a physisorption isotherm can be produced both for the adsorption and desorption of the material. This isotherm can be used to obtain information related to the

pore structure such as specific surface area, meso and macropore size distribution and volume, micropore volume or the pore classification – i.e. ordered, disordered or even non-existing.

A typical analysis will start with the removal of adsorbed contaminants such as water and carbon dioxide by pre-treatment using heat, vacuum and possibly a flowing gas. The material to be analysed is cryogenically cooled and maintained at 77K using liquid nitrogen. This allows the N_2 gas equivalent to be introduced as an adsorptive in controlled doses. After allowing pressure to equilibrate, the amount of gas adsorbed is calculated. The quantity adsorbed for a range of pressures –and fixed temperature- can be used to define an isotherm. Although nitrogen is typically used for reasons of cost, chemical inertness and instrument compatibility, other gases either as nitrogen mixtures or in isolation such as Ar, Kr, He, CO, CO_2, H_2 and H_2O can be employed, with alternative benefits. For example Argon being smaller than the diatomic nitrogen can fill pores in the micropore range of 0.5 to 1 nm; water being smaller still, can be used to determine pore size in the ultra-micropore range[62].

2.1.3.1 Pore Classification

IUPAC have identified and defined physisorption curves that describe 6 classical profiles observed (Figure 2-5 A) when a material has a specific porous structure.[63]

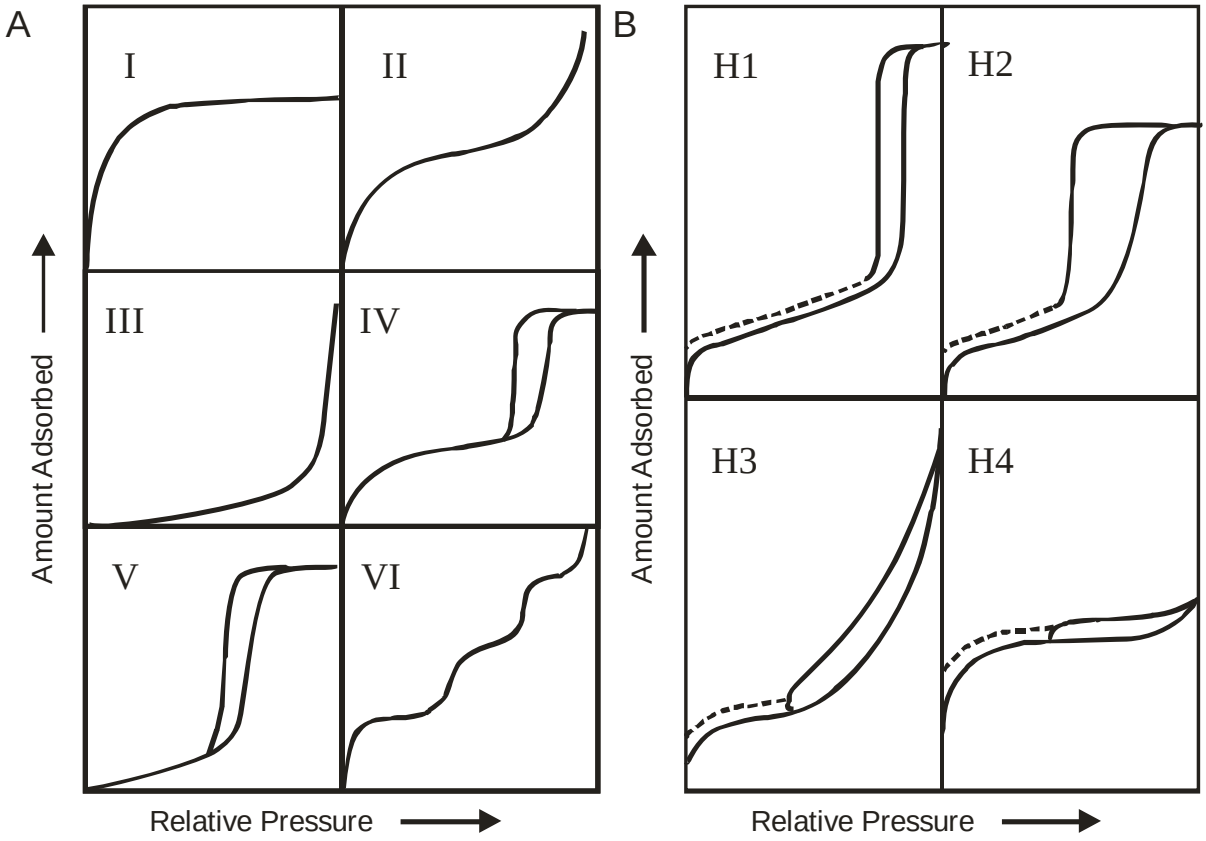

Figure 2-5: IUPAC defined (A) physisorption isotherms (B) sorption hysteresis loops.

The IUPAC classifications are defined as follows:

- Type I isotherms are characteristic of microporous (<2 nm pore diameter) solids. Small pores lead to high adsorption at low pressure and there is no hysteresis observed.
- Type II isotherms are typical of non-porous and macroporous (>50 nm diameter) materials and also carbons with both micro- and mesopores. Monolayer formation at low pressure is followed by a linear profile thereafter, unlimited multilayer formation occurs.
- Type III isotherms are characteristic of materials that have weak adsorbate-adsorbent interactions and therefore do not adsorb at low pressures. Once nucleated at higher pressures, the stronger adsorbate-adsorbate interactions become the driving force for adsorption. There is no linear profile. Materials that give a Type III hysteresis are not common (e.g. nitrogen adsorbing on polyethylene).
- Type IV isotherms are typical of mesoporous solids. Monolayers are formed at low pressures followed by a linear profile. Pore filling occurs at higher pressures with hysteresis observed during desorption. At higher pressures multilayer formation may be observed.
- Type V isotherms are related to Type III but the materials have some mesopores which give rise to a blend of the Type III and Type IV curves.
- Type VI isotherms have stepwise multilayer adsorption where each step represents the volume of adsorbate required to cover a single layer of the sample. An example of a Type VI isotherm is argon or krypton adsorbing on graphitised carbon black.

The IUPAC definition for the hysteresis (Figure 2-5 B) is defined as follows:

- Type H1: Uniform spheres in a regular array leading to a narrow pore size distribution (Type H1).
- Type H2: Some corpuscular systems, such as silica aerogels, with a large distribution of pore-size and shape (Type H2). There are conflicting literature reports regarding the types of pore systems the H2 hysteresis may refer. One interpretation is a system with bottlenecked pores in which gas condenses in the pores at high pressure while desorption is limited by reliquefaction in the smaller channels.
- Type H3: Plate-like particles giving rise to slit-shaped pores with unlimited adsorption at high P/P_0 (equilibrium relative pressure).
- Type H4: Narrow slit-shaped pores with a Type I isotherm and limited adsorption at high P/P_0 (equilibrium relative pressure) indicating microporosity.

2.1.3.2 Isotherm Interpretation

The materials analysed in this thesis often produced a Type IV physisorption isotherm. This type of profile has three distinct parts associated with it. The first part relates to low pressure uptake and is typical of monolayer formation and can also be associated with micropore volume. The second part of the isotherm has a characteristic flattening or gradual incline where multilayer formation is occurring. The main characteristic of a Type IV curve is the hysteresis loop between adsorption and desorption profiles which will occur between the intermediate and high pressure range and is indicative of mesopore filling and emptying.

Hysteresis

The mechanism by which mesopores fill is capillary condensation (cylindrical meniscus) however when these pores subsequently empty, the mechanism is a hemispherical meniscus evaporation which has a different associated energy and so gives rise to the hysteresis effect. The profile can be classified against the IUPAC definitions and BJH analysis used to interpret the data.

Langmuir, BET and surface area theory

To calculate the surface area of a material, an analysis of the monolayer coverage based on the Langmuir equation will yield such information and is useful for low gas uptake. However an extension of this monolayer concept, known as the BET equation can be applied which also takes account of multilayer formation expressing the gas adsorption as a function of specific surface area in m^2g^{-1}. The BET equation is an acronym of the researchers Brunauer, Emmett and Teller who first developed the mathematical model.

BJH theory

BJH is an acronym of the Barrett, Joyner and Halenda researchers who first developed a mathematical model as a way of expressing pore diameter, distribution and volume as

determined from the complete filling of pores by gas adsorption. It is a modification of the Kelvin equation which predicts the pressure at which the adsorbate will spontaneously condense (and evaporate). By analysing the adsorptive lost from the isotherm, information such as the thickness of the adsorbed layer remaining on the pore walls can be calculated. Using this information and choosing a pore shape model, average pore size can subsequently be calculated.

t-plot theory

The de Boer t-plot method is a way of estimating micropore volume based on statistical relationships using standard isotherms from non-porous reference samples. The micropore volume is observed as a sharp gas uptake at low pressures as shown in the Type I isotherm.

Interferences

- **Tensile Strength Effect**

While it is possible to interpret data in either the adsorption or desorption isotherm, a known effect described as the Tensile Strength Effect (TSE)[64] is a phenomenon that occurs with materials in the 3.8 nm range of the desorption branch of a samples sorption analysis. It is induced by the forced closure of the hysteresis loop at an equilibrated relative pressure of P/P_0 ≈0.45 and translates into an artificial peak from the BJH calculation. In essence the emptying of condensate from larger pores can reach a critical meniscus size of approximately 4 nm whereby the tensile effects created by interaction of the pore walls leads to instability of the condensate during which the condensate will cease to exist. If the material under analysis exhibits genuine porosity in this range then pore size distribution (PSD) will be evident in both sorption isotherms. Pores under 3.8 nm are below this critical meniscus value and are therefore unaffected by this phenomenon.

- **Pore Network Effects**

Associated with TSE is the pore network effect which magnifies the effect of the forced closure of the hysteresis loop. This occurs when larger pores are interconnected to smaller pores and therefore must evacuate at the rate dictated by the opening of the smaller pore. This type of interconnection is classically described as “ink well” in shape. Consequently, the desorption branch will show step wise decrease(s) in the isotherm profile and a reporting of the PSD towards lower pore size.

2.1.4 *UV-Vis Spectroscopy*

The classic technique of ultraviolet-visible (UV-Vis) spectroscopy is used to measure the energy absorbed by a molecule to drive electronic excitations. This type of absorbance is

often perceptible as the colour of a material due to it falling within the visible region of the spectrum. However, the purpose of the UV-Vis spectrometer in this instance is to utilise a wavelength that can be chosen to avoid interaction with the chosen solvent while at the same time be measured for its intensity. In essence, the total transmittance measured through a colloidal suspension as a summation of both species absorbance and diffuse/specular reflectance. As the majority of interaction is presumed to be from light scattering, the technique is not dissimilar to dynamic light scattering (DLS) methods but while DLS is primarily used to analyse particle size characteristics, the purpose of this technique is to determine concentration of silica species as a factor of their presence in solution i.e. solubility given that the particles are stable in suspension and exhibiting Brownian motion.

2.1.4.1 Beer-Lambert Law

The Beer-Lambert law is shown in Eqn. 11 and describes how the proportion of light absorbed is related to the concentration and sample length. Essentially it compares the original light intensity passing through a sample in solution to that of the exiting light intensity. The passage of the light will be affected by the number of absorbing species for any given wavelength and the path length (thickness) of the solution. Knowing the cell length, the concentration of the sample under test and the measured intensities; the molar absorption coefficient can be calculated. This allows an unknown concentration to be calculated. The cell length is normally a fixed path length of 1 cm.

$$A = \log_{10}\frac{I_o}{I} = \varepsilon\, l\, c \qquad \textit{Eqn. 11}$$

Where	A	Absorbance
	I	Intensity of light through sample cell (Wm^{-2})
	I_o	Intensity of light through reference cell (Wm^{-2})
	ε	Molar absorption coefficient ($Lmol^{-1}cm^{-1}$)
	l	Length of cell (cm)
	c	Concentration of solution ($Lmol^{-1}$)

A second approach is to prepare and test a series of known concentrations and plot the measured values in order to generate a calibration curve. According to the Beer-Lambert Law the absorbance is proportional to concentration which would normally produce a

straight line. This is true for solutions that are dilute but for solutions of higher concentration discrepancies occur such that a curve may be observed under these circumstances.

2.1.5 *X-Ray Diffraction*

As previously mentioned in Figure 2-1, diffraction is a physical phenomenon that occurs when incident radiation is scattered by a diffracting object or slit. As atoms can be considered diffracting objects, they diffract incident radiation. If the atomic arrangement is not ordered, each atom will produce its own diffraction scatter at a non-specific angle which when combined with its neighbouring atoms will produce an incomprehensible series of interactions. If, however, atoms are arranged in a periodic array as found in a crystal lattice, each atom will diffract incident radiation to produce a cumulative series of constructive (and destructive) interference patterns. The greater the long range order, the more intense the signal will be due to the additive nature of interference culminating in a diffraction pattern of the three-dimensional periodic structure. X-ray radiation is used because its wavelength is similar to the interplanar distance in atomic lattices. The relationship which describes the conditions necessary to make the phases coincide is expressed in Eqn. 12 and is referred to as Braggs Law. In Figure 2-6, Bragg's Law is illustrated. Incident radiation strikes an arrangement of atoms as found in a crystal lattice. The incident radiation strikes the material in phase and in parallel. The first beam is deflected by an angle (Θ) whereas another beam may continue into the second layer until itself being scattered. As this second beam has travelled a greater pathlength, the extra distance must be an integral (n) multiple of the wavelength (λ) for the phases of the two reflected beams to be the same. Therefore, when two beams are diffracted in phase, Braggs Law will be satisfied and the distance between the reflecting crystallographic planes (*d*-spacing) can be derived.

$$n\lambda = 2\,d \sin\Theta \qquad \textbf{\textit{Eqn. 12}}$$

λ = wavelength

n = integer (multiple of the wavelength)

d = distance between crystal planes

Θ = angle of diffracted wave

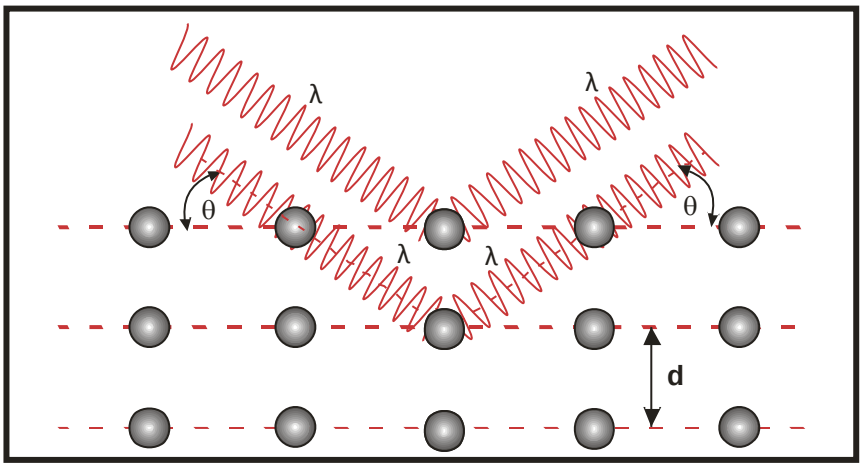

Figure 2-6: Bragg diffraction showing two beams of identical wavelength and phase.

2.1.5.1 Small Angle XRD

While amorphous materials do not produce meaningful interference at the atomic level, materials that have a periodic array of voids such as the repetitive porous nature of silica templates will be subject to the same diffraction principles as that applied to a crystal structure. Repetitive structural dimensions of the nanometre range can be measured at small angles. θ (Figure 2-6) is inversely proportional to ***d.*** For example, scanning 2Θ from 0.5 to 5° covers a range of ***d***-spacings from 17.6 to 1.8 nm respectively.

Due to the random orientation and partial ordering of samples, the observed signal will be effected and is therefore an experimental consideration. This is due to spatial averaging and only the materials of highest long range order will contribute observable signals.

2.1.5.2 Nuclear Magnetic Resonance

Nuclear magnetic resonance is a spectroscopic technique that exploits the magnetic properties of atomic nuclei. By placing nuclei in a strong magnetic field and subjecting them to radiation in the radiofrequency (RF) range they will absorb the RF energy and then subsequently dissipate that energy. This energy sorption from atoms of a chosen element is isotope specific and can be used to reveal information regarding the molecular chemical environment.

Nuclear spin

Given that nuclei are positively charged and have quantum mechanical properties of spin (I), they behave like tiny bar magnets as they have a magnetic moment and therefore a magnetic field. This is often referred to as nuclear spin. If a nucleus has an odd mass number then it will have a half-integer spin whereas an even mass number will have integer spin.

Normally, an atom with integer spin (I=0) will not have an associated magnetic moment and this often represents the main isotope of an element. For example, in the analysis of silicon, the main ^{28}Si isotopes which have an associated abundance of 92.23 % will not produce an NMR signal. However, the ^{29}Si isotopes can be analysed as they will produce a signal given that they have I of a ½. Unlike more naturally abundant half-integer spin isotopes such as ^{1}H, the natural abundance of ^{29}Si is unfortunately only 4.67 % therefore it will produce a much reduced signal although using instrumental techniques such as cross polarisation, meaningful analysis is still possible.

Relaxation

When placed into a stronger magnetic field, these tiny bar magnets (nuclei) will become aligned in one of two positions with each position being opposite to the other. The alignment of these two positions has an associated energy difference (ΔE) which can be increased by placing in a strong magnetic field typically of the 5 to 10 Tesla range. To move from one energy state to the other takes a discrete amount of energy (Larmor frequency) and is affected not only by the type of nucleus but the chemical environment the nucleus is in. The measured signal of interest is actually the difference of the sum of all the individual spins from the two aligned positions. This difference occurs as one position is of lower energy than the other and therefore slightly favoured. This sum difference yields a magnetisation which determines the NMR signal, not the magnetic moment of the individual nuclei. By applying only a pulse of RF energy across the resonance frequency range, there will be a subsequent intra and inter-molecular relaxation referred to as free induction decay which can be measured. Repeated pulsations allows for averaged data to be collected helping improve signal to noise ratios.

Chemical Shift

As mentioned, the Larmor frequency is different for nuclei of different elements; however this RF frequency can be shifted due to differences in the local magnetic field caused by the chemical environment of the isotope of interest. In order to standardise measurements, values are reported in respect to a reference signal, the signals of interest will move relative to this reference and is described as chemical shift. As each isotope is affected by its bonded neighbours, subtle shifts will occur in resonance allowing functional groups and entire molecular structures to be identified. This change in frequency is usually in the Hz range within a spectrometer frequency of MHz and so the shift as a ratio is usually described in parts per million.

Magic Angle Spinning

Sample preparation for NMR spectroscopy can be in the form of liquid or solid state. In conventional NMR, liquid preparation is used with the sample being dissolved in a compatible solvent and placed into a dedicated thin walled borosilicate tube. With this solution state NMR, the anisotropic interactions are time-averaged due to the freedom of the molecular motion. In solid state however, the molecular motion is restricted and a technique known as Magic Angle Spinning (MAS-NMR) is employed that will further enhance the resolution of the generated spectrum. This is achieved by rotating the sample at a specific angle to the static magnetic field of the instrument thus suppressing the anisotropic dipolar interactions by introducing artificial motions of the solid. By spinning in the kHz range and at an angle of $Cos^2\theta_m = 1/3$ (θ=54.74°), averaging of the time–dependant signal which relates to absorption of energy can be employed.

^{28}Si MAS-NMR

Taking silica template as an example, the silicon functional groups can be determined qualitatively. The nomenclature[65] for the silicate anion is Q^n where n represents the four available bonds as connected to oxygen atoms. A pictorial representation of these functional groups in a silica template matrix is show in Figure 2-7 where Q^2 represents two siloxane and two silanol groups, Q^3 represents three siloxane and one silanol group with Q^4 representing four siloxane groups. Q^2 and Q^3 would normally be found at the matrix surface whereas Q^4 would comprise the majority of the bulk structure.

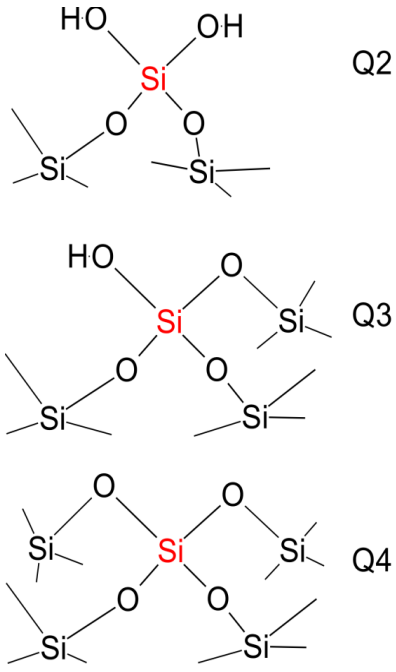

Figure 2-7: Schematic representation of the three Si environments which give rise to the Q2, Q3 and Q4 resonances in the ^{29}Si-MAS-NMR spectra.

2.2 Apparatus

2.2.1 *Ultra-Microtomy*

For transmission electron microscopy it is necessary to have a thin representative sample. Typically, for fine powder samples this is achieved by sweeping a grid through a solvent mixture loaded with suspended nano-particulate material. While this is an effective, quick and cheap method of loading a holey carbon grid for analysis it assumes that the material represents the bulk condition. A holey carbon grid is a copper grid usually 15 mm^2 in diameter covered by a fine mesh of carbon prepared in such a way that the carbon forms with holes of a specific diameter. An alternative method is to prepare a specimen using an ultra-microtomy technique. This is a method of slicing a cross section through material of interest and suspending the obtained thin section on the holey carbon grid. Sections as thin as 35 nm up to a few microns in thickness can be achieved. This method is used to prepare sections of fragile samples usually of a biological nature. The material to be sectioned in the context of these studies is amorphous silica which is naturally presented as a powder and can be prepared following two strategies. The first involves encapsulation of the powder and is achieved by artificially introducing a holding medium in the form of cyanoacrylate resin and sectioning through the complete resin-powder mould. Sometimes however it can be difficult to achieve consistent sectioning and so it is also feasible to cement compacted powder onto a microtome block and perform a dry-cut. The method chosen is dependent on the materials properties and the quality of the section is a function of the skill and experience of the operator and parameters such as cutting speed, knife angle and knife material. Although microtomy can be carried out manually, this is only for observations under light microscopy. Typically ultra-microtomy is required for the preparation of electron microscopy samples. Ultra-microtomy sectioning is carried out under machine control as this allows for a very thin and repeatable section of a desired thickness to be prepared concomitant with the mechanical precision and the quality of the knife, which for inorganic materials is made of gem quality diamond. During ultra-microtome sectioning, the cut sections are collected on the surface of a liquid with consecutive sections forming a ribbon. Transfer of these can be achieved using the Hartweig method[66] which uses an inventive approach of having an eyelash glued onto a toothpick with which ribbon sections can be lifted. A more commercial approach is to use the patented Perfect Loop™ which has been designed to allow a similar approach such that the ribbon cross section can be transferred with minimal folding occurring[67].

2.2.2 *Vacuum Impregnation (VI)*

As a method of impregnating mesoporous hard templates, a liquid phase would normally be added to the solid template and mulled by way of a mortar and pestle. This intimate mixture will allow the liquid precursor to fill the pores channels through a capillary mechanism and is referred to as an incipient wetness technique (IWIT).

An alternative technique involves the use of a vacuum to create a pressure differential in an enclosed environment of template and liquid impregnate. When this closed environment is returned to atmospheric pressure, the inrush of air will function as a piston exerting a pressure on the liquid interface such that the liquid is forced into the template porous structure. The main components of the VI system: Tubing, valves, test tube and dropping funnel are shown in Figure 2-8. The interface between test tube and vacuum pump is protected by a silica gel trap. The equipment configuration allows the test tube chamber containing powder or pellet template to be evacuated separately from the liquid precursor which is contained in the dropping funnel. The test tube chamber can also be selectively subjected to vacuum or atmospheric pressures by way of the integrated valves. By having a sealed graduated dropping funnel on top, the liquid precursor can be opened in a controlled manner to allow ingress of the solution into the test tube. As the test tube is under vacuum conditions, careful opening of valve has to be exercised in order to successfully control the amount of liquid applied.

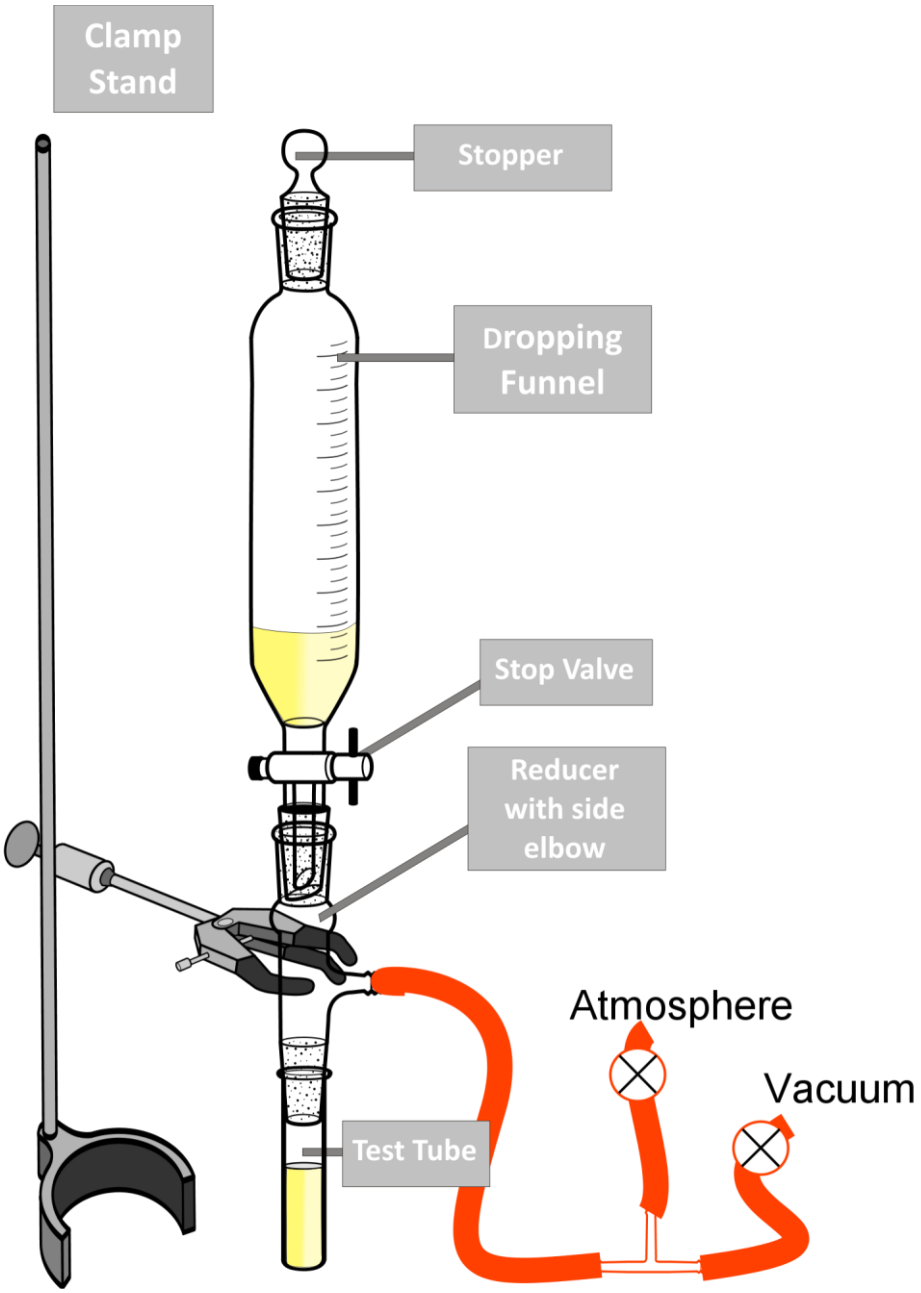

Figure 2-8: Typical setup for vacuum impregnation technique.

2.2.3 *Ultra-Centrifugation*

This is a technique that separates the solids from a liquid medium and is an alternative to more traditional Büchner filtration methods. Unlike standard centrifugation which is typically restrained to below 5,000 rpm, ultra-centrifuges can reach speeds up to 50,000 rpm. This tenfold increase in speed represents a much greater experienced relative centrifugal field (RCF) - *g* force - which at maximum speed will be in the region of 200,000 *g*. The extreme force is possible due to samples being rotationally driven in either swing buckets or fixed rotor heads under vacuum conditions. However such speeds have an associated high kinetic (rotational) energy and risk of serious damage and injury. Safety

features are therefore required in the form of strict maintenance including a lifetime of component schedule due to induced metal fatigue as well as operational interlocks and in-built shielding in case of catastrophic failure. It is also necessary to operate the sample loading in a balanced mode to prevent any weight skew of the rotational axis and correct use of rotor heads and buckets specifically rated for the model unit.

As there is a direct relationship between the rotational speed and the increasing frictional force from the surrounding atmosphere, drag and heat generation are an issue. The use of vacuum substantially reduces these problems as well as allowing control of the temperature of the sample (more critical in a biological context). In general, solids separate out of fluids to create a sedimentary layer at the base of the container in which the fluid is held. Sedimentation is a process whereby gravity (1-*g*) will act upon the mass of a particle as a force and will direct that particle along an axis of travel parallel to the force vector – towards the earth's core in the case of natural gravity. As the force of 1 *g* is fixed, this translates into long periods of time for finer material to settle out with the further inconvenience that particles of the size 0.1 μ or less will be held in Brownian suspension. Augmentation of the force of gravity with centrifugal force can drive the solid towards the sedimentation layer, the result of which is that smaller particles can be retrieved – typically of 10 nm in size and at a much faster rate than that experienced in normal processes. An expression relating these variables is defined by Stokes law (Eqn. 13) and can be used to find a qualitative distribution of the diameter of spherical particles in a sample as a consequence.

Stokes Law

Force of viscosity on a sphere ($\mathbf{F_D}$) **=** $6 \pi \mu R \nu$ ***Eqn. 13***

μ : Dynamic viscosity ($kgms^{-1}$)

R : Radius of spherical object (m)

ν : Particle velocity (ms^{-1})

Chapter 3

Experimental Procedures: Instruments

3.1 Instrumentation

3.1.1 *TEM*

TEM images were obtained using a JEOL JEM 2011 instrument operating with a LaB_6 filament at an accelerating voltage of 200 kV. The images were captured digitally using DigitalMicrograph 3.4.4 software and Gatan CCD camera.

Standard imaging was performed using a single tilt holder with X movement of ± 24 degrees and on occasion a double tilt holder with a ± 24 degrees movement in the X-axis and ±24 degrees in the Y-axis.

Elemental mapping and point source analysis was performed using the EDS setting of the TEM interlinked with an Oxford Instruments Link SemiStem in conjunction with an Oxford Instruments X-ray analysis ISIS 300 detector.

Samples were prepared by taking a few milligrams of powder that was a homogenous representation of the bulk sample and suspending it in a few millilitres of acetone in a vial. This vial was then subjected to ultrasound for a period of five minutes before being allowed to stand for ten minutes allowing a particle gradient to be established. The finer material in the top of the liquid suspension was sampled by pulling a copper 300-mesh holey carbon grid through the top of the suspension. This procedure was repeated three times with 30 min intervals between swipes during which the grid was placed under a halogen lamp to gently dry off the solvent. The final drying step was performed for at least 8 h under the lamp to ensure complete solvent removal.

In order to minimise contamination of samples during TEM sessions (mainly carbon from organic residue built up on the sample during irradiation with the electron beam), a liquid nitrogen cold finger was commonly used.

3.1.2 *SEM*

SEM imaging and analysis was performed using a Jeol JSM-5600 and Jeol proprietary software on a Windows™ 95 platform. A tungsten filament electron source at accelerating voltages from 0.5 to 30 kV was employed. Images were captured using an integrated digital camera. Samples were prepared by dispersing a few micrograms of powder onto a carbon adhesive pad that was placed onto a brass stub designed for an SEM single or quadruple sample holder. The SEM was primarily used as a mechanism to obtain elemental information by way of energy dispersive X-ray spectroscopy (EDX). Three modes of elemental analysis were available from the integrated EDX system: Spectral analysis, Point analysis and Elemental mapping. Semi-quantitative and qualitative elemental analysis were performed by way of an Oxford Instruments X-ray analysis ISIS 300 detector. To ensure a high signal count, the SEM instrument conditions were optimised by setting the sample at 18° tilt angle towards the detector with 10 min acquisition time, spot width of 27 and 30 kV accelerating voltage. No conductive coating was applied to samples as it was not required for the EDX analysis.

3.1.3 *Surface and Porosity Analysis*

Surface analysis and porosity was investigated using a Micrometrics TriStar II 3020 instrument with liquid nitrogen at 77K. Samples were prepared by degassing under vacuum for 6 h minimum at 110°C. Static level control – a technique to control the errors associated with free-space was performed as standard. This employs the use of an isothermal jacket which acts as a liquid nitrogen wick to maintain a constant temperature around the sample tube. A glass filler rod was also employed within the tube to reduce free space. The specific surface area was determined by BET adsorption isotherm calculation using Micromeritics v1.01 software. Similarly, interpretation of the isotherm reveals details about average pore size and shape. BJH (Barrett, Joyner and Halenda) was employed for calculating the specific pore size distribution as described by the Micromeritics publication by Webb[68] and the t-plot method was used to obtain micropore volume.

3.1.4 *UV-Vis Spectroscopy*

Spectroscopic data were collected on a Perkin Elmer Lambda 35 unit using dual beam configuration. As the initial conditions of UV-Visible testing were unknown, a sample scan over the entire wavelength range of 900 to 300 nm was initially performed to determine the optimal absorbance/ transmittance. On the basis of this, subsequent samples were analysed

over a much shorter wavelength range at the 600 nm abscissa value. The cuvettes used were UV-Vis transparent plastic for testing the solution of silica templates as quartz also being silica based could be an interference.

3.1.5 *X-Ray Diffraction (XRD)*

Powder XRD diffraction patterns were recorded using a PANalytical Empyrean Diffractometer in reflectance geometry using Cu $K\alpha_1$ radiation (wavelength $\boldsymbol{\lambda}$ = 0.1540598 nm). Diffraction data were recorded in the range 2θ = 5 - 90° with a step size of 0.0167°. The powder samples were prepared by pressing them into the 0.5 mm deep, 16 mm diameter well in a standard circular steel reflectance holder.

Small angle diffraction patterns were recorded using a PANalytical Empyrean Diffractometer in reflectance geometry using Cu $K\alpha_1$ radiation (wavelength $\boldsymbol{\lambda}$ = 0.1540598 nm). The incident beam was collimated by a series of slits and a beam mask. Diffraction data were recorded in the range 2θ = 0.5 - 5° with a step size of 0.017° with a fixed divergence slit of 0.063°. Powder samples were pressed into the 0.5 mm deep, 16 mm diameter well in a standard circular steel reflectance holder with a PTFE liner. Wide angle patterns were recorded from 10 to 90° at a step size of 0.017° with a fixed divergence slit of 0.5°.

The crystallite size and lattice parameters were calculated using HighScore Plus v. 3.0.3 software. This was achieved by performing background corrections, subtraction of instrumental peak broadening as determined by the silicon calibration standard and Rietveld refinement. A full width at half maximum (FWHM) analysis of the main diffraction peak was used in conjunction with the Scherrer equation (Eqn. 14) to obtain an average value of crystallite diameter.

Scherrer Equation

Average crystallite diameter ($\mathbf{D_{XRD}}$) $= \dfrac{K\lambda}{\beta_{corr}\,Cos\theta}$ ***Eqn. 14***

K : Shape Factor

λ : X-Ray Wavelength (Cu $K\alpha_1$) (Å)

β_{corr} : The corrected FWHM intensity peak

θ : Diffraction Angle (°)

To generate β_{corr} - the corrected intensity peak, the FWHM silicon standard intensity peak (β_{si}) is subtracted from the sample FWHM intensity peak (β_{sam}) (Eqn. 15).

β_{corr} : The corrected FWHM intensity peak $(\beta_{sam}^2 - \beta_{si}^2)^{1/2}$ ***Eqn. 15***

3.1.6 *Nuclear Magnetic Resonance*

Solid-state ^{29}Si MAS-NMR spectra were obtained using three different spectrometers. The first spectrometer- a Varian VNMRS 400 - was used at 79.44 MHz and at a spin rate of 6.8 KHz with 60 s delay between scans. The second spectrometer - a Varian Unity Inova 300- was used at 59.63 MHz and at a spin rate of 6.0 KHz spectrometer with 60 s delay between scans. These were analysed at the national solid state NMR facility at Durham University. One particular sample was ran on a Bruker Avance III spectrometer at 79.5 MHz with 180 s delay between scans using a 9.4 T wide bore superconducting magnet at the University of St-Andrews. This was because of the particularly small amount of sample available in this case and the need for improved resolution.

3.2 Apparatus

3.2.1 *Ultra-Microtomy*

Preparation of ultra-microtomy sections involved trying to encapsulate the product of interest so that a stable platform was achieved when sectioning. Two samples were prepared to determine the practicality of this method.

Sample 1, an SBA-15 template, was prepared in both powder and pellet form. Initial preparation involved encapsulating both powder and pellet in resin. Subsequently it was found that resin was difficult to use and that encapsulation using cyanoacrylate glue was preferential. It was also determined that the powder was easier to use than the pellet as only small particles were required and better particle suspension was obtained. This sample would be placed onto a metal substrate in preparation for sectioning.

Sample 2, was prepared from an SBA-15 template containing SDC product (after impregnation and calcination). This sample was encapsulated into a resin mould. To prepare for sectioning, the resin sample was firstly cyanoacrylate glued onto a metal substrate holder before further encapsulating the resin sample with cyanoacrylate glue. The purpose

of this secondary encapsulation was to hold the sections together when floating on the water of the knife boat.

As an alternative preparation of this second sample, the virgin sample (i.e. no encapsulation or glue) was sectioned using a dry knife.

The sectioning conditions used were as follows:

Sample 1 was sectioned using an ultra 35° knife with a 30 nm feed and sectioning speed of 50 mm sec^{-1}.

Sample 2 was sectioned using an ultra 35° knife with a 30 nm feed and sectioning speed of 50 mm sec^{-1}.

Sample 2 with the alternative preparation was sectioned using a dry knife.

The sections were transferred from the knife boat and picked-up and mounted onto a C-flat™ (Protochips inc.) TEM grid using a perfect loop.

3.2.2 *Ultra-Centrifuge*

In order to retrieve colloidal material from suspension a Beckman-Coulter Optima L-60 Ultra-Centrifuge was used at 40 000 rpm which equates to an RCF (relative centrifugal field – *g* force) of 145 000 g. A fixed angle rotor head designated as 50.2 Ti was used in the preparation of materials. This is a high performance titanium head of fixed 24° angle to the axis of rotation and has numbered tube cavities that are uncapped allowing up to a maximum of 12 tubes in any single operation at a maximum 50 000 rpm rotary speed. The centrifuge tubes (P/N 355631, Beckman Coulter) are thick walled polycarbonate and 25 x 89 mm in dimension. Although a swing head SW40Ti could also be used, the fixed rotor head has several advantages of holding 12 centrifuge tubes of 38 ml capacity (compared with 6 tubes of 10 ml) and being of fixed angle, it shortened the particle path length compared to swinging bucket rotors and generated a pellet which is usually retrieved with ease. Swinging bucket rotors are generally better suited for density gradient separations and require the tubes to be individually capped and sealed.

Chapter 4

Experimental Procedures: Materials

4.1 Introduction

This chapter focuses on the procedures used in synthesising templates and final products as well as highlighting the strategies employed in the general handling of these materials. Three ordered mesoporous silica (OMS) materials were prepared for the purpose of functioning as templates in a nanocast procedure and are referred to as SBA-15, KIT-6 and FDU-12. Through modification of the SBA-15 synthesis, an ultra large pore variety of this material was synthesised. Using standard and ultra large varieties of SBA-15 template, two different attempts at functionalising the surface of the template was attempted using TMDS and APTS silazane chemicals. Three ordered mesoporous carbon (OMC) templates (FDU-14, FDU-15 and FDU-16) were produced. FDU-14 and FDU-16 templates were prepared using a reflux technique. Three synthesis pathways were available for FDU-15. These were based on either a reflux method; evaporation induced self-assembly method or a two-phase separation method. All OMS and OMC templates when synthesised are produced in a powder format with the exception of two-phase prepared FDU-15 which is in monolith form. To facilitate impregnation of precursors, the powders were converted into pellets. This was achieved post synthesise with OMS templates and pre-calcination with OMC templates. The calcination of materials was dependent on the starting template. For OMS templates this was generally in air atmosphere at 500°C. The subsequent impregnated nitrates were calcined at 600°C. OMC templates were susceptible to degradation from oxygen. Synthesis was therefore controlled through inert atmospheric conditions or from a specific amount of oxygen in a nitrogen gas stream. The temperature of calcination was reflected in what type of template was required. The temperatures of 350, 400 and 500°C were used and relate directly to a structural change from polymer to carbon framework. Using these varieties of template, impregnated materials were calcined over a specific range of temperatures as detailed within the relevant results section.

4.2 Silica Template Preparation

4.2.1 *SBA-15*

A typical synthesis was adopted to allow for cross referencing to previous group studies.

To prepare the template, 2 g of non-ionic surfactant Pluronic P123 ($PEO_{20}PPO_{70}PEO_{20}$) (Aldrich) was added to 15 cm^3 of distilled water and 60 cm^3 of 2M HCl and stirred for 8 h at 40°C. This was performed whilst placing a watch glass onto the beaker to retain the solvent. 4.25 g tetraethylorthosilicate (TEOS, Alfa Aesar) was added and the mixture stirred for 24 h at the same temperature. The mixture was then placed in a PTFE container and into an oven for hydrothermal treatment at 100°C for a period of 24 hours. Two volumes of PTFE container were used: 250 ml and 500 ml. It was found subsequently that the container influenced yield (larger container yielded approximately 25 % less product). Analysis of product from both vessels indicated no change in quality or in characteristics such as pore size distribution or specific surface area. The resulting white solid was filtered and washed 3 times using distilled water in 40 ml aliquots by centrifuging at 3600 rpm for 5 min to remove excess surfactant and neutralise the product. The final product was calcined up to 500°C at a rate of 1°C min^{-1} with a dwell period of 5 h before cooling at 5°C min^{-1} to remove surfactants.

4.2.2 *Ultra Large SBA-15*

The synthesis of ultra-large SBA-15 (UL-SBA-15) was achieved using a swelling agent in conjunction with the standard method of SBA-15 preparation. Following the first report in 1998 by Zhao and co-workers[28] using 1,3,5-trimethylbenzene (TMB, Aldrich 99%)) to synthesise an expanded pore structure, various swelling agents have since been used successfully. The particular one used in this procedure was 1,3,5-triisopropylbenzene (TIPB, Aldrich 97 %) as reported by Cao and co-workers[69]. The choice of method was based on the report that ultra-large pore networks could be obtained while at the same time avoiding poorly defined structures. In a typical synthesis, 2.4 g of non-ionic surfactant Pluronic P123 ($PEO_{20}PPO_{70}PEO_{20}$) (Aldrich); was added to 84 ml of 1.3M HCl and stirred in a water bath at 25°C for 6 h with 0.027 g of NH_4F (ammonium fluoride, Aldrich) being added as a catalyst[70]. This was performed whilst placing a watch glass onto the beaker thus retaining the solvent. The solution was then cooled to a temperature of 13°C ± 0.5°C using an insulated beaker in a water bath and allowed to settle for 1 h. After this time 5.9 g tetraethylorthosilicate (TEOS, Alfa Aesar) was added and 1.0 g of the swelling agent TIPB and stirred for 24 h at the

same temperature. The mixture was then placed in a 500 ml PTFE container and into an oven for hydrothermal treatment at 100°C for a period of 24 h. The retrieval and calcination of the product followed that of standard SBA-15 product as described in section 4.2.1.

4.2.3 *KIT-6*

In a typical synthesis[31b], 6 g of non-ionic surfactant, Pluronic P123 (Aldrich), was added to 180 cm^3 of distilled water and 50 cm^3 of 2M HCl and stirred at 35°C for 6 h. This was performed whilst placing a watch glass onto the beaker thus retaining the solvent. After this period, 6 g of n-butanol (Aldrich, 99%) was added and the mixture stirred while maintaining 35°C for 1 h. 12.48 g TEOS was added and stirred for 24 h at the same temperature. The mixture was placed in a 500 ml PTFE container and into an oven for hydrothermal treatment at 100°C for a period of 24 h. The resulting white solid was filtered and washed 3 times using distilled water in 40 ml aliquots by centrifuging at 3600 rpm for 5 min to remove excess surfactant and neutralise the product. The retrieval and calcination of the product followed that of standard SBA-15 product as described in section 4.2.1.

4.2.4 *FDU-12*

In a typical synthesis[40], 2 g of non-ionic surfactant Pluronic F127($PEO_{106}PPO_{70}PEO_{106,}$ Aldrich) and 5 g of Potassium Chloride (Aldrich 99.5%) was added to 120 cm^3 of 2M HCl and stirred at 40°C until clear. 2 g of trimethylbenzene (Aldrich 99%) was added dropwise. The mixture was stirred for 24 h whilst placing a watch glass onto the beaker thus retaining the solvent. 8.3 g of TEOS (Alfa Aesar) was added and the mixture further stirred for 24 h at the same temperature. The mixture was then placed in a 500 ml PTFE container and into an oven for hydrothermal treatment at 100°C for a period of 24 h. The retrieval and calcination of the product followed that of standard SBA-15 product as described in section 4.2.1

4.3 Functionalisation of OMS Templates

4.3.1 *TMDS Functionalisation*

A novel method based on use of 1,1,3,3-tetramethyldisilazane[71]. (TMDS, Aldrich, 97 %) and the experimental procedure from Song et al[45b] was developed as a post synthesis method of surface functionalisation of SBA-15 or ultra large pore SBA-15 material. For this procedure, it is necessary to eliminate residual water. This was achieved by drying all glassware overnight at 100°C in an oven and heating the OMS template under vacuum overnight at 100°C using the vacuum impregnation (VI) equipment described previously

with the test tube placed in an oil bath. Approximately 0.5 g of template material was added to a homogenous solution of 0.65 g TMDS and 10 ml hexane (Aldrich, anhydrous, 97 %) and stirred under vacuum at room temperature for 24 h again using the VI equipment. After which time the solvent will have evaporated. The material was recovered by 3600 rpm centrifugation. After each centrifuge cycle the material was washed by stirring for 5 min using hexane as the washing solvent. This wash procedure was repeated three times through. The material was then dried in an oven overnight at 100°C.

4.3.2 *APTS Functionalisation*

A novel method based on use of (3-Aminopropyl)trimethoxysilane (APTS, Aldrich, 97 %)[72] and the experimental procedure from Song et al[45b] was developed as a post synthesis method of surface functionalisation of SBA-15 or ultra large pore SBA-15 material. For this procedure, it is necessary to eliminate residual water. This was achieved by drying all glassware overnight at 100°C in an oven and heating the OMS template under vacuum overnight at 100°C using the vacuum impregnation (VI) equipment described previously with the test tube placed in an oil bath. Approximately 0.5 g of template material was added to a homogenous solution of 1.2 g APTS and 10 ml hexane (Aldrich, anhydrous, 97 %) and stirred under vacuum at room temperature for 24 h again using the VI equipment. After which time the solvent will have evaporated. The material was recovered by 3600 rpm centrifugation. After each centrifuge cycle the material was washed by stirring for 5 min using hexane as the washing solvent. This wash procedure was repeated three times through. The material was then dried in an oven overnight at 100°C.

4.4 Carbon Template Manufacture

Several published synthesis routes now exist for the preparation of each template type. The majority of these methods have been attempted in order to establish the practicalities and feasibility in their preparation and are given the postfix of A, B, C in order to distinguish which method was used in their manufacture.

4.4.1 *FDU-14*

4.4.1.1 FDU-14A

To synthesis FDU-14, the procedure first reported by Zhang[73] was adapted whereby an initial solution of 4.8 g Pluronic P123 (0.83 mmol, Aldrich) and 50 g deionised water was stirred overnight at room temperature to give a clear solution. A resol solution was prepared by the addition of 2.0 g phenol and 5.0 g of formaldehyde (Aldrich, 37 wt%) solution with 50 ml of 0.1 M NaOH solution into a 100 ml beaker and heated at 72°C for 30 min. The hot resol solution was then directly added into a round bottom flask containing the P123 solution. A white suspended solution was formed after stirring at room temperature (20°C) for 3 h. This solution was then stirred under reflux at 64°C for 120 h whereby it turned from milky to pink in appearance and a build-up of brown particulate was observed. The reflux was continued at an increased temperature of 72°C for 48 h. The brown sediment was collected by centrifugation for 5 min at 3600 rpm. Centrifugation was repeated twice after decanting the effluent and washing afresh with deionised water at each interval. The product was dried overnight in air at 40°C before heating in a tubular furnace at 350°C at a rate of 1°C min^{-1} and dwell of 3 h before cooling at 2°C min^{-1} in nitrogen flow to remove the organic residues. About 2.2 g of product (FDU-14-350) was obtained. A second product was obtained by heating in a tubular furnace to 500°C for 3 h at a rate of 1°C min^{-1} and dwell of 3 h before cooling at 2°C min^{-1} in nitrogen flow (100 cm^3min^{-1}). Latterly, a gas change was used which included a known amount of oxygen (90 cm^3min^{-1} N_2 and 10 cm^3min^{-1} O_2). About 1.3 g of carbonised material (FDU-14-500) was thus obtained.

4.4.1.2 FDU-14B

The FDU-14A procedure was retrospectively refined in accordance with the later publication by Zhang 2006[74]. An initial solution of 4.8 g Pluronic P123 (0.83 mmol, Aldrich) and 50 g deionised water was stirred overnight at room temperature to give a clear solution. A resol solution was prepared by the addition of 2.0 g phenol and 7.0 g of formaldehyde (Aldrich, 37 wt%) solution equivalent to 100 mmol with 50 ml of 0.1 M NaOH solution into a 100 ml beaker and heated at 72°C for 30 min. The hot resol solution was then directly added into a round bottom flask containing the P123 solution. A white suspended solution was formed after stirring at room temperature (20°C) for 3 h. This solution was then stirred under reflux at 64°C for 72 h whereby it turned from milky to pink in appearance and a build-up of brown particulate was observed. The reflux was continued at an increased temperature of 72°C for

24 h. The brown sediment was collected using the same centrifugation and calcination procedures of 4.4.1.1

4.4.2 *FDU-15*

Several methods in the preparation of FDU-15 have been reported with the method reported by Zhang[74] being initially chosen as it involved an aqueous route to synthesis however it was quickly realised that the time involved was of days rather than hours and the precursors being phenol and formaldehyde were of relatively high toxicity. It was also realised that an alternative aqueous route to synthesis had been reported as a one-pot method using the much less toxic precursors of resorcinol and hexamethylenetetramine (HMT) by Liu[75] which was subsequently performed and is detailed below. It is prudent to mention that despite the apparent advantages of time and precursor and the reported scalability of the Liu method, the increased yield and scalability benefits make the Zhang method a feasible alternative.

4.4.3 *FDU-15A by Aqueous One-pot Method*

In an amended procedure, 1.10 g of resorcinol (Aldrich, 95 %), 0.70 g of hexamethylenetetramine (Alfa Aesar 98 %), 2.00 g of Pluronic F127 (Aldrich), 0.40 g of trimethylbenzene (Aldrich 99%) were weighed into a 250 ml round bottom flask. To this mixture of chemicals, 54.0 g of a 0.56 M ammonia solution was added. This ensured that the H_2O ratio was maintained while reducing the potential error in ammonia concentration had the ammonia been added by concentrated volume (28% at 2.00 ml). This mixture was stirred at room temperature for a period of 1 h whereby a change from colourless to dark green was observed. The flask was then transferred to an oil bath maintained at 80°C and further stirred for 24 h under reflux. A black solid product was formed as sediment and retrieved. The black sediment was collected by centrifugation for 5 min at 3600 rpm. Centrifugation was repeated twice after decanting the effluent and washing afresh with deionised water at each interval. The product was dried overnight in air at 40°C. Two separate products were produced from heating in a tubular furnace to either 350°C or 500°C with 3 h dwell. A heating rate of 1°C min^{-1} and cooling rate of 2°C min^{-1} in nitrogen flow (100 cm^3min^{-1}) to remove the organic residues was used. A yield of approximately 2.0 g was produced.

4.4.4 *FDU-15B by Evaporative Induced Self Assembly (EISA) Method*

Following the procedure published by Meng[76]; a two-step process was followed whereby the resol precursor was firstly produced as a base catalysed reaction using 0.61 g of phenol which was melted at a controlled temperature in a water bath at 40 to 42°C in a test tube. This mixture was stirred for 10 min before drop-wise addition of 1.05 g of formaldehyde solution (Aldrich, 37 wt%) ensuring the temperature remained below 50°C. The temperature was then carefully raised to between 70 and 75°C and the mixture stirred at this point for a further 1 h before being allowed to cool to room temperature by removal from the water bath. The pH was then adjusted to approximately 7.0 by the addition of 0.6M HCl which equated to 160 drops. The water in the system was removed overnight by vacuum evaporation at a temperature of between 40 and 50°C being careful not to exceed 50°C. The recovered dried product was re-dissolved in 5g of ethanol. The number of moles of phenol/formaldehyde/NaOH added were 0.0065/0.013/0.00065 and is in accordance with the reported 1:2:0.1 ratio.

To prepare the mesoporous polymer, 1.0 g of F127 (Aldrich) was dissolved in 20.0 g ethanol for between 15 and 30 min; otherwise, phase separation would occur noticeable by clouding of the mixture. The previously made resol solution was added under stirring for 10 minutes so that a homogenous solution was obtained. This mixture was then spread over five 80 mm petri dishes and left for 6 h at room temperature before being transferred into an oven preheated to 100°C for a further 24 h. The obtained transparent film residue was scraped from the dishes and calcined. Two separate products were produced from heating in a tubular furnace to either 350°C or 500°C with 3 h dwell. A heating rate of 1°C min^{-1} and cooling rate of 2°C min^{-1} in nitrogen flow (100 cm^3min^{-1}) to remove the organic residues was used. A yield of approximately 1 g was produced.

4.4.5 *FDU-15C by Two-Phase Method*

The preparation of FDU-15 following a two-phase method was first performed using the method by Gao[77] and co-workers. This method was based on an acid catalysed resorcinol-formaldehyde reaction and required 7 days to complete. A refinement on this method by Xu and co-workers[78] developed the procedure towards using a base catalysed resorcinol-formaldehyde reaction followed by an acid catalysed condensation reaction to create the self-assembled framework. The published procedure was amended by doubling the quantity of reagents in order to generate meaningful working quantities of 1-2 g template. A typical procedure involved mixing in a 50 ml beaker at 18°C, 0.0112 g of Na_2CO_3 in a 2.26 g

formaldehyde solution (Aldrich 37 wt.%) until dissolved. The 18°C temperature was maintained within ±1°C using an insulated water bath. 2.20 g of resorcinol was added under stirring and maintained for 1 h to create a resol polymer solution. A solution of 1.60 g Pluronic F127 (Aldrich), 10.00 g ethanol and 8.00 g of distilled water was prepared in a 50 ml beaker under stirring for a period of between 20 and 30 mins. This was timed to coincide with the completion of the resol solution process so that the F127 solution could be added to the resol solution under vigorous stirring. This was immediately followed by drop-wise addition of 2.00 ml of 2M HCl which would catalyse the framework formation. After 3-5 mins the solution would instantly turn from a clear mixture towards one that was turbid (phase separation). This mixture was then further stirred for 1 h before removing the stirring bar and allowing the mixture to stand for minimum 10 h. After this time the ethanol-water top layer was carefully decanted to waste. The polymer rich bottom layer was left for a minimum period of 8 h to dry at room temperature. This white opaque monolith was then cured in a preheated oven at 80°C for 24 h creating a glass-like orange material. The material (approx. 1-2 g) was then transferred to a tube furnace and calcined under flowing nitrogen (100 cm^3min^{-1}) to a temperature of 400°C at 1°C min^{-1} with a dwell time of 3 h before cooling at a rate of 2°C min^{-1}. A yield of between 1-2 g was frequently produced.

4.4.6 *FDU-16*

To synthesise FDU-16 the procedure first reported by Zhang[73] was adapted whereby an initial solution of 4.4 g Pluronic F127 (0.35 mmol) and 50 g deionised water was mixed to a clear solution overnight at room temperature to ensure homogeneity. A resol solution was prepared by the addition of 2.0 g phenol and 5.0 g of formaldehyde solution (Aldrich 37 wt%) to 50 ml of 0.1 M NaOH solution in a 100 ml beaker and heating at 72°C for 30 min. The hot resol solution was then directly added into a round bottom flask containing the F127 solution. A transparent solution was formed after stirring at 65°C for 3 h. This solution was then stirred under reflux at 65°C for a total of 96 h. A yellow precipitate was observed after 24 h. The reflux was continued at an increased temperature of 70°C for 24 h. The sediment was then collected using centrifuge for a period of 5 min at 3600 rpm. Centrifugation was repeated twice after decanting the effluent and washing afresh with deionised water at each interval. The product was dried overnight in air at 40°C before heating in a tubular furnace at 350°C at a rate of 1°C min^{-1} and dwell of 3 h before cooling at 2°C min^{-1} in nitrogen flow to remove the organic residues. About 2.2 g of product (FDU-16-350) was obtained. A second product was obtained by heating in a tubular furnace to 500°C

for 3 h at a rate of 1°C min^{-1} and dwell of 3 h before cooling at 2°C min^{-1} in nitrogen flow (100 cm^3min^{-1}). Latterly, a gas change was used which included a known amount of oxygen (90 cm^3min^{-1} N_2 and 10 cm^3min^{-1} O_2). About 1.6 g of carbonised material (FDU-16-500) was thus obtained.

4.5 Pellet Formation

In order to minimise the void space between the hard template particles, it was theorised that the silica or carbon template powder could be improved for vacuum impregnation by compressing into pellet form. The technique involved using a bench mounted press (Specac) and cylindrical 13 mm die set. The powder of interest would be placed inside the die cavity and uniaxially compressed using a precisely engineered cylinder.

4.5.1 *OMS Templates*

It was found that various pressures and strategies would improve the quality of pellet produced. This was further complicated as a different strategy had to be employed for each of the template structures. Often the pellet would cleave lateral to the face on removal from the die. To try and reduce friction / jerking, the die was wiped with a very light coating of terpineol (Aldrich, 97%) before use. This practise was carefully controlled as surface coating leading to pore blockage was of concern. However no evidence of any such problems was in evidence during later processing and successful impregnation was visually apparent. Slow removal (gradual build-up of pressure over 20 minutes) reduced but did not eliminate fractures. Optimum compressions of the silica templates are detailed in Table 4-1.

Table 4-1: Optimum conditions used in the pellet formation of various OMS template powders using a Specac manual press and 13 mm diameter die.

Silica Template	Pressure Applied (MPa)	Time Applied (minutes.)
SBA-15	80	30
KIT-6	400	30
FDU-12	400	30

4.5.2 *OMC Templates*

When making pellets from the carbon templates, it was discovered that the powder form of the final template did not compress even under pressures of 300 MPa. A new strategy was

employed whereby the pellet was formed at the green stage of synthesis, before thermal treatment at 350 or 500°C. This allowed pellets to be formed from solid material retrieved after reflux under low pressure. The material had to be wetted to facilitate formation of the pellet but not so wet as to suspend the particles, which would cause difficulty in handling and unnecessary losses of material. It was also realised that the materials often exhibited non-Newtonian behaviour and so release of compression forces would see the pellet return to a sludge if too much water was present.

The green pellets were allowed to dry overnight at a temperature of 80°C in order to reduce the water content. This caused shrinkage on the overall dimensions but rather than create cracks or cleavages, it helped decrease the fragility of pellet. Figure 4-1 shows images of (a) OMC pellet in its green stage after reflux before thermal treatment, (b) OMC based pellet after 350°C thermal treatment in N_2, (c) Carbon based pellet after 500°C thermal treatment in N_2. It was apparent that a large percentage of shrinkage had occurred probably from water removal but the integrity of the pellet remained with no cracking, spalling or cleaving evident.

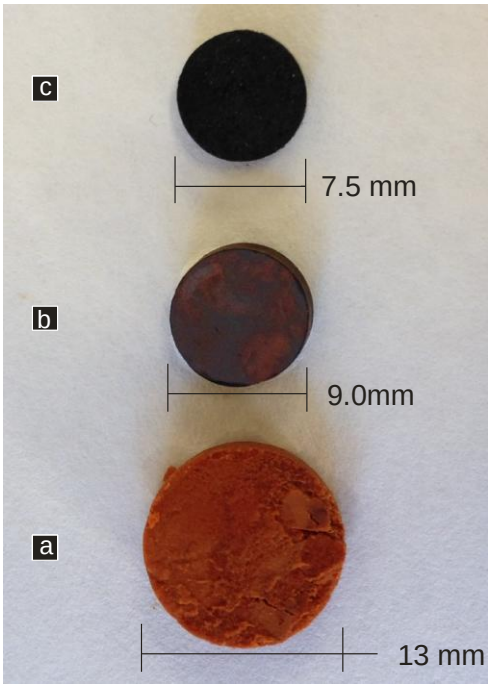

Figure 4-1: (a) OMC pellet in its green stage after reflux before thermal treatment, (b) OMP Pellet after 350°C thermal treatment in N_2, (c) OMC Pellet after 500°C thermal treatment in N_2.

4.6 Preparation of Cerium and Samarium Nitrates

The nitrate compounds of cerium and samarium were chosen as impregnates for reasons of high solubility in ethanol and easy decomposition to the oxide at a low (<200 °C) temperature and commercial availability. In order to achieve an SDC oxide of stoichiometry, $Sm_{0.2}Ce_{0.8}O_{1.9}$, a saturated solution of the nitrates was produced by dissolving 6.95 g of $Ce(NO_3)_3.6H_2O$ (Aldrich, 99.5%) and 1.78 g of $Sm(NO_3)_3.6H_2O$ (Aldrich, 99.5%) in 5 g of ethanol (Appendix 4) while stirring continuously at 40°C for a minimum of 1 h. It was found that 5 g of ethanol was the minimum required to completely dissolve all nitrate crystals. Samarium nitrate proved the lower solubility of the two nitrates. It was also realised that the nitrates being hexahydrate, could also release their water of crystallisation if heated vigorously beyond 60°C such that a solution is possible without the addition of any solvent.

4.7 Preparation of Final Products

4.7.1 *Vacuum Impregnation*

The procedure to vacuum impregnate was initially performed according to previous research work using the template in powder form[79]. Expanding on this technique, SDC material preparation in a variety of templates was attempted. Impregnation of single pellets and then subsequently several pellets at once during each individual experiment was also investigated.

Impregnation was performed using a BOC Edwards RV3 vacuum pump. All ground glass joints were 19/26 size and sealed using a small amount of vacuum grease and 24 mm rubber tubing. The vacuum integrity was tested using a penning gauge to ensure strong vacuum was being obtained. The procedure to impregnate materials involved placing the template usually ranging from 0.3 to 1 g in the form of either powder or pellet into a 25 ml test tube and exposing to a vacuum for minimum 6 hours. When in powder form, the evacuation process could be observed visually as powder eruptions as gas forced its way from the surface. The capacity of the test tube allowed for a maximum of 3 pellets at any one time. When the precursor is initially exposed to vacuum it would often degas generating strong turbulence as bubbles, this effect could be controlled by operating the vacuum valve to slow down the vacuum exposure. The amount added was an excess from the theoretical amount required to fill the pore volume as determined from calculation using gas physisorption porosity data and weight of sample used. This excess would be required to physically coat

the in situ template and create a liquid interface against which the atmospheric pressure could function against.

4.7.1.1 Powder VI

Liquid was added to a powder under vacuum conditions in a drop wise manner and would absorb almost immediately. Continuation of precursor addition would see a saturation of the top layer, from which a liquid layer would form. Only slow ingress into the bulk material occurred thereafter up to a maximum depth of approximately 2 cm.

4.7.1.2 Pellet VI

Pellets were carefully placed on top of a bed of PTFE tape to allow them exposure to liquid precursor which would be carefully added drop wise under vacuum conditions to control the saturation of the pellet. Another variation of this method would see the pellet immersed in an excess of the liquid before careful extraction from the test tube and subsequent removal of excess liquid by placing between two filter papers.

All pellets were left overnight at room temperature to dry for a period of 24 h.
Initial research involved the impregnation of a single pellet however a consequence of this single pellet experiment was that the yield (approximately 0.5 g) of SDC material limited characterisation particularly with low-angle XRD. Flexibility of the VI setup successfully allowed multi-pellet impregnation (physically limited to four) in a single impregnation step. This provided an increased yield of between 1-2 g of SDC material.

4.7.2 *Incipient Wetness*

This procedure involves taking an amount of the template powder that will comfortably reside in a mortar adding saturated precursor solution a few drops at a time and intimately mixing with the pestle. Depending on the properties of the template such as hydrophilicity, the solution was absorbed into the template at a variable rate. The amount of precursor added was calculated based on the maximum pore volume of the template. This pore volume was a known value determined by gas physisorption analysis. The rate of addition of the precursor was dictated by the saturation and subsequent drying of the template as solvent evaporated.

4.7.3 *Template Free Samarium Doped Ceria*

Using the procedure outlined in Section 4.6 approximately 2 ml of saturated samarium and cerium nitrates in ethanol was poured into a large ceramic boat of 105 mm length, 22 mm width and 15 mm depth or small ceramic boat of 88 mm length, 16 mm width and 8 mm depth. This was either subjected to atmospheric calcination (see Section 4.7.5.1) or closed container calcination (see Section 4.7.5.4) When atmospheric calcination was performed, the material was found to rise just above the ceramic boat in a foam-like structure that was easily collapsed and lightly compacted to a powder. The amount of SDC product obtained was approximately 0.15 g per ml of saturated nitrate solution.

4.7.4 *Samarium-Doped Ceria by the Citrate Method*

To produce non mesoporous SDC material for use in comparative purposes, a synthesis procedure known as the citrate method was followed. 0.1 M solutions of the required cation nitrates were combined with 0.2 M of citrate ions such that 1 mole of total metal cations are combined in a ratio of 2 moles of citrate. An SDC oxide of stoichiometric ratio $Sm_{0.2}Ce_{0.8}O_{1.9}$ was required therefore a solution of the nitrates was produced by dissolving 13.69 g of $Ce(NO_3)_3.6H_2O$ (99.5% Aldrich) in 315 ml of distilled water and 3.50 g of $Sm(NO_3)_3.6H_2O$ (99.9% Aldrich) in 79 ml of distilled water. These solutions were stirred continuously at room temperature for a minimum of 1 h. Citric acid solution was prepared under continuous stirring by stirring 15.14 g of anhydrous citric acid in 394 ml of distilled water at room temperature for a minimum of 1 h. These two solutions were then combined and heated for 12 h at 80°C in an oil bath to reduce the water content until a viscous yellow material was formed. This material was then heated in a muffle furnace to 250°C at a heating rate of 2.5°C min^{-1} with a 2 h dwell which produced a yellow foam-like material that was easily compressed by manual compaction. This material was then calcined at 500°C at a heating rate of 2.5°C min^{-1} and dwell time of 2 h.

4.7.5 *Calcination*

4.7.5.1 Atmospheric Calcination

The majority of calcination were performed under normal atmospheric conditions in a tubular furnace with both openings of the tube openly exposed to air.

4.7.5.2 Inert Atmosphere

The calcination and surfactant removal stage of carbon template synthesis should ideally be performed under inert conditions (usually nitrogen) as carbon would otherwise react in air and be lost. To achieve this, the atmosphere within the tube furnace was controlled by capping each end and flushing with nitrogen gas at a flow rate of 100 cm^3 min^{-1}.

4.7.5.3 Controlled Oxygen Atmosphere

Contrary to instinct in some instances of carbon template manufacture, i.e. for FDU-14 and FDU-16, it has been shown by Meng[76] that a small percentage of oxygen present in the calcination gas was beneficial and that only minor losses of final template occurred. From the information presented, the calcination conditions for FDU-14 and 16 were revised to include an additional gas mixed of 10 cm^3 min^{-1} air with 90 cm^3 min^{-1} nitrogen, introducing approximately 2.0 % oxygen into the furnace.

4.7.5.4 Closed Container Atmosphere

The pseudo closure of the ceramic boat was used to control the atmospheric conditions under which material was calcined. Ceramic plates were placed on top of the ceramic boats such that approximately 80 to 90 % of the boat was capped. This was typically followed by an atmospheric calcination. A thermal profile of 1°C min^{-1} heating rate to 200°C with 1 h dwell followed by a 1°C min^{-1} rate to 400°C with 1 h dwell was used. The cooling rate was 5°C min^{-1}.

4.8 Silica Template Removal

Unlike carbon templates which are simply removed by heating in an oxygen atmosphere at 400°C for 3 h at a heating rate of 1°C min^{-1}, silica templates are removed by a wet chemical method that involves dissolving in sodium hydroxide solution. The standard method employed was based on previously performed techniques within the group and involved the washing of less than 0.5 g of impregnated and calcined SDC-silica template product with an excess of 2 M NaOH solution. This was achieved by placing the product into a 50 ml centrifuge tube and stirring in 40 ml of NaOH at room temperature for a period of 2 h minimum whereby it would turn to a yellow sludge. This procedure was repeated twice more in NaOH then 3 times in distilled water with the product being recovered by centrifugation at 3600 rpm for 5 mins between washes.

Chapter 5

Analysis of Silica Templates

5.1 Introduction

Fundamental to the nanocast synthesis of any material is the preparation of templates that have characteristics of long range order, well defined and consistent pore distribution as well as consistent wall thickness and interconnectivity between pores. Such materials have been developed in a range of ordered mesoporous silica's (OMS) using a self-assembly strategy. A primary aim is to reproduce three of these unique structures using well established methods as outlined in Chapter 4. Although a range of silica templates exist, three main types were chosen as representative varieties of structure, namely SBA-15 hexagonal *p6mm,* KIT-6 cubic *Ia3d* and FDU-12 cubic *Fm-3m.* As this is a mature field of study several reviews exist which comprehensively describe siliceous templates.[46, 80] Several authors have researched variations in preparation such as micelle removal using reflux[81] or microwave digestion[82], microwave-hydrothermal preparation[83], surface area and pore volume alteration[84], pore enlargement techniques[28,32, 85] and functionalisation[45b, 71-72, 86]. A secondary aim of the research is to produce modified SBA-15 for reasons of trying to reduce the parasitic remnants of silica from nanocast processes as detailed in Chapter 7. Three modifications were therefore attempted. These include surface functionalised SBA-15, ultra-large SBA-15 and a combination of both - functionalised, ultra-large SBA-15. These properties were determined in both the bulk and the nanoscale by analysis using small angle XRD, gas physisorption and TEM techniques.

5.2 Results

5.2.1 *SBA-15*

In order to establish that the SBA-15 template was of expected porosity and structure, all samples were analysed first by gas physisorption as this would indicate the bulk repeatable nature of the material prepared. The generated isotherms can be interpreted for specific surface area ($\mathbf{S}_{BET}$), pore size distribution ($\boldsymbol{W}_{BJH}$), mesopore volume ($\mathbf{V}_{meso}$) and micropore volume ($\mathbf{V}_{micro}$). As this material was used for a series of experiments, several batches were

prepared over time and this has allowed variation in the quality to be determined. Figure 5-1 shows a typical isotherm and associated specific pore size distribution (PSD) for one of the produced batches of material. The isotherm is typical of a type IV profile with an associated type H3 hysteresis. A narrow 8.4 nm peak is observed from the desorption branch and specific mesopore volume ($\mathbf{V}_{meso}$) of 0.73 cm^3g^{-1} and micropore volume ($\mathbf{V}_{micro}$) of 0.10 cm^3g^{-1}. The average specific surface area ($\mathbf{S}_{BET}$) over eleven batches of product was found to be 868 m^2g^{-1} with a standard deviation of 54 m^2g^{-1} and average pore size of between 7 and 8 nm showing a consistency of production. This is in line with literature reported values[31a].

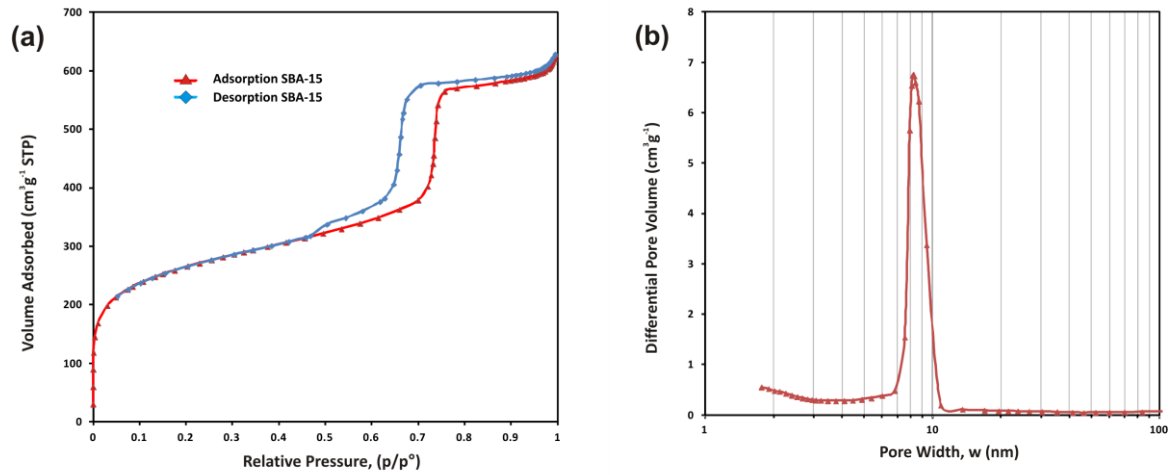

Figure 5-1: Nitrogen physisorption isotherm (a) and specific pore size distribution (b) for SBA-15.

Figure 5-2 presents the low angle XRD data for SBA-15. Analysis of the SBA-15 pattern shows a material with three distinct peaks of the expected 2-D hexagonal structure observable with a ***d***-spacing of 9.8, 5.9 and 5.1 nm which could be assigned to the (100), (110) and (200) Miller indices respectively as presented in Table 5-1. The unit cell parameters of 11.3, 11.7 and 11.8 nm, were calculated respectively using the formulae in Appendix 2, Eqn. 21 and summarised with key data for comparison in Table 5-4.

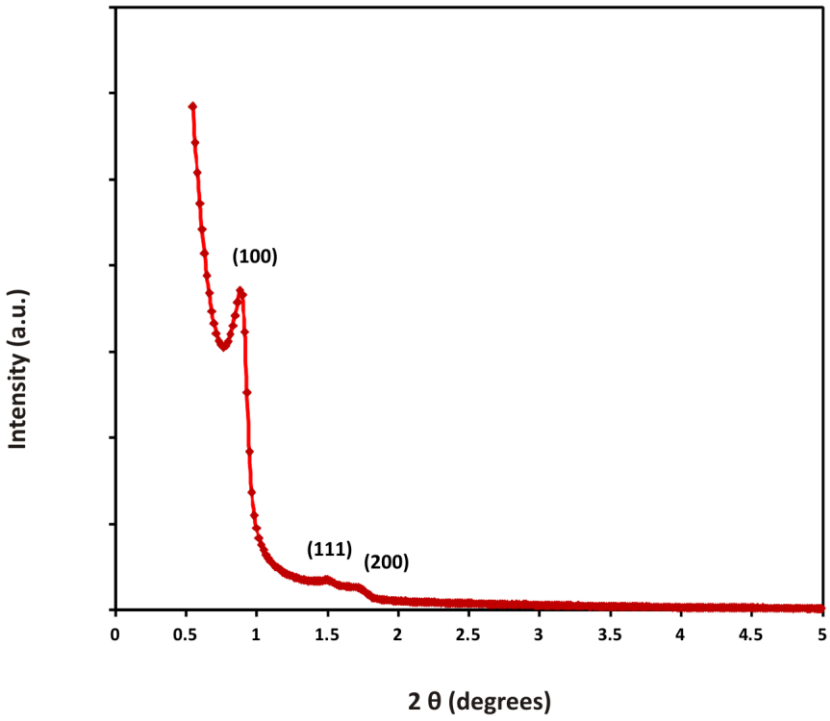

Figure 5-2: SAXS Diffraction pattern and corresponding interplanar ***d***-spacing for SBA-15.

Table 5-1: Calculated d-spacing from 2θ values for SBA-15

2θ (°)	**Indices**	***d*-Spacing (nm)**
0.886	100	9.96
1.516	110	5.82
1.736	200	5.09

The structure of SBA-15, as viewed using TEM analysis details a highly ordered structure of 2-D hexagonally arranged cylindrical pores. Figure 5-3 presents TEM images showing a representative selection of the ordered mesoporous nature. Figure 5-3 (a) highlights the long range order of the parallel pore channels in the [100] direction. The hexagonal pore structure of the material was viewed in Figure 5-3 (b). This hexagonal arrangement was further evidenced in Figure 5-3 (c) including the curvature of the long range parallel channels. Investigations into pore and wall-width analysis using contrast-line scanning perpendicular to the pores and wall channels in Figure 5-3 (a) are shown in Figure 5-3 (d). Analysis of the data estimates a pore size $\boldsymbol{w_{TEM}}$ of 7.5 nm and measured wall thickness $\boldsymbol{t_{TEM}}$ is estimated at 2.2 nm. The digital diffraction pattern obtained from FFT analysis of the red box area as indicated in Figure 5-3 (b) indicates a $\boldsymbol{d_{TEM}}$ interplanar spacing value of 9.5 nm.

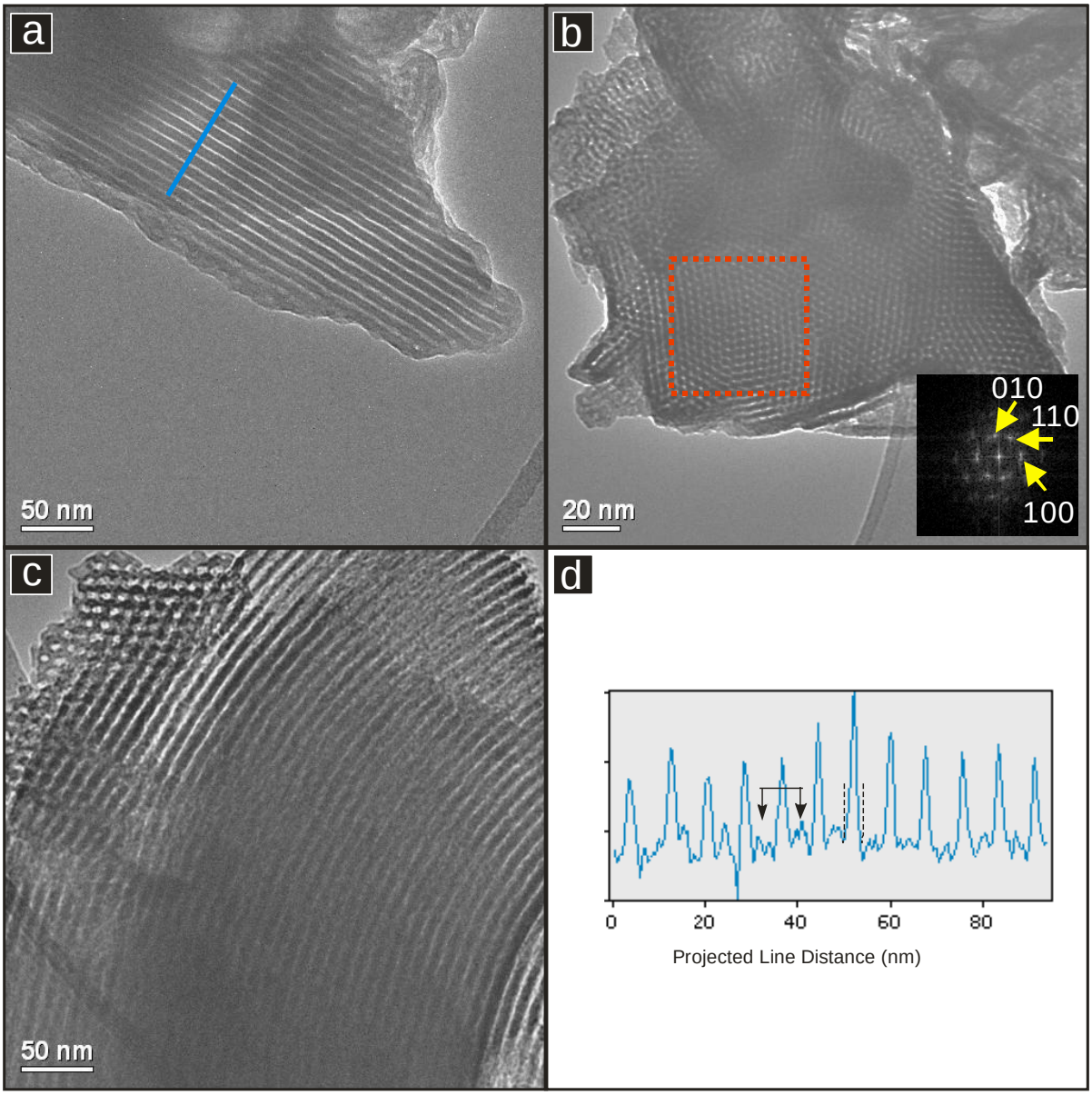

Figure 5-3: TEM images of SBA-15 showing a representative selection of the ordered mesoporous nature : (a) highlights the long range order of the parallel pore channels in the [100] direction, the blue line inset is the histogram range for (d), (b) the parallel pore channels viewed in [110] direction with the hexagonal pore arrangement clearly visible, (c) parallel channels showing long range curvature, (c) image showing a typical long range curvature of the channels, (d) area of integration for image (a). DDP obtained from the red box as indicated in (b) as inset. Miller indices of spots are given.

5.2.2 *SBA-15 Prepared Using Ultra-Microtome Technique.*

As part of the TEM grid preparation, samples of SBA-15 and SBA-15 impregnated with SDC were prepared by microtome sectioning. As these samples were unknown in respect to their performance during sectioning, the quality of section would not be realised until attempted and placed onto a TEM grid. The sectioned SBA-15 materials obtained using the ultra-microtome technique were transferred onto a holey carbon grid for purposes of TEM

analysis. The grid showing the placement of the sectioned material was imaged by light microscopy and presented in Figure 5-4 (a). This image shows the placement of the SBA-15 as prepared from a powder in cyanoacrylate glue. The result indicates that the sample section has been mounted with minimal folding which is highlighted by the red arrow and visible as dark blue features. Figure 5-4 (b) shows the placement of the impregnated SBA-15 as prepared from a resin sample in cyanoacrylate glue. The result indicates that the sample section has been mounted with several areas of folding which is highlighted by the red arrows and visible as dark blue features. Despite the folding there was cautious optimism that there would be enough flat areas to allow for successful TEM viewing when analysed. Figure 5-4 (c) shows the placement of the impregnated SBA-15 as prepared by direct dry knife sectioning. The result indicates that the sample section has been mounted, however difficulties were encountered in mounting the sections on a C-flat grid as the ribbon is not flat but undulating and therefore poorly attached to the grid. This is visible as several areas of folding perpendicular to the length. These are highlighted by several red arrows and visible as dark lines. A method of pressing and flattening down will likely be required in order to view successfully by TEM. In principle though, it has been successful in producing the desired thin section.

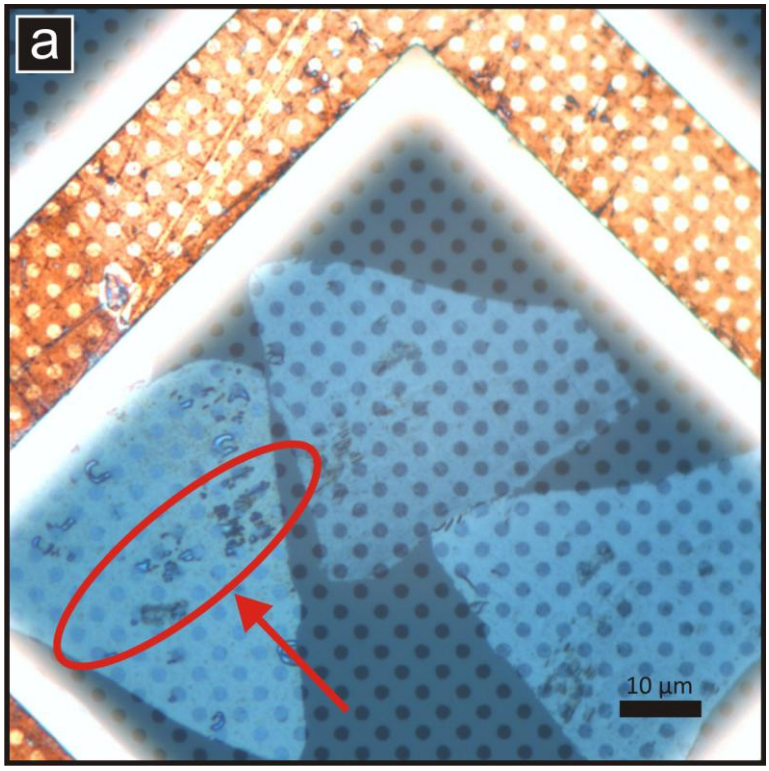

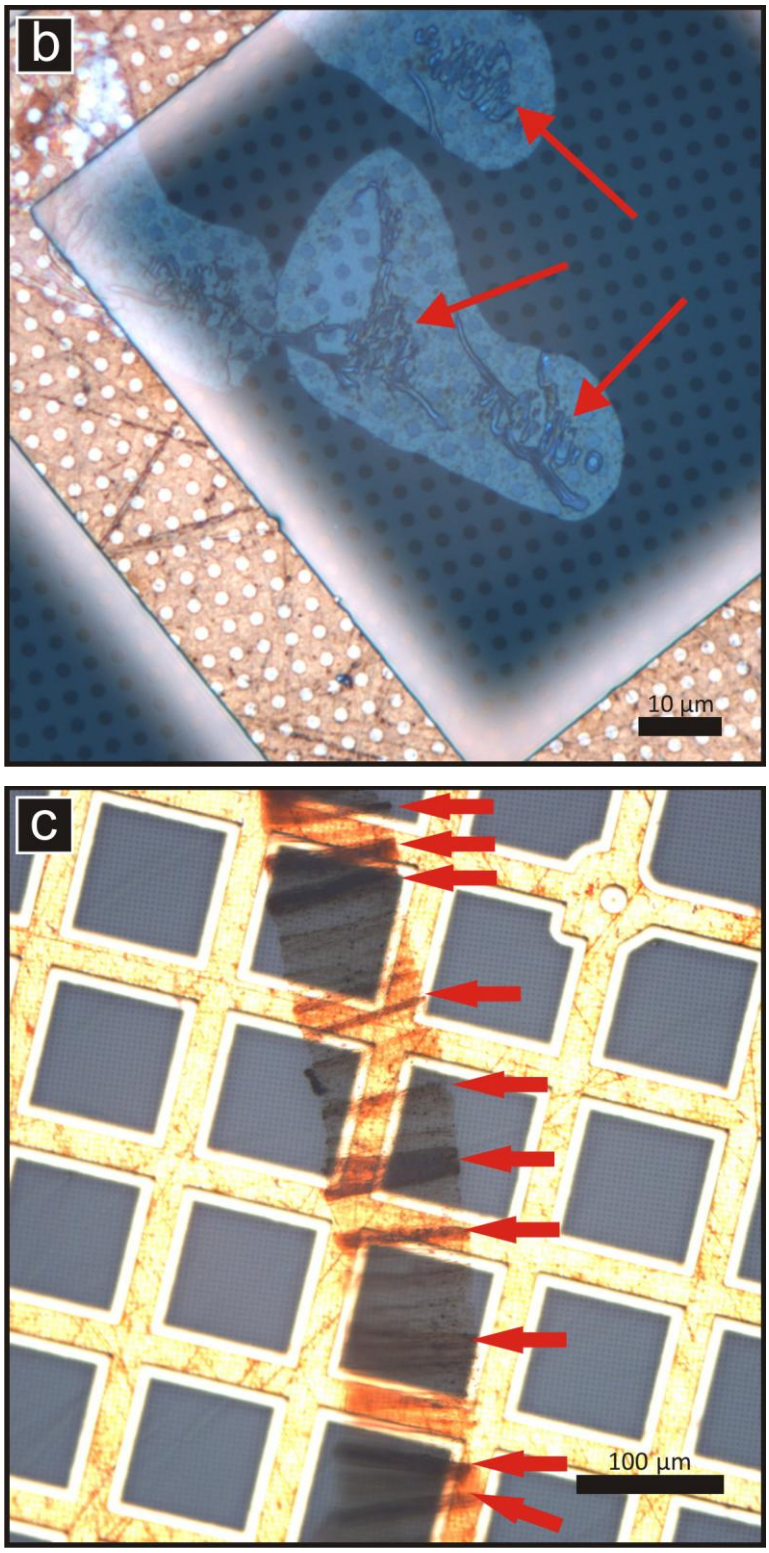

Figure 5-4: Microtome sections as mounted on TEM grids: (a) SBA-15 powder prepared from cyanoacrylate encapsulation, the red area indicates the material of interest (b) cyanoacrylate encapsulated SBA-15 impregnated with SDC before template removal , the red arrows indicate the material of interest, (c) cyanoacrylate encapsulation SBA-15 impregnated with SDC before template removal. The sample produced a long ribbon structure but is poorly attached to the grid and appears to have multiple folds as indicated by the red arrows.

A series of TEM images from the microtome sectioned SBA-15 template were obtained and an example is presented in Figure 5-5. This highlights the long range ordering of the parallel pore structure which when viewed under the TEM microscope was found to be of several microns in length. Figure 5-5 (a,b and d) appear to show the pore channels in a cross-section profile and adds extra detail to what is normally achieved as viewed in Figure 5-3 in respect to the channel formation. There appears to be a discontinuous open channel in the pore section of the material. Whether this is a function of the material formation or consequence of the knife cutting procedure would require further investigation in an attempt to clarify. Figure 5-5 (b) shows the hexagonal pore arrangement over a long range order.

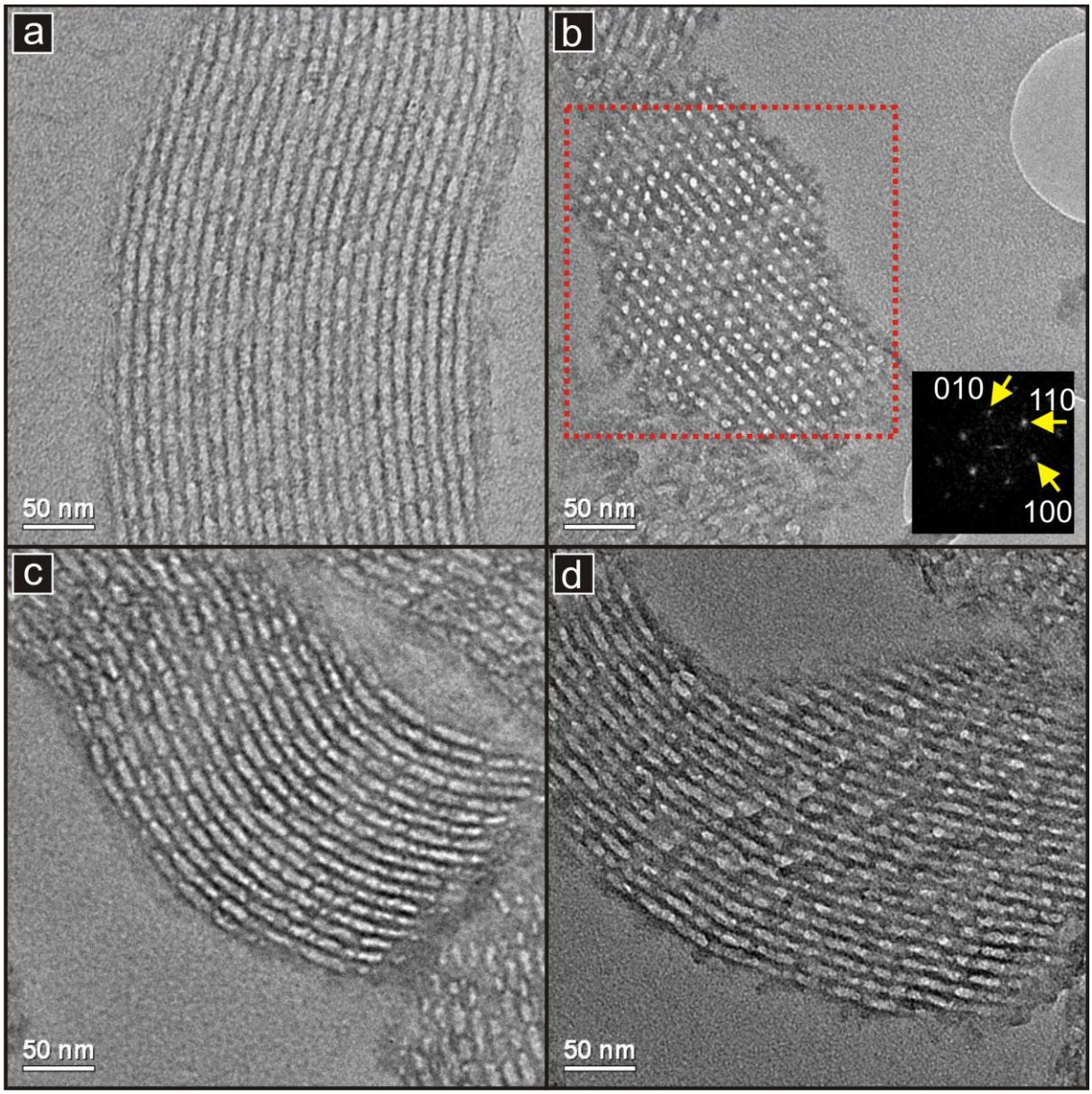

Figure 5-5: TEM image of a microtome section of SBA-15 (a,c and d) rod like structures as viewed along the [100] direction and (b) hexagonal arrangement of the pore structure as viewed along the [001] zone axis. DDPs obtained from red box area in (b) as inset. Miller indices of spots are given.

The particular 'end-on' view down the [001] direction is often difficult to achieve in normal 'swipe' methods of sample preparation and relies on good fortune and patience when analysing. The ultra-microtome method was found to have prepared a significant portion of the material in this direction making analysis easier. The result is encouraging as it also highlights the suitability of ultra-microtomy as a preparatory technique for TEM samples of ordered mesoporous materials.

5.2.3 *KIT-6 Template Analysis*

Kit-6 structure is often interchangeably described in a variety of ways as 3-dimensional hexagonal, cubic bi-continuous, body centered cubic, gyroid-like symmetry, plumbers nightmare[87]. Unfortunately some of these descriptions are not an adequate or appropriate scientific description as they are also relevant to other related structures such as *Im3m* (SBA-16). In order to establish that the Kit-6 template was of expected porosity and structure, all samples were analysed first by gas physisorption as this would indicate the bulk repeatable nature of the material prepared. The generated isotherms can be interpreted for specific surface area ($\mathbf{S}_{BET}$), pore size distribution ($\boldsymbol{W}_{BJH}$), mesopore volume ($\mathbf{V}_{meso}$) and micropore volume ($\mathbf{V}_{micro}$). As this material was used for a series of experiments, several batches were prepared over time and this has allowed variation in the quality to be determined. Figure 5-6 shows a typical isotherm and associated specific pore size distribution (PSD) for one of the produced batches of material. The isotherm is typical of a type IV profile with an associated type H1 hysteresis. A narrow 8.6 nm peak is observed from the desorption branch and specific mesopore volume ($\mathbf{V}_{meso}$) of 0.89 cm^3g^{-1} and micropore volume ($\mathbf{V}_{micro}$) of 0.03 cm^3g^{-1}.

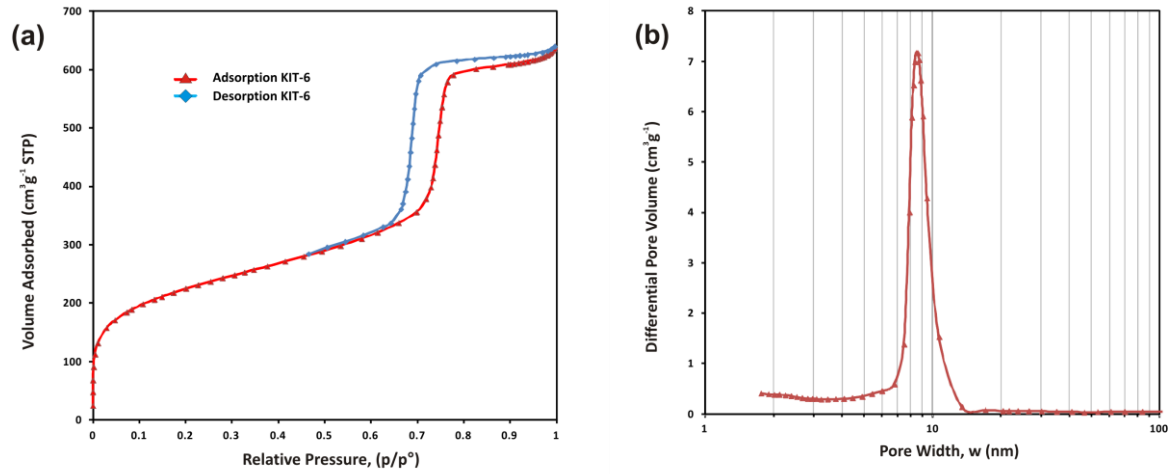

Figure 5-6: Nitrogen physisorption isotherms (a) and specific pore size distributions (b) for KIT-6.

The average specific surface area over nine batches of product was found to be 865 m^2g^{-1} with a standard deviation of 68 m^2g^{-1} and average pore size of between 7 and 8 nm showing a consistency of production. Figure 5-7 presents the low angle XRD data for KIT-6. Analysis of the KIT-6 pattern shows a material with three distinct peaks of the expected face-centred cubic structure observable with a ***d***-spacing of 8.9, 5.4 and 4.7 nm which could be assigned to the (211), (400) and (332) Miller indices respectively as presented in Table 5-2. The unit cell parameters of 21.8, 21.5 and 22.0 nm, were calculated respectively using the formula in Appendix 2, Eqn. 20 and summarised with key data for comparison in Table 5-4.

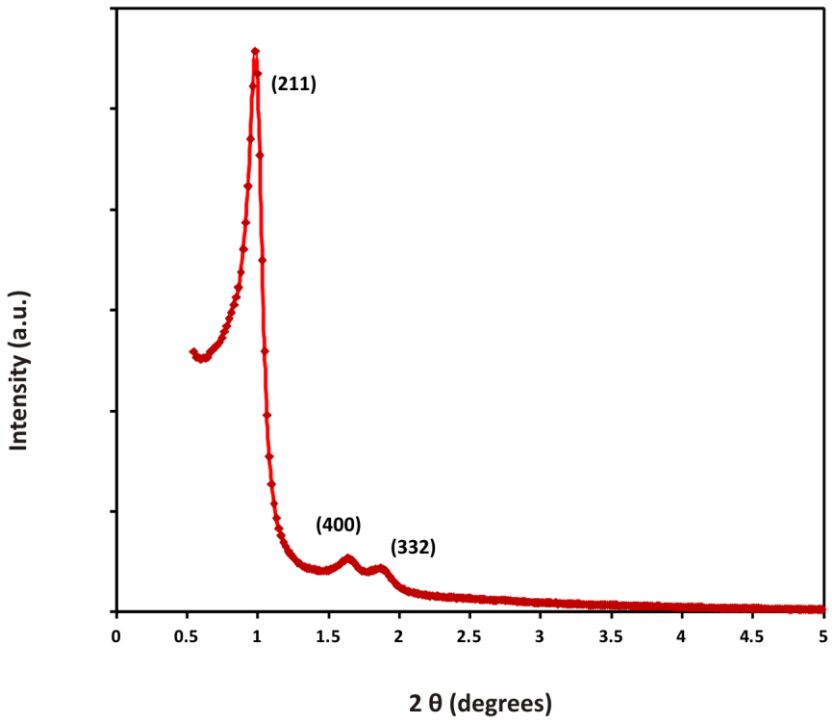

Figure 5-7: SAXS Diffraction pattern and corresponding interplanar ***d***-spacing for KIT-6.

Table 5-2: Calculated d-spacing from 2θ values for KIT-6

2θ (°)	**Indices**	***d*-Spacing (nm)**
0.986	211	8.95
1.647	400	5.35
1.886	332	4.68

TEM images of KIT-6 are presented in Figure 5-8 (a) and (b). Large particles with long range channel uniformity that contained arrays of across their entirety were regularly viewed. Figure 5-8 (c) showed the highly ordered three dimensional arrays of ordered mesopores consistent with that reported in the literature[40] A higher magnification of the amorphous wall and pore structure is presented in Figure 5-8 (d). DDPs were taken and all spots index to the (211) pore orientation with a pore spacing of 8.3 nm.

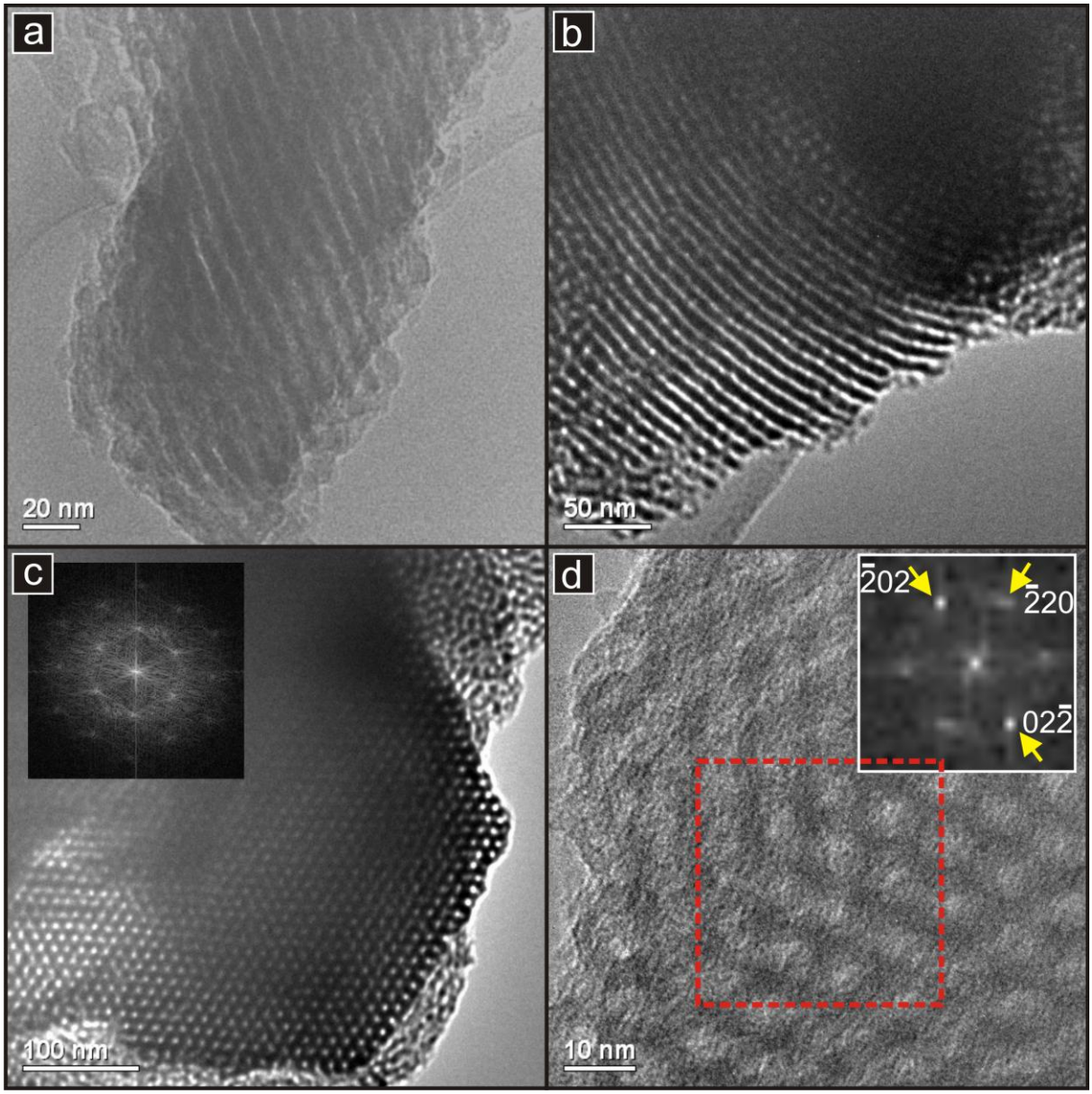

Figure 5-8: (a) TEM images of KIT-6 : (a), (b) Parallel pore channels of the material which highlights the long range order of the mesopore structure (c),(d) TEM image of KIT-6 mesoporous silica template which highlights the cubic arrangement of the pore structure. DDPs obtained from the whole image (c) and the red box as indicated in (d) as inset. Miller indices of spots are given.

5.2.4 FDU-12 Template Analysis

FDU-12 is a face centred cubic structure and regularly defined as having a cage-like framework[88], it is often described pictorially as an array of mesoporous spherical cages each interconnected by six axis orientated channels that are often smaller than the cage centre (Figure 1-3). This cage-channel combination has been described as ink well in shape[89] and leads to a characteristic gas desorption profile. In order to establish that the FDU-12 template was of expected porosity and structure, all samples were first analysed by gas physisorption as this would indicate the bulk repeatable nature of the material prepared. The generated isotherms can be interpreted for specific surface area ($\mathbf{S}_{BET}$), pore size distribution ($\boldsymbol{w}_{BJH}$), mesopore volume ($\mathbf{V}_{meso}$) and micropore volume ($\mathbf{V}_{micro}$). The sorption hysteresis profile observed including the sharp desorption branch at the 0.5 p/p° ratio is characteristic of a cage-like structure and provides evidence towards the synthesis of the expected structure. As this material was used for a series of experiments, several batches were prepared over time and this has allowed variation in the quality to be determined. Figure 5-9 shows a typical isotherm and associated specific pore size distribution (PSD) for one of the produced batches of material. The isotherm is typical of a type IV profile with an associated type H2 hysteresis. A narrow 8.6 nm peak is observed from the desorption branch and specific mesopore volume ($\mathbf{V}_{meso}$) of 0.32 cm^3g^{-1} and micropore volume ($\mathbf{V}_{micro}$) of 0.09 cm^3g^{-1}. The average specific surface area ($\mathbf{S}_{BET}$) over five batches of product was found to be 633 m^2g^{-1} with a standard deviation of 139 m^2g^{-1} and average pore size of between 7 and 9 nm showing a consistency of production.

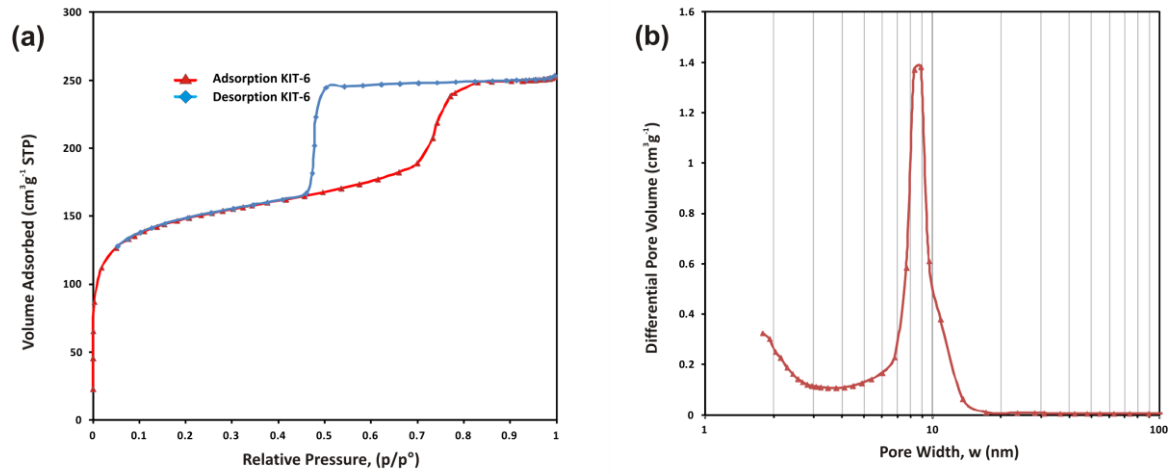

Figure 5-9: Nitrogen physisorption isotherms (a) and specific pore size distributions (b) for FDU-12.

Figure 5-10 presents the low angle XRD data for FDU-12. Analysis of the FDU-12 pattern shows a material with two distinct peaks of the expected face-centred cubic structure observable with a ***d***-spacing of 11.7 and 6.7 nm which could be assigned to the (111) and (220) Miller indices respectively as presented in Table 5-2. The unit cell parameters of 20.3 and 18.8 nm were calculated respectively using the formula in Appendix 2, Eqn. 20 and summarised with key data for comparison in Table 5-4.

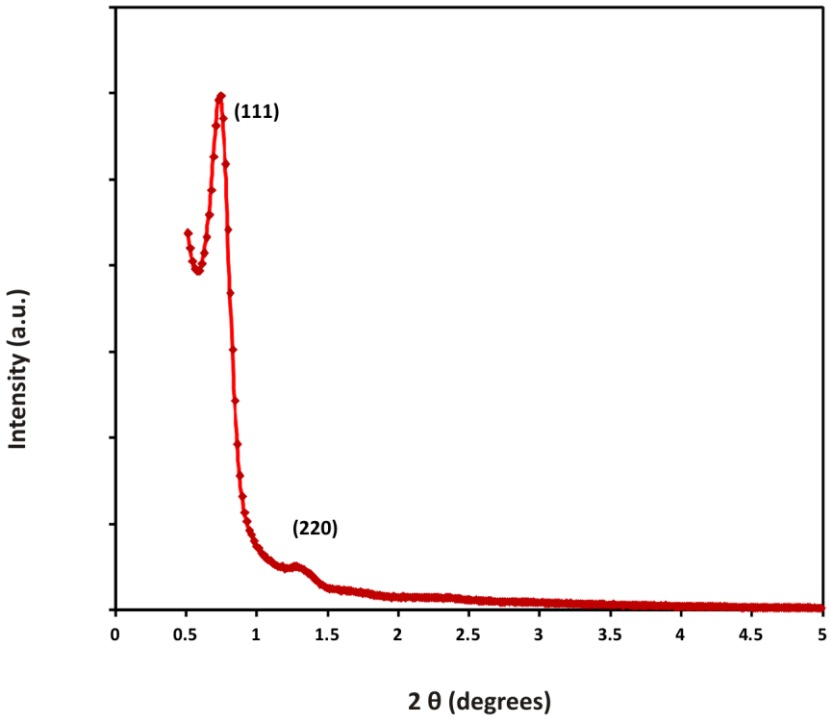

Figure 5-10: SAXS Diffraction pattern and corresponding interplanar ***d***-spacing for FDU-12.

Table 5-3: Calculated d-spacing from 2θ values for FDU-12.

2θ (°)	**Indices**	***d*-Spacing (nm)**
0.748	111	11.81
1.343	220	6.57

TEM images of FDU-12 are presented in Figure 5-11. Large particles, Figure 5-11 (a), with long range pore uniformity assembled in arrays across the entirety of the particles were regularly viewed. Figure 5-11 (b) and (c) detail the array of pores which appear to be of a regular and consistent pore and wall size. A higher magnification of the amorphous wall and pore structure is presented in Figure 5-11 (d). The DDP taken in Figure 5-11 (b) relates to a pore spacing of 12.1 nm.

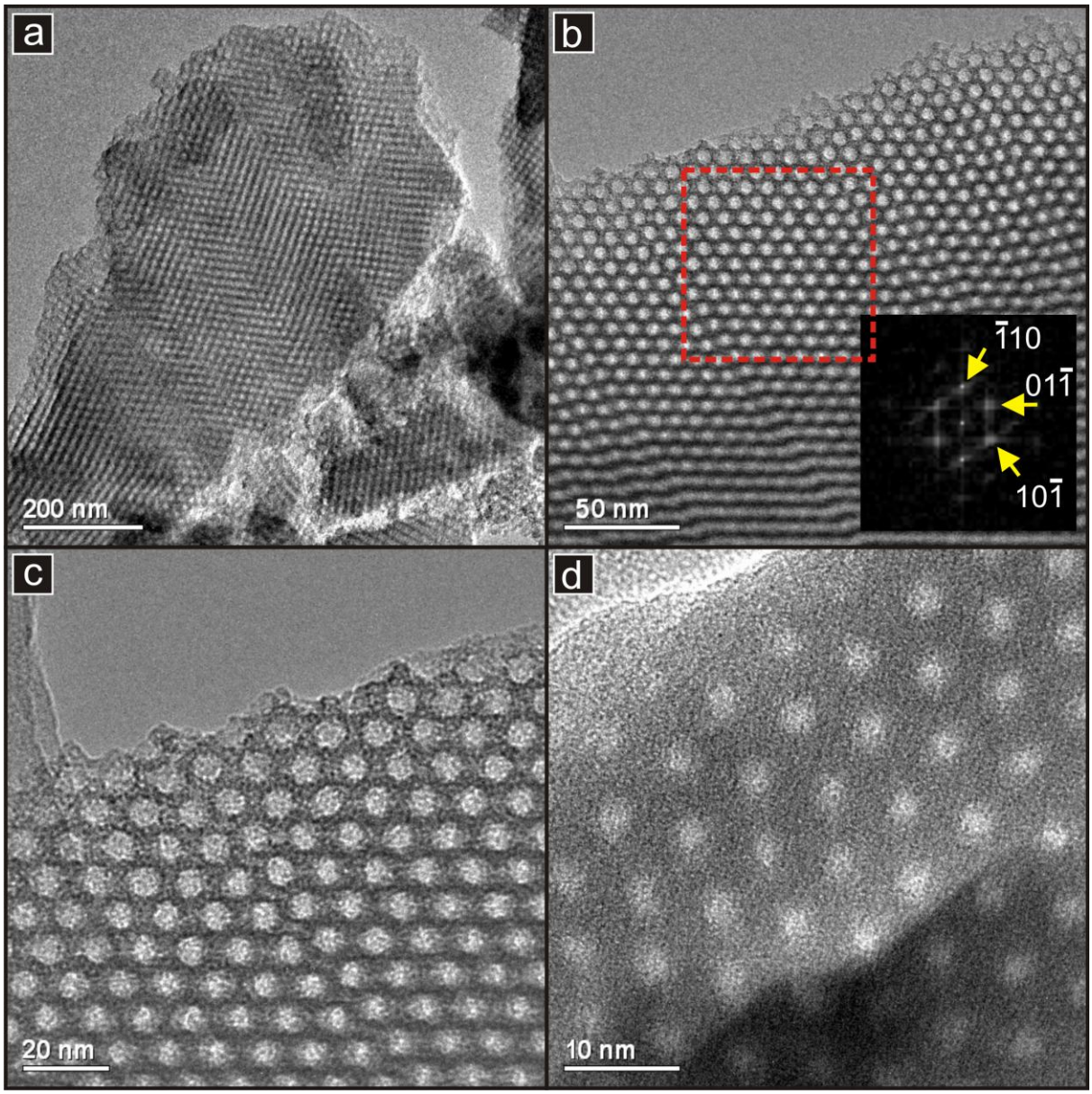

Figure 5-11: TEM images of FDU-12 (a) long range array of pores (b), (c) indicate the pore uniformity across a wide range of the material (d) is a higher magnification of the pore and amorphous wall structure.

5.3 Non-Standard Silica Templates

5.3.1 *Ultra-Large Pore SBA-15*

In order to establish that the UL-SBA-15 template was of expected porosity and structure, all samples were analysed first by gas physisorption as this would indicate the bulk repeatable nature of the material prepared. The generated isotherms can be interpreted for specific surface area ($\mathbf{S}_{BET}$), pore size distribution ($\boldsymbol{W}_{BJH}$), mesopore volume ($\mathbf{V}_{meso}$) and micropore volume ($\mathbf{V}_{micro}$). The isotherm in Figure 5-12 is typical of a type IV profile with an associated type H3 hysteresis. The hysteresis loop profile and additional mesopore presence at 5-8 nm is in agreement with the findings of Cao and co-workers[69]. A PSD range of between 22 and 28 nm was observed from the desorption branch with a specific mesopore volume ($\mathbf{V}_{meso}$) of 0.91 cm^3g^{-1} and micropore volume ($\mathbf{V}_{micro}$) of 0.01 cm^3g^{-1} being recorded. The specific surface area ($\mathbf{S}_{BET}$) was found to be 332 m^2g^{-1}.

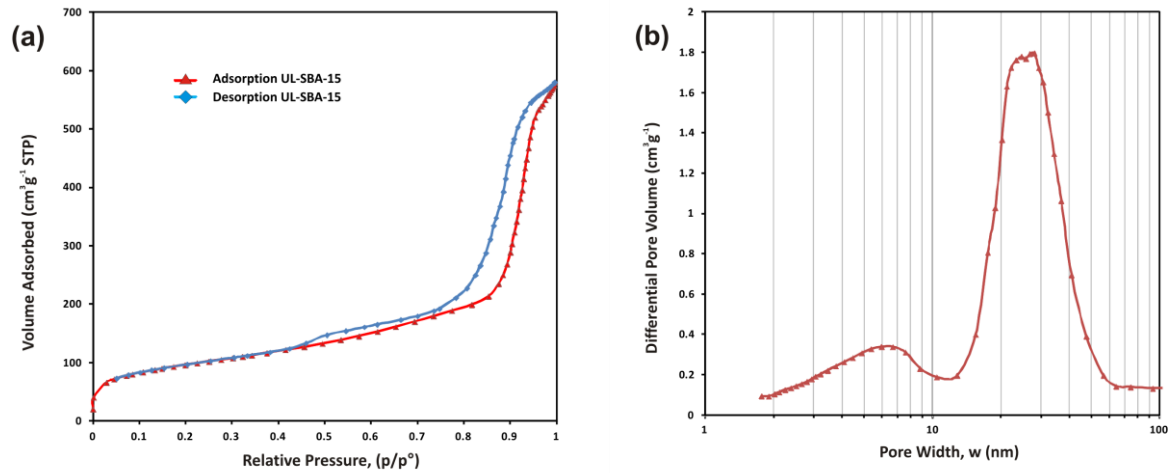

Figure 5-12: Nitrogen physisorption isotherms (a) and specific pore size distributions (b) for UL-SBA-15

Figure 5-13 presents the low angle XRD data for UL-SBA-15. No observable peaks were found to be present.

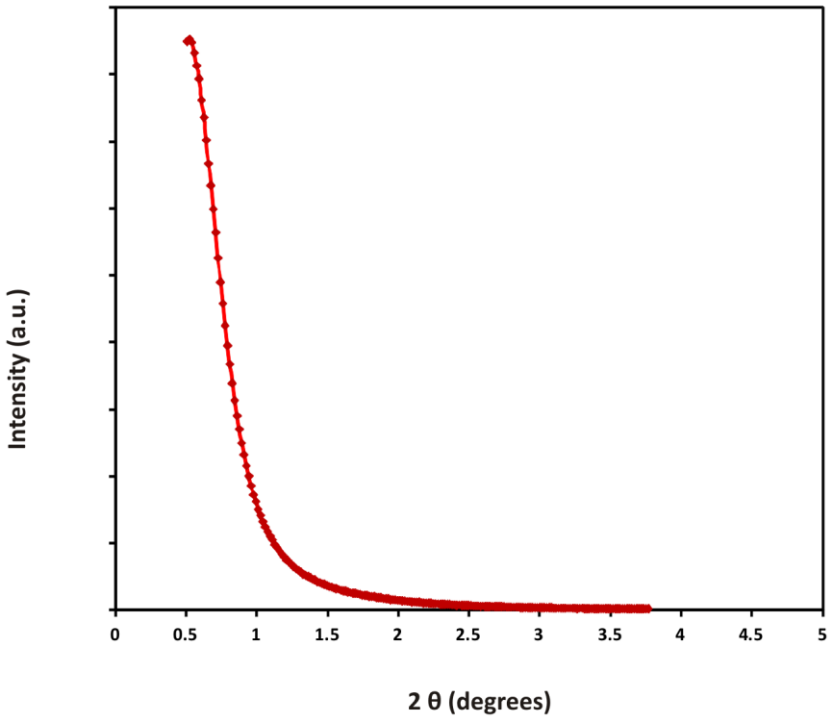

Figure 5-13: SAXS Diffraction pattern and corresponding interplanar ***d***-spacing for UL-SBA-15.

In order to attest the pore expansion and pore ordering, TEM was used to visually verify the structural integrity. Figure 5-14 (a) indicates that the long range pore channels were present and that the material was therefore ordered. In Figure 5-14 (b) and (c), an array of pores was evident but it remains unclear as to whether the ordering is sufficient to produce a hexagonal arrangement. The images indicate the presence of large pores measured as a w_{TEM} of 21.7 nm size. These are surrounded by an amorphous framework with a measured wall thickness t_{TEM} of 4.5 nm. The relative ratio of pore wall thickness to pore size is indicated in Figure 5-14 (d) by the red lines.

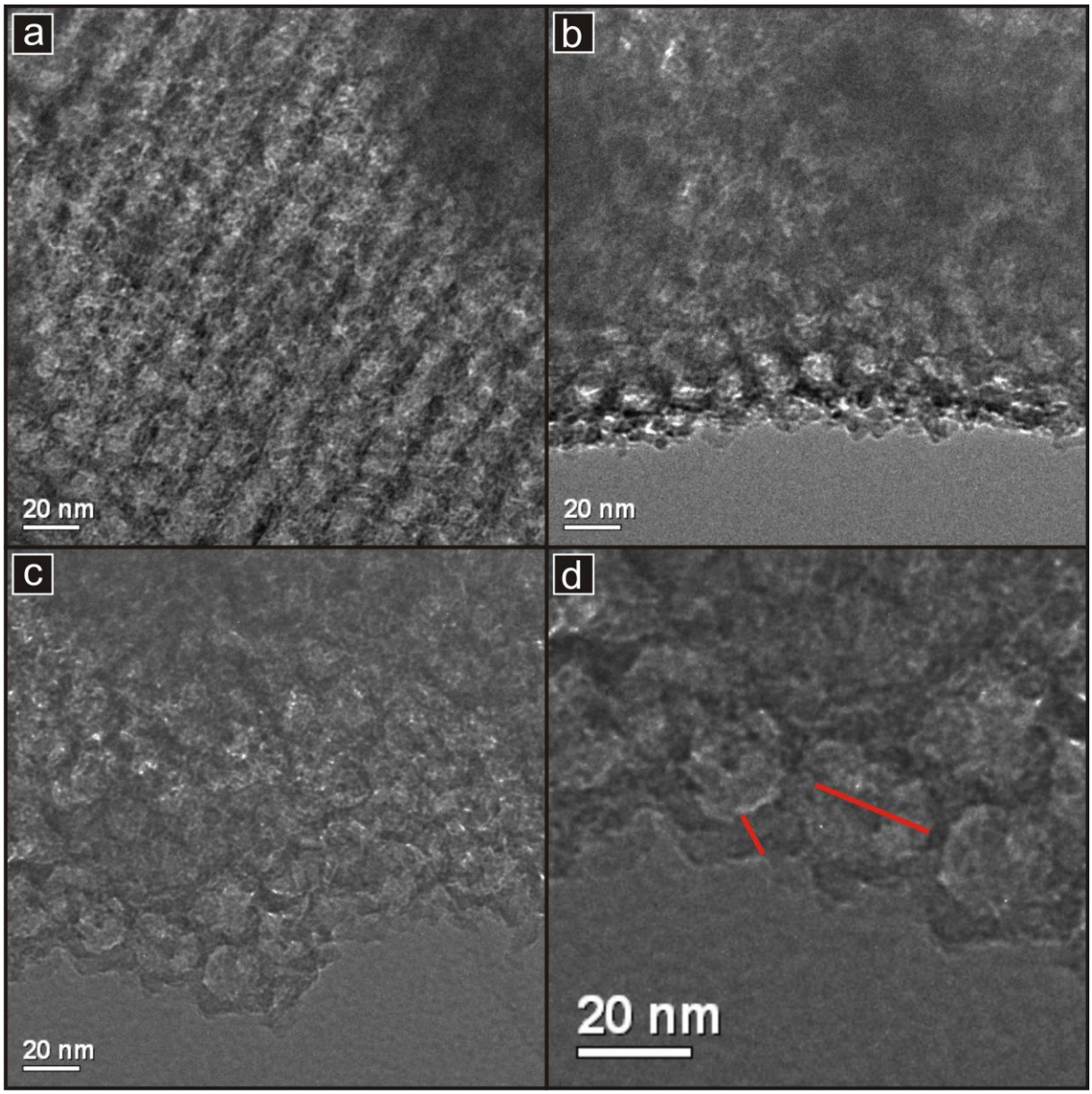

Figure 5-14: (a) TEM image of UL-SBA-15 (a) uniform and parallel channels, (b) and (c) indicate an array of ordered large pore and thin wall formations (d) a higher magnification of the pore and wall structure. Red lines are provided to help indicate the difference in pore to wall ratio.

5.3.2 *Functionalised SBA-15*

One of the major objectives of this research was to produce SDC mesoporous product with reduced residual silica and as such templates were modified by attempting to functionalise the internal wall surface of the silica material. Two different functionalising chemicals were employed: 1,1,3,3-Tetramethyldisilazane (TMDS) and (3-Aminopropyl)trimethoxysilane (APTS); From the gas physisorption analysis of Figure 5-15**,** evidence of TMDS penetration into the pore structure of SBA-15 would be determinable through a decreasing shift in pore size distribution of approximately 1nm due to the surface modification -'adhesion'- from TMDS molecules.

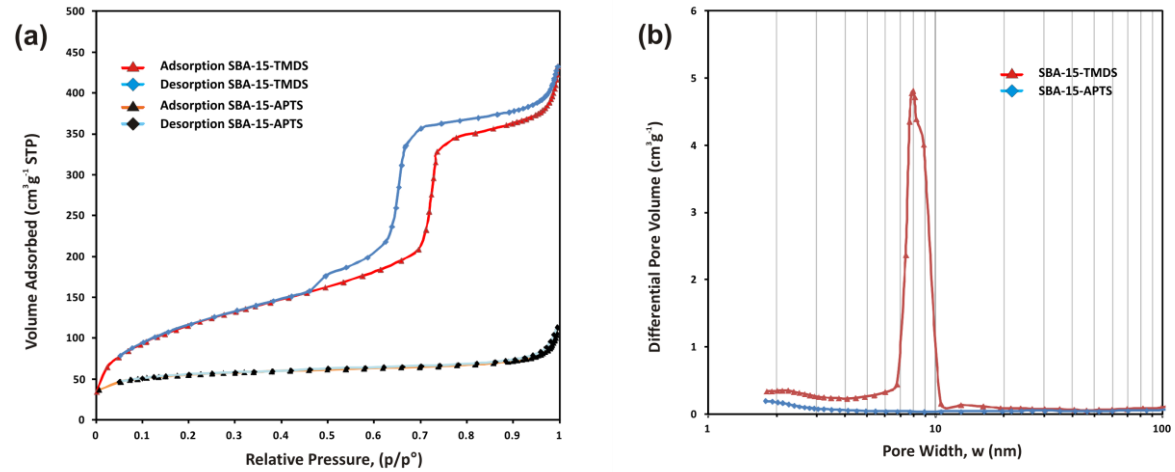

Figure 5-15: Nitrogen physisorption isotherms (a) and specific pore size distributions (b) for functionalised SBA-15 using 1,1,3,3-tetramethyldisilazane or (3-Aminopropyl)trimethoxysilane.

Careful viewing of the PSD reveals that a shoulder is in evidence suggesting that some modification of the larger pore size has occurred. In comparison with the original template Figure 5-1 which reports PSD maximum at 8.4 nm , $\mathbf{V}_{meso}$ of 0.73 cm^3g^{-1} and $\mathbf{V}_{micro}$ of 0.097 cm^3g^{-1}; a new maximum at 7.9 nm and decreased $\mathbf{V}_{meso}$ of 0.71 cm^3g^{-1} and zero $\mathbf{V}_{micro}$ was observed. The attempt at impregnation and functionalisation using APTS produced a material that gave no measurable mesoporous structure.

5.3.3 *Functionalised Ultra-Large Pore SBA-15*

As a method to establish the effectiveness of using silylating reagents as a post grafting technique with UL-SBA-15 template, gas physisorption was utilised to measure any

prospective change in porosity. Two generated isotherms are presented in Figure 5-16 and represent attempted functionalisation using TMDS and APTS. The isotherms are typical of a type IV profile and associated type H3 hysteresis with the APTS modified UL-SBA-15 displaying a much reduced gas uptake. The associated specific pore size distribution (PSD) for TMDS is very similar to UL-SBA-15 PSD with no significant change in PSD value or pore volumes with the exception of a shoulder at the 20-25 nm range indicating a minimal reduction in pore volume. Values of specific mesopore volume ($\mathbf{V}_{meso}$) of 0.82 cm^3g^{-1} and 0.32 cm^3g^{-1}; specific surface area ($\mathbf{S}_{BET}$) of 240 m^2g^{-1} and 71, were reported for TMDS and APTS treatments respectively. No micropore volume ($\mathbf{V}_{micro}$) was reported for either treatment.

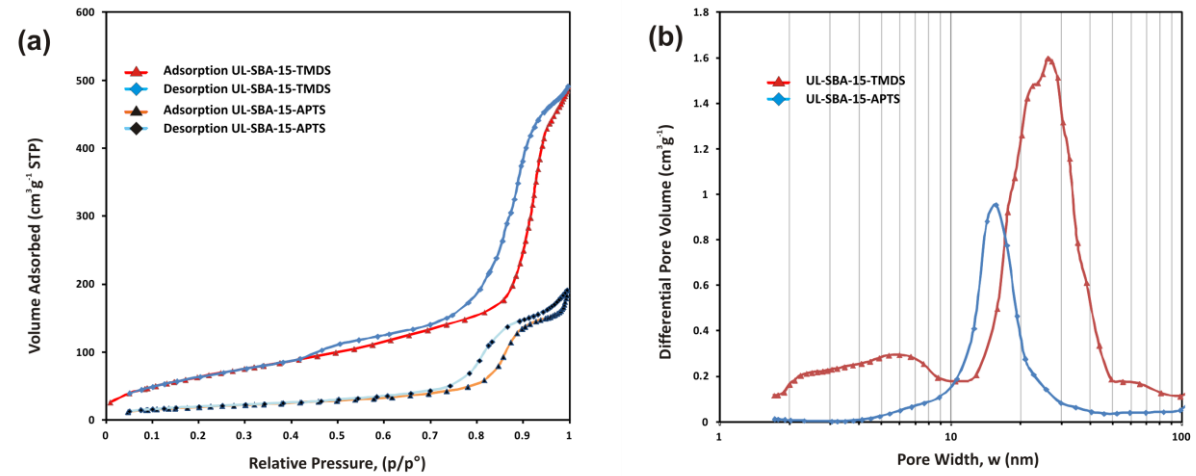

Figure 5-16: Nitrogen physisorption isotherms (a) and specific pore size distributions (b) for functionalised UL-SBA-15 using 1,1,3,3-tetramethyldisilazane or (3-Aminopropyl)trimethoxysilane.

5.4 Discussion

Following the preparation methods for the three structures, batch amounts of template ranging from 1-2 g were produced. After each successive attempt of template synthesis, they were characterised by gas physisorption as a means of quality control and to generate specific data on pore size distribution and pore volume as these were necessary as key parameters to compare any final product from the nanocasting method. Templates were further characterised by means of low angle XRD and TEM imaging such that the data generated was cross compared as presented in Table 5-1. The data obtained is in agreement although the pore size is slightly under reported due to the dimensional assumptions contained in the BJH model.

Table 5-4: Values for unit cell parameters (***$a_0$1 – $a_0$3***), inter-planar spacings (***d***), pore width (***w***) and pore wall thickness (***t***) obtained using the method indicated (BJH, SAXS, TEM) for the samples indicated. All values are in nm. Values of ***a_o*** are calculated from the corresponding ***d_{SAXS}*** value. Miller indices are given in italics below each value of ***d***.

sample	w_{BJH}	$d_{SAXS}1$	$d_{SAXS}2$	$d_{SAXS}3$	a_01	a_02	a_03	d_{TEM}	w_{TEM}	t_{TEM}
SBA-15	8.4	9.8 *(100)*	5.9 *(210)*	5.1 *(100)*[a]	11.3	11.7	11.8	9.5 *(100)*	7.5	2.2
KIT-6	8.6	8.9 *(211)*	5.4 *(400)*	4.7 *(332)*	21.8	21.5	22.0	8.3 *(211)*	7.0	2.8
FDU-12	8.6	11.7 *(111)*	6.7 *(220)*	-	20.3	18.8	-	12.1 *(111)*	9.4	4.7
UL-SBA-15	20-30	- *(100)*	- *(210)*	- *(100)*	-	-	-	26.2 *(100)*	21.7	4.5

[a] second order diffraction,

Table 5-5: A summary of the gas physisorption data between OMS templates. Values for pore width (W_{BJH}), mesopore volume (V_{meso}), micropore volume (V_{micro}), specific surface area (S_{BET}) obtained using the methods indicated (BJH, BJH, t-plot and BET respectively).

Sample	w_{BJH}	V_{meso} (cm^3g^{-1})	V_{micro} (cm^3g^{-1})	S_{BET} (m^2g^{-1})
SBA-15	8.4	0.73	0.10	831
KIT-6	8.6	0.89	0.03	769
FDU-12	8.6	0.32	0.09	490
SBA-15-TMDS	7.9	0.71	nil	417
SBA-15-APTS	nil	0.12	0.03	180
UL-SBA-15	22-28	0.91	0.01	332
UL-SBA-15-TMDS	22-28	0.82	nil	240
UL-SBA-15-APTS	15.3	0.32	nil	71

Ultra-Large SBA-15

The synthesis of ultra-large SBA-15 is dependent on conditions of temperature during micelle assembly, hydrothermal temperature-time and surfactant to micelle expander ratio[69]. Changing any one of these four variables allows for variability in pore size and increase in disorder to occur. The reported synthesis of ultra-large SBA-15 should prepare an ordered mesoporous material with an expanded pore structure while maintaining a consistent but unexpanded silica wall framework. This would indicate that an enlarged pore greater than the standard 8 nm with a pore wall of 4 nm should be achieved. Interpretation of the TEM and gas physisorption supports the successful preparation of the material given that a PSD of 26 nm and pore wall of 4-5 nm was reported. Despite the requirement for careful control, UL-SBA-15 was produced with a controlled PSD range. The value of PSD shows a spread of between 22 and 28 nm which could be explained by not having precise control in the 13°C temperature chosen during micelle assembly as a 1°C shift would produce a 6nm shift in PSD. The values presented here and in particular the sorption profile, are in agreement with that reported[69]. The SAXS diffraction pattern had no discernable peaks indicating either a lack of ordered material or masking of the lower order interplanar ***d***-spacings from the instrument background. The main lattice plane for a structure with a large unit cell size of 30 nm would be positioned in or around a 2θ value of 0.3° and is not obtainable using the instrumentation. As material was evidenced by TEM imaging as having ordered large pores in good agreement with the gas physisorption data and consistent pore wall structure of 5 nm, the material appears to have been successfully produced. Of concern as a strategy in using the material in a nanocast role is the low micropore $\mathbf{V}_{micro}$ value. One possible explanation is that the micropores present in the original structure may have also been subject to swelling effects pushing them into the mesopore range, this may offer an explanation towards the additional mesopore presence at 5-8 nm, which Cao and co-workers hypothesis as a formation of disordered domains.

Functionalised material

An expected consequence of surface modification is for PSD to change. Wang et al[86d] reported PSD changes of approximately 0.5nm for each 5% increase in starting silizane concentration although this was based on a one-pot synthesis as opposed to the post-functionalisation technique applied here. On first observation of the SBA-15 material modified using TMDS, it would appear that no significant change to the material has occurred. However, an observed pore size decrease of 0.5 nm is reported along with an

approximate 50% decreases in SSA (S_{BET}) while V_{meso} is only marginally altered. This would suggest that a controlled amount of grafting has taken place especially as the micropore volume has been removed.

Distribution of the grafted sites may well take place preferentially at the most accessible areas and this would suggest that the external surfaces and pore entrances may well be overloaded before internal grafting takes place. Given that the attempt of functionalisation with APTS gave no measurable mesoporous structure, it would indicate that either complete pore filling occurred, the structure was destroyed in reflux synthesis or the more likely outcome of pore blocking occurred as a consequence of excessive grafting or steric hinderence[71]. Either way, the material produced after APTS treatment was of no practical use as a candidate to synthesis final product.

The functionalisation of UL-SBA-15 was attempted using both TMDS and APTS. As the initial attempts appear to have either failed to impregnate into the channel structure in the case of APTS or blocked the pore entrance in the case of TMDS, a strategy of using a structure with larger pores was researched in anticipation that the extra volume would allow successful impregnation. The fact that the TMDS was not observed as changing the PSD would suggest that either the material was entering the channel or the concentration used may have been too weak to effectively graft enough functional groups. The use of APTS did appear to enter and affect the pore channels sufficiently to change the PSD value. Critically, the specific mesopore volume remains high but no micropore volume is reported. As micropore volume is usually an indicator in SBA-15 material as a measure of the interconnectivity between pore channels, the optimism with the ultra-large material is that the equivalent channel bridges are in the mesopore range.

5.5 Summary

Silica templates were produced in batches that were subsequently analysed and proved to have repeatable characteristics typical of mesoporous materials with long range order. The templates were found to be consistent in their structure with literature reports and methods of synthesis. Ultra-microtomy as a preparatory method in TEM analysis was found to be a good alternative to standard preparation and was particularly useful in viewing the hexagonal pore arrangement i.e. [001] zone axis in SBA-15. The preparation of ultra-large

SBA-15 was successful although difficulties in the preparation due to requirements of carefully controlling temperature were of concern. Attempts were made to alter the surface moieties of SBA-15 and the ultra large variant with amine or methyl terminated silizanes. From the gas physisorption data presented it is suspected that functionalisation of SBA-15 and UL-SBA-15 using TMDS was ineffective as an expected PSD and pore volume change did not occur. Using APTS did appear to have a modifying effect as the gas physisorption data for SBA-15 indicated that pore closure occurred. Modification also occurred with UL-SBA-15 showing a reduction in PSD of 10 nm but this was associated with pore volume changes. Despite the apparent success of modifying UL-SBA-15 template, it would appear that the lack of microporosity ($\mathbf{V}_{micro}$) may render this approach as a nanocasting medium as futile given that $\mathbf{V}_{micro}$ is indicative of the nanobridges that would form from any subsequent casting attempt.

Chapter 6

Thermal Deformation of Silica Templates

6.1 Introduction

In the synthetic methods involved in nanocasting and also in surface modification, and second phase impregnation the OMS is exposed to elevated temperatures. This is also true during applications of OMS materials as, for example, heterogeneous catalysts and gas storage materials. For these reasons, and with a view to these applications, it is important to understand better the thermal stability and thermal evolution of OMS materials. In a detailed thermogravimetric and *in situ* High temperature XRD (HTXRD) study of a number of OMS materials including SBA-15, Kleitz *et al* concentrated on the decomposition of organic templates during the initial calcination and the related changes in pore structure [90]. In a gas adsorption study, Ryoo and coworkers reported a decrease in mesopore diameter with increasing treatment temperature in SBA-15 and identified the existence of micropores interconnecting the mesopores [91]. Shah et al also used HTXRD on SBA-15 and reported thermal contraction with increasing temperature but pore stability up to 1200 °C [92]. Huang *et al* saw pore shrinkage in ultra large pore FDU-12, when they applied calcination temperatures up to 450 °C [93] and Kruk and Hui were able to modify FDU-12 so that its spherical pores became isolated, or entombed, after calcinations at 450 – 640 °C[94]. The latter effect is of interest for the formation of low dielectric insulators and a similar effect – in this case forming entombed cylindrical pores – was reported by Mandal and Kruk for SBA-15 [95].

Here, three widely-used and representative OMS materials with different pore structures – SBA-15, KIT-6 and FDU-12 - were studied as-prepared and after thermal treatment at a wide range of temperatures. Transmission Electron Microscopy (TEM), (*ex-situ*) Small-Angle X-ray diffraction (SAXS), gas physisorption and ^{29}Si Magic Angle Spinning Nuclear Magnetic Resonance (MAS-NMR) were used in each case to obtain the pore size distributions, the unit cell dimensions of the mesopore structures and the relative occupancy of the distinct chemical environments of Si within them. These data were cross-correlated and the evolution of the three OMS structures with treatment temperature was elucidated resulting in a comprehensive and systematic comparative study.

6.2 Experimental

SBA-15, Kit-6 and FDU-12 silicas were synthesised according to the procedures previously outlined in section 4.2.

Each of the three OMS products were subdivided into equal measures of approximately 200 mg for subsequent thermal treatment. This quantity was generally sufficient to allow for the full series of analytical techniques to be applied since these were non-destructive and caused only minimal loss of sample. The thermal treatment consisted of heating the material in air to the desired temperature at a ramp rate of 1 °C min^{-1} and applying a dwell of 5 h. Treatment temperatures, ***T***, of 300, 400, 450, 500, 550, 600, 650, 700, 800 and 900 °C were applied. This temperature range was chosen to include all temperatures of relevance to the various applications of OMS materials, including catalysis and nanocasting. Samples are named as follows: the prefix indicates the OMS structure type and the suffix indicates the treatment temperature. In addition, the untreated, as-prepared samples will be denoted by the suffix, AP. As an example, SBA-15 treated at 900°C is referred to as S-900.

Nitrogen adsorption isotherms were measured at -196 °C using a Micromeritics ASAP 2020 volumetric adsorption analyser. All samples were pre-treated before analysis by outgassing overnight at 120 °C under vacuum.

SAXS patterns were recorded using a PANalytical Empyrean Diffractometer in reflectance geometry using Cu $K\alpha_1$ radiation (wavelength $\boldsymbol{\lambda}$ = 0.1540598 nm). The incident beam was collimated by a series of slits and a beam mask. Diffraction data were recorded in the range 2θ = 0.5 – 5° with a step size of 0.01°. The powder samples were pressed into the 0.5 mm deep, 16 mm diameter well in a standard circular steel reflectance holder with a PTFE liner.

TEM images were obtained using a JEOL JEM 2011 instrument operating with a LaB_6 filament and at an accelerating voltage of 200 kV. The images were captured and analysed using Digital Micrograph 3.4.4 software operating a Gatan CCD camera.

Solid-state ^{29}Si MAS-NMR spectra were obtained at 79.44 MHz at a spin rate of 6.8 KHz on a Varian VNMRS 400 spectrometer for all SBA-15 and KIT-6 samples. The spectra for the FDU-12 samples F-AP, F-450 and F-600 were obtained at 59.63 MHz and at a spin rate of 6.0 KHz on a Varian Unity Inova 300 spectrometer with 60 s delay between scans. The amount of sample available for NMR was small because of the need to use a single batch of material for all treatment temperatures. Because of the particularly small amount of sample available, the spectrum for F-900 was run at 79.5 MHz on a Bruker Avance III spectrometer with 180 s delay between scans using a 9.4 T wide bore superconducting magnet.

For each of the OMS materials, values for interplanar spacings, ***d***, obtained from the SAXS patterns were used to calculate the corresponding unit cell parameters (a_o).

6.3 Results

6.3.1 *Gas Physisorption*

In order to determine the structural changes for the three OMS materials of interest, a series of nitrogen physisorption isotherms were produced from each thermally treated sample and the as-prepared samples (AP). Isotherm plots for the three AP samples together and for the individual samples after heat treatment are presented in Figure 6-1(a) and Figure 6-1 (b-d), respectively. Using Brunauer-Emmett-Teller (BET) the specific surface area (SSA, m^2g^{-1}) was obtained. The Barrett-Joiner-Halenda (BJH) algorithm was utilised to obtain pore size distribution (PSD) and specific mesopore volume ($\mathbf{V}_{meso}$, cm^3g^{-1}, pore diameters of 2 to 50 nm) and the t-plot method was used to obtain values of specific micropore volume ($\mathbf{V}_{micro}$, cm^3g^{-1}, pore diameters under 2 nm). Figure 6-2 presents plots of $\mathbf{V}_{meso}$, $\mathbf{V}_{micro}$ and SSA against treatment temperature for the three OMS materials. For all three materials, $\mathbf{V}_{meso}$ is much larger than $\mathbf{V}_{micro}$. On increasing treatment temperature for SBA-15 and KIT-6, SSA first decreased noticeably for T = 400 °C and continued to decrease roughly linearly until reaching a point of inflection at T ~ 550 °C, after which it declined more sharply.

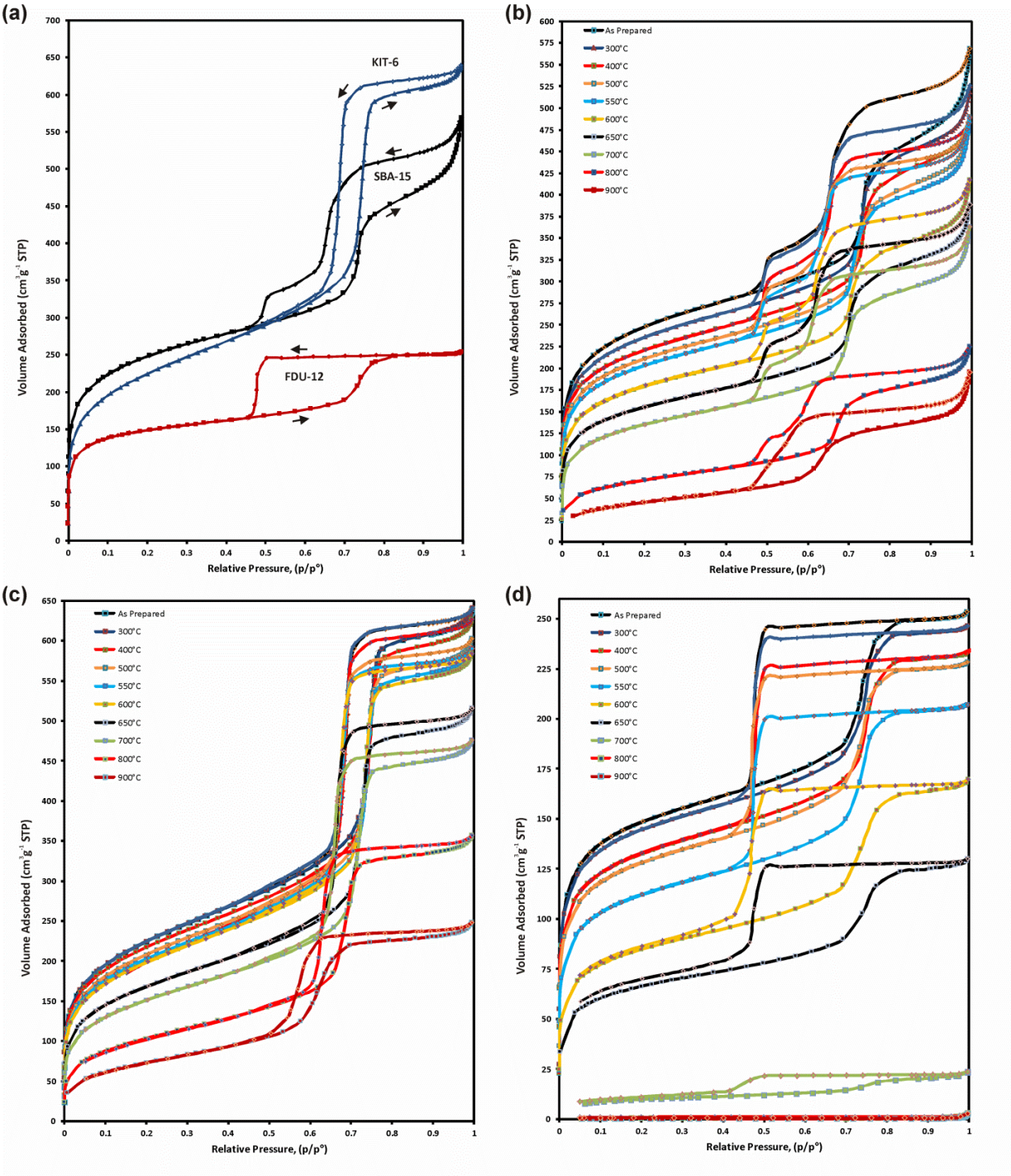

Figure 6-1: (a) Nitrogen physisorption isotherms for all three OMS materials in their as-prepared (AP) states. Arrows indicate the adsorption and desorption branches. Sorption isotherms for all pretreatment temperatures and AP sample as indicated for (b) SBA-15, (c) KIT-6, (d) FDU-12.

Nevertheless, for ***T*** = 900 °C significant SSA remained for both SBA-15 (160 m^2g^{-1}, 20% of the initial value) and KIT-6 (260 m^2g^{-1} and 34%). The SSA appeared to be approaching a plateau for SBA-15 at this temperature but this was not the case for KIT-6. These same trends are closely paralleled in the plots of $\mathbf{V}_{meso}$ against ***T***. The corresponding fall in $\mathbf{V}_{meso}$ suggests that the internal pore structure was in the process of contracting.

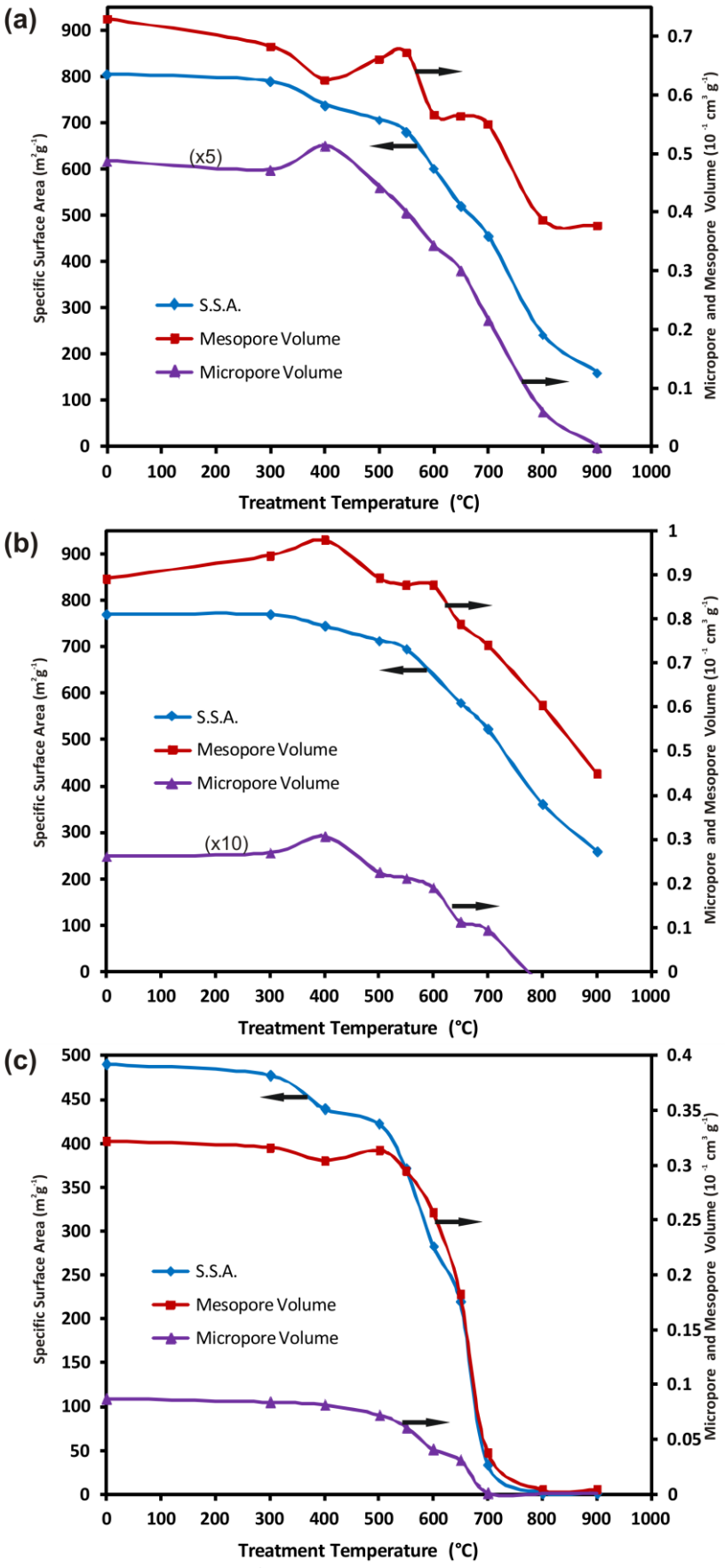

Figure 6-2: Plots of specific surface area (m^2g^{-1}) and specific micro (V_{micro}) and mesopore (V_{meso}) volume (cm^3g^{-1}) as functions of pretreatment temperature for: (a) SBA-15, (b) KIT-6, (c) FDU-12. Data points at 0°C for as-prepared (AP) materials V_{micro} has been multiplied by a factor of 5 for SBA-15 and 10 for KIT-6 for clarity.

Despite this trend, both materials still exhibited significant mesoporosity – around 41 and 44% of the initial values for SBA-15 and KIT-6, respectively – for ***T*** = 900 °C. In Figure 6-2(c) the corresponding plots for FDU-12 showed only small decreases in SSA and $\mathbf{V}_{meso}$ indicating a high tolerance to thermal stress up to and including ***T*** = 500 °C after which both parameters suffered a rapid decline from ***T*** = 700 °C, both reaching values close to zero at higher temperatures. This behavior indicates that differences in pore structure had a considerable influence on the structural integrity of these OMS materials under thermal stress.

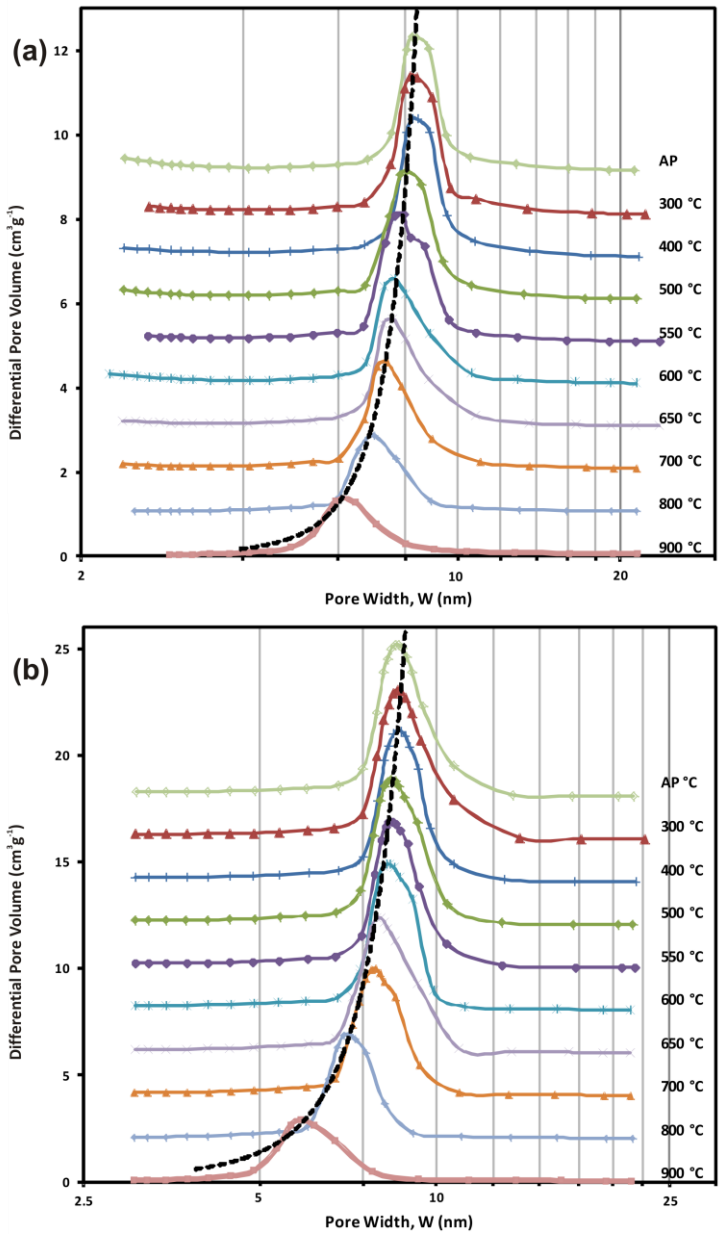

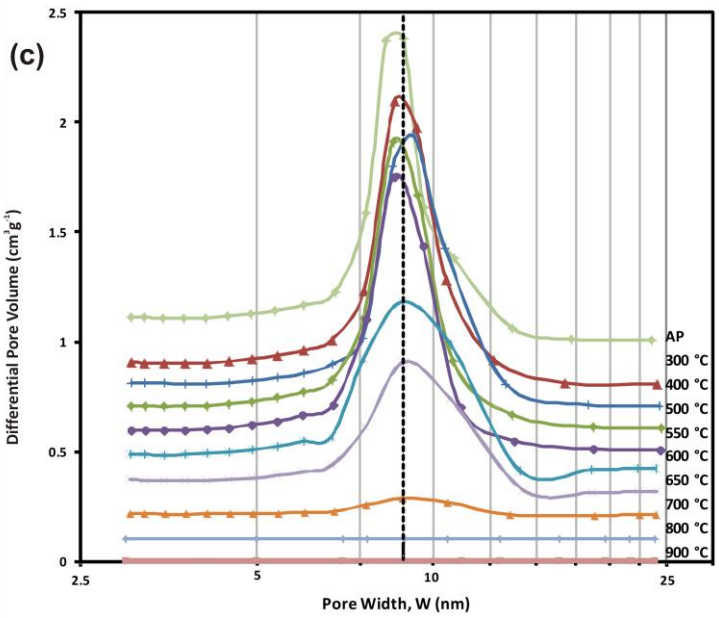

Figure 6-3: Pore volume of (a) SBA-15, (b) KIT-6, (c) FDU-12 from BJH Adsorption Isotherm. Plots have been offset incrementally in the y-axis by (a) 1.0, (b) 2.0 and (c) 0.1 for purposes of clarity.

This phenomenon is strikingly verified by reviewing the plots of pore size distribution in the mesopore region presented in Figure 6-3. For all three as-prepared materials, a clear, single peak was observed and peak size decreased as treatment temperature increased. This corresponds to the significant loss of porosity observed for all samples in Figure 6-2. For SBA-15 and KIT-6 there is a smooth trend in which the peak maximum shifted to lower pore width values as ***T*** increased. The pore widths for all three AP and 900 samples are given in Table 6-1.

Table 6-1: Values for unit cell parameters (***$a_0$1 – $a_0$3***), interplanar spacings (***d***), pore width (***w***) and pore wall thickness (***t***) obtained using the method indicated (BJH, SAXS, TEM) for the samples indicated. All values are in nm. Values of ***a_o*** are calculated from the corresponding ***d_{SAXS}*** value. Miller indices are given in italics below each value of ***d***.

sample	w_{BJH}	$d_{SAXS}1$	$d_{SAXS}2$	$d_{SAXS}3$	$a_0 1$	$a_0 2$	$a_0 3$	d_{TEM}	w_{TEM}	t_{TEM}
S-AP	8.4	9.8 *(100)*	5.9 *(210)*	5.1 *(100)*[a]	11.3	11.7	11.8	9.5 *(100)*	7.5	2.2
S-900	6.2	7.8 *(100)*	4.1 *(210)*	3.1 *(100)*[a]	8.8	8.2	7.0	8.5 *(100)*	5.5	2.2
K-AP	8.6	8.9 *(211)*	5.4 *(400)*	4.7 *(332)*	21.8	21.5	22.0	8.3 *(211)*	7.0	2.8
K-900	5.9	7.2 *(211)*	4.4 *(400)*	3.8 *(332)*	17.7	17.7	18.1	7.3 *(211)*	5.5	4.5
F-AP	8.6	11.7	6.7	-	20.3	18.8	-	12.1	9.4	4.7

		(111)	*(220)*					*(111)*			
F- 900	-	10.6	6.5	-	18.4	18.3	-	-	-	-	
		(111)	*(220)*								

[a] second order diffraction

These shifts in pore peak position also became more marked with increasing ***T*** in what appears to be an approximately exponential (Arrhenius-type) relationship. This is consistent with the thermally-activated shrinkage of the pores in these two materials. The behavior of FDU-12 was very different, however. Figure 6-3 (c) indicates that no significant change in pore width occurred, although, as in the other two materials, the peak height did fall with increasing ***T***, in this case, in fact, to zero. These gas adsorption results strongly indicate that loss of porosity and surface area occurred in SBA-15 and KIT-6 by gradual shrinkage in pore size while in FDU-12 it occurred by rapid loss of individual pores.

Returning to Figure 6-2, it is interesting to review the trends in $\mathbf{V}_{micro}$. In general, $\mathbf{V}_{micro}$ increases in the order: KIT-6 < FDU-12 < SBA-15. This is consistent with the pore structures of these materials. SBA-15 is known to have microchannels between mesopores[96], FDU-12 has cylindrical micropore channels between spherical mesopores but KIT-6 appears to have fewer microchannels between its wormhole-like mesopores[96]. In all cases, $\mathbf{V}_{micro}$ decreases with increasing ***T*** in a similar way $\mathbf{V}_{meso}$. For FDU-12, both parameters fall to zero at 700-800°C. In SBA-15 and KIT-6, however, $\mathbf{V}_{micro}$ falls to zero while $\mathbf{V}_{meso}$ remains at relatively high values, even at ***T***=900°C.

6.3.2 *Small Angle X-Ray Scattering*

SAXS patterns were recorded for all three OMS materials after all treatments and are viewable from Figure 6-4 through Figure 6-7.

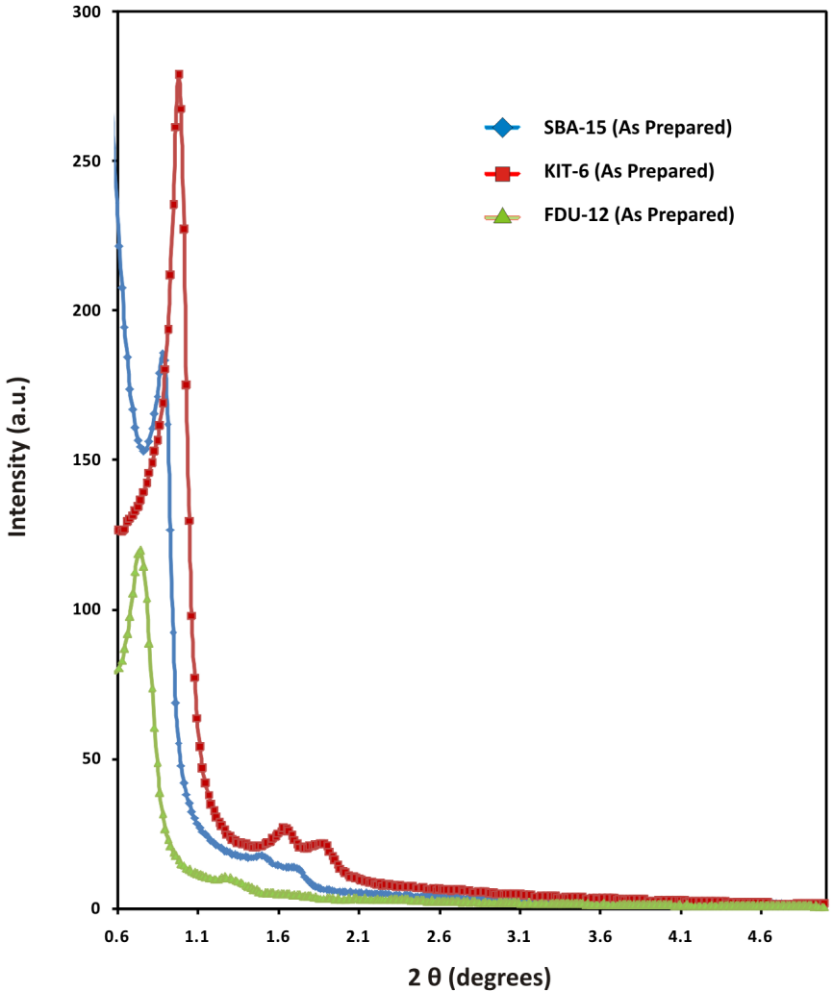

Figure 6-4: Small Angle XRD patterns for As-Prepared SBA-15, KIT-6 and FDU-12 Templates.

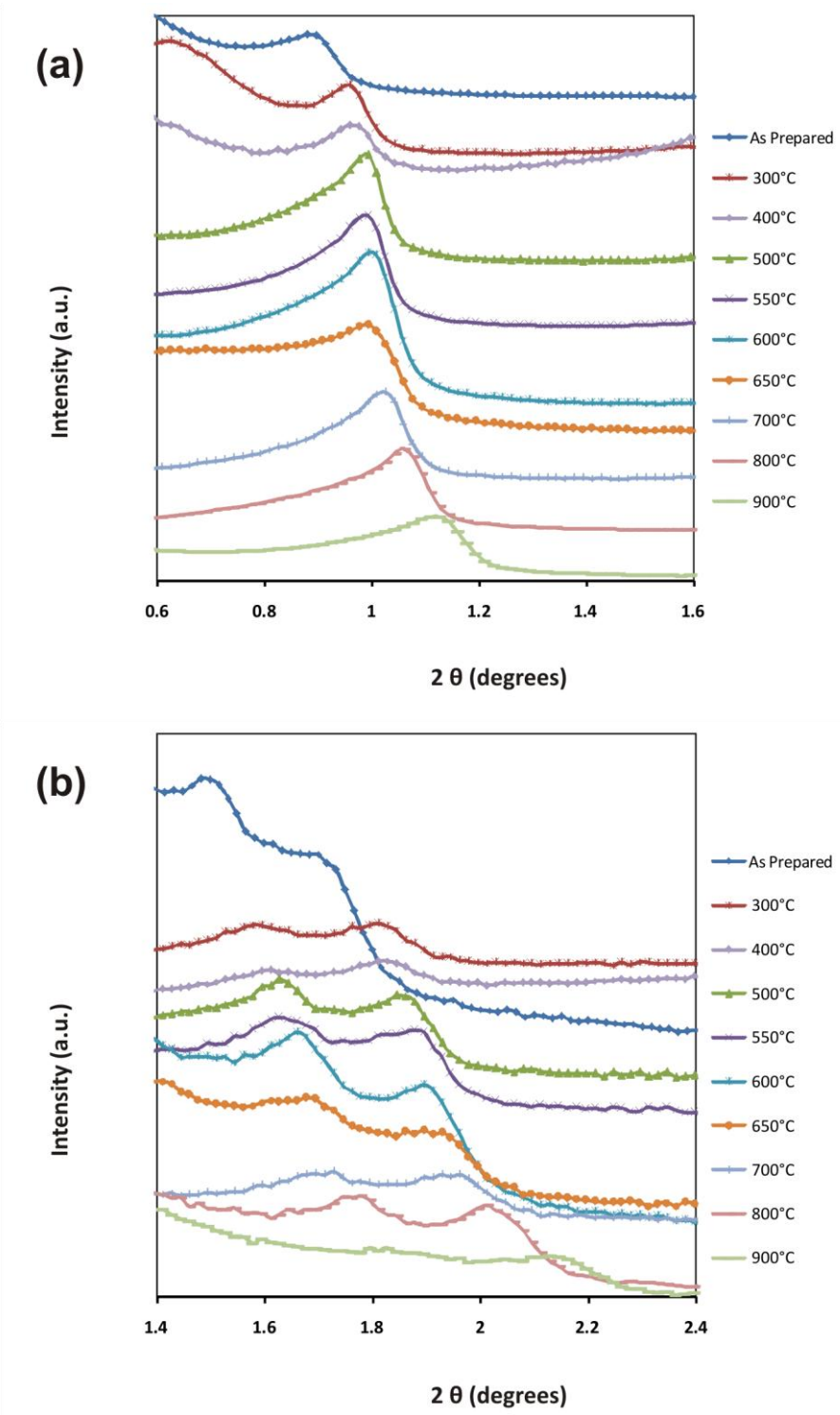

Figure 6-5: Small Angle XRD patterns for SBA-15 thermal treatments showing (a) The main peak (100) and (b) the second (111) and third (200) peaks (Intensity multiplied by a factor of 20), Plots are displaced along intensity axis for clarity.

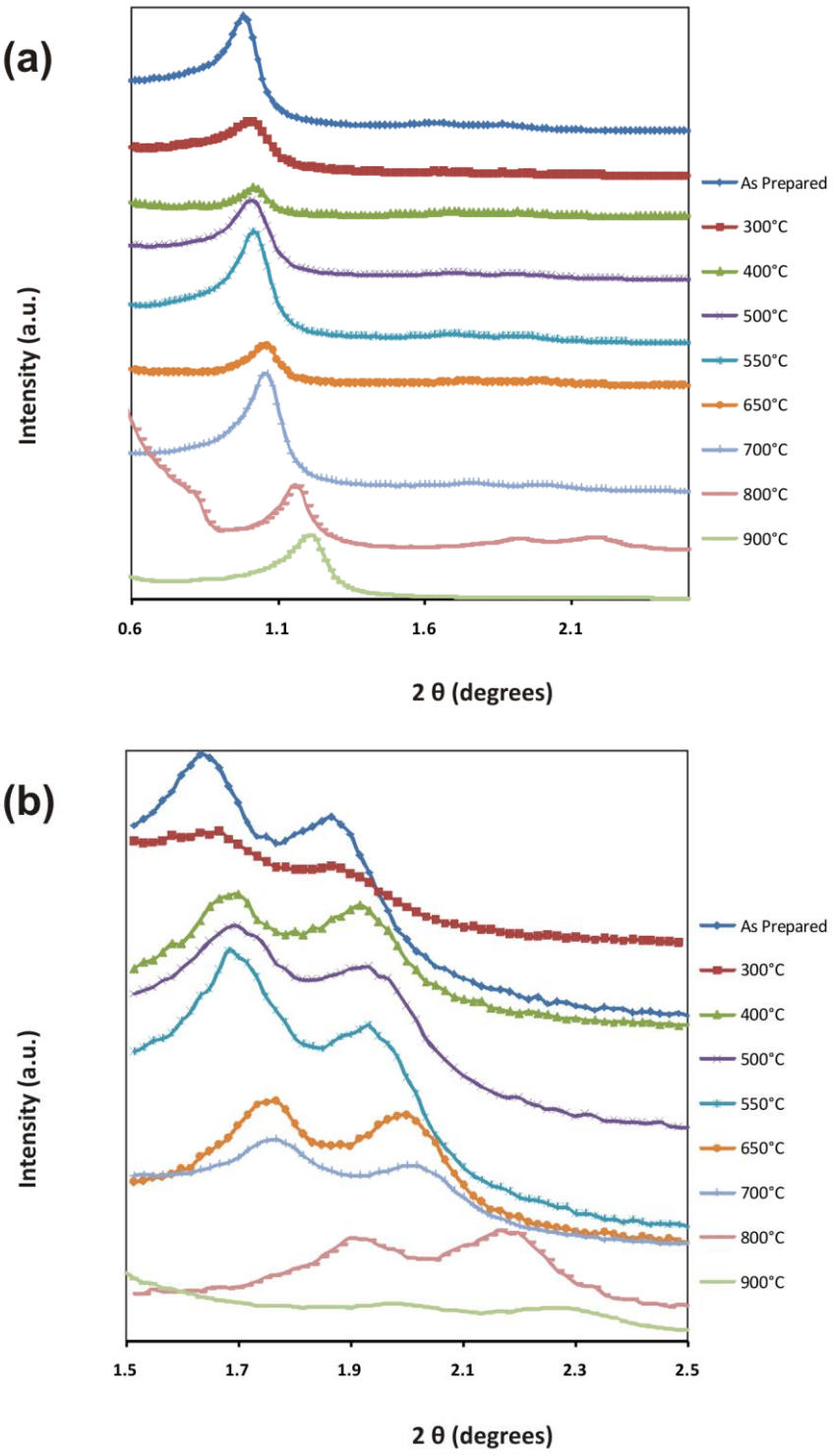

Figure 6-6: Small Angle XRD patterns for KIT-6 thermal treatments showing (a) The main peak (211) and (b) the second (400) and third (332) peaks (Intensity multiplied by a factor of 30), Plots are displaced along intensity axis for clarity.

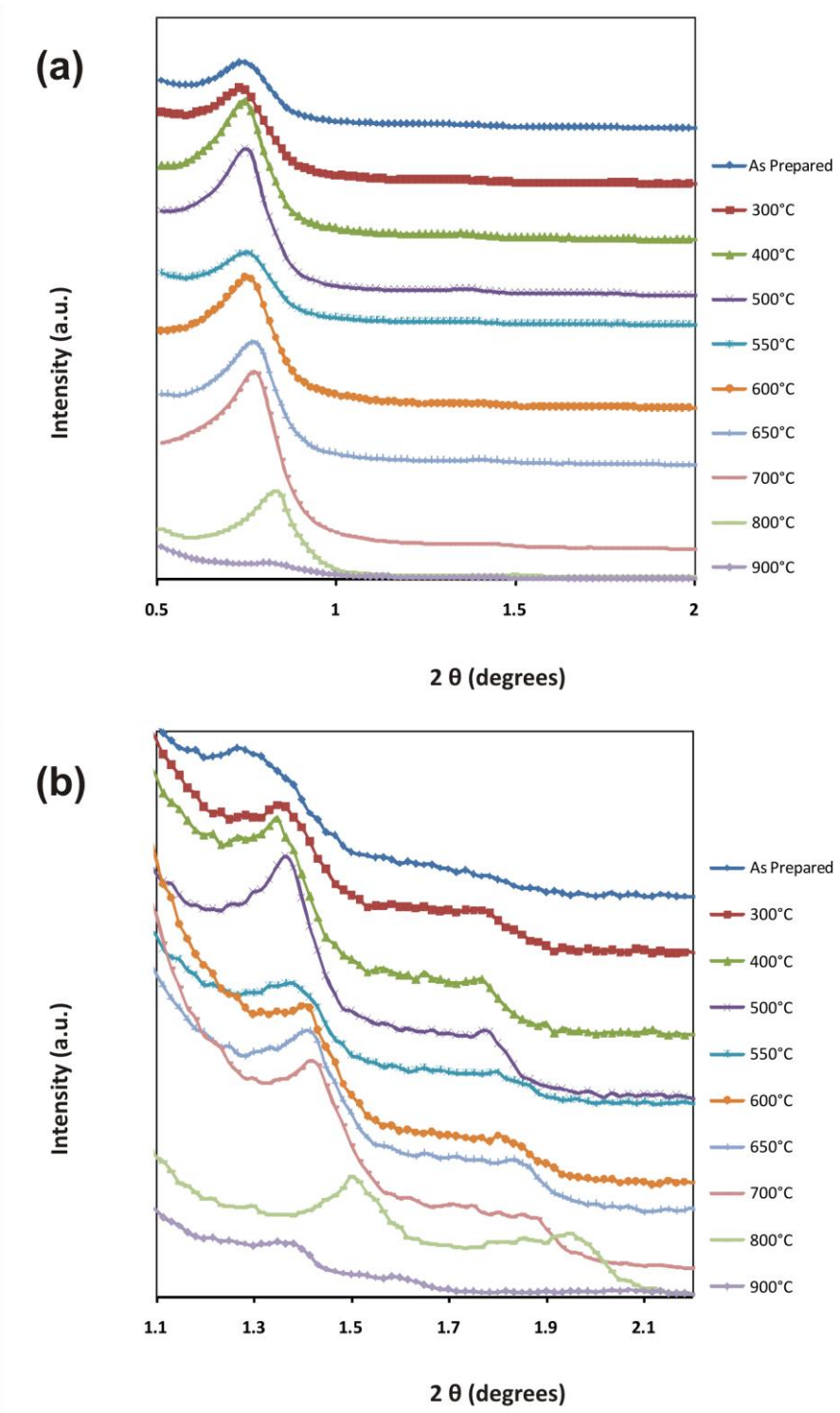

Figure 6-7: Small Angle XRD patterns for FDU-12 thermal treatments showing (a) The main peak (111) and (b) the second (220) peak(Intensity multiplied by a factor of 40), Plots are displaced along intensity axis for clarity.

The positions of peaks in these patterns were used to extract values of interplanar spacings, ***d***, to which Miller indices – relating to the ordered pore structures – were assigned. Interplanar spacings and unit cell dimensions derived from them are given in Table 6-1 for the AP and 900 samples. The evolution of these interplanar spacings with treatment conditions are presented in Figure 6-12 for each OMS type.

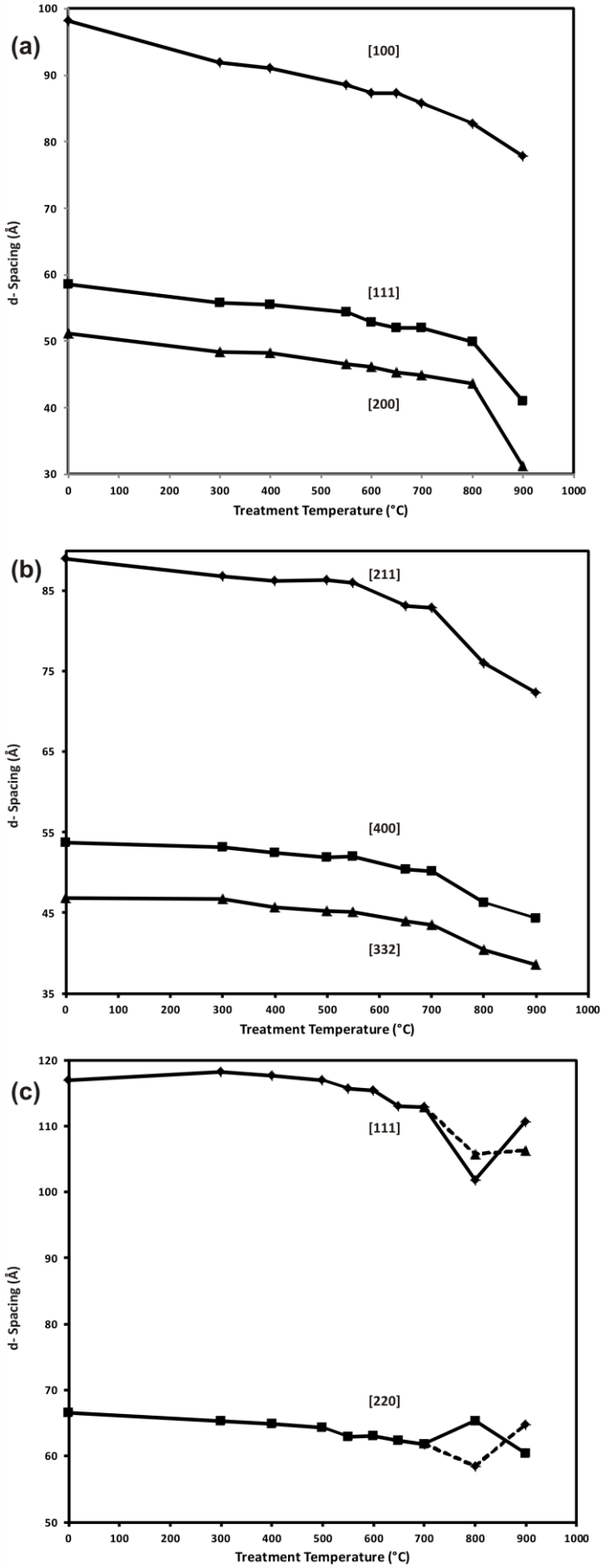

Figure 6-8: Derived ***d***-spacing data from SAXS analysis (a) SBA-15, (b) KIT-6, (c) FDU-12. The dashed line in (c) represents repeat data of samples F-800 and F-900.

Within each of the three plots, the trends in all ***d***-spacing values showed a high degree of similarity, indicating that the data were self-consistent. A general trend of decreasing ***d***-spacing with increasing treatment temperature was seen for all three OMS materials. This implies shrinkage of the unit cells with increasing ***T*** in each case. The shrinkage of the unit cells of SBA-15 and KIT-6 was more marked than for FDU-12. For example, the largest ***d***-spacing for FDU-12 (d_{111}) showed a relative decrease to ***T***=700 °C of 2-3 times more than the largest spacing for the SBA-15 (the d_{100}) and the KIT-6 (d_{211}). The gas adsorption results, presented in Figure 6-1, Figure 6-2 and Figure 6-3, indicated that FDU-12 showed complete loss of SSA and open pore structure after treatment at the highest temperatures. For this reason, the SAXS patterns for the samples F-800 and F-900 were obtained twice. The corresponding ***d***-spacings showed large variances which can be attributed to the small amounts of ordered material remaining in these samples which in turn gave rise to small SAXS peaks. The fact that ***d***-spacings were resolved at all in these two samples, however, is noteworthy given the hypothesis of pore structure collapse.

6.3.3 *Transmission Electron Microscopy*

Figure 6-9, Figure 6-10 and Figure 6-11 present the TEM analyses of the three OMS materials, each in both their as-prepared state and after treatment at 900 °C. Two methods were employed to obtain information on the pore structures. Firstly, Digital Diffraction Patterns (DDPs) were obtained by applying the Fourier transform to selected areas of the TEM images. The ***d***-spacings were then calculated from these. Secondly, line-scans giving the variation in contrast as a function of position were generated from selected images. These were used to extract pore and wall widths. These data are given in Table 6-1.

Figure 6-9 (a) and (b) show the long-range ordering in the as-prepared SBA-15 material viewed in the x- and y-directions (see Figure 1-3(a)), respectively. After heating at 900 °C some structured regions were still observed, as in Figure 6-9 (c) and (d) but essentially non-porous material such as that seen in Figure 6-9 (e) was now also seen. This distinct partitioning of ordered and non-ordered areas was evident throughout the TEM study of this sample. Interplanar spacings were obtained from the DDPs and values for the pore and wall thicknesses in these structures were measured from plots such as those given in parts (i) and (ii) of the figure. These are presented in Table 6-1 and show good agreement with the corresponding data obtained from SAXS. On going from the S-AP to the S-900 sample, both

the unit cell of the pore structure and the pores themselves appeared to have decreased in size while no change in wall thickness was observable in TEM.

The TEM images of KIT-6 in Figure 6-10 reveal very similar behavior to that of SBA-15 in that there was shrinkage of the unit cell and of the pores on thermal treatment and that regions with and without ordered pore structure were present in the thermally-treated sample, K-900. One difference seen in KIT-6 over SBA-15 is that there appeared to be a thickening of the pore walls between K-AP and K-900, as indicated in Table 6-1.

In FDU-12 (Figure 6-11), the thermal treatment had a markedly different effect. The ordered structure of spherical pores seen in F-AP in Figure 6-11 (a) was converted into material which still contained some of these pores but in which they were in a much less ordered arrangement, as seen in Figure 6-11 (c) for F-900. In this sample, no pores were detected by gas adsorption (Figure 6-2, Figure 6-3) yet the SAXS patterns did indicate some ordered structure, although the peaks were much attenuated compared to those for F-AP. These results can be explained by reference to the TEM images. In these, pores were still seen in F-900 and formed a loosely ordered arrangement.

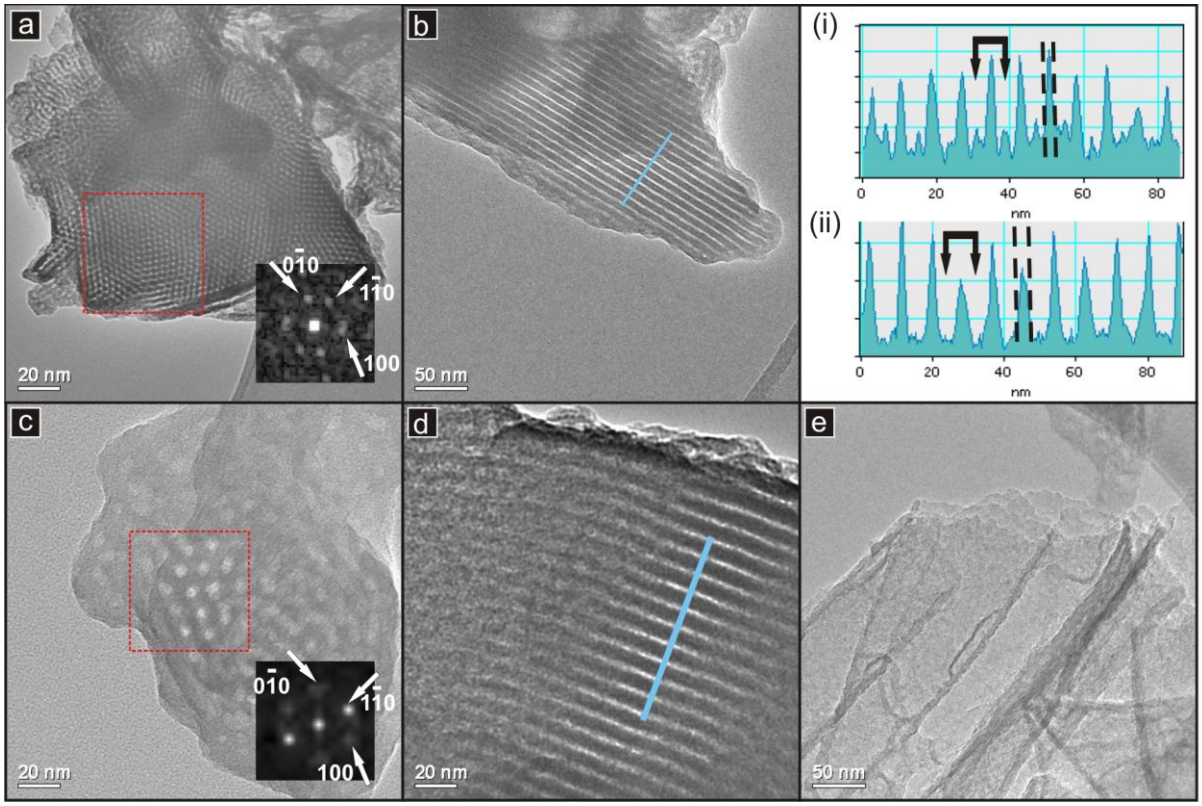

Figure 6-9: TEM images for SBA-15. (a) Image for S-AP with DDP inset and dashed boxed the area of FFT analysis. (b) Image for S-AP representing the linear structure of S-AP, the blue line is histogram (i) area of integration. (c) Image of S-900 with DDP inset and dashed boxed the area of FFT analysis. (d) Image for S-900 representing the linear structure of S-900, the blue line is histogram (ii) area of integration. (e) Image for S-900 highlighting the proximity of the regions of amorphous silica and structured silica.

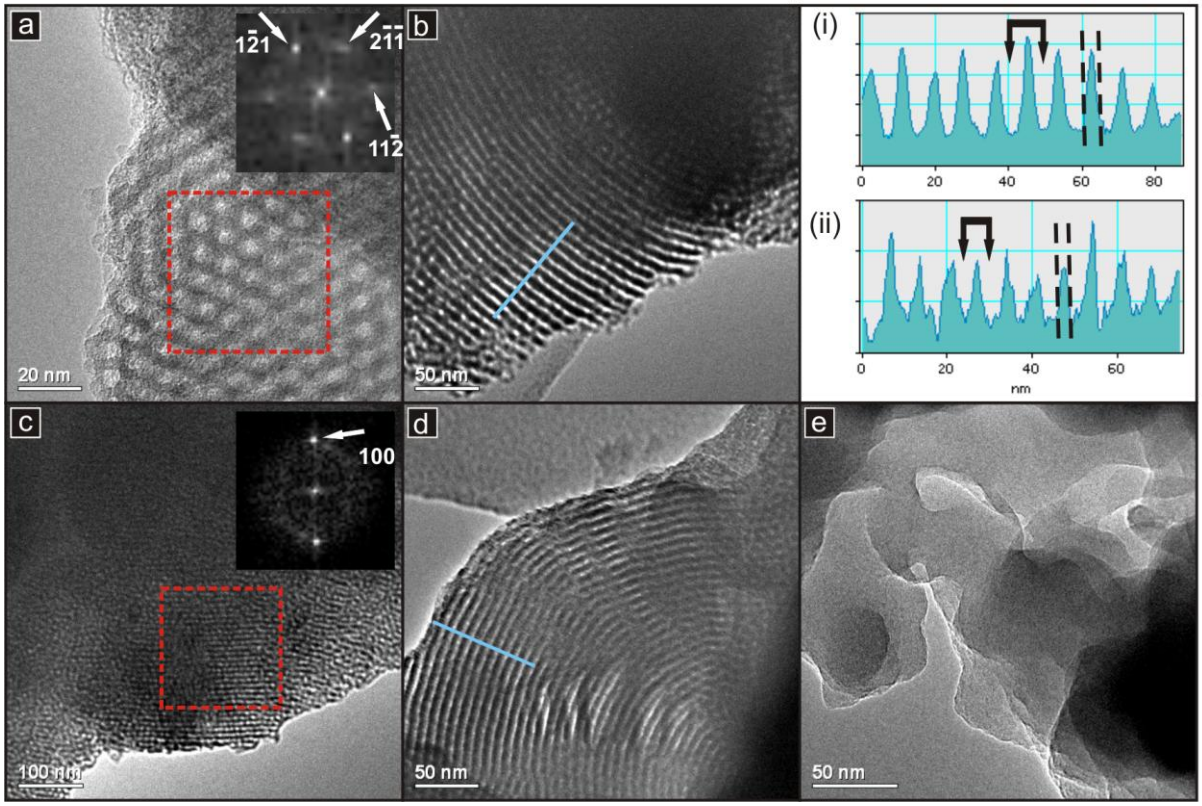

Figure 6-10: TEM images for KIT-6. (a) Image for K-AP with DDP inset and dashed boxed the area of FFT analysis. (b) Image for K-AP representing the linear structure of K-AP, the blue line is histogram (i) area of integration. (c) Image of K-900 with DDP inset and dashed boxed the area of FFT analysis. (d) Image for K-900 representing the linear structure of K-900, the blue line is histogram (ii) area of integration. (e) Image for K-900 highlighting the amorphous silica prevalent within the sample.

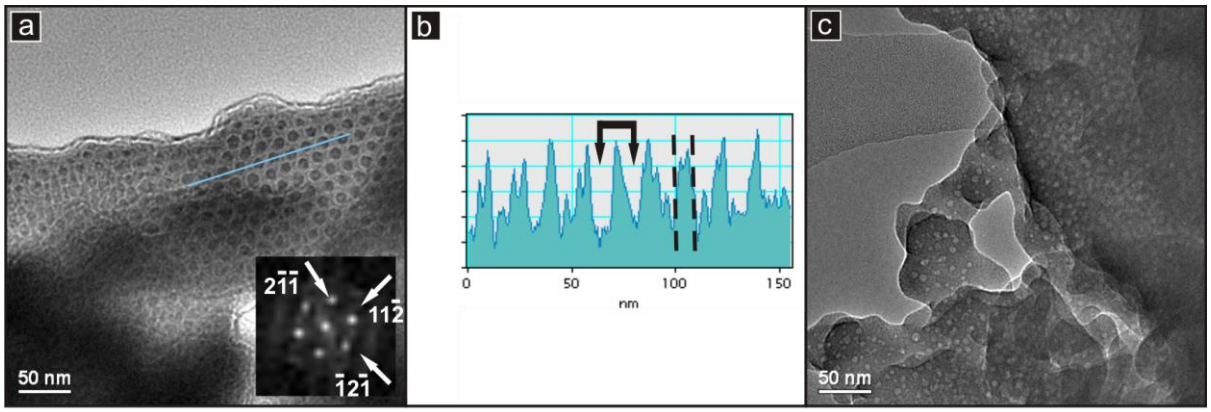

Figure 6-11: TEM images for FDU-12. (a) Image for F-AP with DDP inset, the blue line is histogram (b) area of integration. (c) Image of F-900 highlighting the amorphous silica surrounding an entombed residual porous structure.

However, it appears that the pores had become completely encapsulated within the silica material meaning that gas could not adsorb inside them in the gas adsorption experiments. This indicates that the narrow cylindrical channels forming connections between the

spherical pores in the F-AP material must have failed, filling with silica material and leaving behind encapsulated spherical pores in arrangements ordered enough to be detectable by SAXS but which did not contribute to the measured surface area or pore volume of the sample because they were no longer accessible. This is in agreement with the findings of Kruk and Hui for the encapsulation of the spherical pores in large pore FDU-12 and SBA-16 on heating [24].

6.3.4 *Solid State ^{29}Si NMR*

^{29}Si-MAS-NMR spectra were recorded for each of the three OMS materials after four treatments: AP, 400, 650 and 900. The spectra are presented in Figure 6-12. All spectra showed a major peak at a chemical shift, δ, of around -110 ppm with small shoulders at higher δ. The spectra were deconvoluted into up to three Gaussian peaks.[97] These were assigned as Q2, Q3 and Q4 in order of decreasing δ, according to the convention for identifying the distinct Si environments in silicas and related materials.[98] All peak positions are summarised in Table 6-2. The Q2 resonance at δ ~ -92 ppm corresponds to Si atoms bonded to two siloxane groups and two silanol groups, the Q3 resonance at δ ~ -101 ppm is attributed to Si atoms with three siloxane bonds and one silanol group and Q4 at δ ~-110 ppm is ascribed to Si atoms with four siloxane bonds. This is shown schematically in Figure 6-13. The main peak in all spectra corresponded to the Q4 environment. The relative intensities of the Q2-Q4 resonances as a function of treatment temperature for the three OMS materials are plotted in Figure 6-14. For all three OMS structures, the general trend is for progressive deceases in Q2 and Q3 and a corresponding increase in Q4, starting from around 400°C. It is therefore evident that thermal treatment caused progressive condensation of the Si-OH groups. Since these are expected to be present predominantly at the surfaces of the materials where the silica structure is terminated, this behavior is consistent with the loss of pore structure seen using other techniques above. The biggest change was recorded for SBA-15, suggesting that this is less thermally stable than the KIT-6. The traces for SBA-15 and KIT-6 showed a change towards increasing percentage of Q4 which continued up to the pretreatment temperature of 900°C whereas the trace for the FDU-12 appeared to reach a plateau at the higher temperatures.

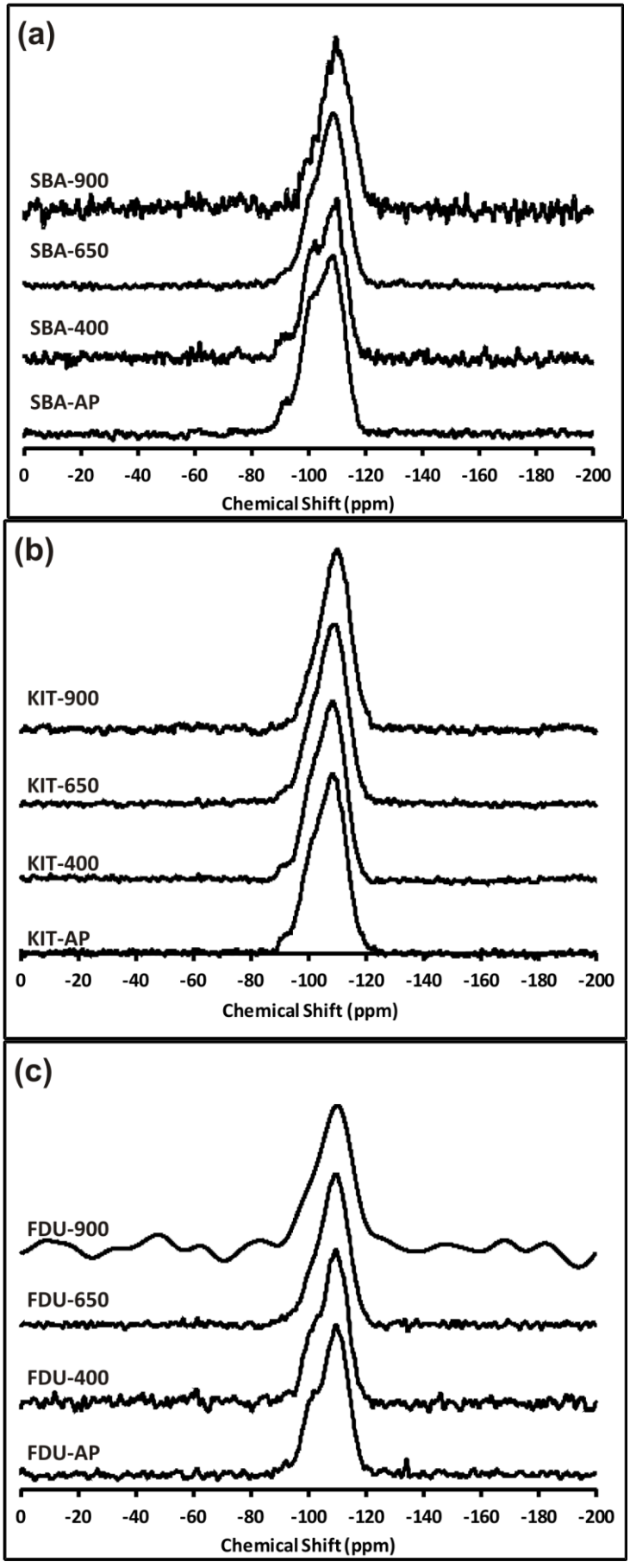

Figure 6-12: The resonance intensity of 29Si-MAS-NMR as a function of chemical shift for (a) SBA-15, (b) KIT-6 and (c) FDU-12 before deconvolution. The values have been offset from the baseline vertically for the purposes of clarity.

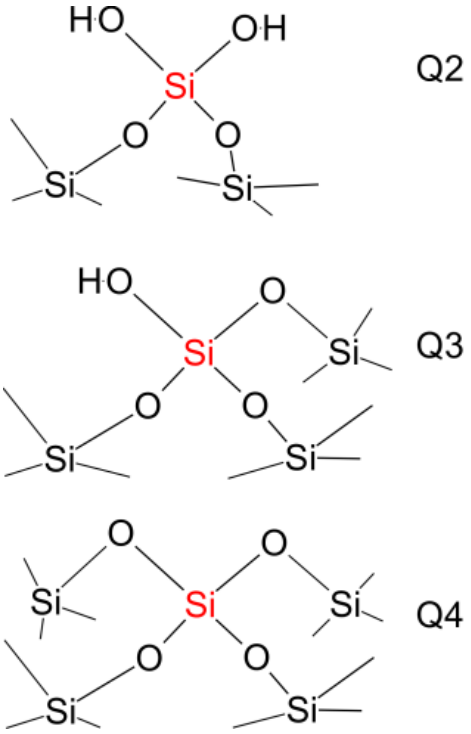

Figure 6-13: Pictorial representation of the silanol and siloxane bonding configurations of a central Si atom which are representative of the Q2, Q3 and Q4 NMR resonance spectra.

6.4 Discussion

Values of the key dimensions relating to the pore structures of the three OMS materials both as-prepared and after thermal treatment at 900 °C are collected together in Table 6-1.

Table 6-2: Chemical shifts, ***δ*** (ppm), from the ^{29}Si MAS-NMR spectra of SBA-15, KIT-6 and FDU-12 recorded after the pretreatments indicated. The positions of the main peak in the raw spectra (data) and of the three peaks obtained by deconvolution (Q2-Q4) are given.

	SBA-15				KIT-6				FDU-12		
	AP	*400*	*650*	*900*	*AP*	*400*	*650*	*900*	*AP*	*400*	*650*
data	-108.8	-110.1	-108.7	-109.8	-108.7	-108.6	-109.4	-110.1	-109.8	-109.8	-109.7
Q2	-91.7	-91.8	-94.3	-	-91.8	-91.4	-91.4	-90.9	-92.1	-92.8	-93.2
Q3	-100.6	-100.7	-100.3	-99.4	-100.2	-100.6	-100.3	-101.4	-100.9	-101.1	-100.9
Q4	-108.9	-109.3	-108.8	-110.0	-108.9	-109.1	-109.2	-110.2	-110.1	-109.9	-109.8

Data obtained from the gas adsorption, SAXS and TEM measurements are compared and show good general agreement. This is despite the difficulties in measuring pore diameter by TEM and of locating the smallest peaks precisely in SAXS patterns, especially those relating to samples treated at high temperature. These data – when taken with the trends in the ***d***-spacing shown in Figure 6-4 through Figure 6-8 – indicate a contraction of the unit cells in all three materials. This was more significant in SBA-15 and KIT-6 than in FDU-12. The gas

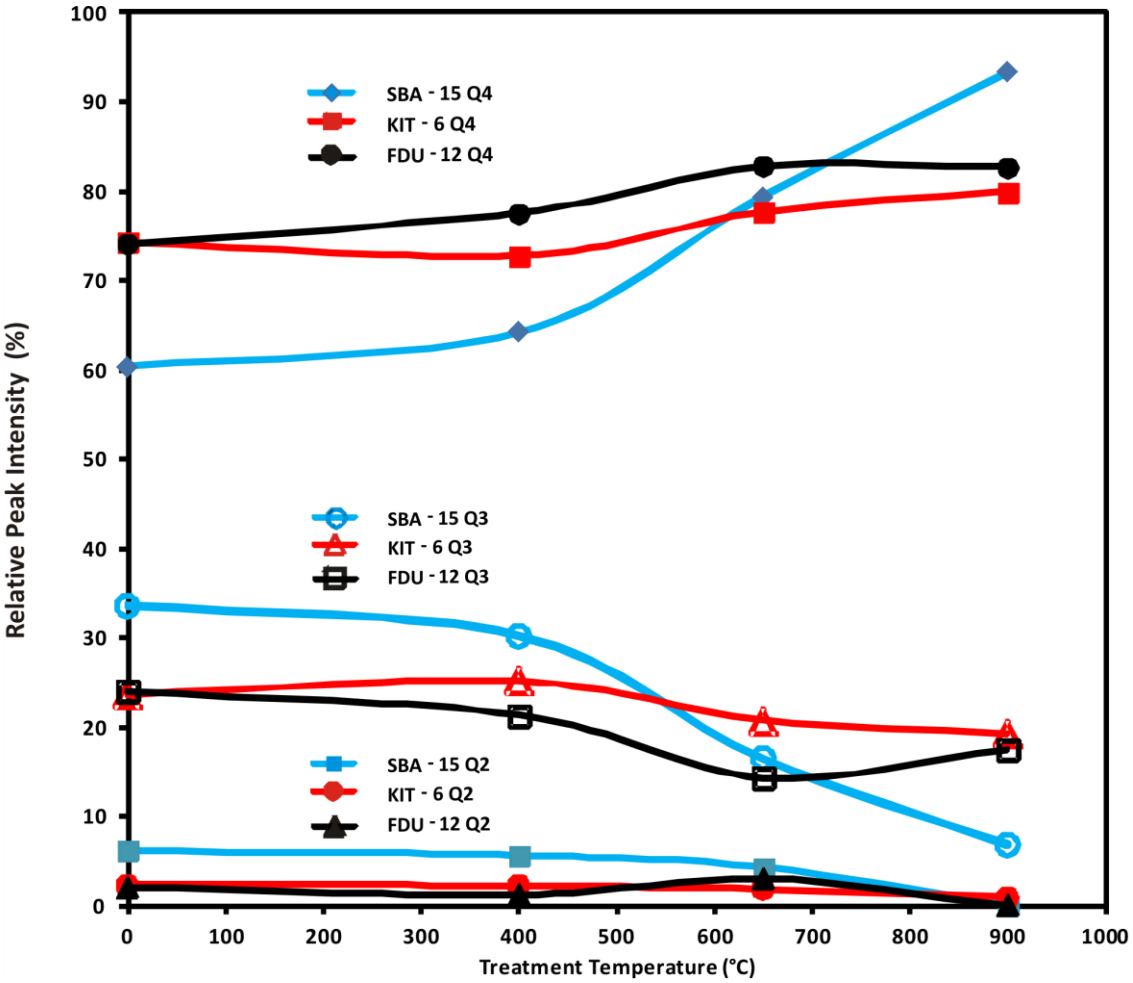

Figure 6-14: The peak intensity percentage of Q2, Q3 and Q4 resonances as a function of each treatment temperature for SBA-15, KIT-6 and FDU-12.

adsorption results in Figure 6-2 and Figure 6-3 and the pore widths measured by TEM together attest to a gradual decrease in pore size and a considerable loss of SSA with increasing treatment temperature for the SBA-15 and KIT-6 materials. Nevertheless, these two materials retained significant SSA and $\mathbf{V}_{meso}$ values even after treatment at 900 °C. This was not the case for FDU-12 which appeared to suffer a complete loss of SSA and $\mathbf{V}_{meso}$ in Figure 6-2(c) while pore size (Figure 6-3) did not change with treatment temperature. However, the trends in ***d***-spacing for this material (Figure 6-8) show a smaller contraction than for the other two materials and the TEM images of F-900 (Figure 6-11) show that this

sample retained many pores. This apparent contradiction can be explained if these pores had become isolated from the external gas atmosphere and therefore inaccessible in the gas adsorption experiments. This is confirmed by study of the TEM images of F-900 in which the narrow channels connecting the larger spherical pores seem to have been filled and by the coincident complete loss of both $\mathbf{V}_{meso}$ and $\mathbf{V}_{micro}$ (Figure 6-2(c)). Despite being isolated, these pores still retained some structural order which was detected by SAXS. It appears that a different process occurred in SBA-15 and KIT-6 – which do not contain large, spherical pores – whereby their cylindrical pores were gradually filled. After treatment at 900 °C, loss of pore volume was broadly similar for these two materials, although SBA-15 lost more SSA than KIT-6. The NMR results also clearly indicate more significant condensation of Si-OH groups – associated with loss of surface area – for the SBA-15. On balance, this suggests that the SBA-15 is the less thermally stable structure of the two and this is consistent with its one-dimensional pore structure which might be expected to be more vulnerable to contraction than the cubic, bicontinuous intertwined channel structure of KIT-6. Another, subtle, difference is that the pore walls in SBA-15 appeared to remain the same thickness as treatment temperature increased whereas those of KIT-6 showed evidence of an increase in thickness in TEM (Table 6-1). However, there is no necessity for the walls in SBA-15 to become thicker when the pore diameters and the dimensions obtained from SAXS decrease. Because of the two-dimensional pore structure of SBA-15, contraction parallel to the pores is not detected in SAXS. The data indicate, therefore, that contraction may not in fact occur along the pores but only parallel to them. Further work would be needed to confirm this.

6.5 Summary

By performing a systematic study on three widely-used and representative OMS materials – SBA-15, KIT-6 and FDU-12 – using complementary analysis techniques the effect on their pore structures of thermal treatment was examined in detail.

Broadly speaking, SBA-15 and KIT-6 maintain their original pore structures to treatment temperatures of 600°C while FDU-12 maintains its pore structure to 500°C.

SBA-15 and KIT-6 exhibited similarities in the contraction of their pore structures and reduction in SSA. They differed however in the mode of structural collapse indicating that stability was likely influenced by the nature of the pore structure, i.e. 2-D as opposed to 3-D. FDU-12 exhibited a somewhat different behavior in which the narrow channels between its larger spherical pores filled first, isolating the pores from the external gas atmosphere.

^{29}Si MAS NMR data clearly showed a shift to higher Q values (Q2 and Q3 to Q4) in all three structures, implying the progressive loss of Si-OH groups through condensation with increasing treatment temperature. Since these and related materials are increasingly widely considered and applied for processes involving exposure to high temperatures – such as catalysis, gas storage and nanocasting – it is hoped that these findings will help facilitate informed choices of structure type and of preparation and operating conditions for such applications.

Chapter 7

Preparation of SDC from Silica Templates

7.1 Introduction.

Since the realisation that materials could be self-assembled into structures with ordered pore frameworks there has been several approaches to utilise their unique properties. Ordered mesoporous silica's (OMSs) is one such classification of these materials which can be used in a nanocasting procedure. The nanocasting procedure is a particularly useful application of silica templates given their structural stability particularly in air atmosphere over a range of high temperatures as described in Chapter 6. As the desired material is a samara doped ceria (SDC) of ratio $Sm_{0.2}Ce_{0.8}O_{1.9}$, this product was synthesised and analysed having used SBA-15, KIT-6 and FDU-12 as starting templates. $Sm_{0.2}Ce_{0.8}O_{1.9}$ as an end product was of particular interest given its high ionic conductivity[99] and interesting catalytic properties[100]. A nomenclature of FP or IT in conjunction with the template name is used to refer to materials as the oxide final product with template removed (FP) or intermediate oxide material that still has the initial template present (IT). Beyond the preparation and physical characterisation of the SDC material, a comprehensive study into the removal of the silica template using a variety of wet chemical methods was also conducted. Critical to the success of preparing SDC materials with unique structures are the procedures of precursor impregnation, nitrate conversion and template removal. Each of these stages has been investigated in-depth in an attempt to achieve a product of high quality, reproducibility and purity.

7.2 Impregnation of Silica Templates

Impregnation of templates with liquid nitrate precursors was performed using two techniques. The first technique, incipient wetness impregnation technique (IWIT), exploits capillary action of the liquid precursor through the mesoporous channels in the silica template. The intimate mixing of liquid and powder template allows controlled impregnation to be realised. This is achieved by grinding the template material with dropwise additions of the precursor using a mortar and pestle. The technique has the

benefit of allowing fine control on the saturation level of the template. The second method known as vacuum impregnation (VI), exploits atmospheric pressure in forcing the liquid to penetrate the previously evacuated porous channels of the template. The IWIT method was restricted to mixing liquid precursor with template in a powder format. The VI method however allows for powder and pellet materials to be impregnated.

The stages of vacuum impregnation of a pellet (or several pellets in some experiments) could be viewed visually in Figure 7-1. Having followed the procedure detailed in Chapter 4.5.1, starting pellet templates of 13 mm diameter were produced. These starting pellets shown in Figure 7-1 (a) were initially subjected to a vacuum according to the VI technique before being exposed to a controlled amount of liquid nitrate precursor. Figure 7-1 (c) shows a pellet directly after impregnation with the effect of liquid penetration observed as a visual change from opaque to translucent. Towards the end of the VI procedure with the pellet having reached a partially but stabilised impregnation, there was a visual indication of rapid liquid movement within the pellet when the system was returned back to atmosphere. This was achieved by prompt opening of the atmospheric tap. If a pellet was simply left in precursor solution without vacuum pre-treatment then no observable impregnation takes place. The liquid ingress is evidenced visually by a change in translucence, Figure 7-1 (c). This makes it a good indicator that the vacuum process is having a positive impregnation effect. When removed from the apparatus, there would be a reversal back to an opaque pellet over a period of about an hour. Figure 7-1 (b) shows the pellet where the solvent has evaporated and the nitrates have started crystallising. Handling experience of the pellets indicated that they would maintain sufficient strength and integrity through the various preparation stages. To ensure a stabilised pellet, a resting period of several hours, as determined through the monitoring of weight change was necessary. This would allow for complete crystallisation of the nitrate mixture and associated ethanol evaporation under STP conditions. An extended time period of 24 h was used as a matter of routine.

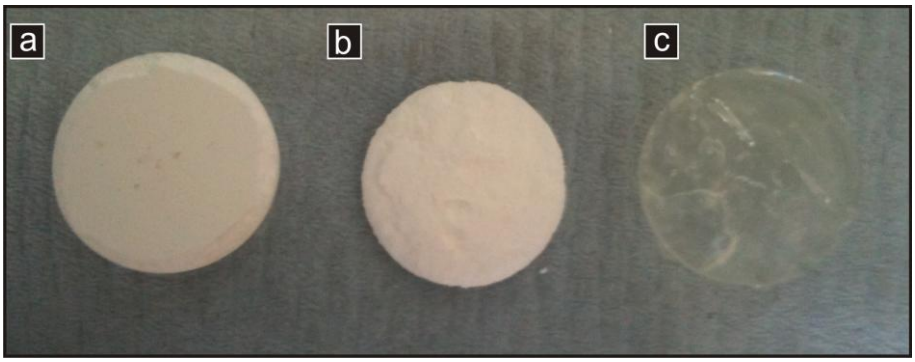

Figure 7-1: Silica template pellet in various stages of impregnation: (a) pellet with no impregnation, (b) pellet 1 hour after impregnation, (c) freshly impregnated.

7.3 Results

Recent work [79] has shown that nanocasting ceria and gadolinium doped ceria using a VI technique into a variety of silica template powders achieves a final product of reverse image crystalline structure. As an extension of this method, samarium-doped ceria material has been produced using pellets in a modified VI technique and is presented. A summary of gas physisorption PSD results for all SDC products are also presented in Appendix 1 to allow useful cross comparison between results and are presented in conjunction with associated templates.

7.3.1 *SDC Prepared From SBA-15*

The data presented is separated according to two differing experiments. Experiment 1 represents IT and FP materials produced using SBA-15 but having been calcined 1 h after VI impregnation. The second set of data differs by allowing the pellet to dry for an extended period of time as indicated by a stabilised weight of pellet. This material has been referenced as IT(2) and FP(2). The generated isotherms were interpreted for specific surface area ($\mathbf{S}_{BET}$), pore size distribution (w_{BJH}), mesopore volume ($\mathbf{V}_{meso}$) and micropore volume ($\mathbf{V}_{micro}$). Figure 7-2 (a) and (b) show a typical isotherm and associated specific pore size distribution (PSD) for IT(1) and FP(1) materials. The isotherm for IT(1) is typical of a type IV profile with an associated type H3 hysteresis. The FP(1) product has an isotherm of type IV profile with a hysteresis best defined as H2. The IT(1) has two distinct peaks observed at 7.6 and 17 nm whereas the FP(1) has a single broad peak centred at 16 nm as observed from the desorption branch. Specific mesopore volumes ($\mathbf{V}_{meso}$) of 0.28 cm^3g^{-1} and 0.42 cm^3g^{-1} , micropore volumes ($\mathbf{V}_{micro}$) of 0.02 cm^3g and nil cm^3g^{-1} , average specific surface area ($\mathbf{S}_{BET}$) of 182 m^2g^{-1} and 115 m^2g^{-1} were recorded for IT(1) and FP(1) respectively. Figure 7-2 (c) and (d)

show a typical isotherm and associated specific pore size distribution (PSD) for IT(2) and FP(2) materials. The isotherms for IT(2) and FP(2) are typical of type IV profiles with associated type H3 hysteresis The IT(2) has one distinct peak observed at 6.9 nm whereas the FP(2) has a two broad peaks centred at 4 nm and 8-9 nm as observed from the desorption branch. Specific mesopore volumes ($\mathbf{V}_{meso}$) of 0.26 cm^3g^{-1} and 0.20 cm^3g^{-1} , micropore volumes ($\mathbf{V}_{micro}$) of 0.03 cm^3g and nil cm^3g^{-1} , average specific surface area ($\mathbf{S}_{BET}$) of 254 m^2g^{-1} and 140 m^2g^{-1} were recorded for IT(1) and FP(1) respectively.

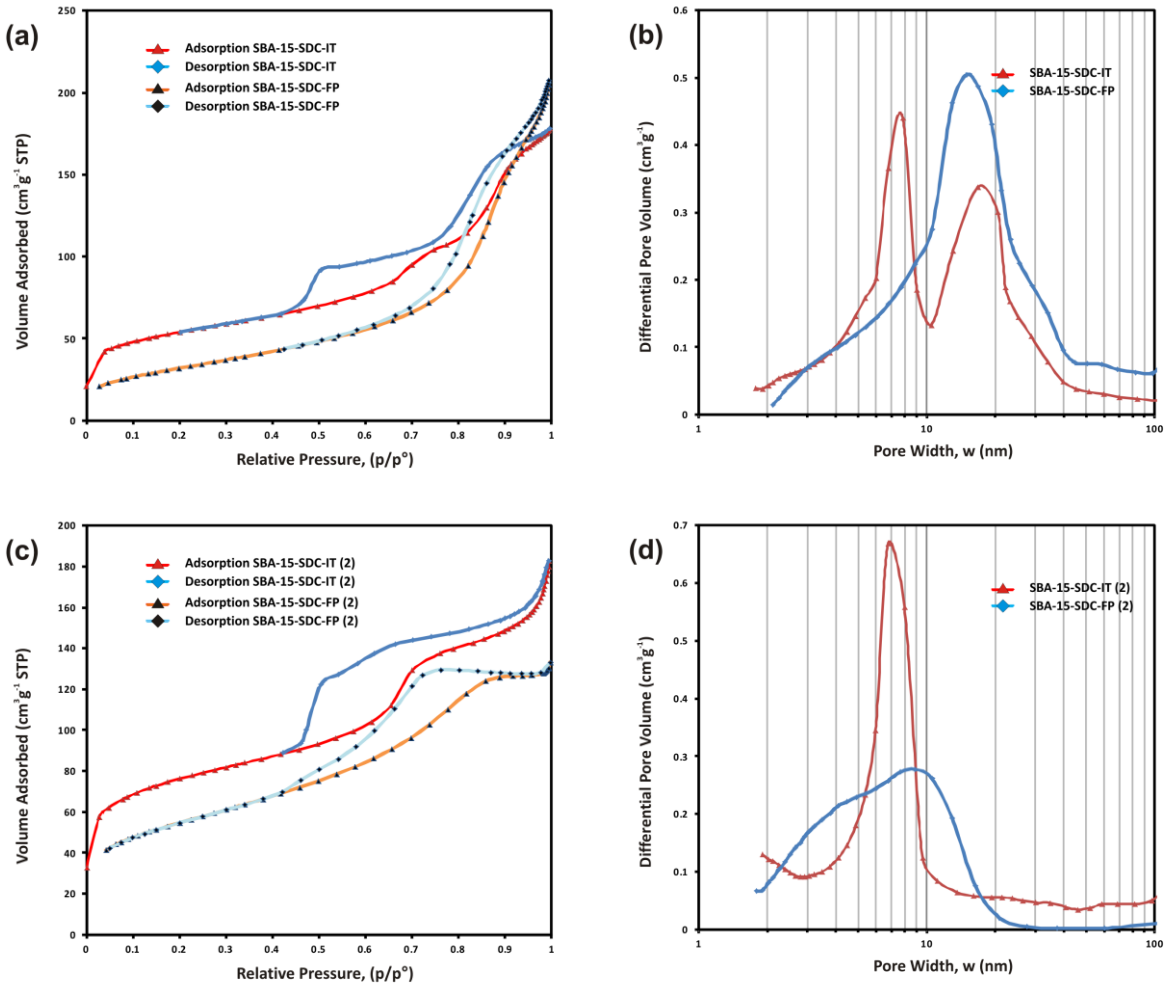

Figure 7-2: SBA-15-SDC-IT and SBA-15-SDC-FP material (first experiment): nitrogen physisorption isotherms (a) and specific pore size distributions (b) ; SBA-15-SDC-IT(2) and SBA-15-SDC-FP(2) material (repeat experiment): nitrogen physisorption isotherms (c) and specific pore size distributions (d).

Figure 7-3 presents patterns of low angle XRD data with a background subtraction included to help better resolve the diffraction peaks. Analysis of the SBA-15-SDC-FP(2) pattern shows a material with one distinct peak at 11.1 nm. The unit cell parameter of 12.8 nm was calculated using the formula in Appendix 2, Eqn. 20.

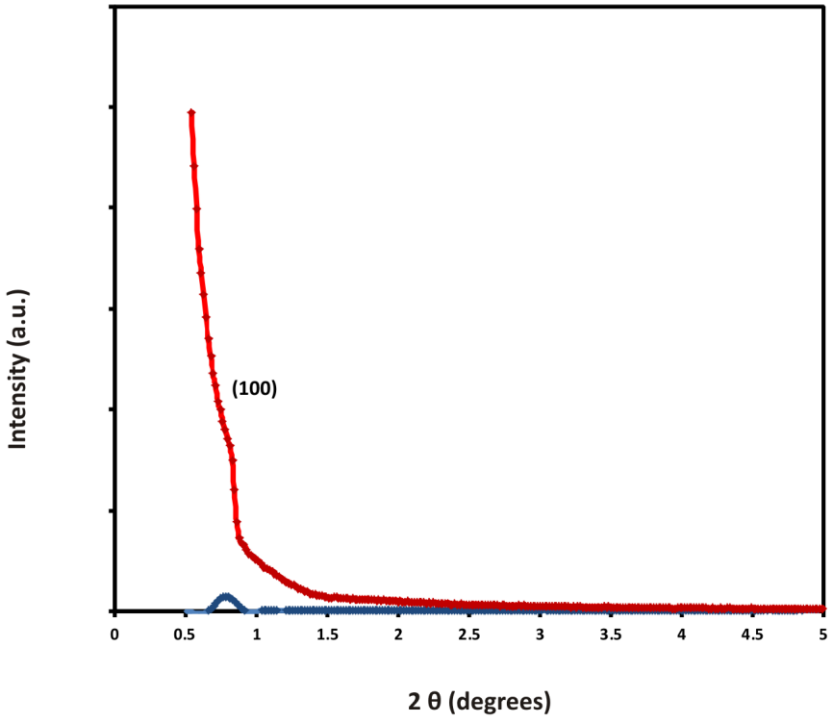

Figure 7-3: Low angle XRD patterns for SBA-15-SDC-FP.

Table 7-1: Calculated *d*-spacing from 2θ values for SBA-15-SDC-FP.

2θ (°)	**Indices**	***d*-Spacing (nm)**
0.794	100	11.12

In order to verify the expected inverse structure of SBA-15, TEM analysis was performed and is presented in Figure 7-4. The inverse replication would be expected to be composed of bundled rod like structures formed from within the original SBA-15 pore space. The removal of the silica template which was present as channel walls will be the basis of the new structures porosity. In other words; the template pore-channel sequence will become a channel-pore sequence in the nanocast structure. Figure 7-4 (a) and (b) visually indicate individual SDC channels formed over a long range order and separated by porous channels that extend along the length of the rod. Figure 7-4 (d) shows a high magnification of an isolated rod with the lattice planes in evidence indicating the crystallinity of the entire rod. The crystal planes run across the entirety of the rod in a parallel fashion as visualised by the red markings. This indicates that the rod has formed as a single crystal. The measured pore width $\boldsymbol{w_{TEM}}$ was found to be in the 3 to 4 nm range and wall (rod) thickness $\boldsymbol{d_{TEM}}$ found to be 8 nm. This is in good agreement with the reported PSD for the material and concurs with the inverse values of PSD for the template. Figure 7-4 (e) and (f) show the material viewed in

the [001] direction with a clearly visible hexagonal pattern that is the inverse of the template. The included DDP shows the repeat ordered nature of the material.

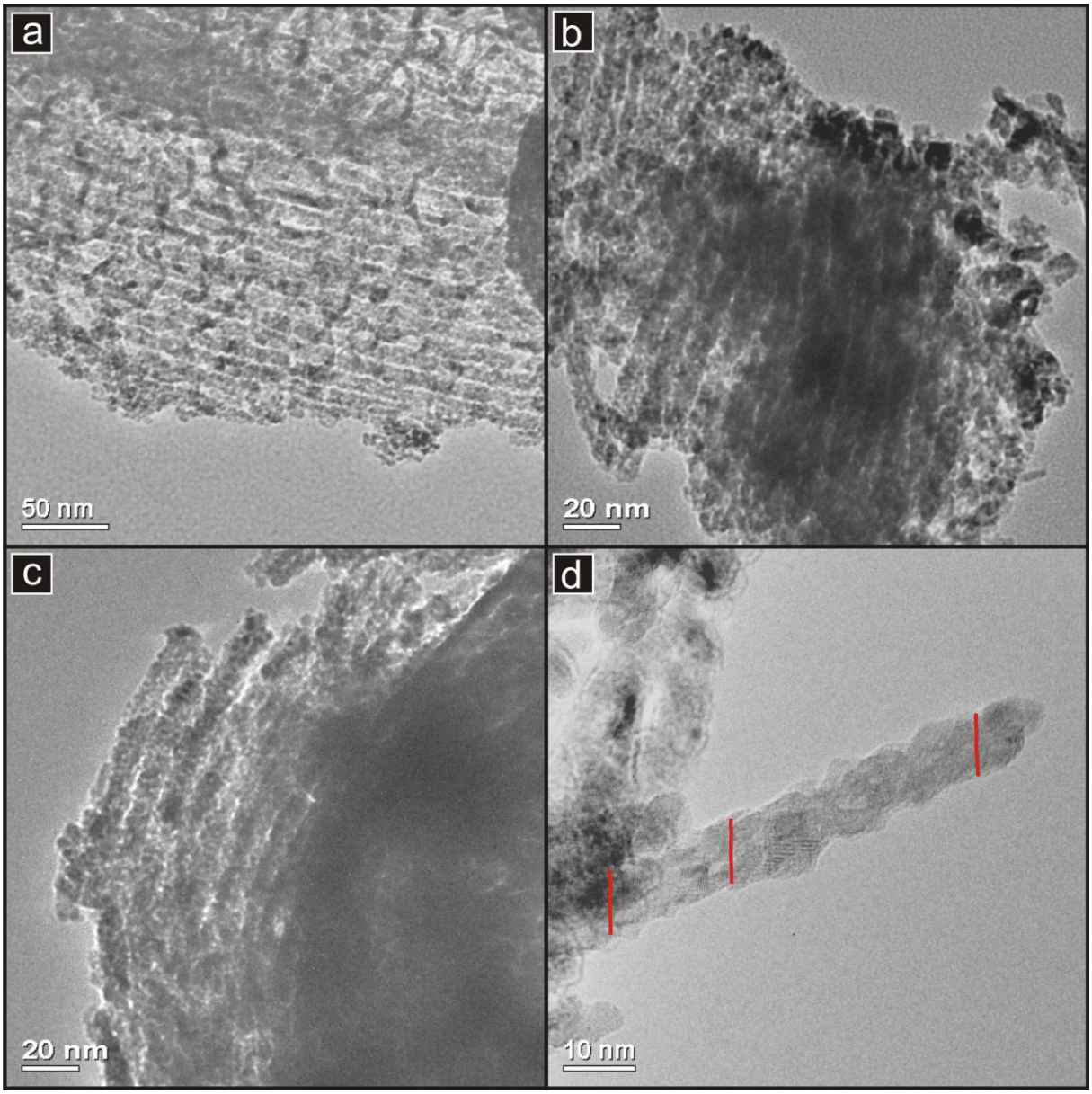

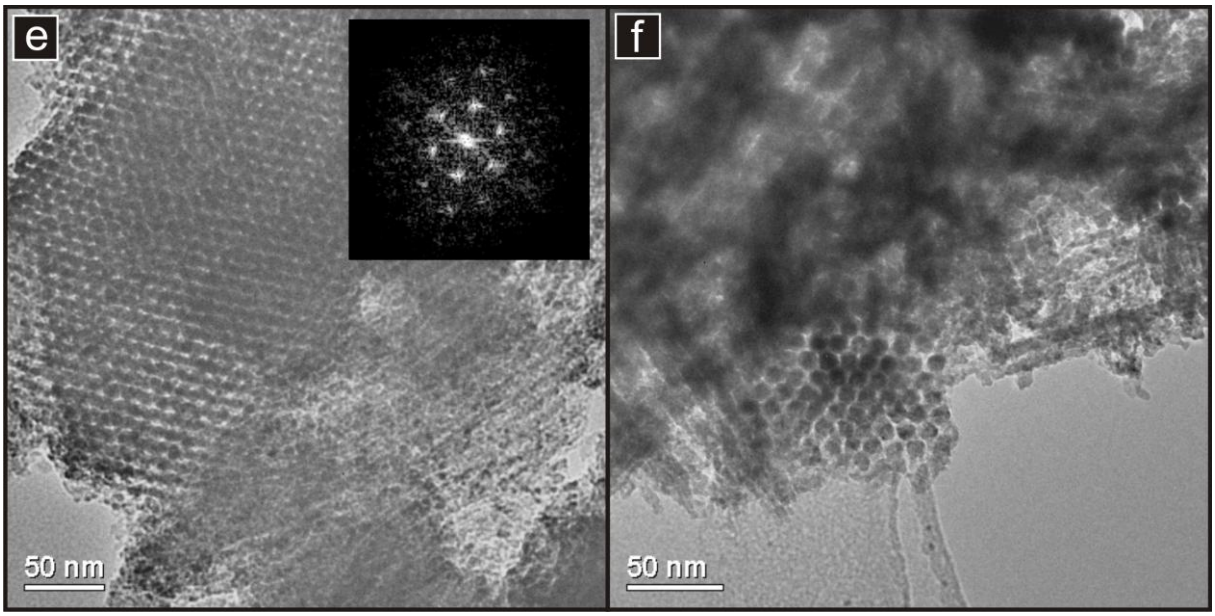

Figure 7-4: TEM images of SBA-15-SDC-FP: (a) and (b) particles with long range wall and pore channel order, (c) pore channels disconnected, (d) a single rod indicating a homogenous crystal growth through its entirety as indicated by the red lines, (e) a [001] large area view of the hexagonal arrangement of the rod structure with DDP inset, (f) a well resolved [001] view of the hexagonal arrangement.

In order to verify the absence of template from the SDC final product, the intermediate as well as final SDC products were analysed using gas physisorption. This would provide data on the porosity change from template, filled template through to SDC final product. It is expected that filled template (intermediate) would ideally indicate a gas physisorption of low specific surface area (SSA), low porosity volume and significant reduction in the 8.4 nm mesopore size distribution (PSD) peak associated with SBA-15 template.

Review of the results suggests that the template is being partially filled in both experiments as the mesopore volume ($\mathbf{V}_{meso}$) and micropore volume ($\mathbf{V}_{micro}$) have both decreased and the main 8.4 nm peak is approximately 30% of the original template value. The main PSD peak associated with the SBA-15 template of 8.4 nm has also shifted to a lower value of 6.9 nm as expected for a thermal exposure of 600°C during the calcination process[101]. Despite a weakly resolved main peak assigned to the (100) Miller index from low angle XRD analysis, it would suggest that an amount of ordered material exists in the bulk material. As the templating process has a natural loss in fidelity through small variations in the crystal growth and by association, pore size, the cumulative effect will be to diminish any observed signal. This loss of fidelity can be observed in the TEM images where the inverse structure which is clearly composed of bundled rods, exhibit intermittent width variations along their lengths. This is further verified by the DDP in Figure 7-4(e) which displays a resolved diffraction pattern but with distortions. A variation exists between the PSDs of SDC

materials from both experiments. In the first experiment in which a pellet with ethanol solvent still within its matrix is calcined, a profile was produced that can be best explained as a solvo-thermal effect. This effect is discussed in greater detail in Chapter 10. It is a mechanism that produces a crystalline SDC framework composed of disordered pores specifically in the range that is observed. The SBA-15-SDC-FP(1) is a close fit in all the data parameters of SSA, PSD and sorption profile of a 600°C solvo-thermal produced material. The material is also present at the intermediate stage suggesting that the formation is independent of any casting influence. The PSD observed for the second experiment has two peaks within a broad spectrum that is confined to the low mesopore range. The peaks at 4 nm and 8-9 nm are distinctly different from that of the starting SBA-15 material even allowing for thermal shrinkage. They are also different from the first experiment indicating that the final product is structurally altered.

7.3.2 *Ultra-Microtomy Analysis*

Figure 7-5 (a) and (b) are TEM images of SBA-15 template at the intermediate stage and prepared using a standard grid swipe method through material in solvent suspension. In Figure 7-5 (a), the SBA-15 template structure was found to be present and highlighted at different points by three red arrows, obscuring the observation of the structure was foreign material that was likely to be from an excess of SDC. .

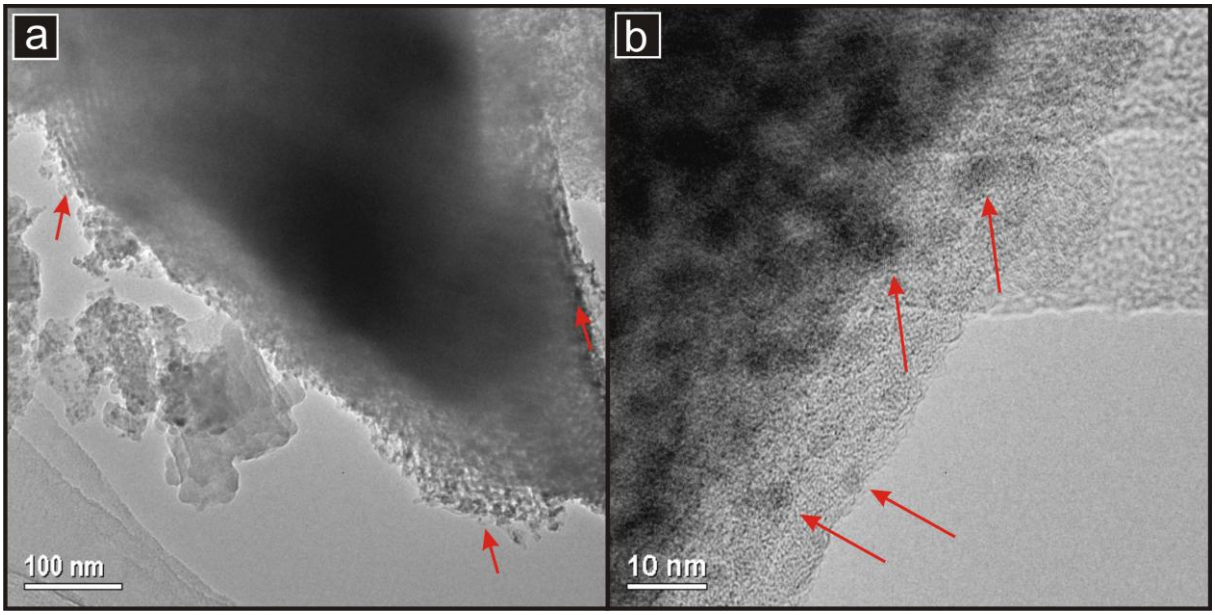

Figure 7-5: TEM images of SBA-15-SDC-IT without ultra-microtomy preparation: (a) representative image of a particle showing some channel ordering as highlighted by the arrows but masked by large SDC growth, (b) high resolution of a channel showing some crystallised particles. It is unclear if the particles highlighted by the arrows are on the surface or within the channel.

This was a typical finding of the observation of intermediate materials using this method of sample preparation. In Figure 7-5 (b), one of the pore channels was observed at higher magnification. Along the length several crystal particles were observed but since the depth of focus is limited, it cannot be ascertained if the particle is within or out with the channel

Figure 7-6 is a series of TEM images of the intermediate material that was prepared using an ultra-microtome technique. The sequence of images are all in the [001] direction which was commonly present throughout the prepared sample grid. .

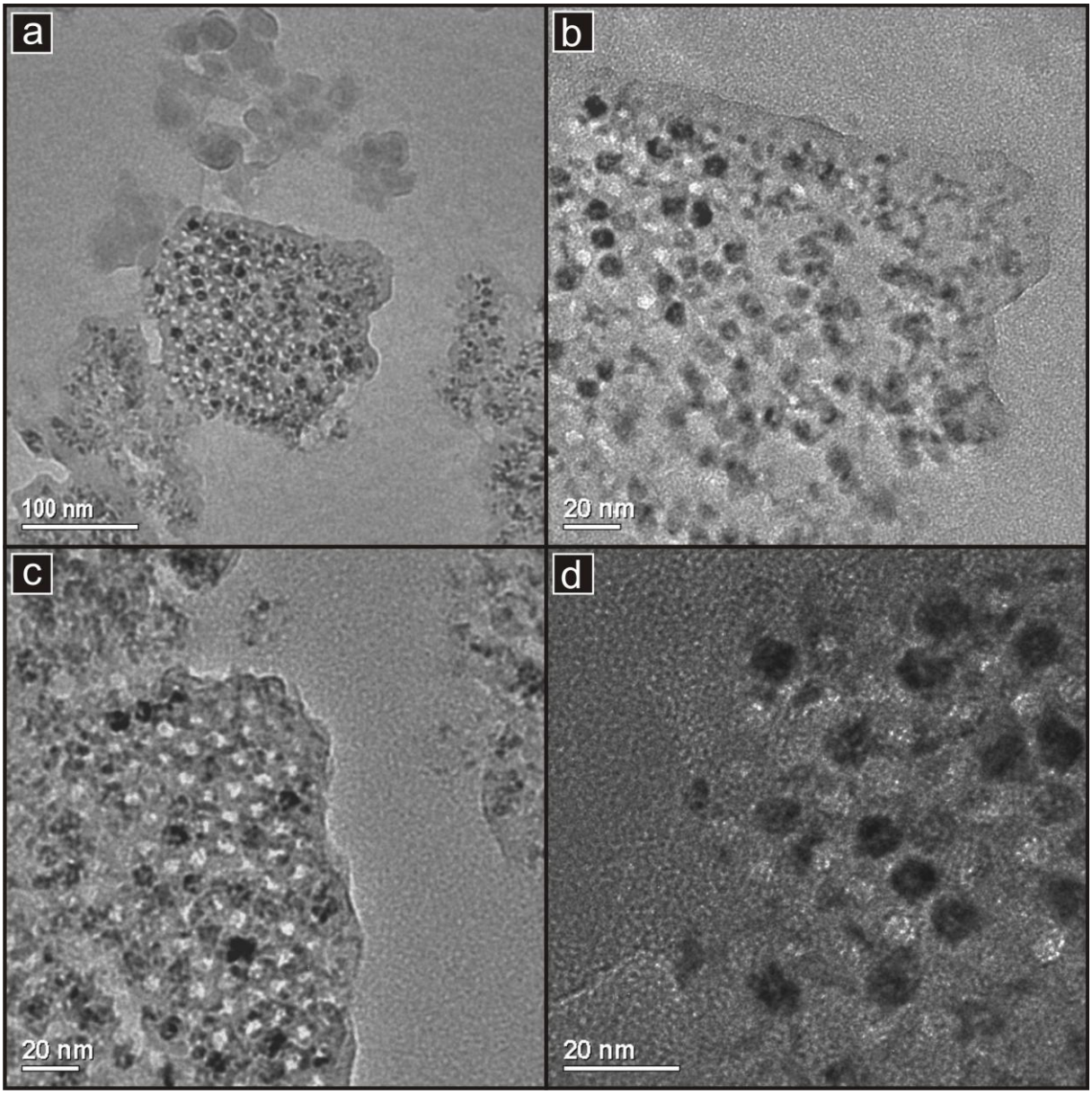

Figure 7-6: TEM images of SBA-15-SDC-IT prepared by ultra-microtomy and viewed in the [001] direction: (a) representative image of a sectioned particle, (b) impregnated SBA-15 with the contrasting light and dark pores clearly visible, (c) An area of the SBA-15-SDC intermediate with a majority of unfilled pores (light), (d) An area of the SBA-15-SDC intermediate with a majority of filled pores (dark).

The contrast between the pores was evident with the darker pores having a greater density from SDC being present and lighter where they were still vacant. The benefit of this method was to show qualitatively the amount and the random nature in which pores were being filled

7.3.3 *SDC Prepared From KIT-6*

In order to establish that the Kit-6-SDC-FP material was of expected porosity and structure for a material nanocast from KIT-6, the samples were analysed by gas physisorption as this would indicate the bulk repeatable nature of the material prepared. The generated isotherms can be interpreted for specific surface area ($\mathbf{S}_{BET}$), pore size distribution ($\boldsymbol{W}_{BJH}$), mesopore volume ($\mathbf{V}_{meso}$) and micropore volume ($\mathbf{V}_{micro}$). Figure 7-7 (a) and (b) show a typical isotherm and associated specific pore size distribution (PSD) for IT and FP materials. The isotherm for IT is typical of a type IV profile with an associated hysteresis that is somewhere between a type H2 and H4. The FP product has an isotherm of type I profile with a hysteresis best defined as H4. The IT has one distinct peaks observed at 7.6 nm whereas the FP has a single broad peak centred at in the low mesopore range but skewed towards the 3 nm range as observed from the desorption branch. Specific mesopore volumes ($\mathbf{V}_{meso}$) of 0.33 cm^3g^{-1} and 0.34 cm^3g^{-1} , micropore volumes ($\mathbf{V}_{micro}$) of 0.01 cm^3g and 0.01 cm^3g^{-1} , average specific surface area ($\mathbf{S}_{BET}$) of 291 m^2g^{-1} and 195 m^2g^{-1} were recorded for IT and FP respectively.

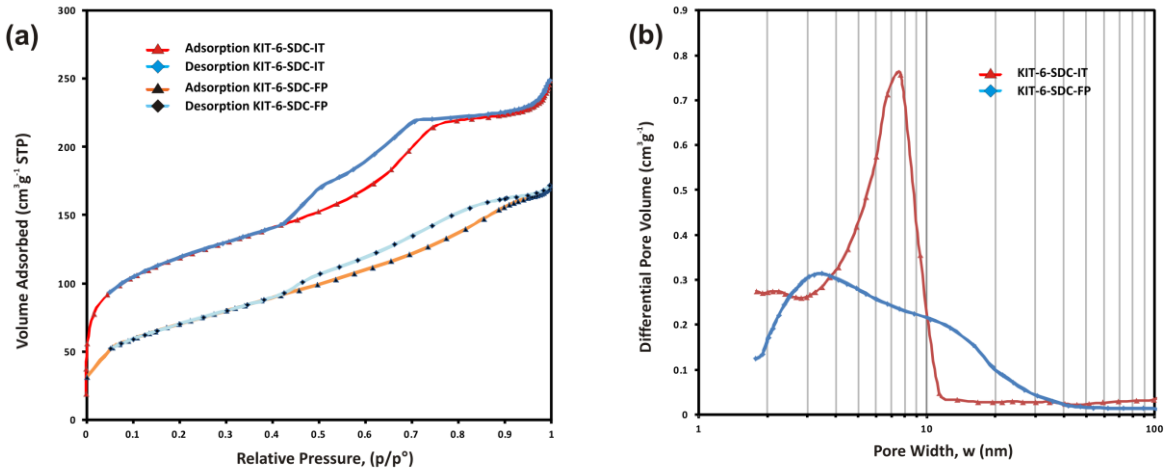

Figure 7-7: Nitrogen physisorption isotherms (a) and specific pore size distributions (b) for KIT-6.

Figure 7-8 presents patterns of low angle XRD data with a background subtraction included to help better resolve the diffraction peaks. Analysis of the KIT-6-SDC-FP pattern shows a

material with one distinct peak at 11.75 nm. The unit cell parameter of 28.8 nm was calculated using the formula in Appendix 2, Eqn. 20.

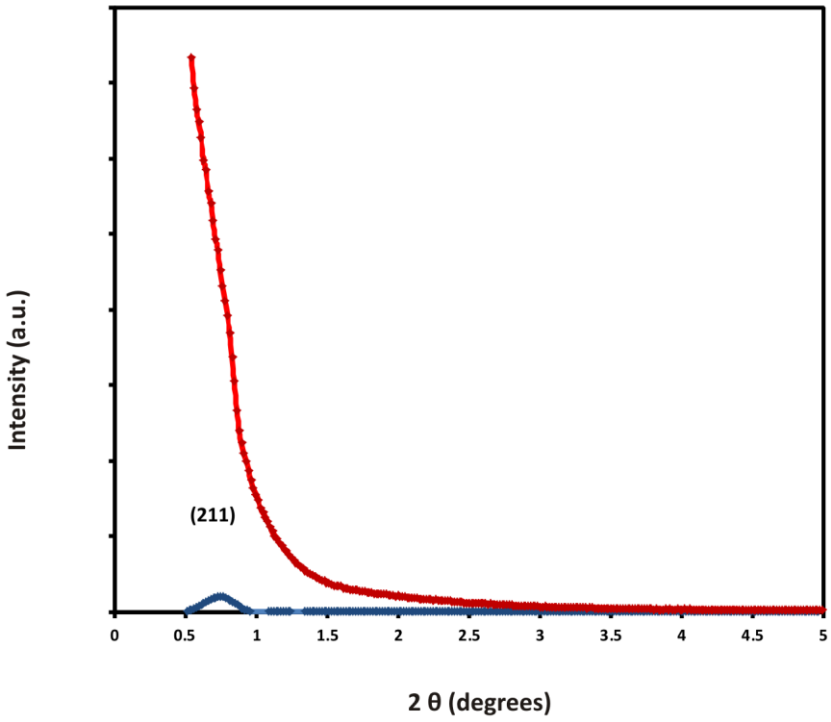

Figure 7-8: SAXS Diffraction pattern and corresponding interplanar ***d***-spacing for KIT-6-SDC-FP.

Table 7-2: Calculated *d*-spacing from 2θ values for KIT-6-SDC-FP.

2θ (°)	**Indices**	***d*-Spacing (nm)**
0.752	211	11.75

In order to verify the expected inverse structure of Kit-6, TEM analysis was performed and is presented in Figure 7-9. The sample displayed an amount of structured material but was not verified as having repeat porous order. Figure 7-9 (c) and (d) show the bundling of the rods and although porous channels are evident by the lighter fringes around the rods, they were not well enough resolved to indicate if porous ordering existed. Figure 7-9 (e) is a high magnification of two rods with an adjoining bridge highlighted between the two red lines. The crystal lattice planes can be seen to extend into both rods. Figure 7-9 (f) is another high magnification of two rods that have extensive unidirectional lattice planes that run laterally along the length of both rods indicating that the crystal growth of both rods is somehow connected. The width w_{TEM} could not be reliably measured, however wall (rod) thickness d_{TEM} was found to be 7 nm. This is in good agreement with the reported PSD for the material and concurs with the inverse values of PSD for the template.

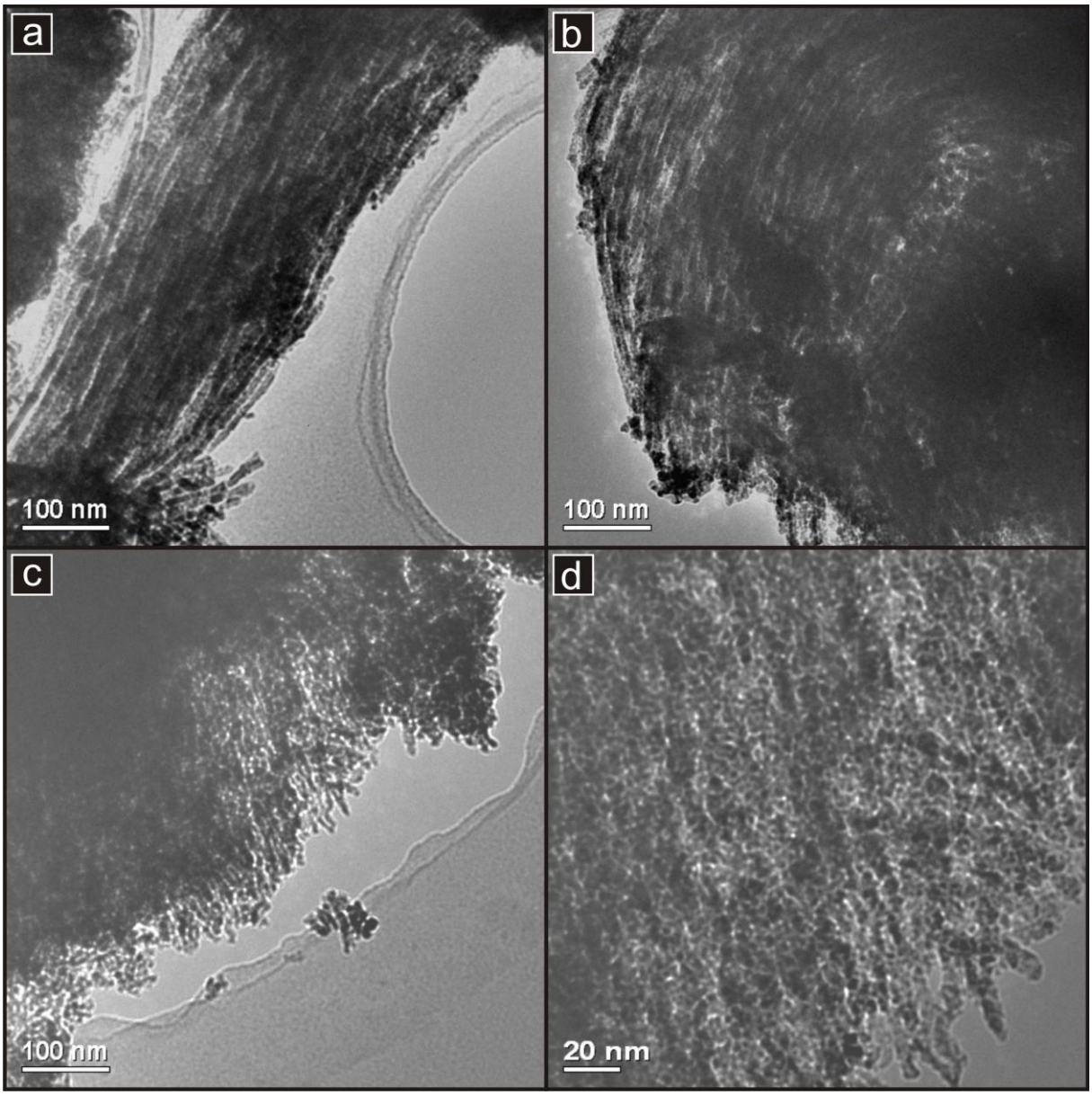
a
100 nm
b
100 nm
c
100 nm
d
20 nm

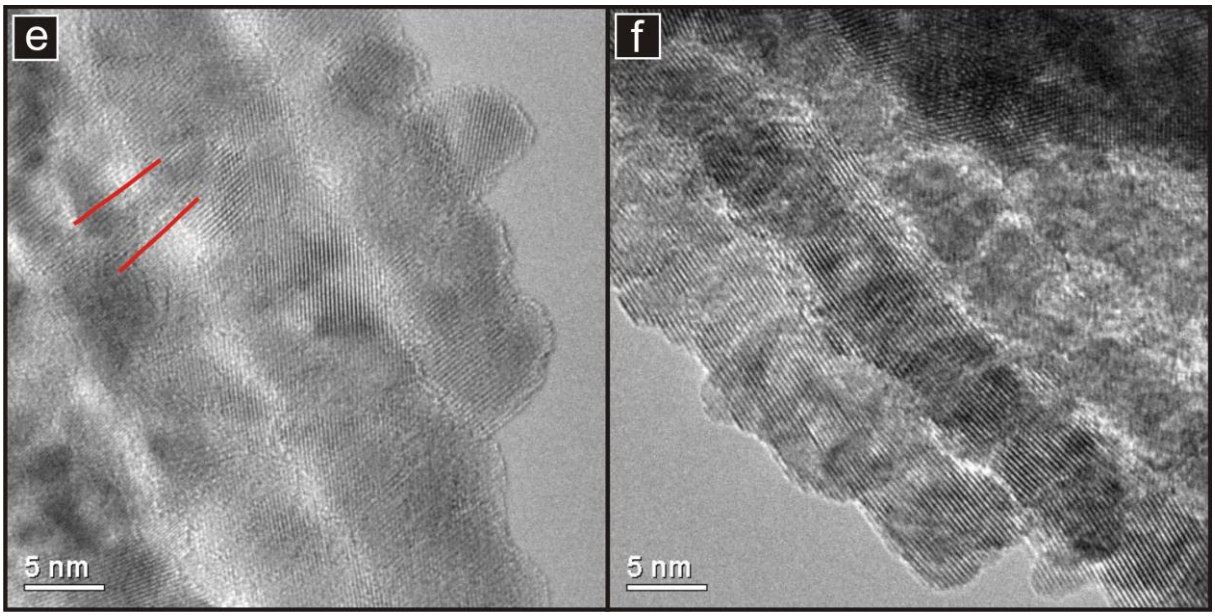

Figure 7-9: TEM images of KIT-6-SDC-FP: (a) and (b) bundled structures showing long range rods, (c) and (d) rod like structures but disordered in their spacing, (e) high magnification of some rods with a nanobridge highlighted between the two red lines, (e) high magnification of two rods with crystal lattice planes in the same direction.

The replication of metal oxides from KIT-6 has been shown to be dependent on the hydrothermal temperature preparation of KIT-6. Tuysuz and co-workers[96] have reported a direct relationship with the replication of the two pore systems of the bi-continuous structure. From a preparation range of 40 to 130°C, there is a gradual increase in the cross linkage between the bi-continuous pore systems. In the same way that nanobridges are important for SBA-15 replication, this same inter structure joining is critical to creating a dense product of high repeatable order. The alternative in the formation is to produce structures formed from only one pore system thus creating relatively open structures. The change in the isotherm hysteresis from the template H2 through to FP with H4 indicates a change in the pore type. H1 is more associated with uniform spheres in a regular array whereas H4 is associated with narrow slit like pores and may be a function of the new pore range that has been formed. The bi-continuous nature of the material was not conclusively viewed in the TEM images although an ordered structure was evident. The SDC displays evidence of high porosity, SSA and crystallinity associated with a material of this nature and is summarised in Table 8-6.

7.3.4 *SDC Prepared From FDU-12*

In order to establish that the FDU-12-SDC-FP material was of expected porosity and structure for a material nanocast from FDU-12, the samples were analysed by gas physisorption as this would indicate the bulk repeatable nature of the material prepared. The generated isotherms can be interpreted for specific surface area ($\mathbf{S}_{BET}$), pore size distribution ($\boldsymbol{w}_{BJH}$), mesopore volume ($\mathbf{V}_{meso}$) and micropore volume ($\mathbf{V}_{micro}$). Figure 7-10 (a) and (b) show a typical isotherm and associated specific pore size distribution (PSD) for IT and FP materials. The isotherm for IT is typical of a type IV profile with an associated hysteresis that is type H2. The FP product has an isotherm of type I profile with a hysteresis best defined as H4. The IT has one distinct peak observed at 10.1 nm and range of lower mesopores extending into the micropore range. The FP has a broad peak that appears to have two maximums centred at the 4-5 nm and 15 nm intervals as observed from the desorption branch. Specific mesopore volumes ($\mathbf{V}_{meso}$) of 0.18 cm^3g^{-1} and 0.27 cm^3g^{-1} , micropore volumes ($\mathbf{V}_{micro}$) of 0.04 cm^3g and nil cm^3g^{-1} , average specific surface area ($\mathbf{S}_{BET}$) of 258 m^2g^{-1} and 150 m^2g^{-1} were recorded for IT and FP respectively.

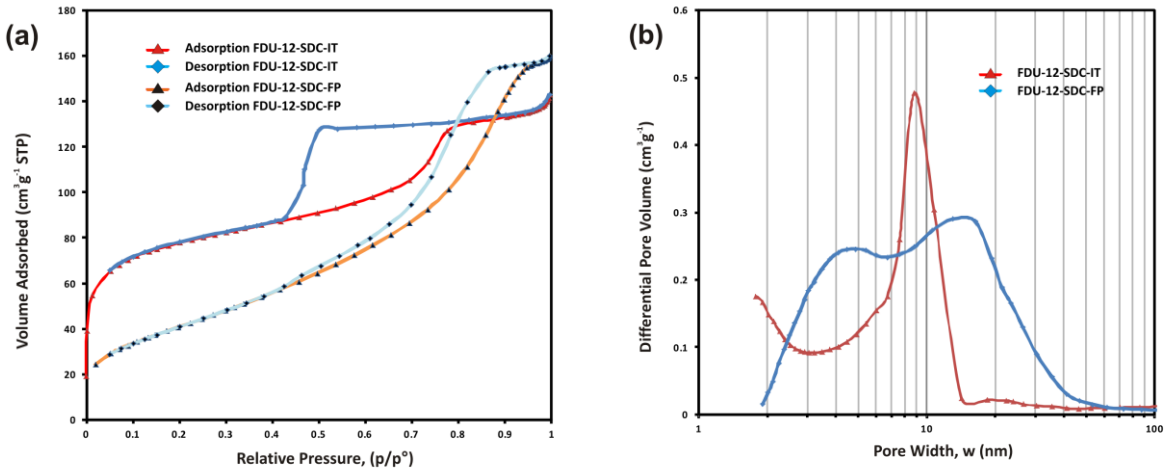

Figure 7-10: Nitrogen physisorption isotherms (a) and specific pore size distributions (b) for SDC material prepared using FDU-12 template.

Figure 7-11 presents patterns of low angle XRD data with a background subtraction included to help better resolve the diffraction peaks. Analysis of the KIT-6-SDC-FP pattern shows a material with one distinct peak at 10.61 nm. The unit cell parameter of 26.0 nm was calculated using the formula in Appendix 2, Eqn. 20.

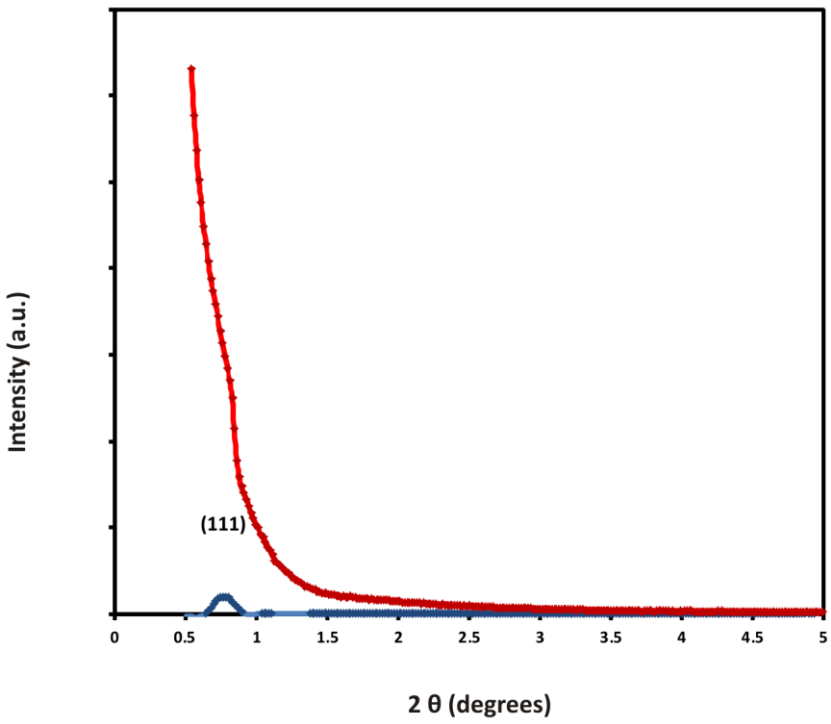

Figure 7-11: SAXS Diffraction pattern and corresponding interplanar ***d***-spacing for FDU-12-SDC-FP.

Table 7-3: Calculated *d*-spacing from 2θ values for FDU-12-SDC-FP.

2θ (°)	**Indices**	***d*-Spacing (nm)**
0.832	111	10.61

TEM images in Figure 7-12 did not reveal any ordered material despite the indication from both low angle SAXS and gas physisorption to the contrary. Figure 7-12 (a) was representative of this sample grid and highlights one such particle which is composed of a range of spherical clusters very similar in size. Figure 7-12 (b) is a higher magnification of one of these clusters with an exploded view shown in the inset. The sphere with small nodules is similar to an individual inverse cage. Incomplete bridging between spheres would offer a possible explanation for their existence and is comparative to the individual rods often associated with incomplete bridging in SBA-15 material.

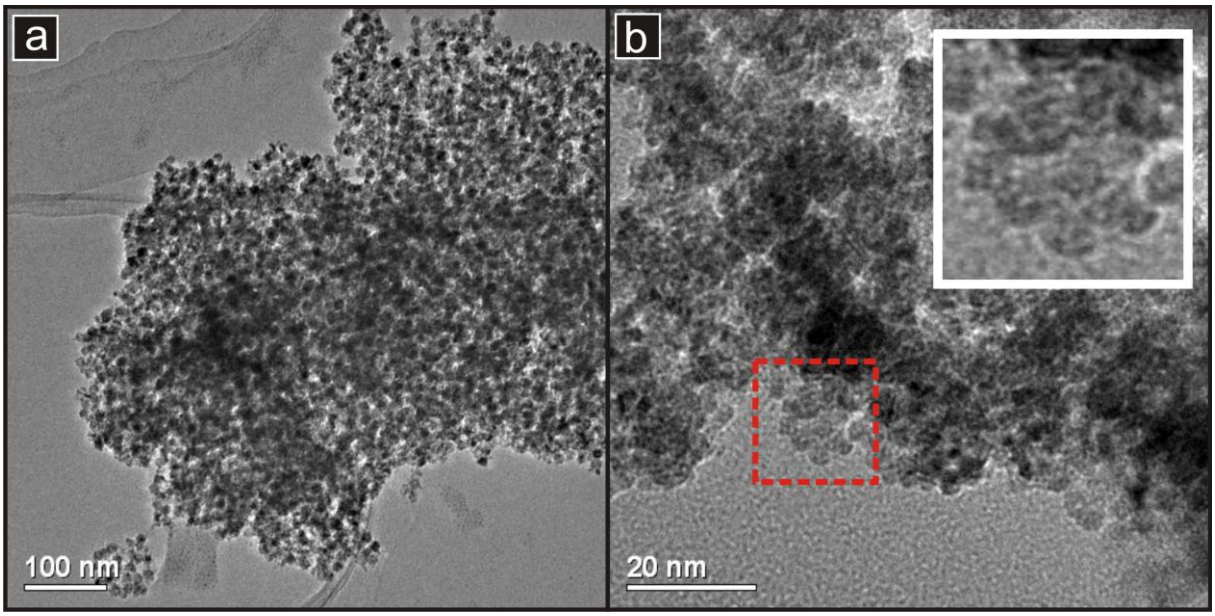

Figure 7-12: TEM images of FDU-12-SDC-FP: (a) representative image of a particle showing no ordered structure but composed of spherical clusters, (b) higher magnification of the cluster arrangement. One such cluster is highlighted by the red circle and displayed as a magnified inset.

Review of the results suggests that the template is being partially filled as the mesopore volume ($\mathbf{V}_{meso}$) and micropore volume ($\mathbf{V}_{micro}$) have both decreased and the main PSD peak at 8.8 nm is approximately 30% of the original template value. This main PSD peak associated with the FDU-12 template remains unchanged in range despite a thermal exposure of 600°C during the calcination process. This is in good agreement with the thermal deformation reported for FDU-12 in Chapter 6[101]. Despite the main peak assigned to the (111) Miller index from low angle XRD analysis being weakly resolved, it would suggest that an amount of ordered material exists in the bulk material. As the templating process has a natural loss in fidelity through small variations in the crystal growth and by association, pore size, the cumulative effect will be to diminish any observed signal.

7.3.5 *X-Ray Diffraction of SDC Materials Prepared From Silica Template*

In order to verify the crystalline nature of the SDC final products templated from the silica structures, X-Ray diffraction was performed over a range of 5 to 90° in order to view the crystal lattices and compare with SDC prepared without the use of template but with similar 600°C calcination. As the first viewable peak is at 28.5°, the range displayed has been curtailed to a starting point of 20°. The diffraction patterns were consistent with the fluorite phase of samarium doped ceria.[149]

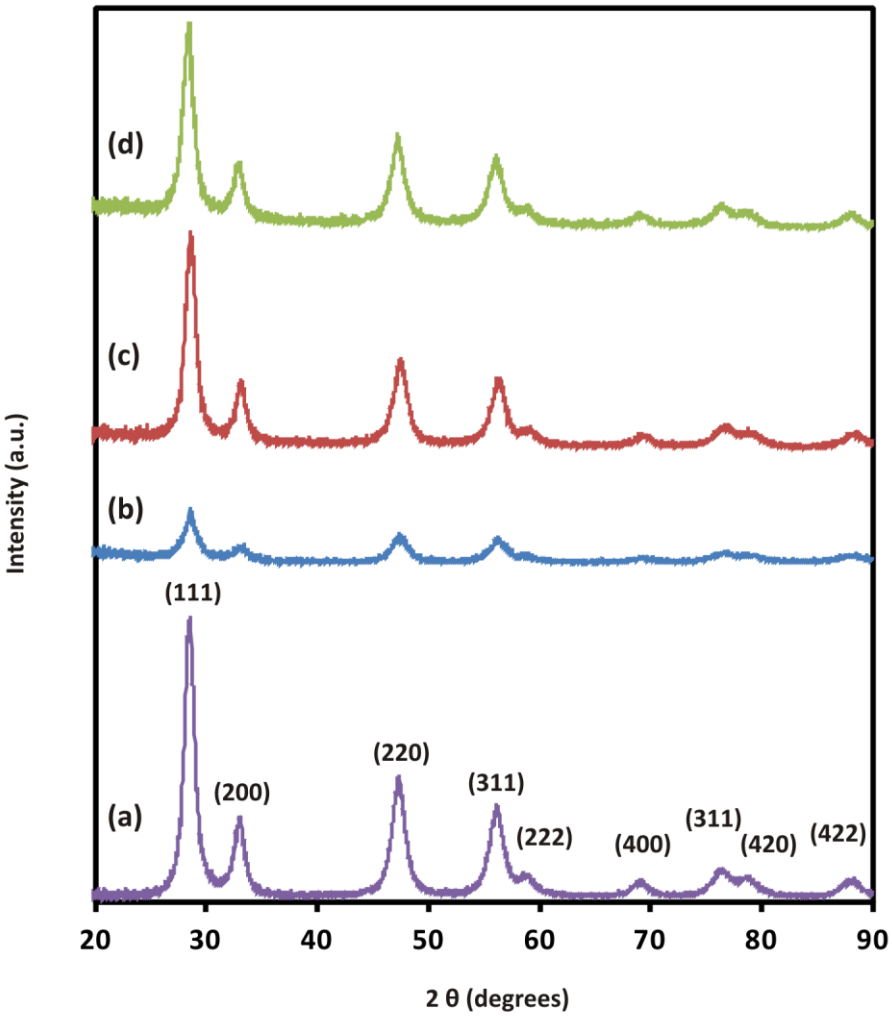

Figure 7-13: XRD Patterns of SDC final product templated from the silica structures of (b) FDU-12, (c) KIT-6 and (d) SBA-15 and compared to (a) template free 600°C.

7.4 Non-Standard Silica Templates

7.4.1 *SDC Prepared From Functionalised SBA-15*

Having prepared two SBA-15 functionalised templates with either APTS or TMDS, an attempt was made to impregnate the TMDS only. APTS was not attempted due to the gas physisorption report that the pore had become blocked. As with the standard SBA-15 impregnation, the IT and FP materials were analysed using gas physisorption.

The generated isotherms can be interpreted for specific surface area ($\mathbf{S}_{BET}$), pore size distribution (w_{BJH}), mesopore volume ($\mathbf{V}_{meso}$) and micropore volume ($\mathbf{V}_{micro}$). Figure 7-14 (a) and (b) show a typical isotherm and associated specific pore size distribution (PSD) for IT and FP materials. The isotherm for IT is typical of a type IV profile with an associated hysteresis that is type H2. The FP product has an isotherm of type I profile with minimal hysteresis. The IT has one distinct peak observed at 7.6 nm and range of lower mesopores

extending into the micropore range as observed from the desorption branch. The FP has a broad range greater than 20 nm and minimal mesopore volume below this value. Specific mesopore volumes ($\mathbf{V}_{meso}$) of 0.44 cm^3g^{-1} and 0.35 cm^3g^{-1} , micropore volumes ($\mathbf{V}_{micro}$) of 0.03 cm^3g and 0.01 cm^3g^{-1} , average specific surface area ($\mathbf{S}_{BET}$) of 276 m^2g^{-1} and 84 m^2g^{-1} were recorded for IT and FP respectively.

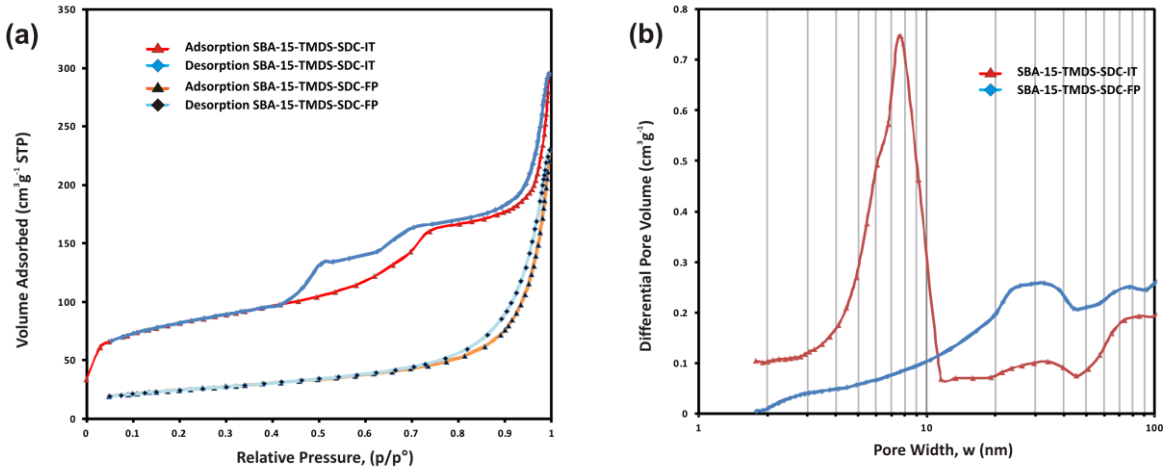

Figure 7-14: Nitrogen physisorption isotherms (a) and specific pore size distributions (b) for SBA-15-TMDS-SDC-IT and SBA-15-TMDS-SDC-FP.

Review of the data from Figure 7-14 suggests that the template is being partially filled as the mesopore volume ($\mathbf{V}_{meso}$) and micropore volume ($\mathbf{V}_{micro}$) have both decreased and the main PSD peak at 7.6 nm is approximately 15 % of the original template value. The FP material produced appears to have no significant mesopores in the low mesopore range as might have been expected. The mesopore volume being greater than 20 nm suggests that only inter-particle porosity exists from agglomeration. It appears that functionalisation has had a detrimental effect on producing any meaningful material. Had functionalisation not occurred within the pores then the template should function as a standard SBA-15 template and a result similar to section 7.3.1 would be observed. One concern was that the organic moieties grafted onto the silica surface would be susceptible to pyrolysis from the calcination but it was hypothesised that the nitrate conversion to oxide would occur at a lower temperature.

7.4.2 *SDC Prepared From Ultra-Large Pore SBA-15*

The generated isotherms were interpreted for specific surface area ($\mathbf{S}_{BET}$), pore size distribution (w_{BJH}), mesopore volume ($\mathbf{V}_{meso}$) and micropore volume ($\mathbf{V}_{micro}$). Figure 7-15(a) and (b) show a typical isotherm and associated specific pore size distribution (PSD) for IT and FP materials. The isotherm for IT is typical of a type IV profile with an associated type

H3 hysteresis. The FP product has an isotherm of type IV profile with a hysteresis best defined as H2. The IT has two distinct peaks observed at 5 and 24 nm whereas the FP has a single broad peak centred at 12 nm as observed from the desorption branch. Specific mesopore volumes ($\mathbf{V}_{meso}$) of 0.46 cm^3g^{-1} and 0.31 cm^3g^{-1}, micropore volumes ($\mathbf{V}_{micro}$) of 0.01 cm^3g and 0.01 cm^3g^{-1}, average specific surface area ($\mathbf{S}_{BET}$) of 243 m^2g^{-1} and 185 m^2g^{-1} were recorded for IT and FP respectively. The low angle XRD was found to give a background signal with no observable or attributable reflections for UL-SBA-15-SDC-FP. The TEM images were also inconclusive.

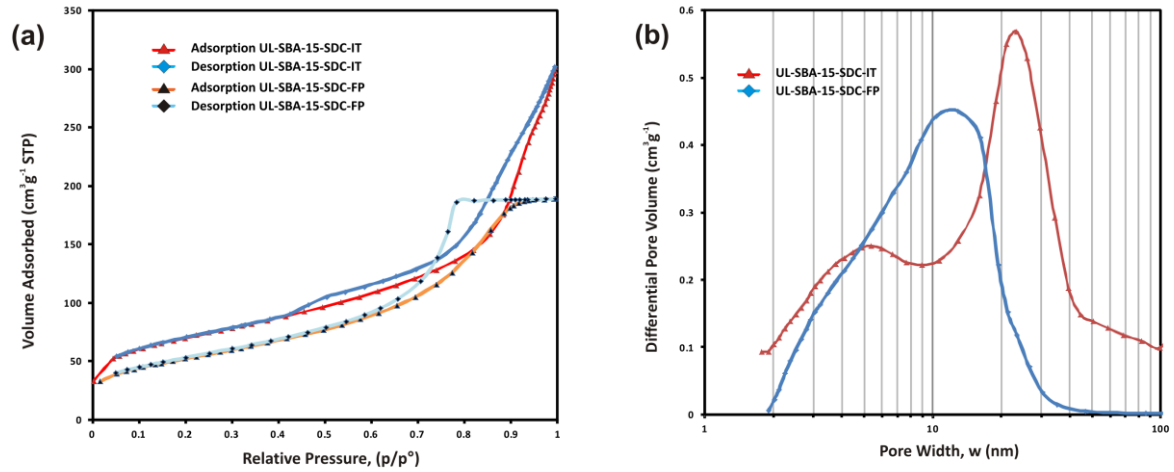

Figure 7-15: Nitrogen physisorption isotherms (a) and specific pore size distributions (b) for ultra-large SBA-15.

7.4.3 *SDC Prepared From Ultra-Large Pore SBA-15 and Functionalised with TMDS*

The generated isotherms were interpreted for specific surface area ($\mathbf{S}_{BET}$), pore size distribution (w_{BJH}), mesopore volume ($\mathbf{V}_{meso}$) and micropore volume ($\mathbf{V}_{micro}$). Figure 7-16 (a) and (b) show a typical isotherm and associated specific pore size distribution (PSD) for IT and FP materials. The isotherm for IT is typical of a type IV profile with an associated type H3 hysteresis. The FP product has an isotherm of type IV profile with a hysteresis best defined as H2. The IT has two distinct peaks observed at 5 and 24 nm whereas the FP has a single broad peak centred at 12 nm as observed from the desorption branch. Specific mesopore volumes ($\mathbf{V}_{meso}$) of 0.41 cm^3g^{-1} and 0.31 cm^3g^{-1}, micropore volumes ($\mathbf{V}_{micro}$) of 0.01 cm^3g and 0.01 cm^3g^{-1}, average specific surface area ($\mathbf{S}_{BET}$) of 217 m^2g^{-1} and 172 m^2g^{-1} were recorded for IT and FP respectively.

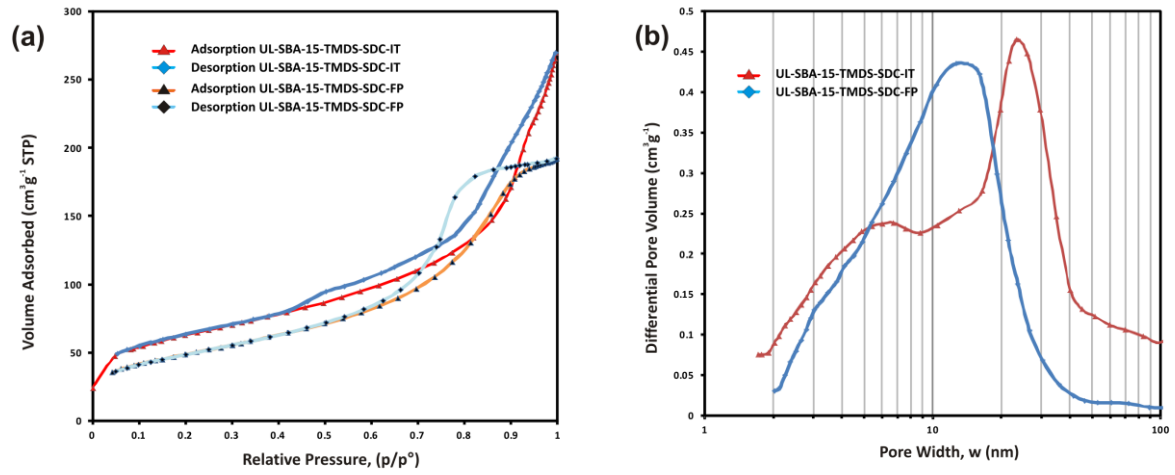

Figure 7-16: Nitrogen physisorption isotherms (a) and specific pore size distributions (b) for ultra-large SBA-15 functionalised with TMDS.

As with UL-SBA-15-SDC-FP, the low angle XRD was found to give a background signal with no observable or attributable reflections. The TEM images were also inconclusive. The observed PSD and associated physisorption characteristics were almost identical between the UL-SBA-15-SDC-FP and UL-SBA-15-TMDS-SDC-FP samples indicating that the observed effect is repeatable and not some random formation of mesopores. One possible explanation is the solvo-thermal effect. Comparison of PSD indicates a similarity to that observed in Figure 7-2 (b) and for a 600°C material produced using the solvo-thermal method. Details of the effect observed with SBA-15-SDC are presented in Figure 7-2. The same effect is covered in greater detail in Chapter 10 with gas physisorption data in Table 10-2 and Figure 10-2. As these samples had been prepared from drying at room temperature over a 24 h period, it was expected that no ethanol precursor should be present. One possible explanation is that due to the enlarged pore size, solvent may have been trapped within the structure. A notable difference between the UL prepared materials and solvo-thermal materials was that the characteristic second pore range at the 20 to 30 nm interval and present in all the observed solvo-thermal materials, is absent in the UL materials.

7.4.4 *Summary*

Table 7-4 is a summary of the key data parameters observed for the final SDC products.

Table 7-4. OMS prepared SDC materials: Values for unit cell parameters ($a_0 1 - a_0 3$), interplanar spacings (d), pore width (w) and pore wall thickness (t) obtained using the method indicated (BJH, SAXS, TEM). All values are in nm. Values of a_o are calculated from the corresponding d_{SAXS} value. Miller indices are given in italics below each value of d.

Sample	w_{BJH} (nm)	S_{BET} (m^2g^{-1})	V_{meso} (cm^3g^{-1})	V_{micro} (cm^3g^{-1})	$d_{SAXS}{}^1$ (nm)	$a_0{}^1$ (nm)	w_{TEM} (nm)	t_{TEM} (nm)
SBA-15-SDC-FP	4, 8.5	140	0.42	nil	11.12 *(100)*	12.8 *(100)*	3.5	8
KIT-6-SDC-FP	3, 2-15	195	0.34	0.01	11.75 *(211)*	28.8 *(211)*	-	7
FDU-12-SDC-FP	5, 15	150	0.18	nil	10.61 *(111)*	26.0 *(111)*	-	-
SBA-15-TMDS-SDC-FP	>20	84	0.03	0.01	-	-	-	-
UL-SBA-15-SDC-FP	12	185	0.31	0.01	-	-	-	-
UL-SBA-15-TMDS-SDC-FP	12	172	0.31	0.01	-	-	-	-

7.5 Removal of Silica Template by Wet Chemical Methods

7.5.1 *Purpose of Study.*

One of the potential end applications for nanocasted SDC material is the anode section of a fuel cell. However, it is known that even ppm amounts of silicon will migrate towards grain boundaries and detrimentally affect operational characteristics[58]. Despite several authors showing successful manufacture of ceria based materials from a silica nanocasting process, no reports of the remnant silica has been reported other than a few observations that state non-empirically that it remains in small quantities[57]. This study attempts to quantify the remaining silica as well as reduce and possibly eliminate the silica content using a variety of wet chemical methods. The standard removal method of silica template is typically through the use of basic sodium hydroxide (NaOH) or acidic hydrofluoric (HF) solutions. The use of HF acid is to be avoided though for two main reasons; the safety implication of such a chemical and the fact that it is known to dissolve ceria. For this reason HF acid was avoided. An extensive search was carried out to determine potential alternatives that could either dissolve the silica template or help 'polish' the final product as is often the approach in the manufacture of semiconductors when controlling the etch rates of silicon crystals or silica

layers. As a starting point, the dissolution of the silica template was characterised when subjected to NaOH solution and to see what affect time, concentration and structure would have on the ability to achieve a completely dissolved condition. A set of experimental parameters would then be tested to see what the maximum and most efficient method of silica removal would be. This was further extended by trying three alternative chemical approaches and examining final products using SEM-EDX spectroscopy. The alternative chemicals used were: Ammonium Bifluoride (IUPAC: ammonium hydrogen fluoride), Tetra Methyl Ammonium Hydroxide (TMAH) and Catechol (IUPAC: 1,2-dihydroxybenzene).

7.5.2 *Dissolving Silica using Sodium Hydroxide.*

n initial investigation was performed to determine how effectively OMS templates – namely SBA-15, KIT-6 and FDU-12 – would dissolve in a solution of NaOH. In order to analyse the dissolution of these mesoporous silica templates and determine the effectiveness of NaOH as a template removal reagent, a range of silica weights were examined for their rate of change in colloidal suspension when placed in a NaOH solution. This rate of change would be monitored by UV-Visible transmittance spectroscopy.

Silica is an inherently stable material and is normally only dissolved by alkali hydroxides or hydrofluoric acid. It has therefore received much attention especially in the advent of semiconductor technology. In a simple stoichiometric equation (Eqn. 16) it would appear that in combination with an alkali hydroxide the following would be observed:

$$\mathbf{SiO_2 + 2NaOH \rightarrow H_2O + Na_2SiO_3} \qquad \textit{Eqn. 16}$$

where the alkali metal is in a 2 to 1 stoichiometric ratio with silicon. It has since been shown that such a simple equation is not always applicable and that a much more complex reaction mechanism is in effect. Studies by Iler[102] highlighted that the mechanisms are also further complicated by the crystalline SiO_2 states that exist and this has a direct correlation with the rate of dissolution in a hydroxide medium.

In respect to amorphous silica, a range of solubility values from 70 to 150 ppm at 25°C have been reported with factors such as particle size, degree of hydration, and impurity concentrations being key factors affecting solubility. The rate of equilibrium is established slowly unless the silica material has a high specific surface area, as is the case of mesoporous templates. The mechanism for this retardation of dissolution is one of $Si(OH)_4$ adsorbing onto the surface of the silica.[103],[104],[105].

Further, Anderson and Burnham [106] have detailed a mechanism where SiO_2 is complexed by water and NaOH as detailed in Eqn. 17 and the solubility stoichiometry will be nearer to a 1:1 ratio of Na:Si, with the equilibrium position far to the right. As this is a protonic reaction, it also highlights the pH dependency.

$$NaOH + H_4SiO_4 \leftrightarrows NaH_3SiO_4 + H_2O \qquad \textit{Eqn. 17}$$

7.5.2.1 Colloidal Stability

Initially it was thought that UV-Visible analysis would be invalid as silica is well known for its inertness in the UV-visible spectrum [107]. It was hypothesised however that the particle size characteristics of the mesoporous structures would allow for a colloidal solution to be achieved by being suspended in solution from Brownian forces. Also, as the powder is white and therefore inherently reflective and scattering of light it should be possible to measure this effect. An attempt was therefore undertaken to analyse by diffuse transmittance mode on a UV-visible spectrometer. Initial results were promising with little evidence of the powder falling out of solution even at the higher weight level of 100 mg. In order to verify the stability of a freshly prepared homogenous sample, a series of samples of KIT-6 ranging from zero to 60 mg in 10 ml of distilled water was prepared and analysed immediately and after a 24 h period. The sample was initially analysed over the UV-visible range with 600 nm being chosen as a stable mid-range wavelength. As is evidenced by Figure 7-17, the colloidal suspension is remarkably stable over 24 hours making this a viable technique for analysis. The result of which indicates that there is a good degree of repeatability thus suggesting that a homogenous solution can be obtained that will remain in a physically constant state for the duration of testing. The result also suggests there is a stability in the opacity of the mesoporous structure, had the silica absorbed the water, the refractive properties may have changed (this is observed when silica templates are impregnated in ethanol solvent – Figure 7-1) making the spectroscopic analysis method invalid.

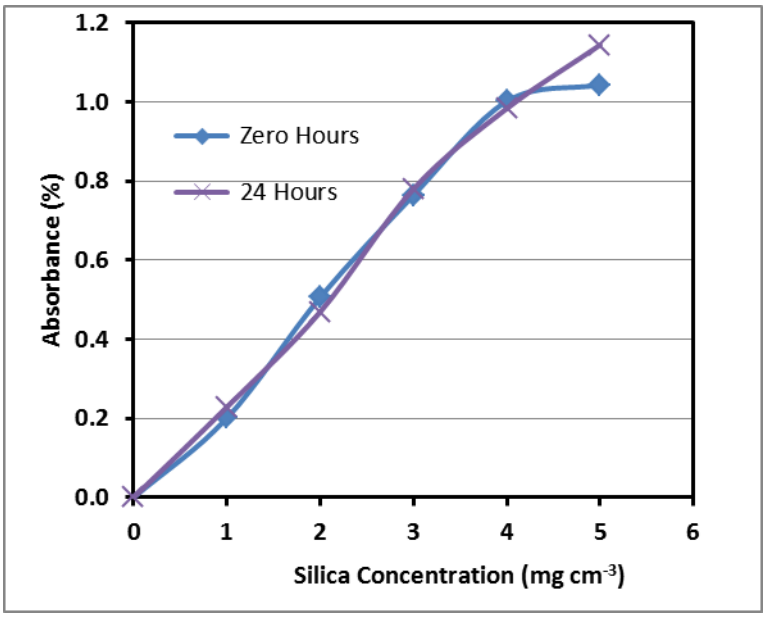

Figure 7-17: Stability of the colloidal suspensions of silica template in H_2O over a range of concentrations in a 24 hour period.

7.5.2.2 Sample Preparation

Having determined the feasibility and concentration range for silica template in water, a series of samples were prepared so that the dissolving of template could be observed in real time in a weak solution of 0.1M NaOH.

A range of silica templates were weighed into 20 ml plastic cups. The amount ranged from zero mg up to 50 mg in 10 mg increments. An analytical balance was used to provide an accuracy of ± 0.05 mg. Fresh 0.1M NaOH was prepared by way of volumetric flask. Each cup had 10 ml of NaOH added and timing began. At 10 minute time intervals, the sample under analysis would be transferred into a 1 cm plastic cuvette. A 5 ml sample would be taken by syringe and transferred from the cup to the cuvette. The syringe type was chosen to allow quick and easy mixing of the liquid silica samples such that a homogenous sample would be quickly transferrable into the cuvette. This technique involved quickly pulling the mixture into the syringe and expelling back into the remaining liquid to cause turbulence; repeated at least three times. The cuvette would then be analysed in the spectrometer at 600 nm before being transferred back into the original sample cup to await the next test interval. This procedure was repeated for each weight increment using each of the three silica types: SBA-15, KIT-6 and FDU-12.

7.5.2.3 Results of Silica Dissolution Study

Figure 7-18 (a-d) graphically indicate OMSs being dissolved in 10ml of 0.1M NaOH. Each line represents a weight of silica and the change of transmittance over a period of 90 minutes.

The graphs are presented to highlight the dissolution rate through a series of increasing weight concentrations. Figure 7-18 (a) indicates that dissolution occurs in a controlled manner until approximately the 60 minute period whereby the dissolution slows and stabilises above the 100% transmittance value. Figure 7-18 (b) similarly shows KIT-6 silica being dissolved with the results comparable to SBA-15. Figure 7-18 (c) graphically illustrates the FDU-12 silica through the same series of weight increments. Unlike SBA-15 and KIT-6 this OMS appears to resist dissolution for an initial period of between 10 and 30 minutes before a controlled increase in transmittance was observed. A stabilisation above the 100 % transmittance value was viewed in Figure 7-18 (a) and (b), however the absolute values were higher.

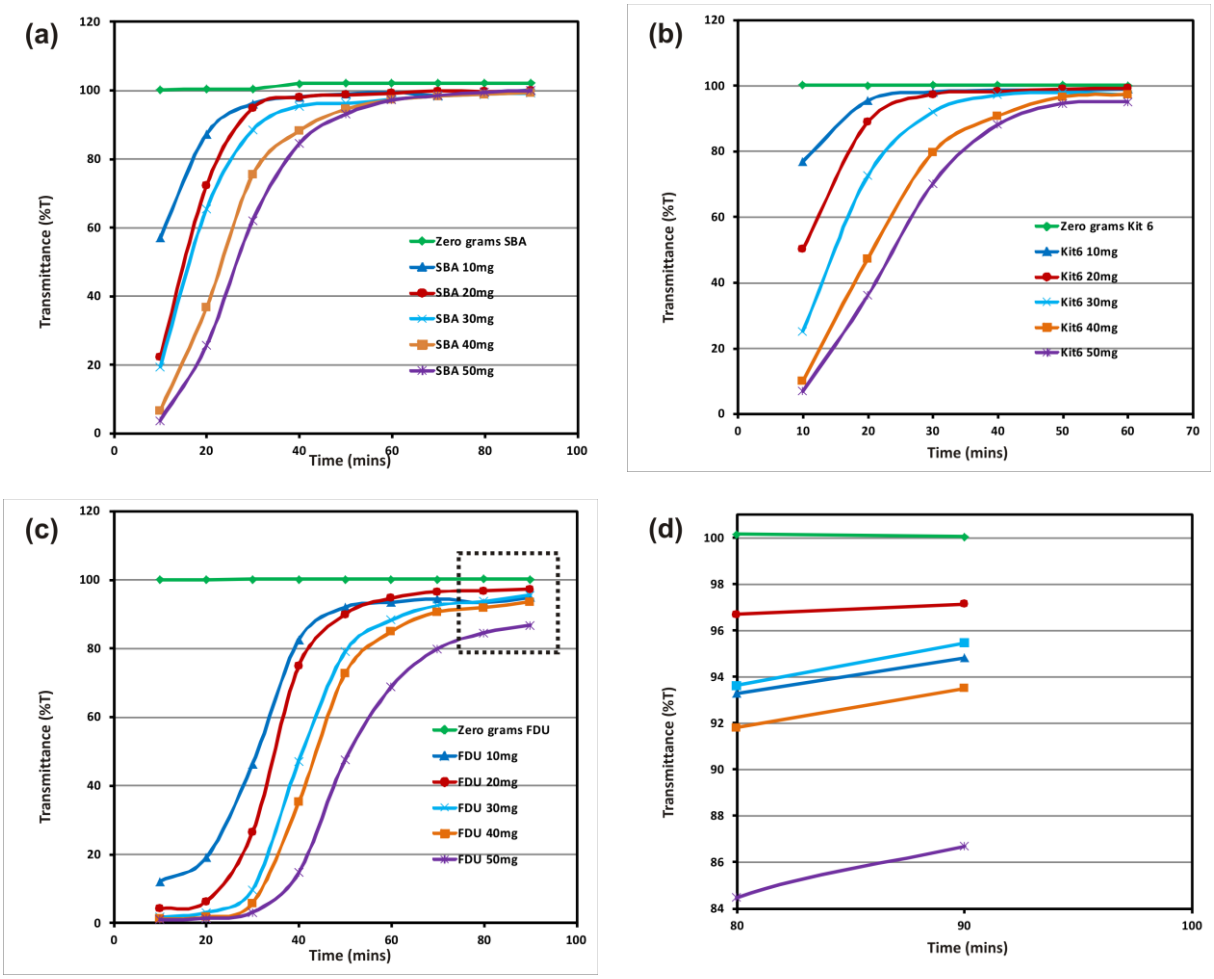

Figure 7-18: The dissolving rate for a range of incremental weights (0♦, 10▲, 20●, 30×, 40■ and 50∗ mg) of each of the 3 templates (a) SBA-15 (b) KIT-6 (c) FDU-12 in 0.1M NaOH solution, the boxed area is provided as an expanded view (d).

The final values in Figure 7-18 (d) show that all the weight loadings remain above the background reading. A possible explanation may be that a change of the refractive properties of the liquid occurs from dissolved silica as opposed to reflectance from the

physical material. However, since the weight of all three OMS materials were consistent and of the same elemental constituency differing only in structure, the amount of silica available for dissolution should be the same. This would suggest that the dissolution of FDU-12 has not reached completion within the 90 min time frame with an upward trend towards maximum transmittance still on going.

In Figure 7-19 (a-e), each graph displays the dissolution rate for 10 mg incremental weight increases and is a direct comparison in the rate of dissolution between each of the three OMS templates..

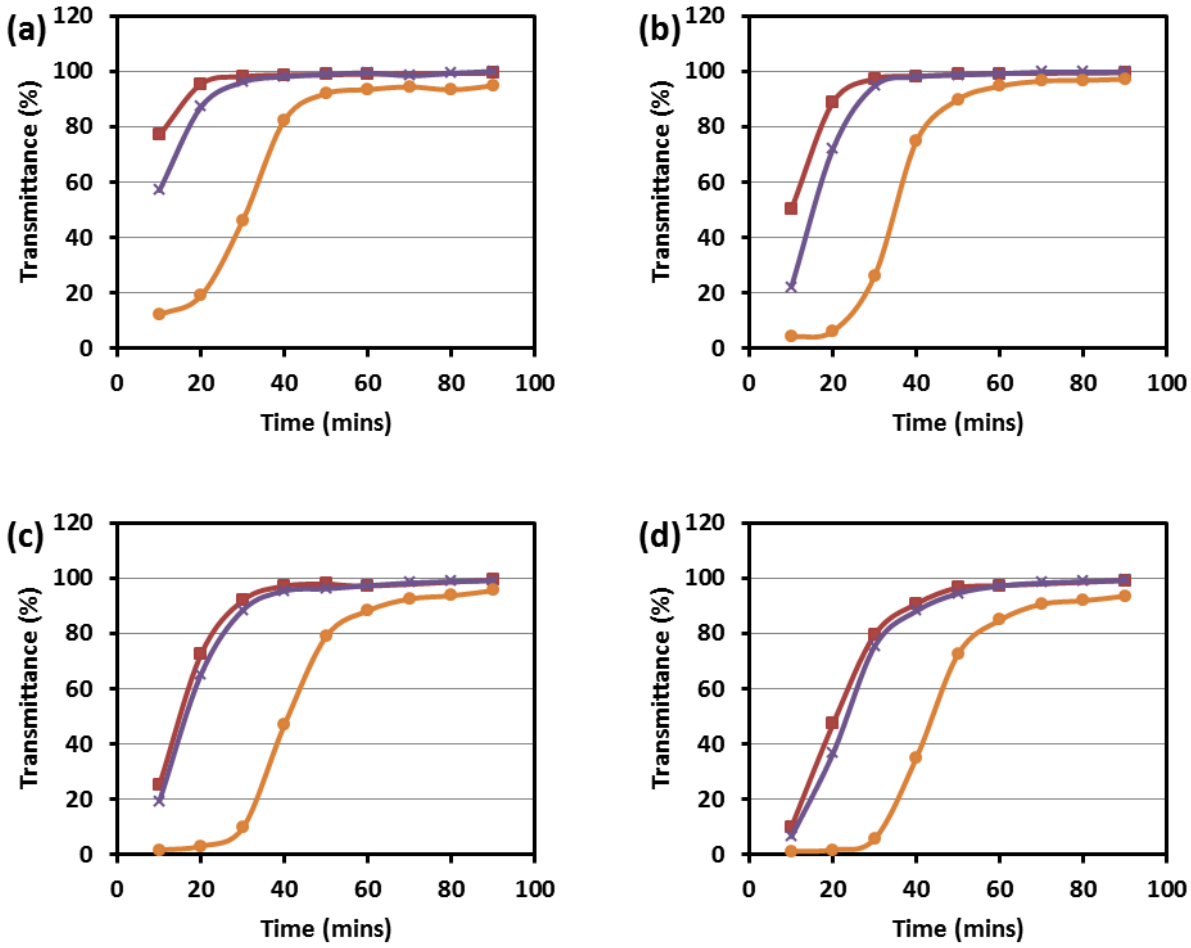

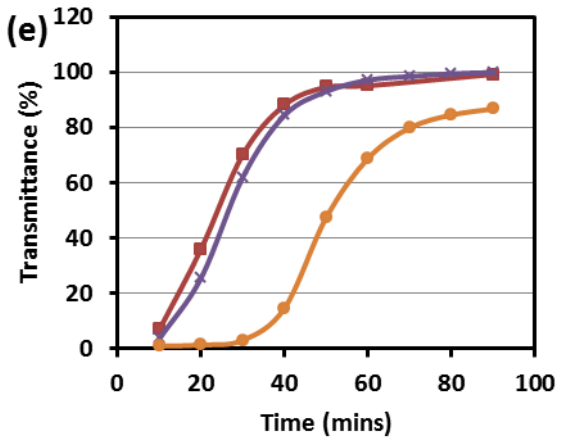

Figure 7-19: A comparison of the dissolving rate for 3 templates SBA-15×, KIT-6 ■ and FDU-12● at incremental weight loadings of (a) 10 (b) 20 (c) 30 (d) 40 and (e) 50 mg prepared in 10ml of 0.1M NaOH.

As the weight loading increased through the series of graphs, it appeared that the time taken to reach a stabilised dissolution point also increased. The rate at which this occurred was very similar for the OMS SBA-15 and KIT-6 materials. The FDU-12 material was longer at every weight loading in reaching this same point of stabilisation. The data also highlights the importance of weight loading versus the time to dissolve. For SBA-15 and KIT-6 this was found to be approximately 40, 50, 60, 70 and 80 mins for weight loadings of 10, 20, 30, 40 and 50 mg respectively. For FDU-12 this was found to be 60, 70, 80, 90 and an estimated 100 mins for weight loadings of 10, 20, 30, 40 and 50 mg respectively

7.5.2.4 Summary

The use of UV-vis spectroscopy has been shown to be useful in understanding the dissolution rate of three OMS materials. Each material has a distinctive dissolution rate with SBA-15 and KIT-6 being similar in profile. FDU-12 was found to be significantly slower in comparison. It is hypothesised that the observations were due to structural differences which are closely related to physical characteristics of pore volume and SSA. The SSA values for the SBA-15, KIT-6 and FDU-12 templates used were 891, 861 and 490 m^2g^{-1} and correlate with the observed rates of dissolution of 20, 25 and 45 mins per 10 g of material in 0.1M NaOH solution respectively.

7.6 Silica Template Removal From SDC Products

7.6.1 *Silica Template Removal Using Sodium Hydroxide.*

Following the experiments to get a quantitative assessment on the time and concentration factors driving the dissolution of the silica templates in sodium hydroxide, a series of wash procedures were performed on impregnated-calcined materials (intermediate products).

A standard procedure of three 40 ml 0.1M NaOH washes followed by three distilled water washes was routinely performed to remove the silica template from approximately 1 g of material. In Figure 7-20 (a), the intermediate material is presented having been analysed using SEM-EDX spectroscopy. The intermediate material with the silica template still intact shows a ratio of 5 mol Si to 1 mol of Ce. After the standard NaOH wash, samples were routinely analysed. A typical spectrum is presented in Figure 7-20 (b). This showed that the Si ratio fell to an average 0.5 mol for every 1 mol of Ce. A series of washes were then performed to see if the silica removal could be improved. This involved changing five main variables: molarity of NaOH, volume of NaOH solution, temperature, wash sequence and time of wash.

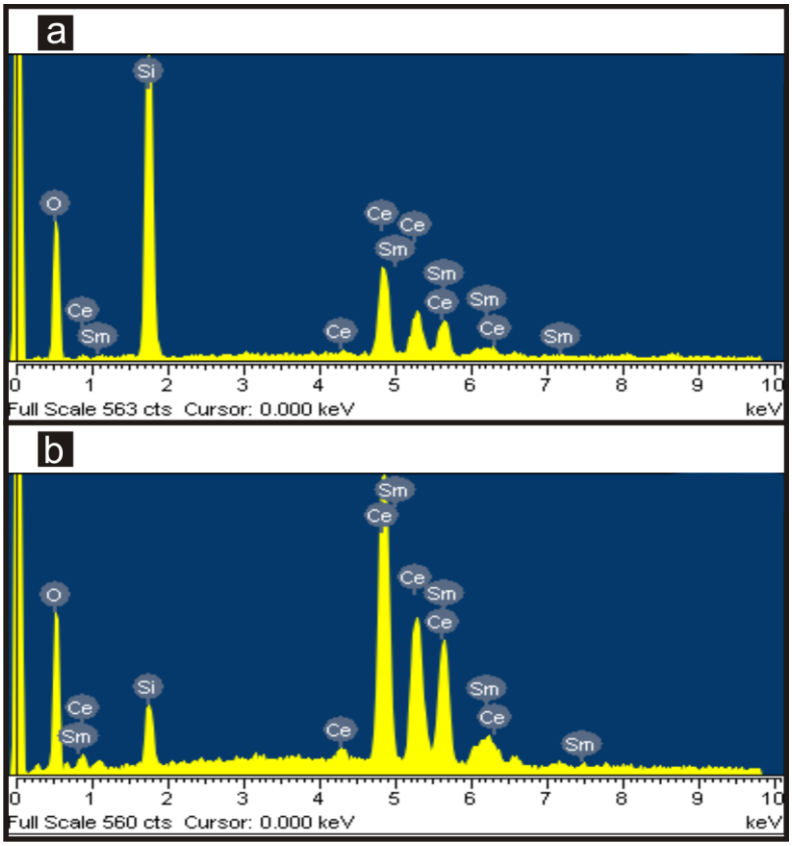

Figure 7-20: SEM-EDX analysis of final products after silica template removal using a standard wash procedure.

Using a matrix approach with the variables listed in Table 7-5, a sequence of tests was performed. The EDX results of these were almost identical to the standard wash procedure indicating that the variables applied had minimal influence.

Table 7-5: Matrix of variables applied in dissolving OMS templates.

Variable	***Value 1***	***Value 2***	***Value 3***
Molarity	0.1 M	1 M	5 M
Volume	40 ml	1000 ml	-
Temperature	20°C	40°C	60°C
Sequence of washes	Alternating between NaOH and H_2O	Sequential NaOH with one final H_2O	-
Time of washes	30 mins	60 mins	24 h

The second strategy was to increase the number of washes to quantify the rate of silica removal and the residual silicon content at each wash stage. This was also compared to a nickel oxide material that was prepared in an identical fashion to the SDC material and is presented in Figure 7-21. The number of washes totalled twelve and consisted of three NaOH washes followed by a distilled water wash, a sequence that was repeated three times through.

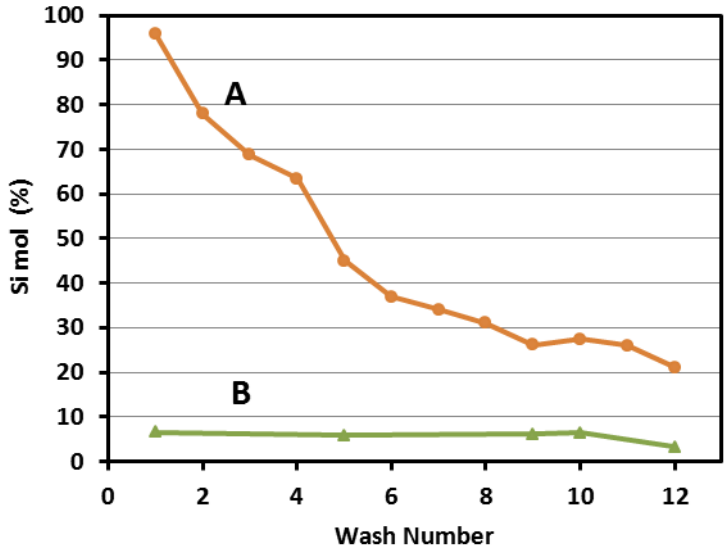

Figure 7-21: The mole % of Silicon after successive NaOH and distilled H_2O washes. Every 4^{th}, 8^{th} and 12^{th} interval is an H_2O wash. (A) normalised against cerium content in an SDC final product, (B) normalised against nickel in a similarly prepared NiO final product.

The data indicates that after one wash, the silicon to cerium is almost in a 1:1 mol ratio whereas the nickel sample has lost almost all the silica to a point where the reported amount is being detected but within the limitations of background noise of the EDX technique. A subsequent protracted series of washes of the SDC product has the silica level fall to a value that is still at 20 mol% of silicon to cerium.

It is also worthy to note that because the procedure involves a lengthy series of washes, it is necessary to perform ultra-centrifugation techniques to recover the finer material. This was found to be essential as washing in distilled water (but not NaOH solution) dispersed the product into solution and could not be recovered by normal centrifugation to the extent that almost all material would be lost after the three distilled water washes.

7.6.2 *Silica Template Removal Using Ammonium Bifluoride.*

It has been well documented by many authors that silica removal is achieved by the use of HF (hydrofluoric acid), the mechanism of the reaction (Eqn. 18) being reported by Prigogine et al[108].

$$SiO_{2(s)} + 4HF_{(aq)} \rightarrow SiF4_{(aq)} + 2H_2O \qquad \textit{Eqn. 18}$$

Given that HF acid has extreme safety implications, ammonium bifluoride ($[NH_4]HF_2$) was tested as an alternative, armed with the knowledge that it can be commonly utilised as a glass etchant. The reaction mechanism of this is presented in Eqn. 19.

$$SiO_{2(s)} + 4\,[NH_4][HF_2]_{(aq)} \rightarrow SiF_{4\,(aq)} + 4\,[NH_4]F_{\,(aq)} + 2\,H_2O \qquad \textit{Eqn. 19}$$

An initial exploratory bulk test showed that SBA-15 silica template dissolved over a period of 72 hours. Given the positive result, it was decided that the standard template dissolution procedure would be amended as described in Table 7-6. This involved an initial step of using NaOH as the bulk silica removal reagent before neutralising with a DI water wash. The ammonium bifluoride was then used at concentrations of 0.5M and 0.01M before a final neutralising wash with DI water. In all instances centrifuge filtering was used to separate the product from reagent with the final product being dried in an oven at 100°C overnight.

The EDX analysis of the retrieved and dried product is presented in Figure 7-22 and shows the material prepared using two different concentrations of the ammonium bifluoride.

Table 7-6: NaOH / Ammonium BiFluoride procedure used to dissolve silica mesoporous templates.

Step 1	***Step 2***	***Step 3***	***Step 4***
1M NaOH	DI water	1M $[NH_4]HF_2$	DI water
1 hour, stirred, RTP	30 mins, stirred, RTP	1 hour, stirred, RTP	30 mins, stirred, RTP
Centrifuge 6mins, 3500 rpm	Centrifuge 6mins, 3500 rpm	Centrifuge 6mins, 3500 rpm	Centrifuge 6mins, 3500 rpm
Repeated 4X	Repeated 3X	No Repeat	Repeated 3X

Figure 7-22 (a) was prepared using 0.01M. The amount of silicon present at K_α 1.739, was found to be unchanged with a small but significant peak attributed to the fluorine K_α 0.677 present. When the concentration of ammonium bifluoride was prepared at 0.5M (Figure 7-22 (b)), the silicon (silica) was removed but this was to the detriment of reducing the oxygen K_α 0.525 peak significantly and contaminating the sample with a high percentage of fluorine. This would indicate that the ammonium bifluoride is effective in removing the silica but only at higher concentrations and the inclusion of fluorine into the sample would be inevitable.

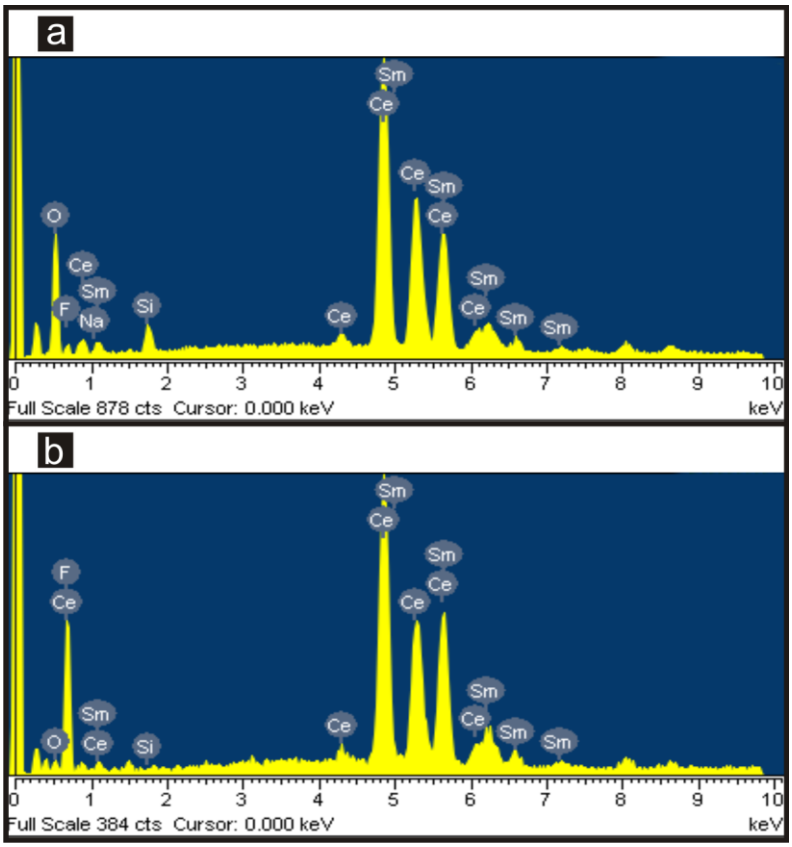

Figure 7-22: EDX analysis of SDC product after washing to remove silica template using (a) 0.01M and (b) 0.5M concentrations of ammonium bifluoride.

7.6.3 *Silica Template Removal Using Tetramethylammonium Hydroxide.*

An initial study of the use of ammonium hydroxide solution as a silica solvent was performed and it was quickly realised that it had little or no effect. However, it has been reported that a chemical alternative, TMAH, does dissolve silicon (and also SiO_2) [109]. It was therefore tested to examine its potential with an explorative experiment. Using concentrated TMAH (Sigma Aldrich, 25 wt% in H_2O) solution the yellow pellet had disintegrated into yellow sludge over a 24 h period. From this initial result, it was decided that an amendment to the original template removal procedure would be attempted. The exact procedure is detailed in a step by step layout in Table 7-7 and again highlights the extreme number of washes that was performed:

Table 7-7: Procedure detailing the steps taken to dissolve silica mesoporous template with a final etch in ammonium bifluoride.

Step 1	**Step 2**	**Step 3**	**Step 4**
1M NaOH	Distilled water	TMAH [25wt.% in H_2O]	Distilled water
1 hour, stirred, @20°C	30 mins, stirred, @20°C	24 hour, stirred, @20°C	30 mins, stirred, @60°C
Centrifuge 6mins, 3500 rpm	Centrifuge 6mins, 3500 rpm	Centrifuge 6mins, 3500 rpm	Ultra-Centrifuge 1h, 40 000 rpm
Repeated 4X	Repeated 3X	No Repeat	Repeated 3X

The EDX analysis of the retrieved and dried product is presented in Figure 7-23. The amount of silicon present at K_α 1.739, was found to be similar to that from a standard series of NaOH washes.

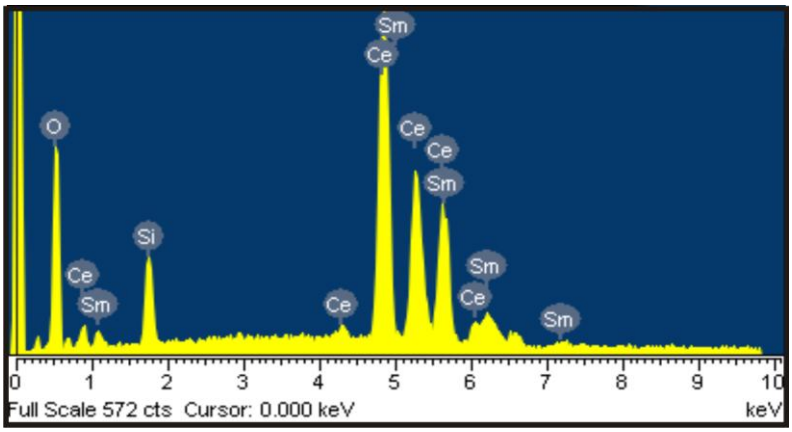

Figure 7-23: EDX analysis of SDC product after washing to remove silica template using TMAH.

7.6.4 *Silica Template Removal Using Catechol.*

As an alternative to using NaOH, catechol was employed to remove silica template. A report by Barnum[110] shows that catechol can be used as an inorganic method of removing silicon (in silica form) as a coordination complex (Figure 7-24) and so a series of experiments were conducted. This required catechol to be used as a saturated solution prepared in ammonium hydroxide. A typical procedure would use 20 g of catechol dissolved into 30 ml of ammonia in a 50 ml centrifuge tube under stirring at a temperature of 90°C. Approximately 1 g of intermediate silica-SDC material would be used and left for 24 h before being retrieved back out of solution. At the end of the dissolving period, catechol could easily crystallise if a significant drop in temperature was experienced. To avoid this, the solution was diluted using distilled water into two separate 50 ml centrifuge tubes and filled approximately to the 40 ml mark without delay. Ultra-centrifuge was used to recover the material after successive washes.

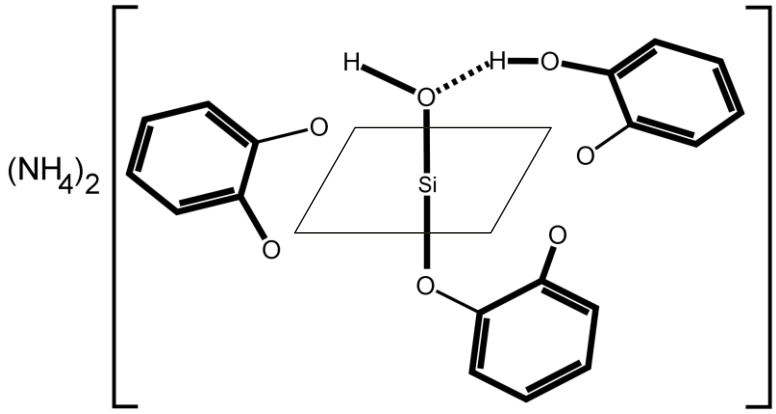

Figure 7-24: The silicon-catechol complex showing the octahedral structure formed from the bidentate ligands of the catechol ions.[110]

The EDX analysis of the retrieved and dried product is presented in Figure 7-25. The amount of silicon present at K_α 1.739, was found to have been reduced in comparison to that from a standard series of NaOH washes. Four samples were prepared using the sequence of three catechol washes followed by a distilled water wash. Two samples were nanocast from SBA-15 and two from KIT-6. The silicon values were 0.10, 0.12, 0.16 and 0.14 mol for every 1 mol of Ce. Each of these samples was analysed using gas physisorption and TEM and found to be in agreement with samples prepared using NaOH.

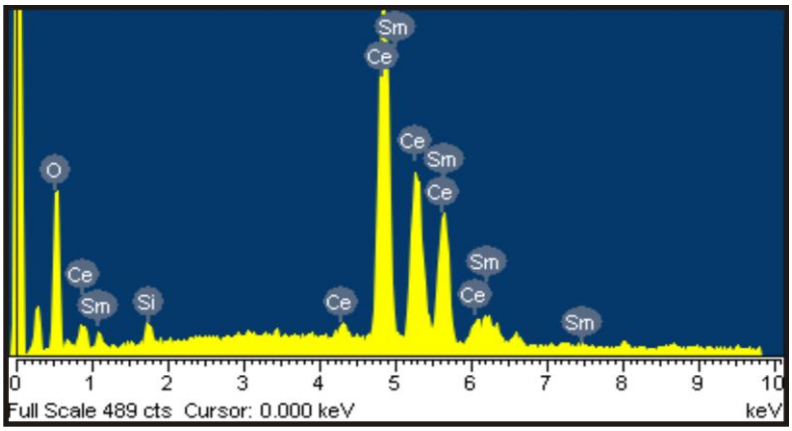

Figure 7-25: EDX analysis of SDC product after washing to remove silica template using catechol.

7.6.5 *Discussion*

One hypothesis for the silica proving to be difficult in removal is that the energy required to break the covalent bond of the geminal Si-O-Ce species is almost identical. For this reason when a chemical such as the ammonium bifluoride has a strong affinity with the silicon, it is at the expense of the SDC structure, replacing not only the silicon but the oxygen with fluorine. The weaker TMAH and NaOH are unable to cleave the silicon from the surface of the SDC material but capable in removing bulk silica following the mechanism discussed in ***Eqn. 17***. As catechol is removing the silica through complexing with the silicon, it may be more efficient in its removal but still unable to remove surface silanols. When compared with the bond energy of nickel, it appears that less energy would be required to cleave the nickel – oxygen covalent bond thereby removing the silica (Si-O) from the Si-O-Ni species. This may be a factor in why the silica removal from the nickel was found to be more efficient. The bond dissociation energy for each of the diatomic molecules are reported in Table 7-8.

Table 7-8: Bond dissociation energies of selected diatomic molecules.

Molecule	**BDE** (kJ mol^{-1})	**Uncertainty**
Ce-O	790	Not reported
Si-O	799.6	± 13.4
Ni-O	366	± 30.0

The use of EDX spectroscopy was able to provide semi-quantitative results on the residual value of silicon and a qualitative assessment in the effectiveness of the chemical ability to remove template. The instrumental resolution of the peaks of interest has started to become a factor in determining absolute silicon content values when using catechol. While silica still unequivocally exists in the sample, any future improvements would have to be analysed using a different technique such as ICP-MS.

As a method of removing silica, the use of catechol would be a limited technique due to the high amount of chemical used which for three washes was 60 g catechol and 90 ml ammonia solution. Retrieval of final products also requires the use of an ultra-centrifuge.

7.7 Summary

A series of SDC structures prepared from the nanocast of SBA-15, KIT-6 and FDU-12 have been produced using a vacuum impregnation (VI) technique. The VI technique was adapted to allow for flexibility of impregnating template in either powder or pellet form. The SDC intermediate and final product materials have primarily been analysed using gas physisorption, low angle XRD and TEM. A sample preparation method using an ultra-microtome to prepare SBA-15-IT and FP materials was found to be beneficial and allowed clear imaging particularly of the impregnated material *in-situ* of the SBA-15 pores. Data analysis showed that SDC prepared from SBA-15 template was synthesised in an expected reverse structure with high physical characteristics of SSA and mesopore volume and in a crystalline mesoporous framework. The observed PSD change from template to final product was in agreement with changing to the inverse structure. Formation of the SDC material from KIT-6 and FDU-12 proved to be more difficult to characterise as TEM imaging was inconclusive although low angle SAXS and gas physisorption data indicates material with repeat mesopore ordering. A solvo-thermal effect was also observed and would occur

if the pellet was calcined with residual ethanol present. Despite several strategies to remove remnant silica from the SDC product, it was found that it remained stubbornly high. As silicon and ceria have similar chemical bond energies, the cleavage of silicon from the cerium structure appears to be only possible at the expense of destroying the SDC product as observed when using ammonium bifluoride. When catechol was used, the silicon content was reduced significantly when compared to NaOH washes but still remains at unacceptable levels. A strategy of using functionalised and ultra-large pore silica templates did not help facilitate the removal of silica. Apart from the extra resources required to make these materials, it was found that the nanocast SDC was comprised in regards quality of structure and yield. For this reason a different strategy based on avoiding silica as a template would be considered.

Chapter 8

Preparation of Carbon Templates

8.1 Introduction

The purpose of preparing carbon based ordered mesoporous templates was primarily to circumvent the problems with incomplete removal and associated contamination of the nanocast products by silica that can be detrimental in the final application of nanocast mixed metal oxides. Despite the perceived advantages and desire to prepare a carbon template, a single step synthesis has historically proven to be difficult until recently.

A first method centred on nanocasting mesoporous carbons from a hard silica template with the carbon template recovered with the inverse structure to the silica template. The series – designated CMK[111] – was proven to be industrially unfavourable, requiring preparation of silica template, nanocasting from a carbon precursor and subsequent removal of this original template with obvious disadvantages of time, cost, materials, quality and quantity of ordered mesoporous carbon (OMC) template. A long desired strategy based on self-assembly as is used in the preparation of silica templates was eventually realised and first published in 2006[112]. This has allowed the silicon bi-continuous pore structured KIT-6 with space group *Ia3d* to be replicated as the carbon analogue FDU-14; the silica with hexagonal mesopore structure, SBA-15, with space group *p6mm,* to be synthesised as the carbon analogue, FDU-15, and the cubic silica SBA-16 with space group *Im3m* to be synthesised as the carbon analogue, FDU-16. The soft template methods follow a four step process, simplified as (1): low weight polymer formation (normally a resol polymer); (2): thermo-polymerisation step to crosslink the resol polymer in a framework around a structure directing agent (normally a tri-block copolymer); (3): removal of the structure directing agent; and (4): carbonisation (or conversion from ordered mesoporous polymer (OMP) to OMC).

8.2 Preparation

The initial attempts to directly create an ordered mesoporous carbon framework centred on the silica analogue strategy of using self-assembling tri-block copolymers and surrounding these with organic cyclic compounds that could crosslink in a thermo-polymerisation

reaction. However, early attempts struggled to control the structural integrity before and during the crosslinking step as there is a reliance on weak hydrogen bonds to maintain the resol in proximity around the tri-block copolymer, a balance that is easily disrupted. The judicious use of resol polymer has been a major factor in the realisation of OMC materials due in part to its low molecular weight (hence limited stereochemical restriction in its alignment around micelles)[113], large number of hydroxyl groups which allow hydrogen bond interaction[114] and tri-substituted benzene ring structures that can thermo-polymerise forming a strong covalently bonded framework[115]. The formation of resol and the interaction with the triblock copolymer has been attempted in several ways and this is often the main difference between attempted methods of synthesis. It has also been reported that the resol polymer which forms the basis of the framework can be formed by selective consideration of different reagents. The first reported attempts at producing carbon templates relied on a resol formation using formaldehyde and phenol as the starting reagents but it has since been shown that reagent selection from the arenol series has a direct effect on the rate of polymerisation such that rate of polymerisation increases from phenol < resorcinol < phloroglucinol[116] . The phenol has been reported to give desired (resol) polymers in the required range of M_W=500 – 5000 g mol^{-1} [117] but the rate at which the reaction proceeds is rather slow often taking several days to complete. Using resorcinol has been shown to greatly increase the speed and has found favour in most of the synthesis techniques that are now being reported, the reaction rate appearing to be optimal [112]. The formation of low weight polymer is a catalytic reaction and apart from the choice of reagents, the condition under which the reaction proceeds is also affected by pH and temperature[118]. The pH can be chosen to be in the acidic or basic range with each offering a distinctly different route to framework formation. If acidic conditions are chosen then a novolac polymer is formed whereas the basic route will form resol polymers. Each polymer can successfully crosslink to form an OMP framework, however the properties of the novolac to those of the resol are quite distinct and would have different synthesis requirements. For example, resol unlike novolac is soluble in both organic solvents and water which often results in an easier synthesis procedure[112].

After formation of the low weight polymer, the crosslinking of these units into a three dimensional network is the next step. If an ordered mesoporous framework is to be realised, it needs to form around a structure-directing agent. Again, pH is an important variable. The resorcinol-formaldehyde (RF) resol forms linear polymeric networks in an acidic medium with the structure more susceptible to collapse during carbonisation, the use

of a basic medium increase the crosslinking of resol resulting in a more stable structure after calcination[119]. In this regard, there is no difference from making the OMS analogue and the same factors apply. Critical micelle concentration, critical temperature and choice of directing agent between Pluronic™ P123 and F127 must be considered in order to direct the material into the hexagonal *p6mm*, cubic *Ia3d* or cubic *Im3m* choice of structures. Having selected the directing agent and generated the self-assembled amphiphile solution with desired structure, for example, a 2-D hexagonal arrangement of rods, cross polymerisation of the resol can occur. However, this is again within subject to variation caused by the choice of critical conditions. It is interesting to note that the materials produced in silica tend to have a larger pore size, pore volume and specific surface area than the carbon equivalents despite their being structurally equivalent (Table 8-1).

Table 8-1: A comparison between silica and carbon based frameworks of identical space group structures synthesised at calcination temperatures of 500°C.

Framework Material	**Template**	**Space Group**	**Pore Description**	**Pore Size (nm)**	**Total Specific Pore Volume (cm^3g^{-1})**	**Specific Surface Area (m^2g^{-1})**
Silica	SBA -15	*p6mm*	2-D Hex	~ 9	~ 1.2	~ 800
Carbon	FDU-15	*p6mm*	2-D Hex	~ 4	~ 0.4	~ 670
Silica	Kit -6	*Ia3d*	3-D Hex	~ 9	~ 1.0	~ 800
Carbon	FDU-14	*Ia3d*	3-D Hex	~ 5	~ 0.4	~ 660
Silica[39]	SBA-16	*Im3m*	3D Cubic	~ 5	~ 0.5	~ 750
Carbon	FDU-16	*Im3m*	3D Cubic	~ 3	~ 0.3	~ 750

Recent reports have seen a steady simplification in synthesis procedures and a careful selection of these are reported below. Although an exhaustive review has not been attempted, the majority of methods have been considered within the limits of equipment availability, time of synthesis and reports of further successful applications of the template materials. This chapter reports the preparation of viable OMC structures, the investigation of their potential suitability for nanocasting and evaluation of the fidelity and yield of nanocast product prepared. A full listing of all known procedures in synthesising FDU-14, 15 and 16 and related structures with associated data is included for comparison in Appendix 3.

8.3 Results

8.3.1 *FDU-14*

The results presented below represent material synthesised using method FDU-14B which was an amendment to the FDU-14A method with the main difference being synthesis time as outlined in section 4.4.1. Calcination temperatures of 350 and 500°C were used and reported as FDU-14-350 and FDU-14-500, respectively. Calcination atmosphere (section 4.7.5) of nitrogen and controlled 2 % oxygen was used. These are reported as FDU-14-350 and FDU-14-350-O2 respectively.

The isotherm observed for FDU-14-350-O2 in Figure 8-1(a) is typical of a type I profile with no hysteresis present. There is strong gas uptake and this is due to the high degree of microporosity as indicated by the large adsorption at low relative pressure. The pore size distribution for the FDU-14-350-O2 shows a large feature growing from 2 nm to lower values and is at the lower measurement limit of the instrument (Figure 8-1(b)). Total mesopore volume ($\mathbf{V}_{meso}$) of 0.04 cm^3g^{-1}, micropore volume ($\mathbf{V}_{micro}$) of 0.11 cm^3g^{-1} and specific surface area ($\mathbf{S}_{BET}$) of 422 m^2g^{-1} were recorded. FDU-14-350 which is the inert atmosphere variant, has a similar isotherm but without microporosity. Despite the low gas uptake for FDU-14-350, a specific pore size distribution (PSD) maximum at 3 nm is observed. Total mesopore volume ($\mathbf{V}_{meso}$) of 0.02 cm^3g^{-1} and specific surface area ($\mathbf{S}_{BET}$) of 46 m^2g^{-1} were recorded. There was no microporosity present with ($\mathbf{V}_{micro}$) reported as being nil. A similar picture is revealed Figure 8-1 (c and d) for the FDU-14-500-O2 and FDU-14-500 in regards isotherm shape and PSD. The isotherm observed for FDU-14-500-O2 in is typical of a type I profile with no hysteresis present. There is strong gas uptake and this is due to the high degree of microporosity as seen by the high adsorption at low relative pressure. In the PSD for FDU-14-500-O2, a large peak is observed at below 2 nm and is at the limit of what can be achieved by the instrument. A total mesopore volume ($\mathbf{V}_{meso}$) 0.07 cm^3g^{-1}, micropore volume ($\mathbf{V}_{micro}$) 0.16 cm^3g^{-1} and specific surface area ($\mathbf{S}_{BET}$) 522 m^2g^{-1} were recorded. FDU-14-500 which is the inert atmosphere variation, has a similar isotherm profile but without the microporosity aspect. Despite the low uptake for FDU-14-500, a PSD maximised at 2 nm is observed although this is at the lower measurement limit of the instrument. A total mesopore volume ($\mathbf{V}_{meso}$) of 0.02 cm^3g^{-1}, micropore volume ($\mathbf{V}_{micro}$) of 0.02 cm^3g^{-1} and specific surface area ($\mathbf{S}_{BET}$) of 109 m^2g^{-1} were recorded.

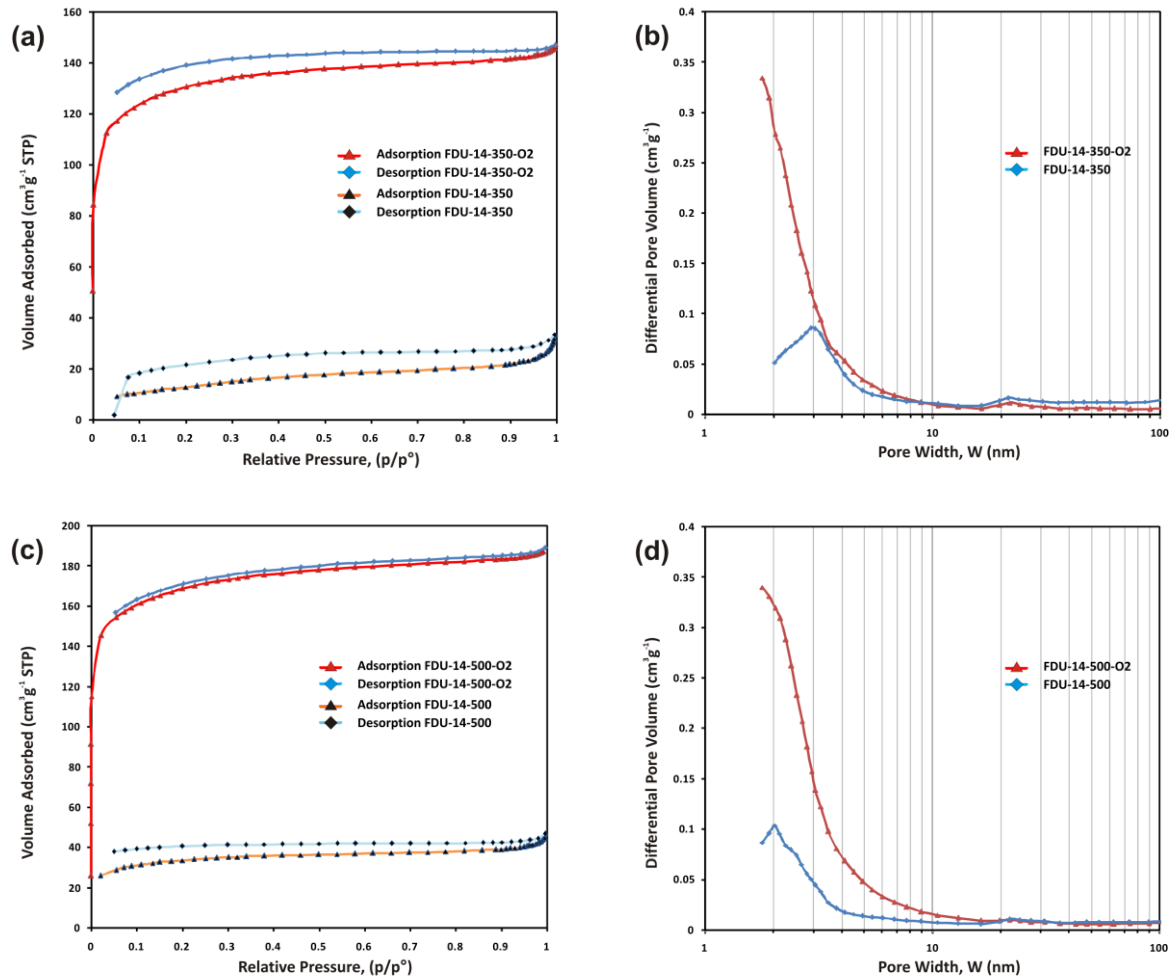

Figure 8-1: Nitrogen physisorption isotherms (a) and specific pore size distributions (b) for FDU-14-350-O2 and FDU-14-350; Nitrogen physisorption isotherms (c) and specific pore size distributions (d) for FDU-14-500-O2 and FDU-14-500.

Table 8-2 summarises the gas physisorption data obtained using the BET (specific surface area), t-plot (micropore volume) and BJH (mesopore size distribution and volume) methods.

Table 8-2. Gas physisorption data for FDU-14 template: Values for specific pore size distribution (w_{BJH}), specific surface area (S_{BET}), mesopore volume (V_{meso}) and micropore volume (V_{micro}).

Sample	w_{BJH} (nm)	S_{BET} (m^2g^{-1})	V_{meso} (cm^3g^{-1})	V_{micro} (cm^3g^{-1})
FDU-14-350	3.0	46	0.02	Nil
FDU-14-350-O2	~1.5	422	0.04	0.11
FDU-14-500	~2.0	109	0.02	0.02
FDU-14-500-O2	~1.5	552	0.07	0.16

Figure 8-2 presents patterns of low angle XRD data with a background subtraction included to help better resolve the diffraction peaks. Analysis of the FDU-14-350, Table 8-3, pattern shows a material with one distinct peak of the expected bi-continuous cubic structure observable with a ***d***-spacing of 8.37 nm and assigned a 211 index. The unit cell parameter of 20.5 nm was calculated using the formula in Appendix 2, Eqn. 20. A secondary weak peak that has been attributed to a weak 110 reflection peak is observed at low 2θ angle at 0.578°. Using a ***d***-spacing ratio of $\sqrt{6}$, $\sqrt{14}$ ($\sqrt{16}$), $\sqrt{20}$ ($\sqrt{18}$); the main peak of FDU-14-350-O2, Table 8-4, was resolved and indexed as 211. However the broad nature of the subsequent peaks limits the assignation as either 321 or 400 and 332 or 420 reflections. A weak 110 peak was also observed at 0.658° and attributed to a 110 reflection. The associated ***d***-spacings for the three reflections have been calculated as 7.13, 4.47, and 3.84 nm and relate to a unit cell parameter of 17.5 nm using the formula in Appendix 2, Eqn. 20. The low angle XRD data in Figure 8-2(c) and (d) for FDU-14-500 displays no discernible diffraction peaks, while the FDU-14-500-O2, Table 8-5, has one small diffraction peak at a ***d***-spacing value of 14.34 and again assigned to a weak 110 reflection.

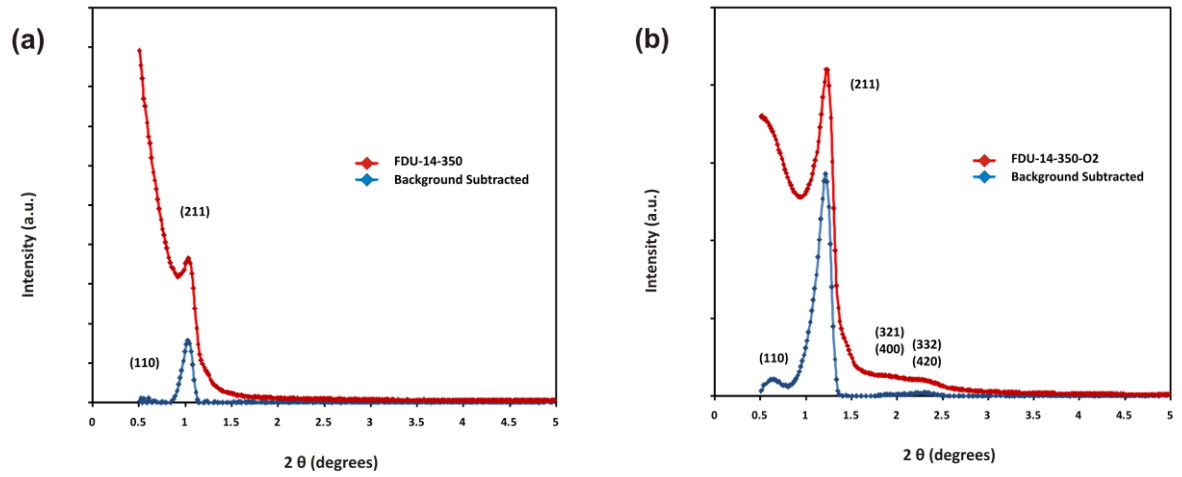

Table 8-3: Calculated d-spacing from 2θ values for FDU-14-350

2θ (°)	**Indices**	***d*-Spacing (nm)**
0.578	(110)	15.28
1.054	(211)	8.37

Table 8-4: Calculated d-spacing from 2θ values for FDU-14-350-O2

2θ (°)	Indices	*d*-Spacing (nm)
0.658	(110)	13.40
1.238	(211)	7.13
1.976	(321) (400)	4.47
2.300	(332) (420)	3.84

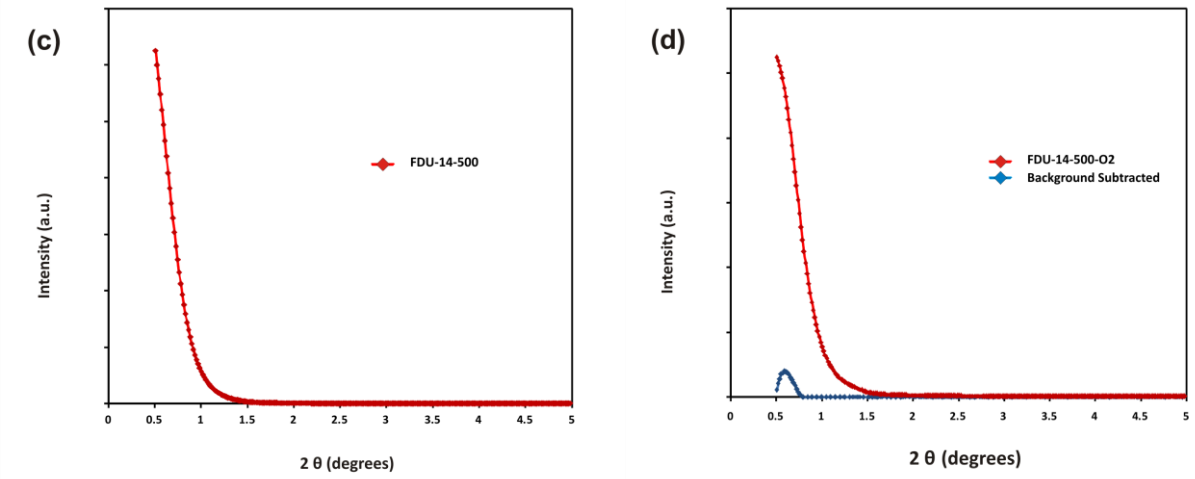

Figure 8-2: low angle XRD patterns for: (a) FDU-14-350, (b) FDU-14-350-O2 (c) FDU-14-500 (d) FDU-14-500-O2.

Table 8-5: Calculated d-spacing from 2θ values for FDU-14-500-O2

2θ (°)	Indices	*d*-Spacing (nm)
0.6154	(110)	14.34

The TEM images presented are for FDU-14-350-O2 material. No observable structure was found for the other three materials. The image in Figure 8-3 (a) is representative of the majority of the sample and does not show any particular ordering on first observation despite being at a relatively high magnification. Image (b) highlights a portion of the material that is not very well defined in respect to overall ordering although some parallel pore formation is clearly visible in the middle portion of the viewed image. The pore to pore width is measured at 3.1 nm as determined from the included digital diffraction pattern (DDP). Image (c) does not appear to show any structuring on first viewing; however

interplanar spacings were obtained from the DDPs, it was only after adjusting the material out of focus and changing the contrast – image (d)- that evidence of an ordered structure became visible and a further DDP was taken to corroborate this.

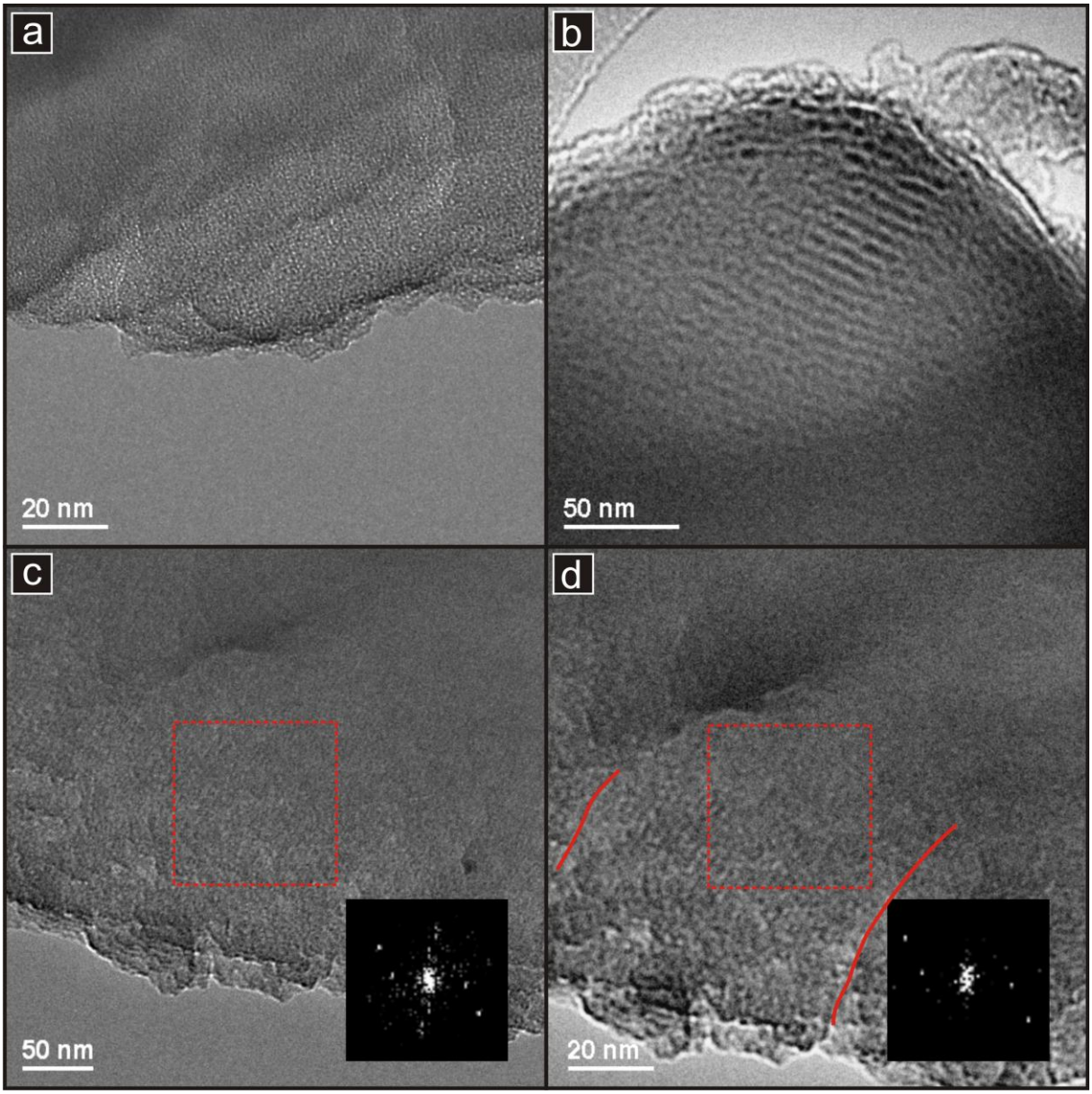

Figure 8-3: TEM images of FDU-14-350-O2 : (a) representative image of the material, (b) observation of some parallel channel formation, (c) barely visible layers of ordered parallel structures, (d) A repeat image of (c) but with slightly different focus highlighting the difference in observation The red lines follow adjacent channels and indicate the boundary between which an area of parallel pore structures can be viewed. DDPs obtained from the red boxes as indicated (c) and (d) as inset.

A summary of the data derived from the analytical techniques is presented in Table 8-6.

Table 8-6. FDU-14 template: Values for unit cell parameters (***$a_0$1 – $a_0$3***), interplanar spacings (***d***), pore width (***w***) and pore wall thickness (***t***) obtained using the method indicated (BJH, SAXS, TEM). All values are in nm. Values of ***a_o*** are calculated from the corresponding ***d_{SAXS}*** value. Miller indices are given in italics below each value of ***d***.

Sample	w_{BJH}	$d_{SAXS}0$	$d_{SAXS}1$	$d_{SAXS}2$	$d_{SAXS}3$	$a_0 1$	$a_0 2$	$a_0 3$	d_{TEM}	w_{TEM}	t_{TEM}
FDU-14-350	3.0	15.3 *(110)*	8.4 *(211)*	-	-	20.6	-	-	-	-	-
FDU-14-350-O2	~1.5	13.4 *(110)*	7.1 *(211)*	4.5 *(321)* *(400)*	3.8 *(420)* *(332)*	17.4 *(211)*	16.8 *(321)* 18.0 *(400)*	17.0 *(420)* 17.8 *(332)*	3.4	1.5	2.5
FDU-14-500	~2.0	-	-	-	-	-	-	-	-	-	-
FDU-14-500-O2	~1.5	14.3	-	-	-	-	-	-	-	-	-

8.3.2 *FDU-15*

The synthesis of FDU-15 formed the majority of the carbon template strategy for nanocasting. As a method of producing ordered mesoporous templates it was found that the manufacture of FDU-15 was far simpler than the other two structural alternatives (FDU-14 and 16), due in part to the simpler control of micelle phase and therefore greater range of control variables such as temperature and concentration. This respective ease of synthesis being reflected by the greater number of published methods. As there were several reported methods of production, each method was attempted in turn in order to discover information on the practicability in generating a final template product. The methods outlined in section 4.4 listed three main methods each of which was based on a slightly different approach, namely: aqueous one step hydrothermal (A), evaporation induced self-assembly -(EISA)- (B) and two-phase separation (C). In regards practicality it was found that method A and C were the easiest to perform for several reasons: the equipment required was simple, the time factor was much reduced and the yield was better particularly for method (C). While method (A) has been reported as being able to multiply the reactant quantities to increase yield, the difficulty would lie in glassware and associated oil baths etc. such that any meaningful increase in size would prove to be impracticable. As

several grams of template was required as a working amount, Method C was found to be resolute to scale increases while able to maintain a product that was consistent in quality within and across batches. Due to the elemental oxygen content in the framework being sufficient to allow pore formation during the calcination of FDU-15 [76], material was produced in an inert atmosphere devoid of oxygen. Unlike FDU-14 and FDU-16, the use of oxygen in the gas stream was avoided given that it is detrimental to yield. Initial research focussed on the reproducibility of the published methods (A and B approaches), for this reason material was prepared using calcination temperatures of 350 and 500°C. Having established these methods, Method C was attempted to further improve the efficiency and ease of manufacture while at the same time a calcination temperature of 400°C was chosen to reflect the requirements of the nanocasting procedure.

The isotherm observed for FDU-15-350A in Figure 8-4(a) is typical of a type II profile with an H2 hysteresis. There is gas uptake at low relative pressure and indicates a degree of microporosity. Observation of the pore size distribution (Figure 8-4(b)) indicates the majority of the pores to be within an average size of 4.8 nm ±1.5 nm. A total mesopore volume ($\mathbf{V}_{meso}$) 0.32 cm^3g^{-1}, micropore volume ($\mathbf{V}_{micro}$) 0.05 cm^3g^{-1} and specific surface area ($\mathbf{S}_{BET}$) 425 m^2g^{-1} were recorded. FDU-15-350B has a much reduced isotherm profile with no microporosity observed although a partial hysteresis effect is evident. Despite the low gas uptake for FDU-15-350B, a similar pore size distribution maximised at 4.5 nm is observed although the pore volume is much reduced. A total mesopore volume ($\mathbf{V}_{meso}$) 0.07 cm^3g^{-1} and specific surface area ($\mathbf{S}_{BET}$) 105 m^2g^{-1} were recorded. There was no meaningful microporosity present with ($\mathbf{V}_{micro}$) reported as being nil cm^3g^{-1}.

The isotherm observed for FDU-15-500A in Figure 8-4(c) is typical of a type II profile with an H2 hysteresis. There is gas uptake at low relative pressure and indicates a degree of microporosity. Observation of the pore size distribution (Figure 8-4(b)) indicates the majority of the pores to be within an average size of 4.8 nm ±1.5 nm. A total mesopore volume ($\mathbf{V}_{meso}$) 0.32 cm^3g^{-1}, micropore volume ($\mathbf{V}_{micro}$) 0.06 cm^3g^{-1} and specific surface area ($\mathbf{S}_{BET}$) 451 m^2g^{-1} were recorded. FDU-15-500B has a similar isotherm profile typical of a type II profile with an H2 hysteresis. At the higher partial pressure range, a larger volume of gas has been adsorbed. This is also reflected in the PSD in Figure 8-4(d) indicating that larger meso and macropores exist. There is gas uptake at low relative pressure and indicates a degree of microporosity. Despite the observation of micropores and a broad range of

mesopore sizes, a grouping of mesopores maximised at 5.4 nm ±1.5 nm is in evidence. A total mesopore volume ($\mathbf{V}_{meso}$) 0.51 cm^3g^{-1}, micropore volume ($\mathbf{V}_{micro}$) 0.07 cm^3g^{-1} and specific surface area ($\mathbf{S}_{BET}$) 459 m^2g^{-1} were recorded.

The isotherm observed for FDU-15-400C in Figure 8-4(e) is typical of a type IV profile with an H2 hysteresis. There is gas uptake at low relative pressure and indicates a degree of microporosity. Observation of the pore size distribution (Figure 8-4(f)) indicates the majority of the pores to be within an average size of 7.8 nm ±1.5 nm. A total mesopore volume ($\mathbf{V}_{meso}$) 0.54 cm^3g^{-1}, micropore volume ($\mathbf{V}_{micro}$) 0.04 cm^3g^{-1} and specific surface area ($\mathbf{S}_{BET}$) 519 m^2g^{-1} were recorded.

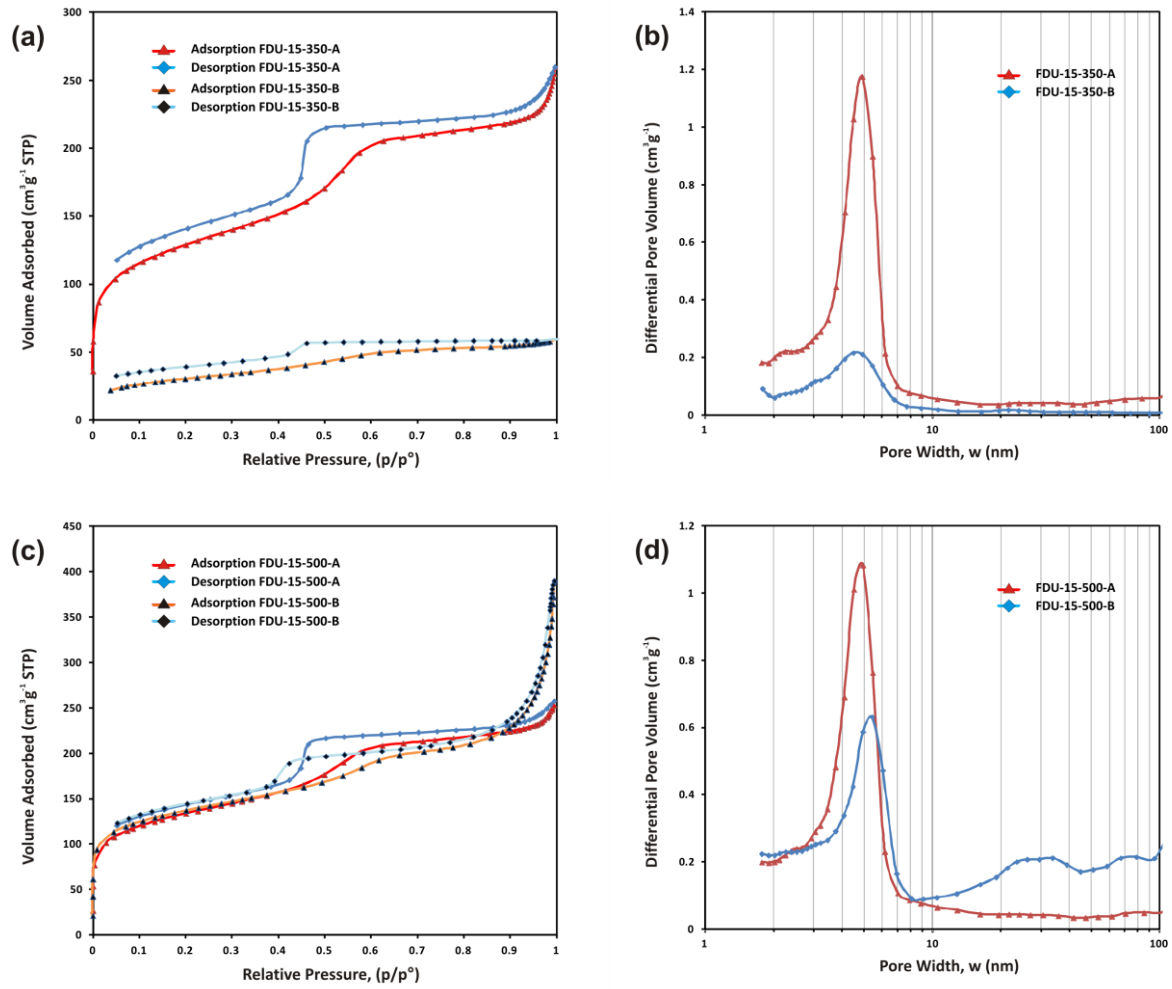

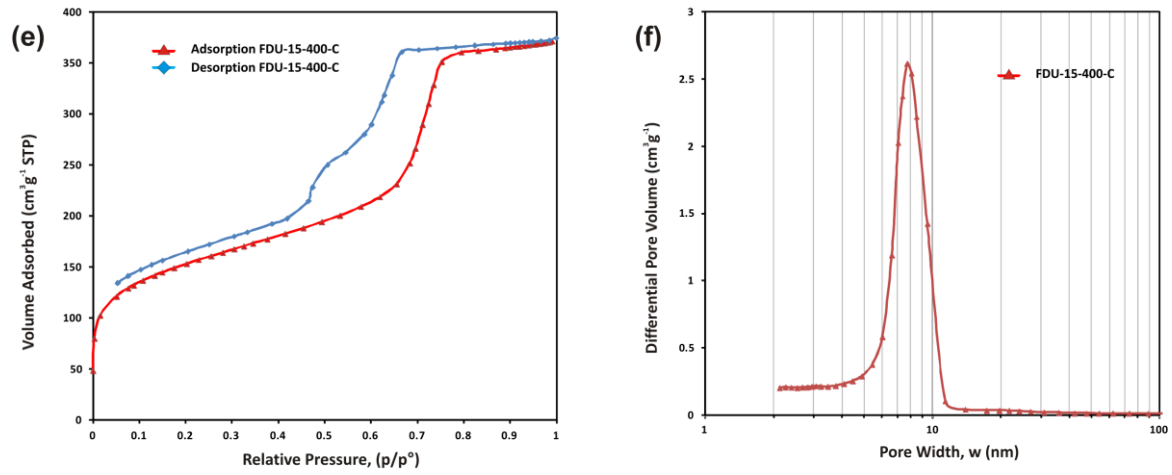

Figure 8-4: Nitrogen physisorption isotherms (a, c, e) and specific pore size distributions (b, d, f) for FDU-15; materials prepared as indicated: (a, b) by Methods A and B with calcinations at 350°C; (c, d) by Methods A and B with calcinations at 500°C; (e ,f) by Method C with calcinations at 400°C.

Table 8-7 summarises the gas physisorption data obtained using the BET (specific surface area), t-plot (microporosity volume) and BJH (mesopore size distribution and volume) methods.

Table 8-7. Gas physisorption data for FDU-15 template: Values for specific pore size distribution (w_{BJH}), specific surface area (S_{BET}), mesopore volume (V_{meso}) and micropore volume (V_{micro}).

Sample	w_{BJH} (nm)	S_{BET} (m^2g^{-1})	V_{meso} (cm^3g^{-1})	V_{micro} (cm^3g^{-1})
FDU-15-350A	4.8	425	0.32	0.05
FDU-15-350B	4.5	105	0.07	nil
FDU-15-500A	4.8	451	0.32	0.06
FDU-15-500B	5.4	459	0.51	0.07
FDU-15-400C	7.8	519	0.54	0.04

Figure 8-5 and Figure 8-6 present patterns of low angle XRD data with background subtractions included to help better resolve the diffraction peaks. The peaks have been indexed according to a 2-D hexagonal structure using a ***d***-spacing ratio of $\sqrt{1}$, $\sqrt{2}$, $\sqrt{5}$ and assigned (100), (110) and (210) indices respectively. Analysis of Figure 8-5(a), Table 8-8, FDU-15-350A pattern shows a material with one distinct peak of the expected 2-D hexagonal structure observable with a ***d***-spacing of 10.92 nm and assigned a 100 index. A weak secondary peak a ***d***-spacing of 10.92 nm has been assigned a 110 index. The unit cell parameter of 12.61 nm was calculated using the formula in Appendix 2, Eqn. 21a.

Figure 8-5(b), Table 8-9, FDU-15-350B pattern shows a material with one weak peak at a ***d***-spacing of 14.02 nm and assigned a 100 index. The unit cell parameter of 16.18 nm was calculated using the formula in Appendix 2, Eqn. 21b. Figure 8-5(c), Table 8-10, FDU-15-500A pattern shows a material with one distinct peak of the expected 2-d hexagonal structure observable with a ***d***-spacing of 11.07 nm and assigned a 100 index. A second peak with ***d***-spacing of 5.76 nm and third peak with ***d***-spacing of 4.35 nm have been assigned a 110 and 210 indices respectively. The unit cell parameter of 12.78 nm was calculated using the formula in Appendix 2, Eqn. 21. Figure 8-5(d), Table 8-11, FDU-15-500B pattern shows a material with one weak peak at a ***d***-spacing of 12.61 nm and assigned a 100 index. The unit cell parameter of 14.56 nm was calculated using the formula in Appendix 2, Eqn. 21c.

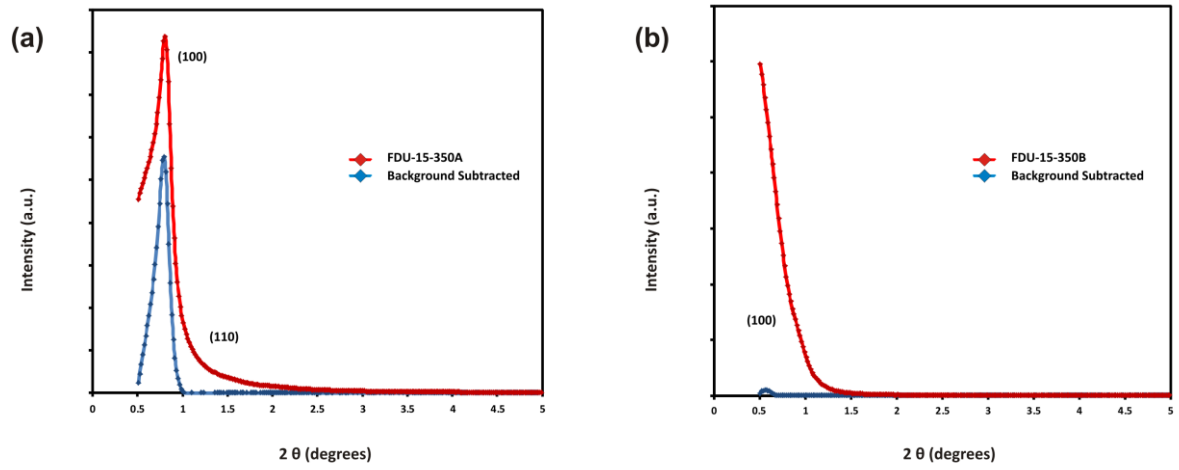

Table 8-8: Calculated d-spacing from 2θ values for FDU-15-350A

2θ (°)	**Indices**	***d*-Spacing (nm)**
0.809	(100)	10.92
1.556	(110)	5.67

Table 8-9: Calculated d-spacing from 2θ values for FDU-15-350B

2θ (°)	**Indices**	***d*-Spacing (nm)**
0.630	(100)	14.02

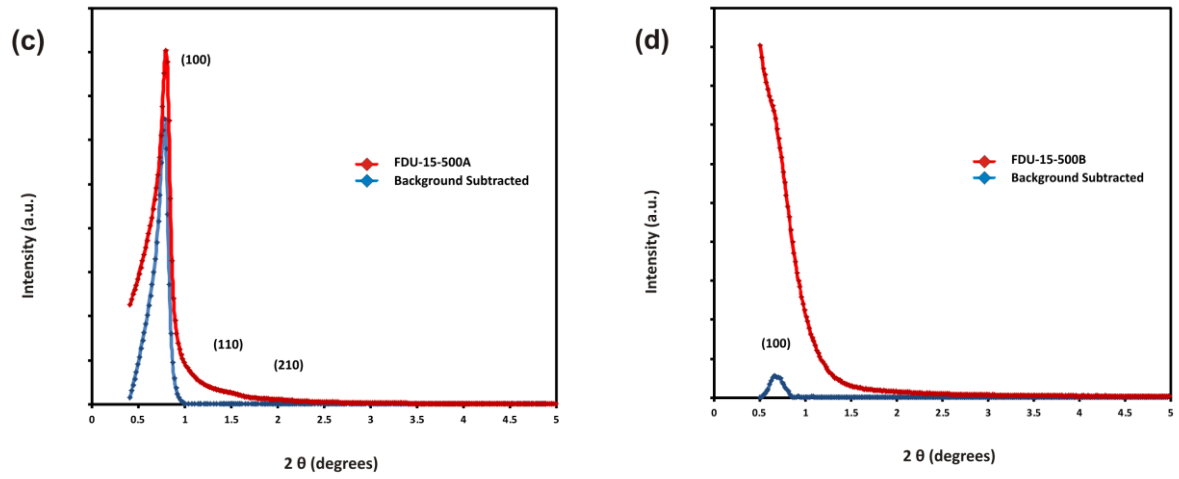

Figure 8-5: low angle XRD patterns (a) FDU-15-350A, (b) FDU-15-350B (c) FDU-15-500A (d) FDU-15-500B.

Table 8-10: Calculated d-spacing from 2θ values for FDU-15-500A

2θ (°)	**Indices**	***d*-Spacing (nm)**
0.798	(100)	11.07
1.532	(110)	5.76
2.030	(210)	4.35

Table 8-11: Calculated d-spacing from 2θ values for FDU-15-500B

2θ (°)	**Indices**	***d*-Spacing (nm)**
0.700	(110)	12.61

Analysis of Figure 8-6(a),Table 8-12, FDU-15-400C-Pellet pattern shows a material with one distinct peak of the expected 2-d hexagonal structure observable with a ***d***-spacing of 10.61 nm and assigned a 100 index. A secondary peak a ***d***-spacing of 6.20 nm has been assigned a 110 index. The unit cell parameter of 11.73 nm was calculated using the formula in Eqn. 21. Figure 8-6(b), Table 8-13, FDU-15-400C-Powder pattern shows a material with one distinct peak of the expected 2-d hexagonal structure observable with a ***d***-spacing of 10.16 nm and assigned a 100 index. A secondary peak a ***d***-spacing of 5.93 nm has been assigned a 110 index. The unit cell parameter of 12.25 nm was calculated using the formula in Eqn. 21.

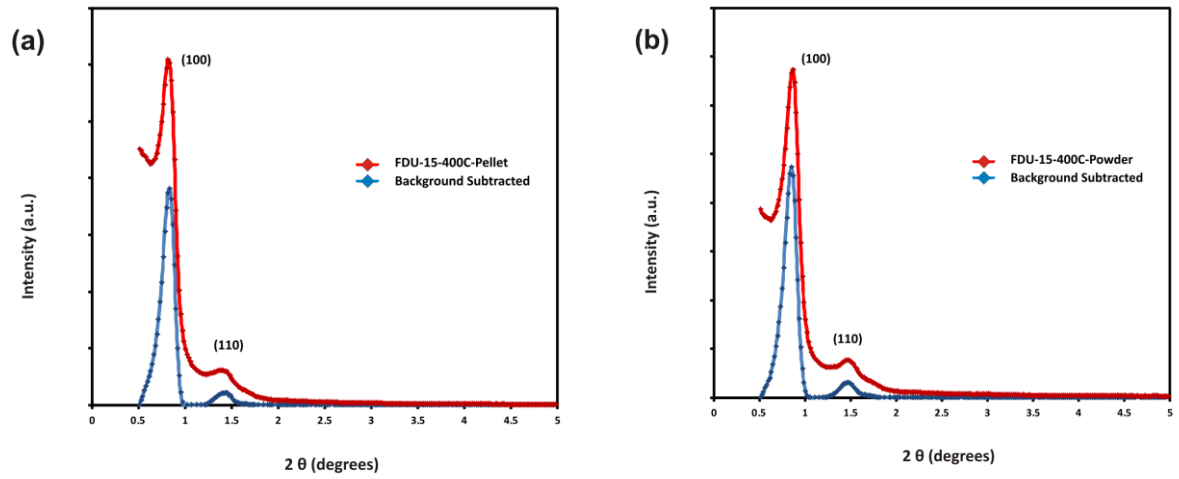

Figure 8-6: low angle XRD patterns (a) FDU-15-400C as pellet, (b) FDU-15-400C as powder

Table 8-12: Calculated d-spacing from 2θ values for FDU-15-400C Pellet.

2θ (°)	Indices	*d*-Spacing (nm)
0.832	(100)	10.61
1.425	(110)	6.20

Table 8-13: Calculated d-spacing from 2θ values for FDU-15-400C Powder.

2θ (°)	Indices	*d*-Spacing (nm)
0.869	(100)	10.16
1.489	(110)	5.93

TEM images in Figure 8-7 for FDU-15-350A show that the material is consistent with a 2-D hexagonal structure. Figure 8-7(a) is a low magnification of the particle with classic long curving channels that is often observed in the SBA-15 equivalent. The Image (b) is an end-on view of the channels and highlights the hexagonal arrangement of pores. The parallel formation of the channels as shown in image (c) extends into a longer range (image (a)). The repetitive and consistent pore-wall size of the channels are visible with the pore to pore width being measured at 3.1 nm as determined from the included digital diffraction pattern (DDP). The image (d) is a higher magnification of the pore structure. The order of the pores, their relative size, spacing and the wall thickness are all clearly visible. Interplanar spacings were obtained from the inset DDP and values for the pore and a wall thickness in the structure was measured.

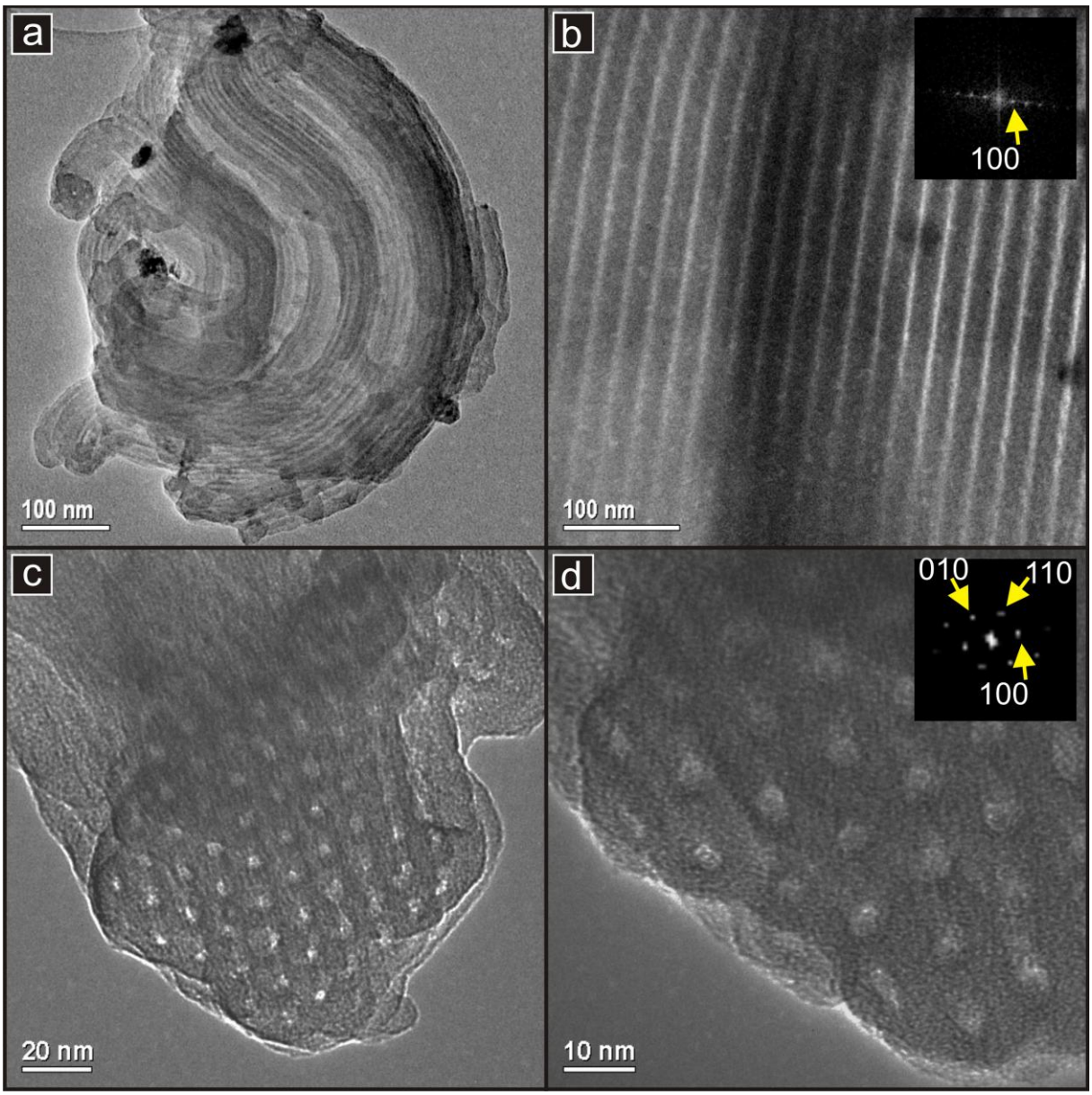

Figure 8-7: TEM images of FDU-15-350A: (a) low magnification of the material showing a typical long range curvature of the channels, (b) the parallel pore channels as viewed in the [100] direction, (c) the parallel pore channels viewed in [001] direction with the hexagonal pore arrangement clearly visible, (d) A higher magnification of image (c). DDPs obtained from the whole image in (b) and (d) as inset. Miller indices of spots are given.

The TEM images in Figure 8-8 represent the material FDU-15-500A and indicate visually the formation of ordered structures. Image (a) is representative of the commonly visualised pore channel feature of a 2-d hexagonal structure as seen along the [100] direction. Figure 8-7(b) is a high magnification image of the parallel formation of the channels with the amorphous carbon walls (black) and porous channels (white) visible. Image (c) shows the structural formation in both the [100] and [001] direction and includes a DDP which relates to a ***d***-spacing of 8.7 nm. The image (d) shows the same directions but with a DDP inset

taken from the hexagonal pore arrangement as viewed in the [001] direction. The pore wall w_{TEM} and pore size t_{TEM} were measured as 3.5 and 5.5 nm respectively.

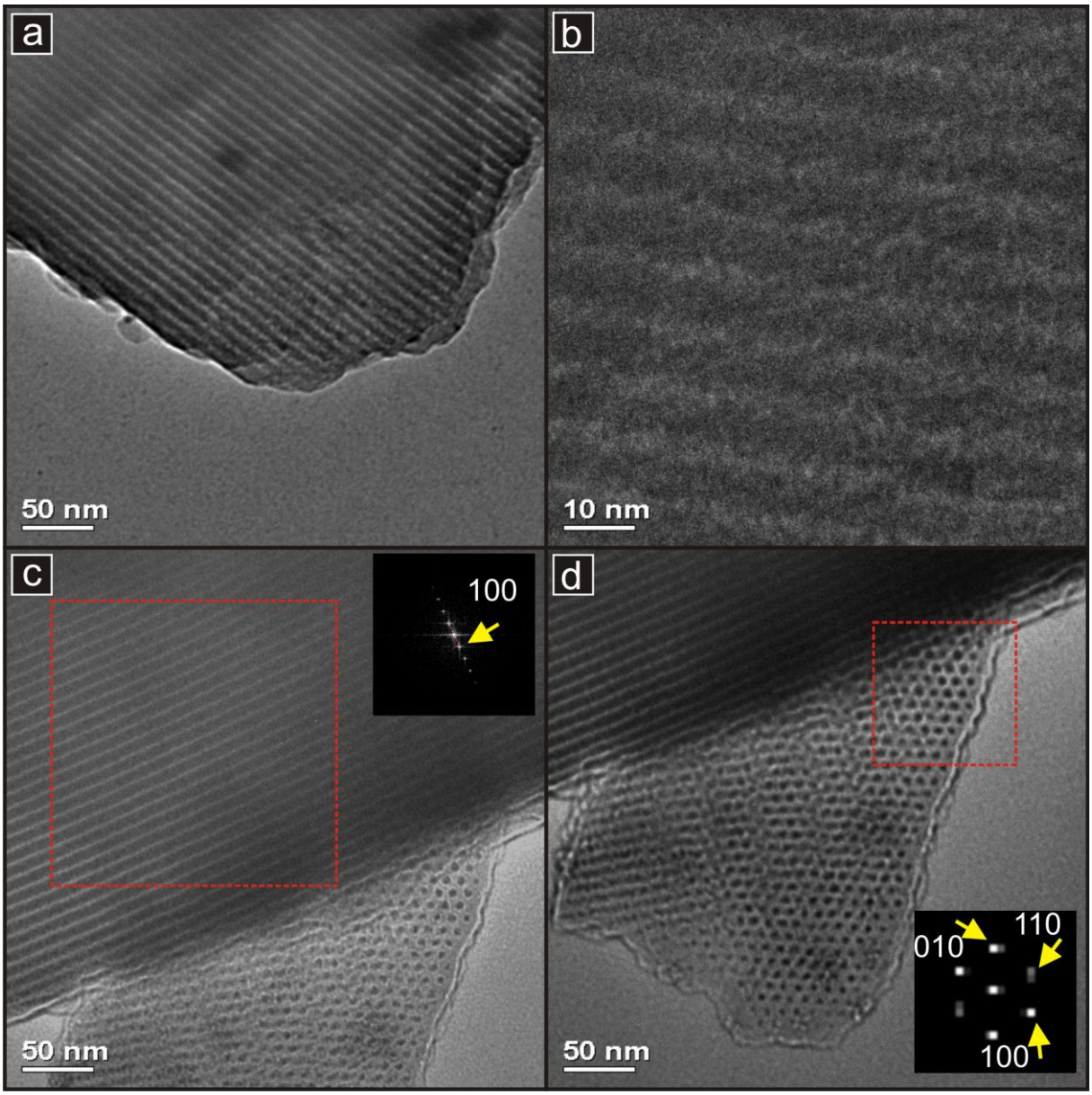

Figure 8-8: TEM images of FDU-15-500A: (a) parallel pore channels, (b) high magnification of the parallel channels showing the amorphous nature of the walls, (c) long range uniformity of channels, (d) the parallel pore channels viewed in [001] direction with the hexagonal pore arrangement clearly visible. DDPs obtained from the red boxes as indicated in (c) and (d) as inset. Miller indices of spots are given.

The TEM images in Figure 8-9 represent the material FDU-15-400C and indicate visually the formation of ordered structures. Image (a) is representative of the commonly visualised pore channel feature of a 2-d hexagonal structure as seen along the [100] direction. Figure 8-7(b) is a high magnification image of the parallel formation of the channels with the amorphous carbon walls (black) and porous channels (white) visible. Image (c) shows the

structural formation in both the [001] direction. The image (d) shows the same direction with a DDP inset taken from the hexagonal pore arrangement as viewed in the [001] direction which relates to a ***d***-spacing of 7.8 nm. The pore wall w_{TEM} and pore size t_{TEM} were measured as 5.5 and 6.5 nm respectively.

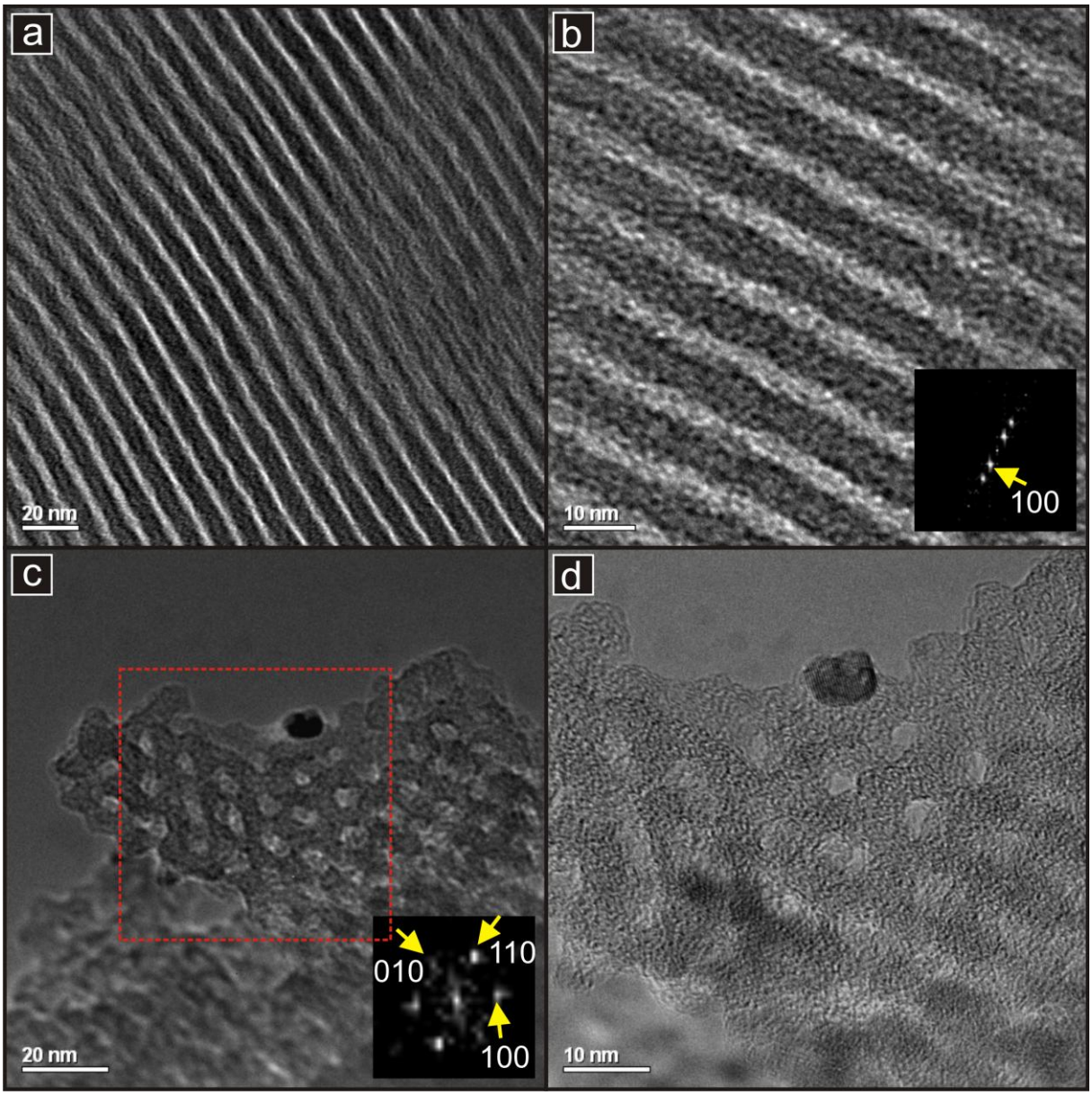

Figure 8-9: TEM images of FDU-15-400C : (a) parallel pore channels, (b) high magnification of the parallel channels showing the amorphous nature of the walls, (c) the parallel pore channels viewed in [001] direction with the hexagonal pore arrangement clearly visible (d) A higher magnification of (c) with the pore arrangement clearly visible. DDPs obtained from the whole image as indicated in (b) and the red box (c) as inset. Miller indices of spots are given.

A summary of the data derived from the analytical techniques is presented in Table 8-14.

Table 8-14. FDU-15 template: Values for unit cell parameters (***$a_0$1 – $a_0$3***), interplanar spacings (***d***), pore width (***w***) and pore wall thickness (***t***) obtained using the method indicated (BJH, SAXS, TEM). All values are in nm. Values of a_o are calculated from the corresponding d_{SAXS} value. Miller indices are given in italics below each value of ***d***.

Sample	w_{BJH}	d_{SAXS} 1	d_{SAXS} 2	d_{SAXS} 3	$a_0$1	$a_0$2	$a_0$3	d_{TEM}	w_{TEM}	t_{TEM}
FDU-15-350A	4.9	10.9 *(100)*	5.7 *(110)*	-	12.6 *(100)*	11.3 *(110)*	- *(200)*	10.0	4.0	7.0
FDU-15-350B	4.5	*14.0* *(100)*	-	-	16.2 *(100)*	-	-	-	-	-
FDU-15-500A	4.9	11.1 *(100)*	5.8 *(110)*	4.4 *(200)*	12.8 *(100)*	11.5 *(110)*	10.1 *(200)*	8.7	3.5	5.5
FDU-15-500B	5.5	*12.6* *(100)*	-	-	14.6 *(100)*	-	-	-	-	-
FDU-15-400C (powder)	7.8	10.2 *(100)*	5.9 *(110)*	-	11.7 *(100)*	*(110)*	-	7.8	5.5	6.5
FDU-15-400C (pellet)	-	10.6 *(100)*	6.2 *(110)*	-	12.3 *(100)*	*(110)*	-	-	-	-

8.3.3 *FDU-16*

When the calcination atmosphere outlined in section 4.7.5 was altered between inert atmosphere and controlled oxygen atmosphere it has been reported as FDU-16-350 and FDU-16-350-O2 respectively. The isotherm observed for FDU-16-350-O2 in Figure 8-10(a) is a type II profile with an H2 hysteresis and is typical for a carbon material with both micropores and mesopores. There is strong gas uptake and this is due to the high degree of microporosity as seen by the large adsorption at low relative pressure. Observation of the pore size distribution in Figure 8-10(b) indicates the majority of the pores to be within an average size of 3.4 nm ±1.5 nm. A total mesopore volume ($\mathbf{V}_{meso}$) 0.27 cm^3g^{-1}, micropore volume ($\mathbf{V}_{micro}$) 0.14 cm^3g^{-1} and specific surface area ($\mathbf{S}_{BET}$) 546 m^2g^{-1} were recorded. FDU-16-350 has no distinguishable profile due to limited gas uptake and has therefore no corresponding pore distribution A total mesopore volume ($\mathbf{V}_{meso}$) 0.02 cm^3g^{-1}, micropore volume ($\mathbf{V}_{micro}$) 0.01 cm^3g^{-1} and specific surface area ($\mathbf{S}_{BET}$) 19 m^2g^{-1} were recorded. The isotherms observed in Figure 8-10(c) for FDU-16-500-O2 and FDU-16-500 are very similar and are of a type II profile with H2 hysteresis present. FDU-16-500-O2 in Figure 8-10(d) indicates a pore size distribution maximised at 3.8 nm. A total mesopore volume ($\mathbf{V}_{meso}$) 0.19

cm^3g^{-1}, micropore volume ($\mathbf{V}_{micro}$) 0.15 cm^3g^{-1} and specific surface area ($\mathbf{S}_{BET}$) 574 m^2g^{-1} were recorded. FDU-16-500-O2 indicates a pore size distribution maximised at 3.8 nm. A total mesopore volume ($\mathbf{V}_{meso}$) 0.18 cm^3g^{-1}, micropore volume ($\mathbf{V}_{micro}$) 0.15 cm^3g^{-1} and specific surface area ($\mathbf{S}_{BET}$) 566 m^2g^{-1} were recorded.

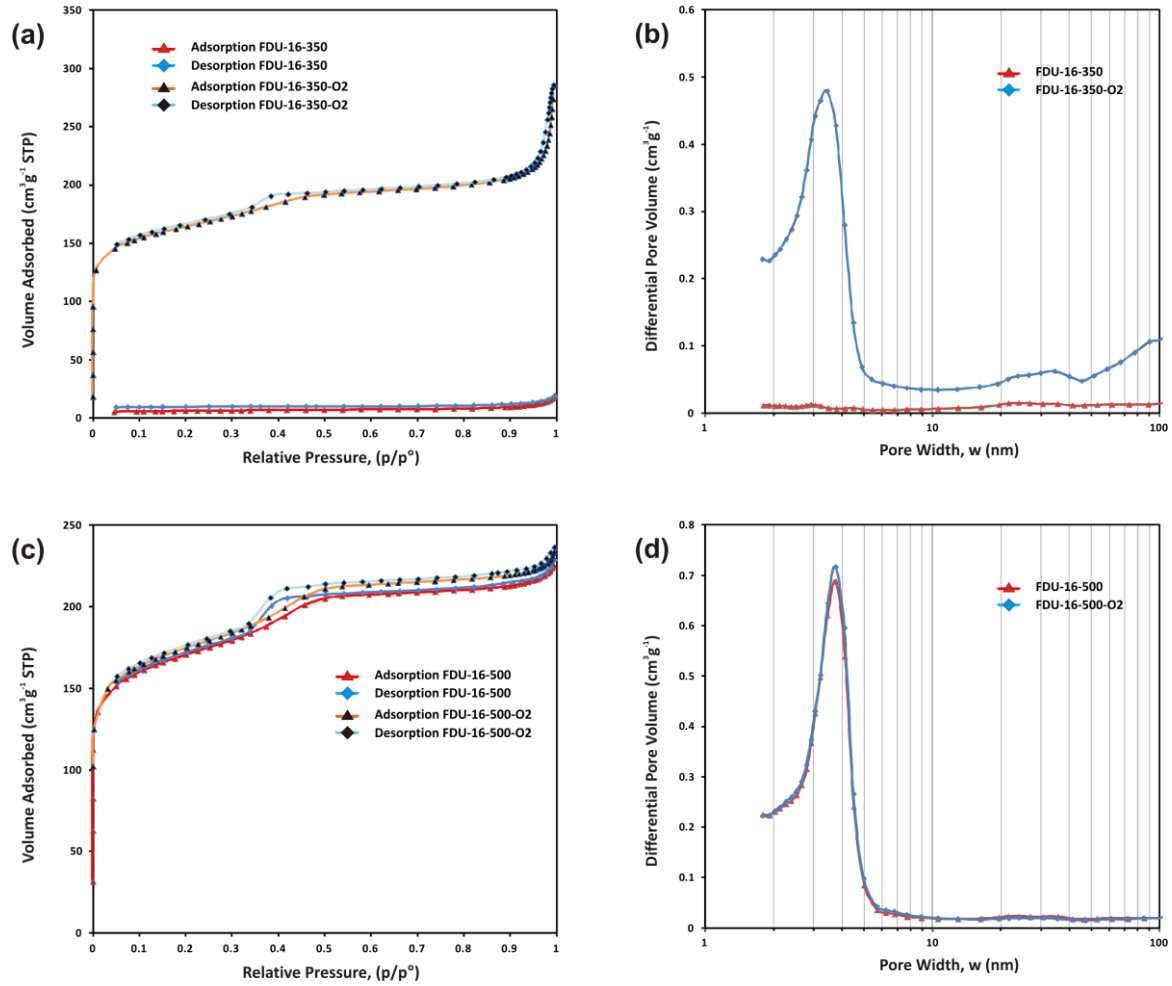

Figure 8-10: Nitrogen physisorption isotherm (a) and specific pore size distributions (b) for FDU-16-350; nitrogen physisorption isotherm (c) and specific pore size distributions (d) for FDU-16-500

Table 8-15 summarises the gas physisorption data obtained using the BET (specific surface area), t-plot (microporosity volume) and BJH (mesopore size distribution and volume) methods. Analysis of low angle XRD data as presented in Figure 8-11 reveals diffraction peaks in both FDU-16-350 (a),Table 8-16, and FDU-16-500 (b),Table 8-17. Using resolved diffraction peaks with a ***d***-spacing ratio of 1:1, 1:(1/√2), 1:(1/√3), the peaks are indexed as 110, 200 and 211 diffractions. In order to better resolve the diffraction peaks the data is presented with the background subtracted.

Table 8-15. Gas physisorption data for FDU-16 template: Values for specific pore size distribution (w_{BJH}), specific surface area (S_{BET}), mesopore volume (V_{meso}) and micropore volume (V_{micro}).

Sample	w_{BJH} (nm)	S_{BET} (m^2g^{-1})	V_{meso} (cm^3g^{-1})	V_{micro} (cm^3g^{-1})
FDU-16-350	nil	19	0.02	0.01
FDU-16-350-O2	3.4	546	0.27	0.14
FDU-16-500	3.8	566	0.18	0.15
FDU-16-500-O2	3.8	574	0.19	0.15

The FDU-16-350 has two easily observable peaks with the (110) index resolved with a ***d***-spacing of 9.50 nm and the (200) resolved with a ***d***-spacing of 6.10 nm and corresponds to the diffractions of a body centred cubic structure. The FDU-16-500 has three easily observable peaks with the (110) index resolved with a ***d***-spacing of 8.72 nm, the (200) index resolved with a ***d***-spacing of 6.26 nm and the (211) index resolved with a ***d***-spacing of 5.15 nm and corresponds to the diffractions of a body centred cubic structure. This relates to a unit cell parameter of 13.4 and 12.3 for FDU-16-350 and FDU-16-500 respectively. These values were calculated using the formula in Eqn. 20

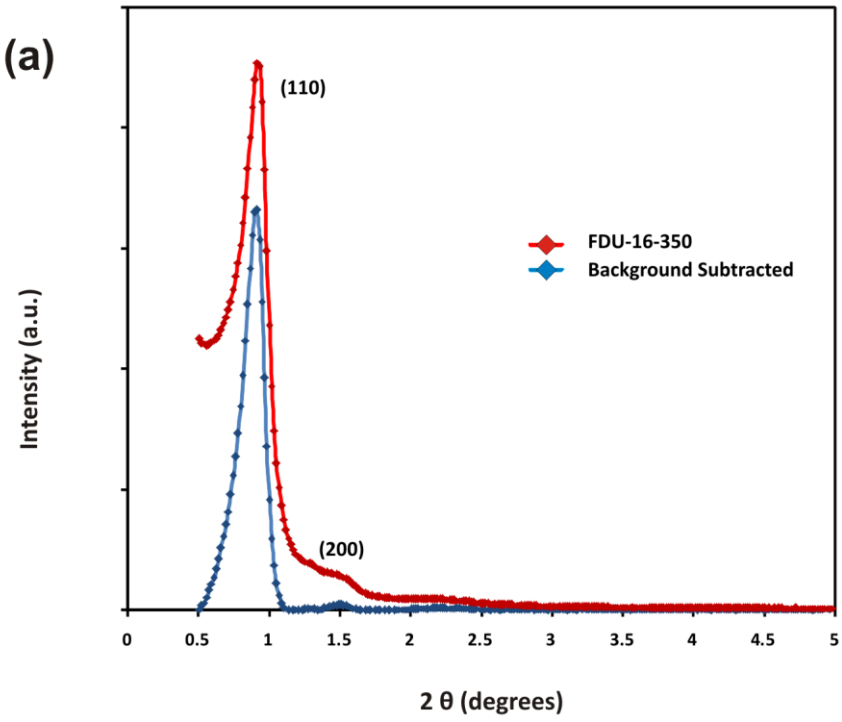

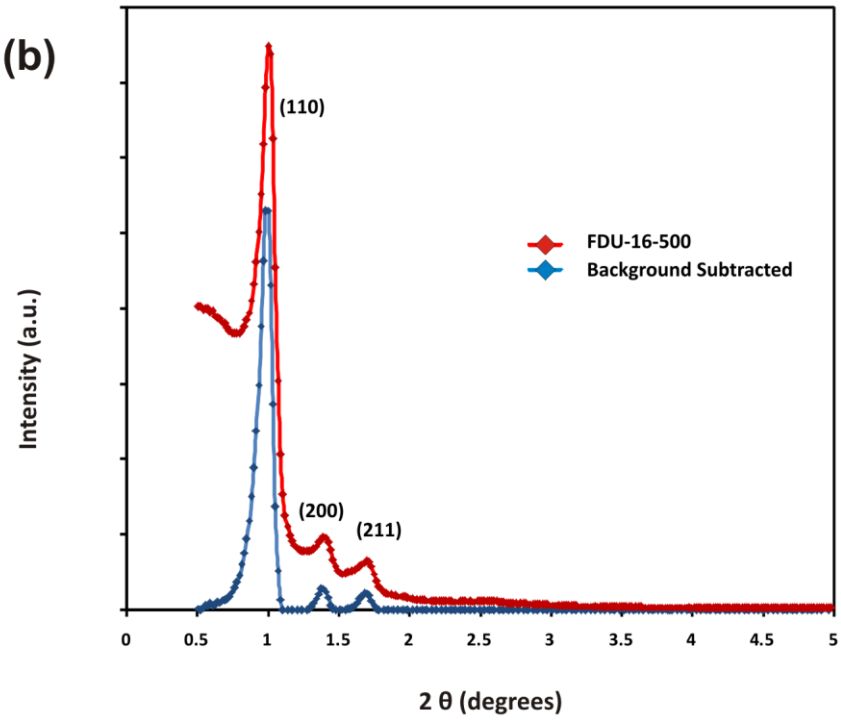

Figure 8-11: Low Angle XRD patterns (a) FDU-16-350 and associated d-spacing values, (b) FDU-16-500 and associated d-spacing values.

Table 8-16: Calculated d-spacing from 2θ values for FDU-16-350.

2θ (°)	Indices	*d*-Spacing (nm)
0.929	110	9.50
1.448	200	6.10

Table 8-17: Calculated d-spacing from 2θ values for FDU-16-500

2θ (°)	Indices	*d*-Spacing (nm)
1.012	110	8.72
1.410	200	6.26
1.713	211	5.15

Figure 8-12 presents representative TEM analyses of the FDU-16-500 material. Image (a) is a low magnification of the sample showing the typical spherical clusters observed with image (b) a magnified example of one such cluster highlighting the porous nature of the material. Image (c) displays the material with long range ordering across the entirety of the material. The image (d) indicates the lattice arrangement of walls around a porous network in a cubic arrangement.

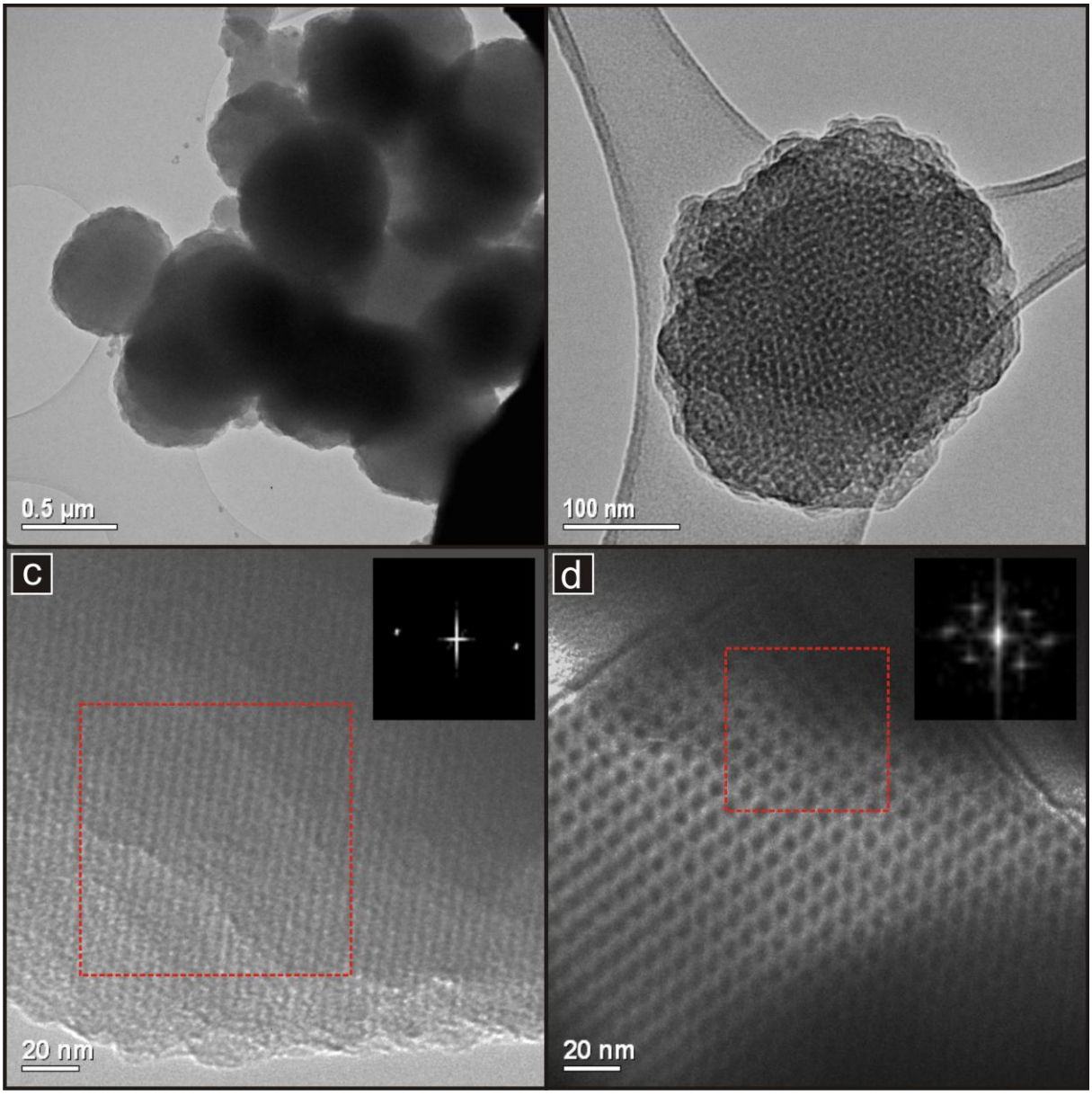

Figure 8-12: TEM images of FDU-16-500 : (a) low magnification image of spherical clusters, (b) spherical cluster showing porous arrangement, (c) parallel pore structure across the sample (d) the cubic lattice arrangement of pores. DDPs obtained from the red boxes as indicated in (c) and (d) as inset.

A summary of the data derived from the analytical techniques is presented in Table 8-18.

Table 8-18. FDU-16 template: Values for unit cell parameters (***$a_0$1 – $a_0$3***), interplanar spacings (***d***), pore width (***w***) and pore wall thickness (***t***) obtained using the method indicated (BJH, SAXS, TEM). All values are in nm. Values of ***a_o*** are calculated from the corresponding ***d_{SAXS}*** value. Miller indices are given in italics below each value of ***d***.

Sample	w_{BJH}	$d_{SAXS}1$	$d_{SAXS}2$	$d_{SAXS}3$	$a_0 1$	$a_0 2$	$a_0 3$	d_{TEM}	w_{TEM}	t_{TEM}
FDU-16-350	nil	9.5	6.1	-	13.4	12.2	-	-	-	-
		(110)	*(200)*		*(110)*	*(200)*				
FDU-16-350-O2	3.4	-	-	-	-	-	-	-	-	-
FDU-16-500	3.8	8.7	6.3	5.2	12.3	12.6	12.7	14.2	4.0	4.2
		(110)	*(200)*	*(211)*	*(110)*	*(200)*	*(211)*			
FDU-16-500-O2	3.8	-	-	-	-	-	-	-	-	-

8.4 Discussion

8.4.1 *FDU-14*

The most distinctive difference between samples is the use of oxygen in the calcination gas stream. As the materials have been prepared identically except for calcination conditions, the material has shown to benefit from the use of oxygen with a dramatic increase in the reported SSA and pore volumes and is indicative of micelle removal.

A typical isotherm profile would often see the adsorption and desorption profiles be in close proximity except when a period of hysteresis occurs. When the polymer materials were studied, the isotherm shows a distinctive departure from the respective sorption profiles and is more prevalent the lower (less carbonaceous) the product is. The lack of closure of the adsorption and desorption isotherms of any particular polymer material at relatively low relative pressures is attributable to the ability of the polymer to swell when exposed to condensed nitrogen[120].

The observed PSD of the materials was found to be tending towards the micropore end of the width distribution. As the Micromeritics Tristar is limited in its capability to measure in the micropore range, a definitive value is not able to be obtained. As it would appear that

the pore formation is occurring in the 1-2nm range, it is fortuitously just within observation. This indicates, in association with the observed low angle XRD data, that an ordered material is being produced for the FDU-14-350 materials. Ideally though, a larger pore size would be preferred as the material is being synthesised with the proposal to impregnate with a liquid precursor in a nanocasting procedure. The low angle XRD data displays a peak in the vicinity of the low 2θ value ~ 0.6° for all the materials (with the exception of FDU-14-500) and is attributed to a weak 110 reflection peak. It is thought that the $\sqrt{8}$ reflection is not observed as this is often a weak reflection and not always resolved from the main peak[121]. The main peak has been indexed as $\sqrt{6}$ with the $\sqrt{14}$ ($\sqrt{16}$) and $\sqrt{20}$ ($\sqrt{18}$) peaks also being indexed in agreement with an *Ia3d* space group representing the bi-continuous nature of the material.

Initial TEM analysis of FDU-14-350-O2 proved to be difficult given that the structures were in the micro and not the normally observed mesopore range. Figure 8-3(a) shows the material at a relatively high magnification with no observable ordered structure apparent. The image (b) shows a formation of parallel structures indicating that some ordered formation has occurred. Image (c) at first glance appears to be an amorphous particle devoid of structure but closer inspection reveals a parallel structure with stacking and by taking the image with different focus and contrast, this ordering becomes more visible. The associated DDP images reveal repeat structural features. The red lines in image (d) are included to help the reader view the direction of the repeat parallel channels that are observable and indicate the boundary between which an area of stacked parallel pore structures can be viewed. Measurements from the FDU-14-350-O2 TEM images reveals a maximum 3.1 nm pore to pore width and is in good agreement compared with the gas physisorption result which indicates a pore width distribution of 1-2 nm by interpolation.

The low angle XRD pattern for the FDU-14-500 material is indicating no resolved diffraction peaks along with the lack of any viewable structures in TEM analysis. Similarly, the FDU-14-500-O2 has no resolved peaks other than a small (110) peak which is suspected as being present due to the formation of a separate hexagonal phase structure. This would suggest that either the material is of low yield, not formed properly or somehow being destroyed possibly through pore closure with the increased calcinating temperature. The gas physisorption data indicates that the material has a PSD at the boundary of what is considered micro and mesoporous and so pore closure does not appear to be a viable

explanation. If the micelles are forming but ordered self-assembly is not achieved it could be envisioned that the material realised is through the removal of the micelles leaving behind a material that is disordered.

The difficulty in control of material preparation is possibly due to the susceptibility through minor variations in control parameters. One aspect that is of concern is the control of micelle formation and resol interaction as it is known to be a critical step in the synthesis which in turn is related to the control of the temperature range critical micelle concentration and critical micellation temperature[122]. In aqueous solution, lower critical solution temperature [123] is between 20°C and 60°C for Pluronic™ P123 [124] and it is suggested that the P123 would be optimised at 40°C in deionised water. The procedure used, often did not mention a temperature [74] [120] or stated it as a room temperature (20°C) procedure [73]. As this temperature was sensitive to fluctuations from the ambient surroundings, the desired temperature of 20°C was attempted to be controlled using a static water bath and insulation. Control greater than ±1°C proved to be the best practicably obtainable and a water recirculation chiller unit would be better utilised. A study by Jin and co-workers [125] created a series of OMC materials following a two-phase method whereby the variation in ratio of tri-block copolymer was shown to have a direct consequence on the structure formed. The preferred hexagonal structure was directly influenced by micelle concentration such that a worm-like structure would be formed when higher Pluronic F127 concentration was used. Mixed phase has also been reported during the aqueous one pot method [75] with pure 2-D hexagonal mesophase being unattainable under the synthesising conditions. Similarly bi-continuous FDU-14 showed evidence of mixed phase [73] in a separate study.

8.4.2 *FDU-15*

According to the study by Meng and co-workers[76], the point at which the polymer has completed the transformation into a homologous carbon structure occurs at the 600°C temperature and above. From the lowest reported OMP temperature of preparation (350°C) up to this 600°C value, the degree of transformation into a carbonaceous framework will steadily increase. Initial preparations focused on making OMP material at 350°C and 500°C as this was the widely reported temperatures at which material was being synthesised. For reasons of using the material as a template in a nanocasting method, 350 and 500°C

represented 2 materials suspected of differing in hydrophobicity. Latterly, the material was synthesised (For FDU-15) at 400°C as this better represented the closed container strategy discussed in chapter 9. The 400°C calcinations were solely performed on material prepared using the two-phase method (C) as this was the preferred method in producing the FDU-15 material.

Review of the sorption profiles of all the FDU-15 materials show a similar departure from the adsorption to desorption profiles as found in the FDU-14 materials. The effect is not as pronounced as occurs in FDU-14 probably due to the difference between structures.

From the gas physisorption data it would appear that all three methods (A, B and C) are producing ordered mesoporous materials. The material produced by method (B) is showing a lesser amount of ordered mesopores in comparison to the other methods. FDU-15-350-B has virtually no ordered mesoporosity, further verified by the lack of diffraction in the low angle XRD pattern and failure to find any structures through TEM imaging. The 500°C material indicates a greater specific pore formation at the expected 5 nm range but is associated with a larger spread of mesopores and a higher microporosity than any other material indicating that quality of the material is in doubt. This is further verified by low angle XRD analysis where a single diffraction peak is present but poorly resolved indicating minimal ordered material to be present.

The FDU-15-500A material is showing strong mesopore formation at the 5 nm range with expected values of SSA, mesoporosity, microporosity and unit cell parameter that compare with other values reported in Appendix 3. Unlike the FDU-15-500B, there is no significant mesopore size deviation which would indicate that majority of the material is structurally refined. Comparison between data for FDU-15-350A and FDU-15-500A highlights shrinkage of both the pore size and wall thickness indicating an overall reduction in the framework which is expected given the increase in temperature. The calculated unit cell parameter from low angle XRD does not corroborate this as there is only a minor difference in values. It would appear that the FDU-15-350B and FDU-15-500B is undergoing a greater degree of structural change which is significant enough that a decrease in unit cell value is recorded although this is subject to uncertainty given the poorly resolved patterns.

FDU-15-400C has the greatest surface area and largest pore formation of all the materials at approximately 8 nm in size. This larger pore size is a favoured property when attempting the nanocast procedure due to the potential in reducing capillary forces associated with liquid precursor impregnation. Equally important in all the materials is the presence of micropore volume as this indicates the potential with which any nanocasted material has in forming a

bundled structure rather than a series of individual nanorods. As each material (with the exception of FDU-15-350B) has a similar micropore volume in comparison to siliceous SBA-15 analogue, the indication is positive that suitable bridges will be formed between casted pores.

8.4.3 *FDU-16*

The prepared material for FDU-16 was initially completed without the use of oxygen in the calcinating gas stream. When use of oxygen in the calcination gas stream was utilsed, a distinctive difference between samples becomes apparent. As the materials have been prepared identically except for calcination conditions, the material has shown to benefit from the use of oxygen at the 350°C temperature with a dramatic increase in the reported SSA and pore volumes which is indicative of micelle removal. The use of oxygen for the 500°C material is not so apparent but is does serve to show that the oxygen does not appear to degrade the material and that unlike FDU-14, repeatability in the synthesis towards a quality material is achievable.

As with the FDU-14, mixed phase concerns have been reported for FDU-16 with cubic and hexagonal phases existing[75]. It has also been reported that the pore structure is susceptible to fluctuations (defects) with pore doubling and micropore interconnection being observed[126]. Sand difficulties remain despite good physisorption and low angle XRD data that ordered mesoporous material exists in identifying the homogeneity of the *Im3m* structure throughout the bulk of the material. The low angle XRD data indicates that an ordered structural repetition is present and that the FDU-16-500 material is better resolves than the FDU-16-350. There is also an observable reduction in *d*-spacing value indicating an expected shrinkage in the unit cell dimension as temperature increases.

8.4.4 *Metamorphosis of OMP towards OMC*

Often the strategy in fabricating OMC is to prepare firstly the resol polymer which is then added to the tri-block copolymer solution, However it has been shown that the resol can be formed in-situ with the triblock copolymer already dispersed resulting in a phase separation of the polymer gel[77, 118].

Figure 8-13: Gas physisorption tubes showing the degree of hydrophobicity of carbon template (FDU-15) in water. The left tube is 350°C material and the right tube is 500°C.

One of the overall objectives of synthesising the templates was to create a product that maximised the hydrophilic character of the material (important for nanocasting involving the use of a polar solution). As the resol framework thermo-polymerisation involves a curing process that will see progressive condensation of the hydroxyl bonds as the temperature (degree of carbonisation) increases, it was important to try and maximise (maintain) the surface functionalisation as it was suspected as being directly related to the hydrophilic nature of the material. Figure 8-13 is a visual indication of this phenomenon showing two gas physisorption glass tubes with 350°C template (left) and 500°C template (right). The flocculation of the 500°C visually indicates higher degree of hydrophobicity in water medium.

8.4.5 *Considerations of Quality and Quantity*

An important factor in the preparation of carbon templates (and silica) is the final quantity realised from the starting reagents. It was discovered early on that the preparation using a one pot synthesis route[75] was an uncomplicated method using basic laboratory equipment to prepare FDU-15 and FDU-16 template and in a time frame of 24 hours as opposed to 7 days[74]. Although this method was highlighted as being scalable, the practicalities of scale versus product quantity merited reverting to the longer process as typical quantities were 0.5 g versus 2.5 g respectively. These methods were subsequently replaced (FDU-15 only) with the more favourable two-phase method which would produce a typical yield of 1 g for the reported methodology. This two-phase method was found to be beneficial in

comparison having a short preparation time (24 hours), scalability and quality of product. In regards scalability the two-phase method should in theory be limited only by the size of the vessel in which the reaction proceeds. In order to have enough material to characterise and subsequently utilise as a template, it was deemed that 2 g was a useful quantity to proceed with. The material was therefore prepared using double reagent quantities from the methodology as published and no degradation was observed in the quality of product. Unfortunately in respect to FDU-14 and FDU-16 preparation, reported methods still remain scarce and so there is a limitation in choice of preparation procedures.

As several methods and batches were prepared for the FDU-15 material, a summary of the main gas physisorption data is presented in Table 8-19 as this is a good indicator of the quality control of the material. From this data it is evident that for methods A and C, the material can be synthesised successfully with repeatability.

Table 8-19. A summary of the variation in gas physisorption data between batches of FDU-15 carbon templates. Values for mesopore volume (V_{meso}), micropore volume (V_{micro}), specific surface area (S_{BET}) and associated standard deviations (**s.d.**) from the batches produced obtained using the methods indicated (BJH, BJH, t-plot and BET respectively).

Sample	***Method***	***No. of batches***	V_{meso} (cm^3g^{-1})	***s.d.*** (cm^3g^{-1})	V_{micro} (cm^3g^{-1})	***s.d.*** (cm^3g^{-1})	S_{BET} (m^2g^{-1})	***s.d*** (m^2g^{-1})
FDU-15-350	One-Pot Aqueous (A)	4	0.36	0.04	0.05	0.01	434	3
FDU-15-400	Two-Phase I	6	0.64	0.11	0.07	0.01	536	88
FDU-15-500	One-Pot Aqueous (A)	4	0.30	0.02	0.09	0.06	509	83
FDU-15-350	EISA (B)	2*	0.09	-	nil	-	105	-

* Standard deviation not obtainable.

8.5 Summary

While it would appear that the FDU-14 material synthesised is greatly improved upon in regards pore opening by using an amount of oxygen in the calcination step, the formation of the pores in the micropore range is unfavourable. The material produced at 500°C appears to show a similar pore width distribution however lack of resolved low angle XRD data could

be highlighting a formation problem. It is also a concern that mixed phase could occur and affect the quality of the product. The preparation of FDU-16-350 with open pore structure has been shown to be difficult if the published procedures are followed verbatim, however the recent publication by Meng[76] and co-workers indicates that a FDU-16-350 material should be feasible using a small percentage of oxygen in the calcinating gas stream. Unlike the 350°C material, it has been shown that the FDU-16-500 material can be successfully prepared in an inert atmosphere in accordance with that reported by Meng.

With the FDU-15 structure the easiest to generate in meaningful quantities. It has an additional benefit of short preparation time of 2 days into a final calcined product which can be easily scaled up using a two-phase method.
Unfortunately, the method to make different structures (FDU-14 and FDU-16) follow a different synthesis route (hydrothermal) and appears to be more susceptible to minor variations in synthesis parameters. The difficulty in preparations especially with the reported hydrothermal methods may be attributable to the low temperature of micelle generation and that a change from the utilised 20°C towards 40°C – which is in alignment with the optimal micelle formation temperature – could see a better quality of product for FDU-14 and FDU-16. The fact that very few published preparations exist highlights the difficulty in controlling manufacture. Given the limitations of characterisation, it is difficult to say whether the FDU-14 and 16 products obtained are homogenous in structural ordering. Other review publications have also intimated similar concerns [74].

Obtaining polymer or carbon materials with a high degree of structural ordering in the low mesoporous range makes them potentially useful for nanocasting. Although each of the three types of carbon template are able to be successfully synthesised with characteristic properties associated with repeat mesoporous ordering, concerns remain about the FDU-14 and FDU-16 in regards yield of ordered mesoporous material.

Chapter 9

Preparation of SDC from Carbon Templates

9.1 Introduction

In this chapter, synthesis of three types of ordered mesoporous carbon (OMC) templates – namely FDU-14, FDU-15 and FDU-16 were used in a nanocast method. Ordered mesoporous templates for nanocasting can be synthesised from a variety of materials such as silica, aluminosilicate[37], polymer, carbon or silica-carbon. Despite successful preparation of samarium-doped ceria (SDC) material from silica templates, the complete removal of silica is extremely difficult to achieve as outlined in Chapter 7. Early research into the use of mesoporous carbon as a template centred on a series designated CMK. The CMK series of carbon templates was prepared directly by nanocasting from silica templates. CMK templates have been used to prepare a number of mixed metal oxides[127]. Recently, researchers have been able to prepare ordered mesoporous metal oxides using a combination of (soft) self-assembly and hard (nanocasting) techniques. This is referred to as CASH chemistry[128] [129] and has been used to make disordered mesoporous ceria which is also crystalline using a carbon matrix [130]. However, to date only one report exists of nanocasting from directly prepared ordered mesoporous carbons (OMCs) of magnesium oxide material[131]. No reports of mixed metal oxides or ceria-based oxides have been reported to the best of the authors knowledge.

The potentially limited ability to impregnate carbon based templates because of their hydrophobic nature is a concern. For this reason, surface modification of the template was considered in this work. Apart from the use of extra reagents, surface modification has the major drawback of modifying the pore structures. The addition of functional groups would reduce the diameter of the pores or, worse still, block them. Other methods of functionalisation whether wet or dry, use conditions that are also detrimental to either the pores or the mesostructure and a comprehensive list of treatments have been compiled by Wu and co-workers[132]. For these reasons, the strategy of changing the hydrophobic nature of the carbon template through functionalisation was dismissed. However, ordered mesoporous polymers (OMPs) are constructed from organic resol molecules and so hydroxyl species are inherently present at pore surfaces. This inherent functionalisation gives the

surface a hydrophilic character. This decreases the higher the temperature of subsequent conversion to more carbonaceous and eventually graphitic OMCs. Beyond the apprehension over impregnation, the conversion to a carbonaceous material is associated with framework shrinkage. A balance between hydrophilic character and framework stability was necessary. The formation of OMP is reported to occur at 350°C with complete conversion to OMC occurring at 600°C. Therefore in this work templates were prepared at 350 and 500°C in order to fall within this range. This evolved into using an FDU-15 template prepared at 400°C for two reasons: (1): 400°C would be the maximum thermal exposure during closed container calcination. (2): OMP materials are reported to be stable up to 350°C in an oxidative atmosphere. However if the thermal exposure is in an inert atmosphere this is extended by a further 50°C[133]. The investigation into the manufacture of carbon templates in Chapter 8 revealed three main structures as being potential candidates for nanocasting. Successful nanocasting from FDU-14, FDU-15 and FDU-16 should produce inverse structures shown in Figure 1-4 (a), (b) and (c) respectively. The inverse FDU-14 structure is formed from a bi-continuous entwinement of two enantiomeric pore channel systems as depicted in Figure 1-3 (b). The pictorial representation in Figure 1-4 (a) highlights only one of the replicated channel systems for reasons of clarity.

9.2 Results

A summary of gas physisorption PSD results for all SDC products are also presented in Appendix 1 to allow useful cross comparison between results and are presented in conjunction with associated templates.

9.2.1 *SDC Prepared From FDU-14 Template*

Two SDC materials (FDU-14-350-O2-SDC-FP) and (FDU-14-500-O2-SDC-FP) were prepared using FDU-14B template. They are differentiated by the template synthesis temperature of 350 and 500°C respectively. Both templates were prepared using 2% oxygen in the gas stream as outlined in Chapter 8. In order to create an SDC final product, the template was used in pellet form and vacuum impregnated with nitrate precursor solution using the preparation methods as presented in Chapter 4. The material was then calcined in an inert atmosphere to 600°C and referred to as the intermediate product (IT) with the nomenclature FDU-14-350-O2-SDC-IT or FDU-14-500-O2-SDC-IT. Final product was prepared from intermediate material by removal of the carbon template and was achieved by heating in air atmosphere at 400°C for 3 h using a ramp rate of 1°C min^{-1}. These final products are

indicated with the post-fix FP. Attempts to prepare final product that had been made at from 350 or 500°C inert gas atmosphere prepared FDU-14 templates did not yield product with any meaningful characterisation and no data is therefore presented.

The isotherm observed for FDU-14-350-O2-SDC-IT in Figure 9-1 (a) is typical of a type I profile with a slight hysteresis present. There was a strong gas uptake which was due to the high degree of microporosity as seen by the large adsorption at low relative pressure. In the PSD of Figure 9-1 (b), a large peak was observed at below 2 nm and was at the measuring limit of the instrument, a secondary broad peak was observed in the low mesopore range below 15 nm although the associated gas uptake was low but not insignificant. A total mesopore volume ($\mathbf{V}_{meso}$) of 0.08 cm^3g^{-1}, micropore volume ($\mathbf{V}_{micro}$) of 0.13 cm^3g^{-1} and specific surface area ($\mathbf{S}_{BET}$) of 405 m^2g^{-1} were recorded. The SDC product FDU-14-350-O2-SDC-FP has a similar isotherm profile but without the microporosity aspect. The material indicates the presence of inter-particle macroporosity from the steep rise occurring at high relative pressure. Despite the overall low gas uptake for FDU-14-350-O2-SDC-FP, a pore size distribution maximised at 4.7 nm was observed. A total mesopore volume ($\mathbf{V}_{meso}$) of 0.11 cm^3g^{-1} and specific surface area ($\mathbf{S}_{BET}$) of 49 m^2g^{-1} was recorded. There was minimal microporosity present with ($\mathbf{V}_{micro}$) reported as nil cm^3g^{-1}.

The isotherm observed for FDU-14-500-O2-SDC-IT in Figure 9-1 (c) displayed flat sorption profiles associated with minimal gas uptake. A total mesopore volume ($\mathbf{V}_{meso}$) of 0.05 cm^3g^{-1}, micropore volume ($\mathbf{V}_{micro}$) of zero cm^3g^{-1} and specific surface area ($\mathbf{S}_{BET}$) of 3 m^2g^{-1} were recorded. The SDC product is typical of a type I profile with a slight hysteresis present.

A total mesopore volume ($\mathbf{V}_{meso}$) of 0.18 cm^3g^{-1}, micropore volume ($\mathbf{V}_{micro}$) of zero cm^3g^{-1} and specific surface area ($\mathbf{S}_{BET}$) of 142 m^2g^{-1} was recorded. In the PSD of Figure 9-1 (d), a large peak was observed at 2.7 nm for the final product FDU-14-500-O2-SDC-FP. The corresponding IT material has no significant PSDs.

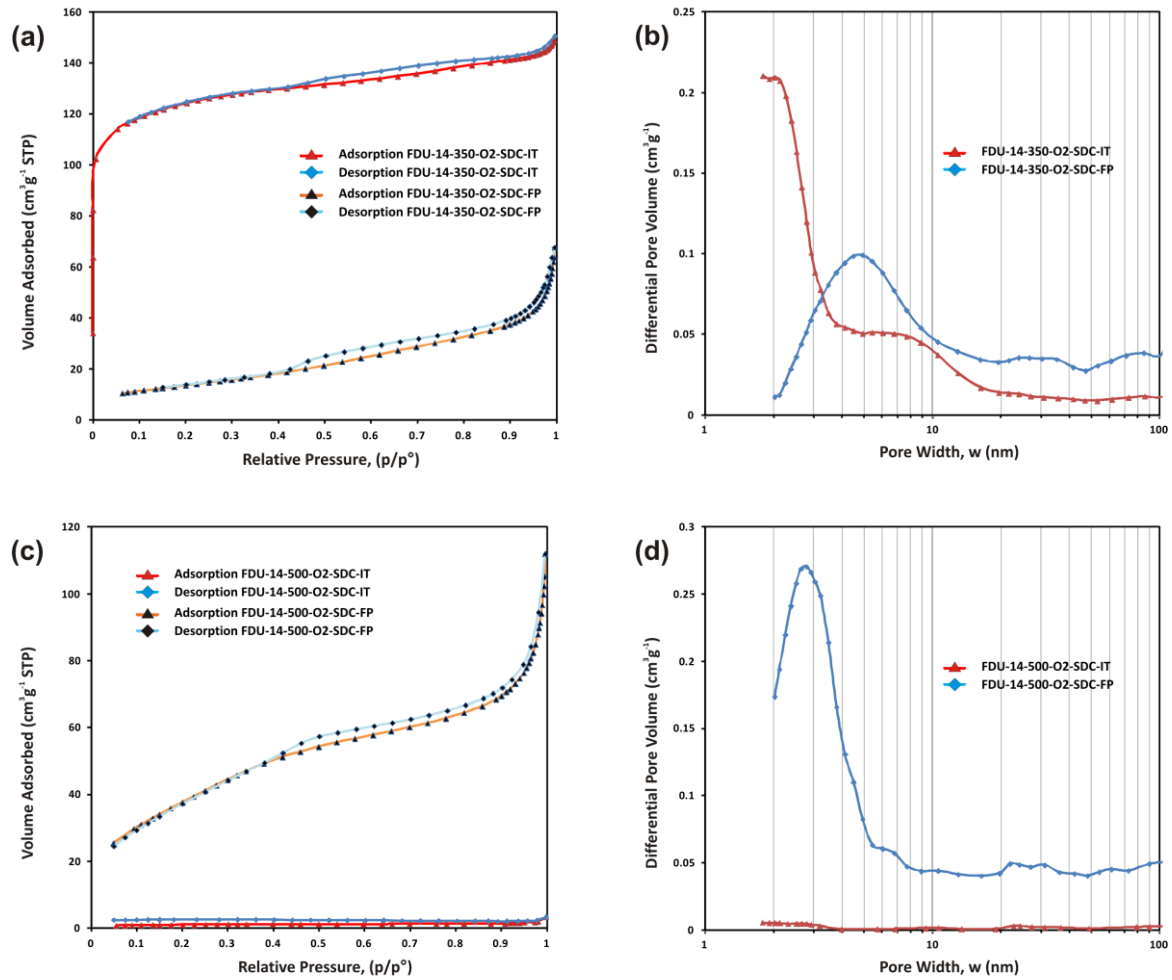

Figure 9-1: Nitrogen physisorption isotherms (a) and pore size distributions (b) for FDU-14-350-O2-SDC-IT and FDU-14-350-O2-SDC-FP. Nitrogen physisorption isotherms (c) and pore size distributions (d) for FDU-14-500-O2-SDC-IT and FDU-14-500-O2-SDC-FP.

A summary of the data values for each intermediate material and final product is presented in Table 9-1.

Table 9-1. Gas physisorption data for FDU-15 template: Values for pore size distribution (w_{BJH}), specific surface area (S_{BET}), mesopore volume (V_{meso}) and micropore volume (V_{micro}).

Sample	w_{BJH} (nm)	S_{BET} (m^2g^{-1})	V_{meso} (cm^3g^{-1})	V_{micro} (cm^3g^{-1})
FDU-14-350-O2-SDC-IT	<2, ~5(2nd peak)	405	0.08	0.13
FDU-14-350-O2-SDC-FP	4.7	49	0.11	nil
FDU-14-500-O2-SDC-IT	Nil	3	nil	nil
FDU-14-500-O2-SDC-FP	2.8	142	0.18	nil

Images presented in Figure 9-2 are representative of the material as viewed using TEM. A significant proportion of the material was found to be composed of nanoparticles of SDC.

These particles were found to be arranged randomly with inter-particle spacing present Figure 9-2 (a). The bulk formation of the particles was a random agglomeration and stacking of individual particles (Figure 9-2 b and c). Particles appeared to be of a consistent size in the 10 nm range and approximately square in dimension - as imaged in 2-D. There was a lack of structured or long range directional growth feature for the majority of the material, however some evidence of partial framework growth was observed. A low resolution image of one such area is shown in Figure 9-2 (e). Closer examination Figure 9-2 (f) of this area highlights areas of dense (dark) material interspersed with pore (light) areas. The image Figure 9-2 (g) indicates that the framework formation possessed a continuous crystalline structure. One such area within this image has been highlighted using red markings to indicate the boundaries of a continuous crystalline structure that extends beyond 30 nm in length. Figure 9-2 (h) is a higher magnification of the continuous framework showing the extended crystalline structure but with disordered formation.

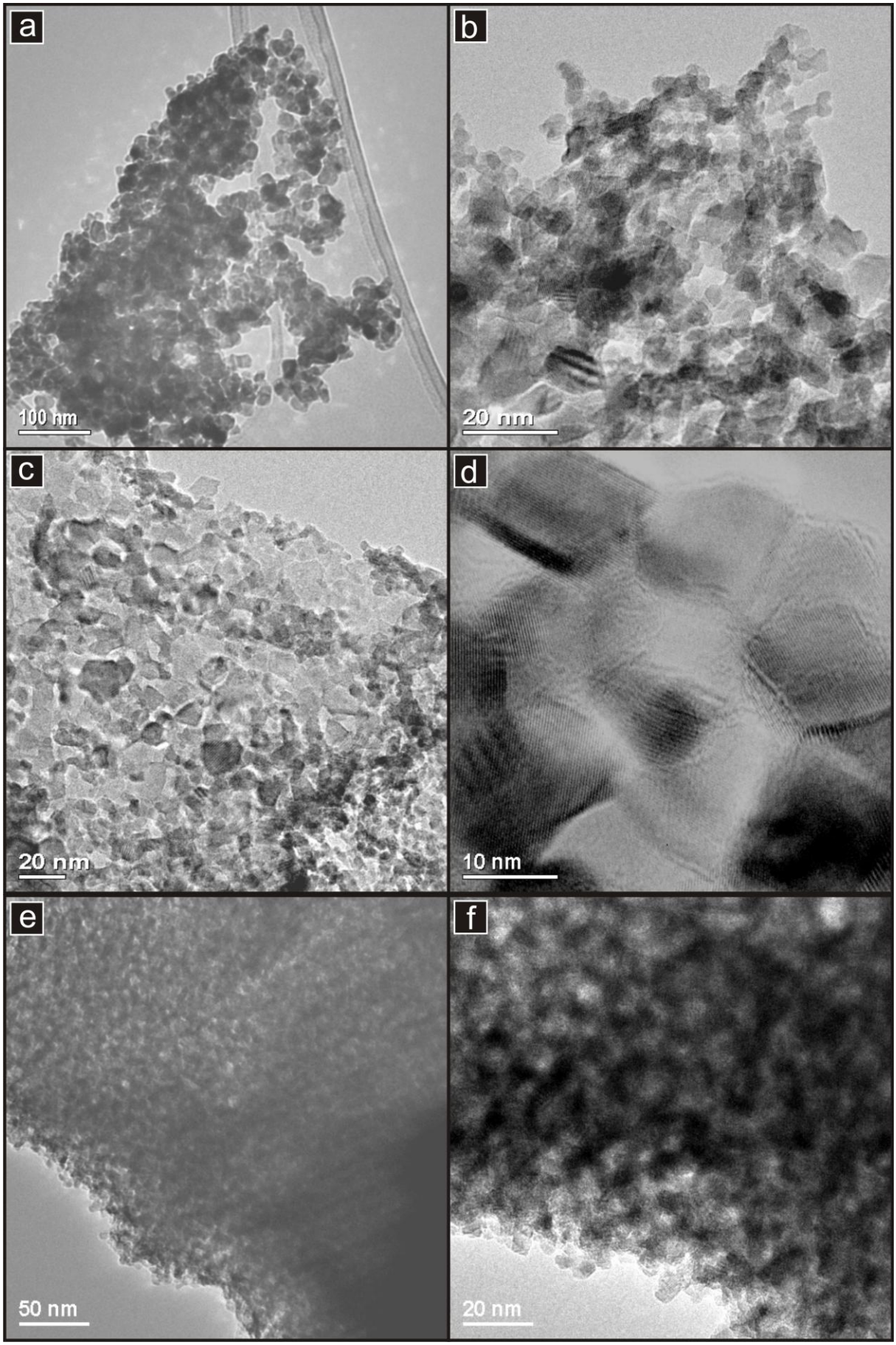
a
100 nm
b
20 nm
c
20 nm
d
10 nm
e
50 nm
f
20 nm

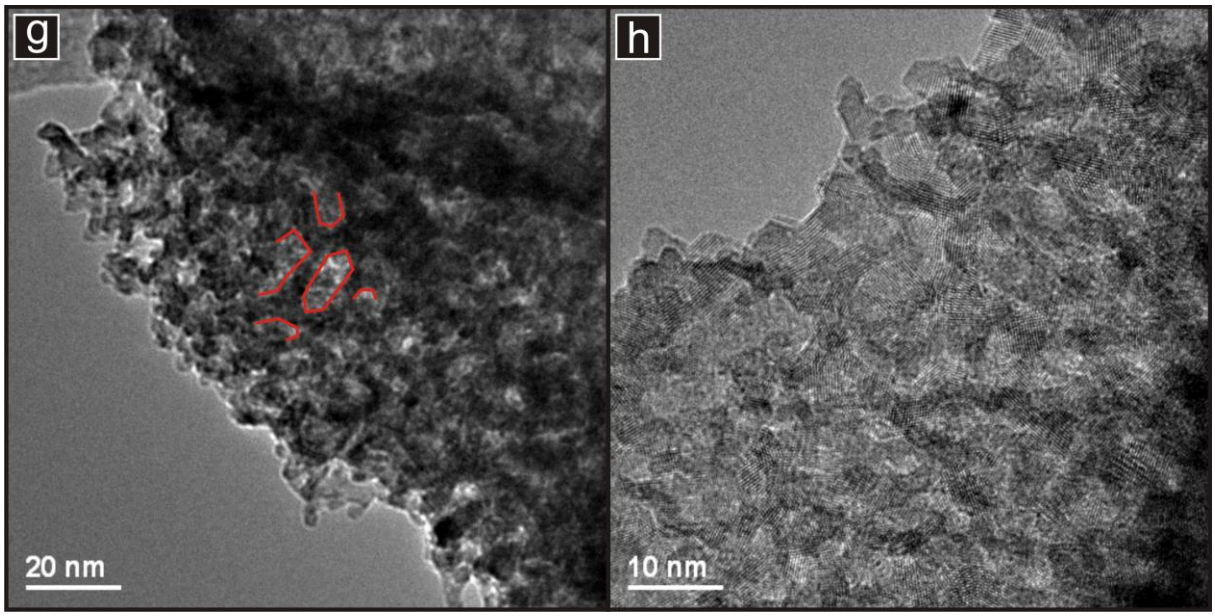

Figure 9-2: TEM images of FDU-14-350-O2-SDC-FP: (a) typical agglomeration with inter-particle spacing evident, (b) and (c) particles agglomerated randomly, (d) high resolution image of particles formed from 200/400 °C calcination, (e) low magnification image of an area displaying framework structure, (f) the framework structure with dense (dark) material interspersed with pore (light) areas, (g) the framework formation with a continuous crystalline structure as highlighted by the boundaries of the red markings, (h) high resolution image of the continuous framework showing a disordered formation.

The final product material prepared as FDU-14-500-O2-SDC-FP when imaged using TEM in Figure 9-3 did not have the same random agglomeration as commonly found in the FDU-14-350-O2-SDC-FP product. The material appeared to have a continuous framework that extended into a long range order with individual pores difficult to view due to the depth and complex branches of the network. Figure 9-3 (e) on close inspection revealed an array of partially visible pores within a crystalline continuous framework. A series of red arrows are pointing towards pore locations. The image Figure 9-3 (f) appeared to indicate that the framework was composed of repeating branched sections. Several of these branches were present and appeared to stack in a repetitive manner. The images (g) and (f) are high resolution images of the framework showing the complex 3-D nature of the mesoporous structure. The pore width w_{TEM} was estimated to be in the 3 to 5 nm range and wall thickness d_{TEM} of 4 nm. This is in good agreement with the reported PSD for the material and concurs with the inverse values of PSD for the template. Figure 9-3 (f) highlighted one particular area of the network indicated from a red outline. The enclosed area surrounds a single crystalline channel with several branches extended as a 3D array. The same area was presented in Figure 9-3 (g) as a high resolution image with continuous crystal planes evident.

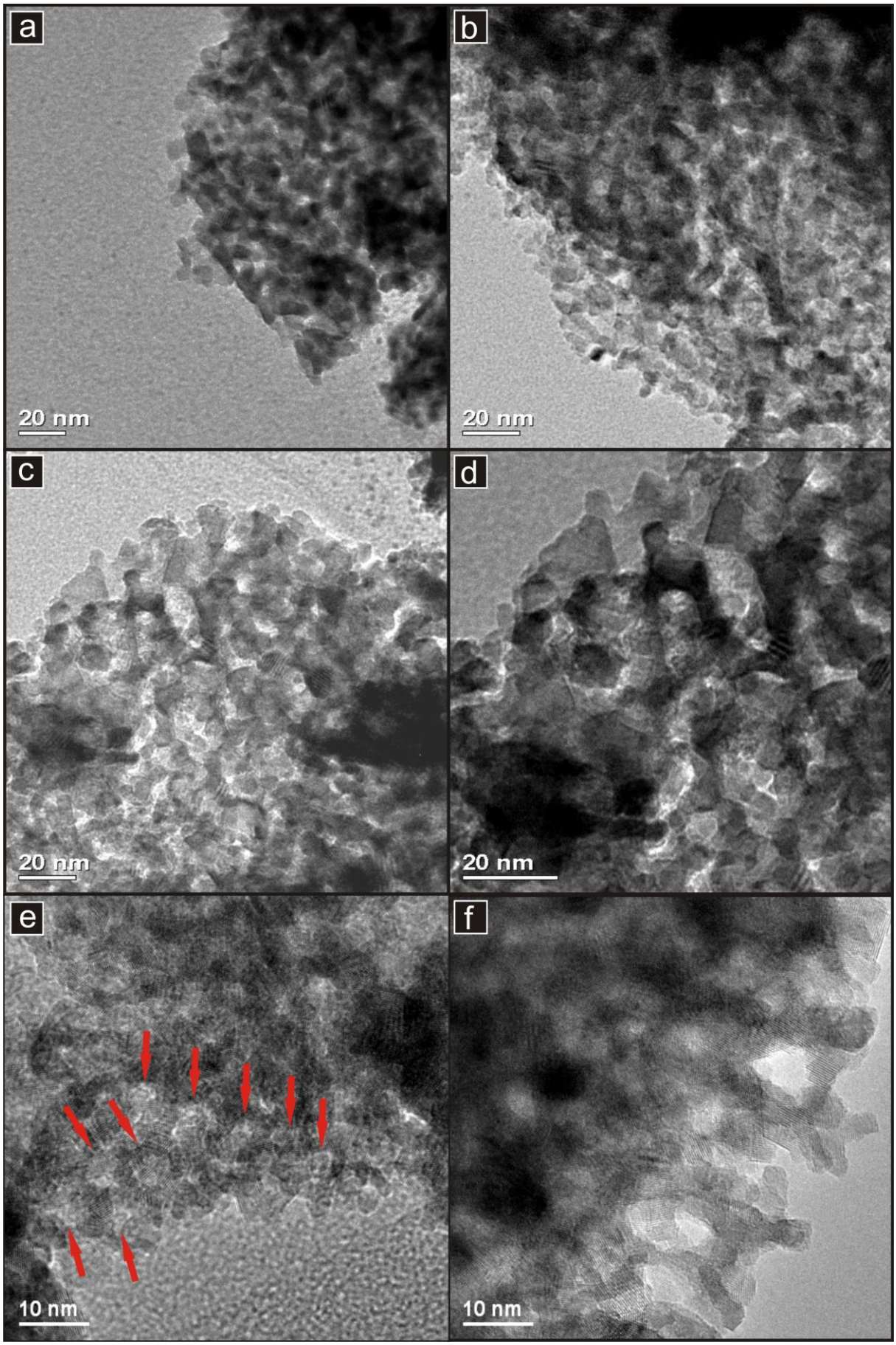
a
20 nm
b
20 nm
c
20 nm
d
20 nm
e
10 nm
f
10 nm

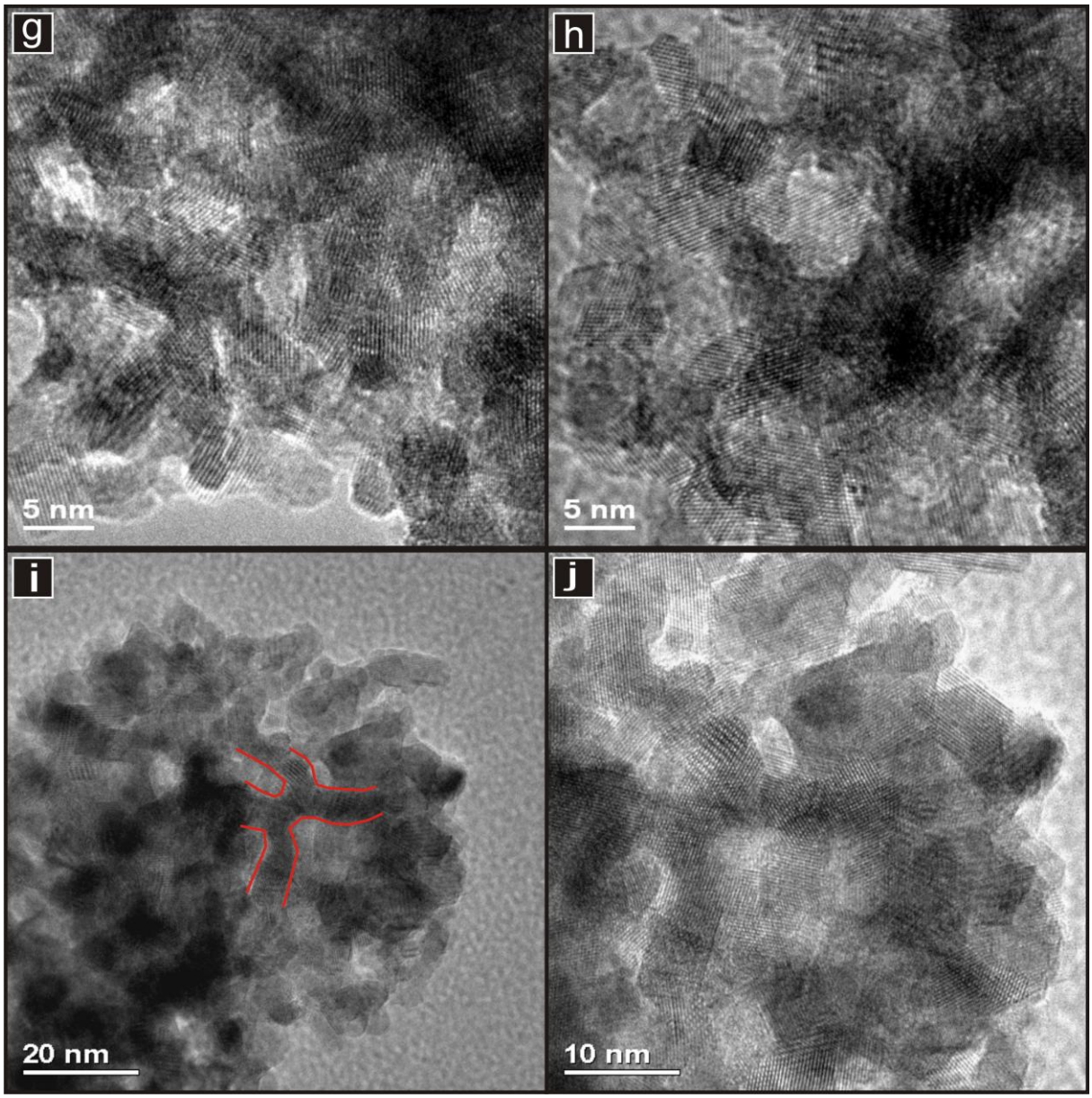

Figure 9-3: TEM images of FDU-14-500-O2-SDC-FP: (a, b) low magnification image of particle clusters, (c) the framework structure with dense (dark) material interspersed with pores (light), (d) higher magnification of (c) showing the complexity of the framework, (e) the framework with an array of nine arranged pores as indicated by the red arrows, (f) a section of framework with repeat units stacked on top of each other, (g) a high resolution image indicating the continuous crystalline nature of the structure and how it extends through 3-dimensions, (h) a high resolution image of the framework structure surrounding a series of pores, (i) a continuous part of the structure with the red areas indicating the boundary as it extends in 3-dimensions, (j) a higher magnification of image (i).

SDC material produced from inert atmosphere synthesised FDU-14 when analysed by gas physisorption indicated very little gas uptake. As the starting template was characterised as having poor structure due to the ineffective removal of triblock copolymer, the result was not unexpected. Comparison of the FDU-14-350-O2-SDC-IT material with the corresponding FDU-14-350-O2 template would suggest that impregnation from the nitrate precursor has

occurred. An approximate 50% reduction in the pore volume of the main micropore peak that is centred at the 1-2nm PSD had occurred. As this occurred at the limit of the instrument ability to record into the micropore range using the BJH algorithm, the volume change between the template and intermediate was reported as a change in the mesopore range ($\mathbf{V}_{meso}$). A secondary peak was present which may be the start of some residual nitrate material forming particulate agglomeration. This SDC agglomeration was the cause of the higher mesopore and macropore formation reported in the final product. This was verified by TEM examination from the selection of images in Figure 8-3 highlighting the particle agglomeration, lack of ordered structured and inter-particle porosity. Comparison of the FDU-14-500-O2-SDC-IT material with the corresponding FDU-14-500-O2 template would suggest that impregnation from the nitrate precursor had occurred. Almost complete reduction in the pore volume of the main micropore peak of the template centred at the 1-2 nm PSD had occurred indicating a high level of impregnation. The inverse material of FDU-14-500-O2-FP indicated an SDC material with PSD of narrow mesoporous range and at a distinctly different range from the starting template. The specific volume associated with this mesopore range was in close agreement with SDC inverse products synthesised from ordered mesoporous silica templating.

Examination of the TEM images, particularly (i) and (j) highlight the extent of a continuous single crystal that forms the basis of a mesoporous-framework. Comparison of this single crystal with a single wall structure from the inverse of a bi-continuous template as pictorialised in Figure 1-4 indicated a correlation in the shape and 3D branches. The single pore filling of bi-continuous framework structures are well observed effects[134] such that the inverse replica is formed from one of the enatiomeric pore systems[135]. Material synthesised from a solvo-thermal procedure showed a similar continuous framework. To try and elucidate whether the framework growth in the FP material was from template nanocasting or from an alternative growth mechanism as observed during synthesis of template free solvo-thermal material, key data could be cross compared. A solvo-thermal effect was unlikely as the pellet was carefully prepared to include an extended drying period of 24 h. Further, no characteristic solvo-thermal peak at the 12 nm range was observed and TEM images as presented in Chapter 10 indicated a larger framework of disordered mesopores. As an inverse structure to FDU-14-O2, the measured wall thickness $\boldsymbol{d}_{TEM}$ of 4 nm should be in close approximation to the PSD of the template. As the template indicated a PSD at 2 nm, the value is in close approximation with the FP wall thickness. Additional crystal growth may be associated with template pyrolysis.

The chemical composition indicating an SDC product free of carbon and other elements was reported. Further details are provided in Section 9.3.

9.2.2 *SDC Prepared From FDU-15 Template*

Three different SDC materials have been prepared using FDU-15 template. They are differentiated by the template synthesis temperature and by the method of production used to prepare the template as described in Chapter 8. The nomenclature used reflects the template synthesis conditions of temperature, method of template production and whether at intermediate (IT) or final product (FP) stage of preparation. Method A materials prepared at 350 and 500°C have been designated as FDU-15-350A-SDC-IT, FDU-15-350A-SDC-FP, FDU-15-500A-SDC-IT and FDU-15-500A-SDC-FP. Method C materials prepared at 400°C have been designated as FDU-15-400C-SDC-IT and FDU-15-400C-SDC-FP. In order to create an SDC final product, the template was used in pellet or monolith form and vacuum impregnated with nitrate precursor solution using the preparation methods as presented in Chapter 4. All impregnated templates were subjected to a calcination profile of 400°C in an inert atmosphere using the pseudo closed container method. The typical thermal profile was in two stages: 200°C at a heating rate of 1°C min^{-1} and 1 h dwell followed by a 1°C min^{-1} rate to 400°C with 1 h dwell. The cooling rate was 2°C min^{-1}. Final product was prepared from intermediate material by removal of the carbon template and was achieved by heating in atmosphere at 400°C for 3 h using a ramp rate of 1°C min^{-1}.

The isotherm observed for FDU-15-350A-SDC-IT in (a) was typical of a type II profile with H2 hysteresis present.

Figure 9-4 (a) and (b) show a typical isotherm and associated specific pore size distribution (PSD) for FDU-15-350A-SDC-IT and FDU-15-350A-SDC-FP materials. The isotherm for FDU-15-350A-SDC-IT was typical of a type II profile with an associated type H2 hysteresis. The FDU-15-350A-SDC-FP product produced an isotherm of type I profile with a hysteresis best defined as H3. The FDU-15-350A-SDC-IT had one distinct peak observed at 3.4 nm whereas the FDU-15-350A-SDC-FP had a single broad peak centred at 4.9 nm as observed from the desorption branch as well as significant broad macropore distribution. Specific mesopore volumes ($\mathbf{V}_{meso}$) of 0.11 cm^3g^{-1} and 0.17 cm^3g^{-1}, micropore volumes ($\mathbf{V}_{micro}$) of 0.08 cm^3g and nil cm^3g^{-1}, average specific surface area ($\mathbf{S}_{BET}$) of 262 m^2g^{-1} and 64 m^2g^{-1} were recorded for FDU-15-350A-SDC-IT and FDU-15-350A-SDC-FP respectively.

Figure 9-4 (c) and (d) show a typical isotherm and associated specific pore size distribution (PSD) for FDU-15-500A-SDC-IT and FDU-15-500A-SDC-FP materials. The isotherm for FDU-

15-500A-SDC-IT was typical of a type II profile with an associated type H2 hysteresis. The FDU-15-500A-SDC-FP product produced an isotherm of type I profile with a hysteresis best defined as H2. The FDU-15-500A-SDC-IT had one distinct peak observed at 3.3 nm whereas the FDU-15-500A-SDC-FP had a single broad peak centred at 3.9 nm as observed from the desorption branch as well as significant broad macropore distribution. Specific mesopore volumes ($\mathbf{V}_{meso}$) of 0.10 cm^3g^{-1} and 0.16 cm^3g^{-1}, micropore volumes ($\mathbf{V}_{micro}$) of 0.06 cm^3g and nil cm^3g^{-1}, average specific surface area ($\mathbf{S}_{BET}$) of 217 m^2g^{-1} and 122 m^2g^{-1} were recorded for FDU-15-500A-SDC-IT and FDU-15A-500-SDC-FP respectively.

Figure 9-4 (e) and (f) show a typical isotherm and associated specific pore size distribution (PSD) for FDU-15-400C-SDC-IT and FDU-15-400C-SDC-FP materials. The isotherm for FDU-15-400C-SDC-IT was typical of a type IV profile with an associated type H2 hysteresis. The FDU-15-400C-SDC-FP product produced an isotherm of type IV profile with a hysteresis best defined as H3. The FDU-15-400C-SDC-IT had one distinct peak observed at 6.3 nm whereas the FDU-15-400C-SDC-FP had a single broad peak centred at 5.5 nm as observed from the desorption branch as well as significant broad macropore distribution. Specific mesopore volumes ($\mathbf{V}_{meso}$) of 0.16 cm^3g^{-1} and 0.21 cm^3g^{-1}, micropore volumes ($\mathbf{V}_{micro}$) of 0.02 cm^3g and nil cm^3g^{-1}, average specific surface area ($\mathbf{S}_{BET}$) of 214 m^2g^{-1} and 147 m^2g^{-1} were recorded for FDU-15-400C-SDC-IT and FDU-15-400C-SDC-FP respectively.

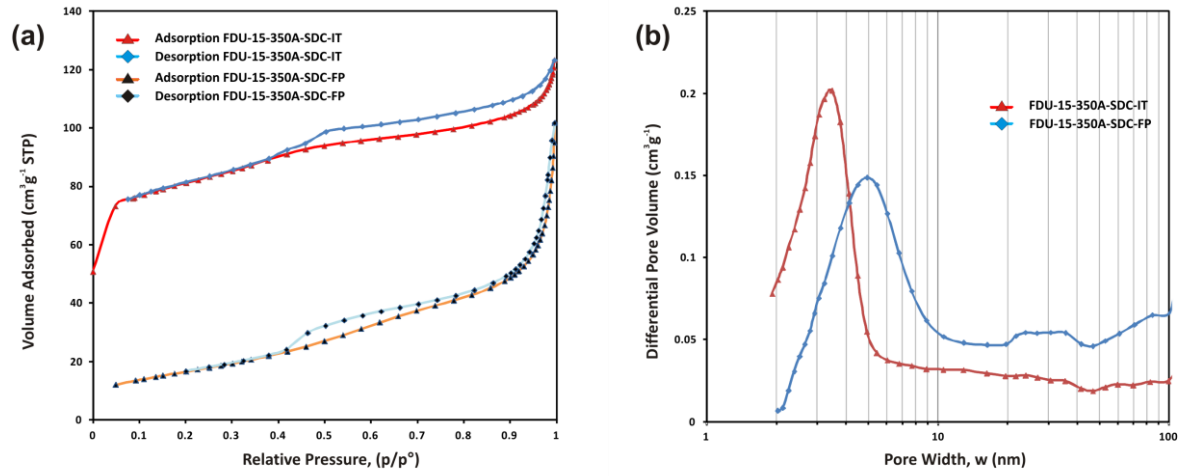

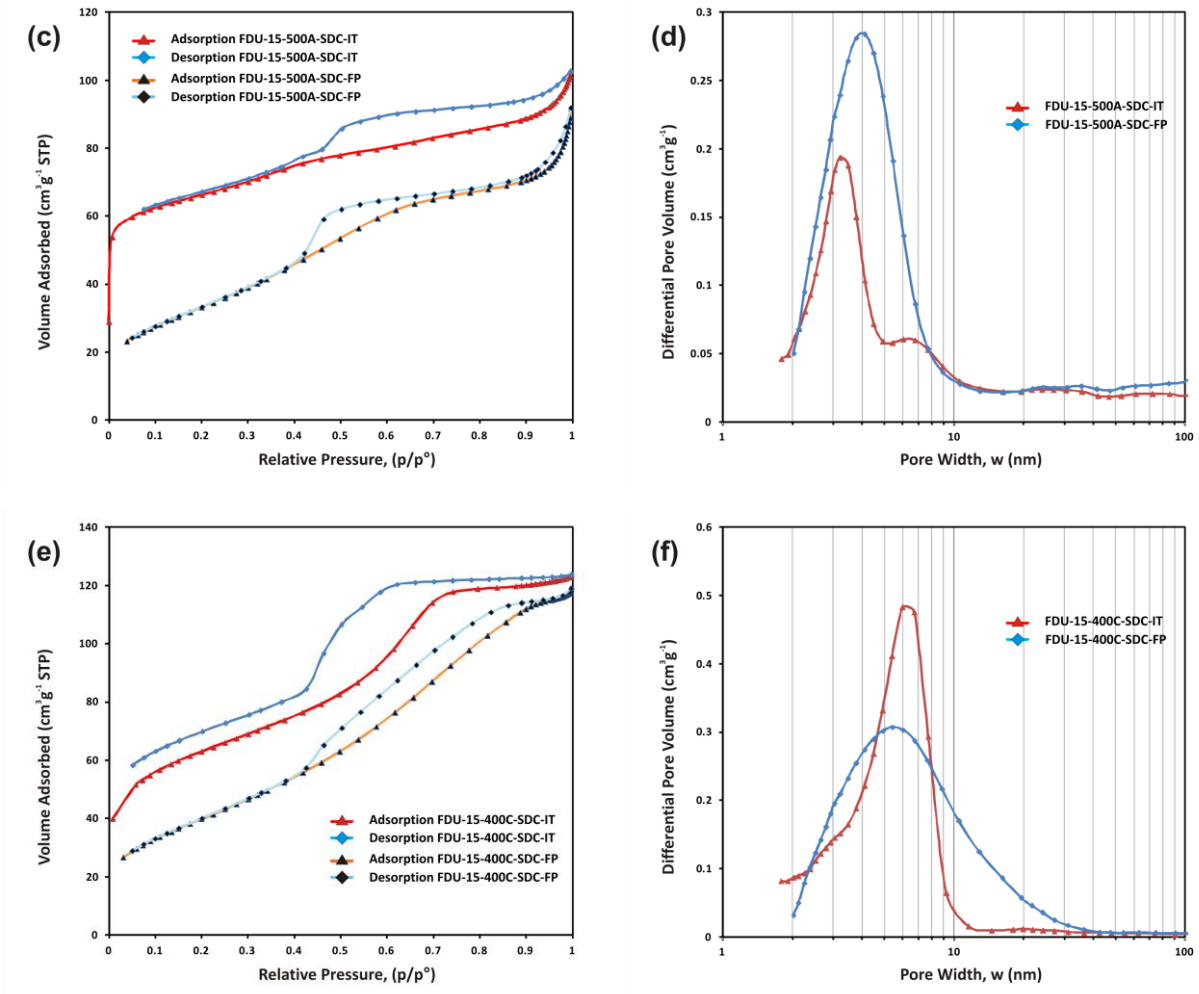

Figure 9-4: Nitrogen physisorption isotherms (a) and Pore size distributions (b) for FDU-15-350A-SDC-IT and FDU-15-350A-SDC-FP; Nitrogen physisorption isotherms (c) and Pore size distributions (d) for FDU-15-500A-SDC-IT and FDU-15-500A-SDC-FP; Nitrogen physisorption isotherms (e) and Pore size distributions (f) for FDU-15-400C-SDC-IT and FDU-15-400C-SDC-FP.

A summary of the data values for each intermediate material and final product is presented in Table 9-2.

Table 9-2. Gas physisorption data for SDC materials prepared using FDU-15 template: Values for pore size distribution (w_{BJH}), specific surface area (S_{BET}), mesopore volume (V_{meso}) and micropore volume (V_{micro}).

Sample	w_{BJH} (nm)	S_{BET} (m^2g^{-1})	V_{meso} (m^3g^{-1})	V_{micro} (cm^3g^{-1})
FDU-15-350A-SDC-IT	3.4	262	0.11	0.08
FDU-15-350A-SDC-FP	4.9	64	0.17	nil
FDU-15-500A-SDC-IT	3.3	217	0.10	0.06
FDU-15-500A-SDC-FP	3.9	122	0.16	nil
FDU-15-400C-SDC-IT	6.2	214	0.16	0.02
FDU-15-400C-SDC-FP	5.5	147	0.21	nil

The images presented in Figure 9-5 are representative of the FDU-15-350C-SDC-FP material as viewed using TEM. A significant proportion of the material was found to be composed of nanoparticles of SDC. Despite this, areas existed where rod like structure formations could be viewed, Figure 9-5 (a), with three areas each highlighted by a red arrow. In Figure 9-5 (b) there appears to be a series of poorly formed rods composed of individual particles partially fused together. No high structural ordering was produced but several long range sequences of poorly formed rod-pore-channels were viewed and presented in the Figure 9-2 (c) and (d).

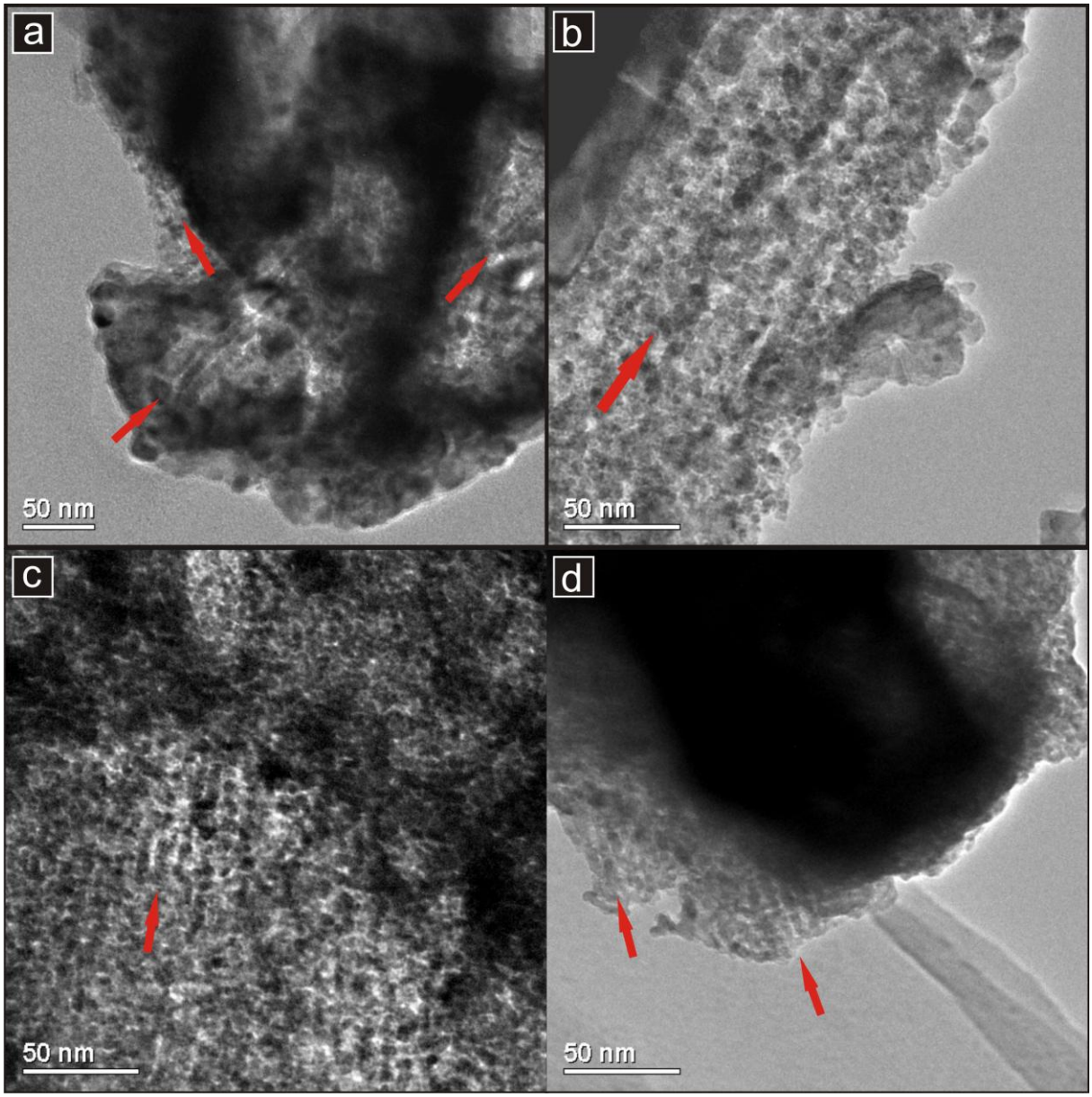

Figure 9-5: TEM images of FDU-15-350A-SDC-FP (a) An image showing the majority of the sample as particulate agglomeration but with rod like structures evident in three areas as indicated by the red arrows. (b) An image with what appears to be particles partial formed into a rod like structure. (c) A large area with poorly defined rod formation. (d) Several rods in parallel with pore channels visible.

The images presented in Figure 9-6 are representative of the FDU-15-500A-SDC-FP material as viewed using TEM. Large particles were frequently viewed with rod like structure formations across entire particles as presented in Figure 9-6 (a) and (b). The structure was unidirectional with a series of well formed, bundled rods each in close proximity with one another and with visible spacing between them Figure 9-6 (c) and (d). However, the rod to rod alignment appeared to be non-uniform. The image Figure 9-6 (e) of a series of rods was presented where some of them appeared to be complete and fused along their length while in some other instances the rods appeared to be composed of individual particles. Figure 9-6 (g) and (h) are higher magnifications of Figure 9-6 (f) where the crystal nature of the rod was evidenced by way of associated lattice planes. A $\boldsymbol{d_{TEM}}$ wall thickness of 8.6 nm was estimated however the pore width $\boldsymbol{w_{TEM}}$ was unable to be reliably determined.

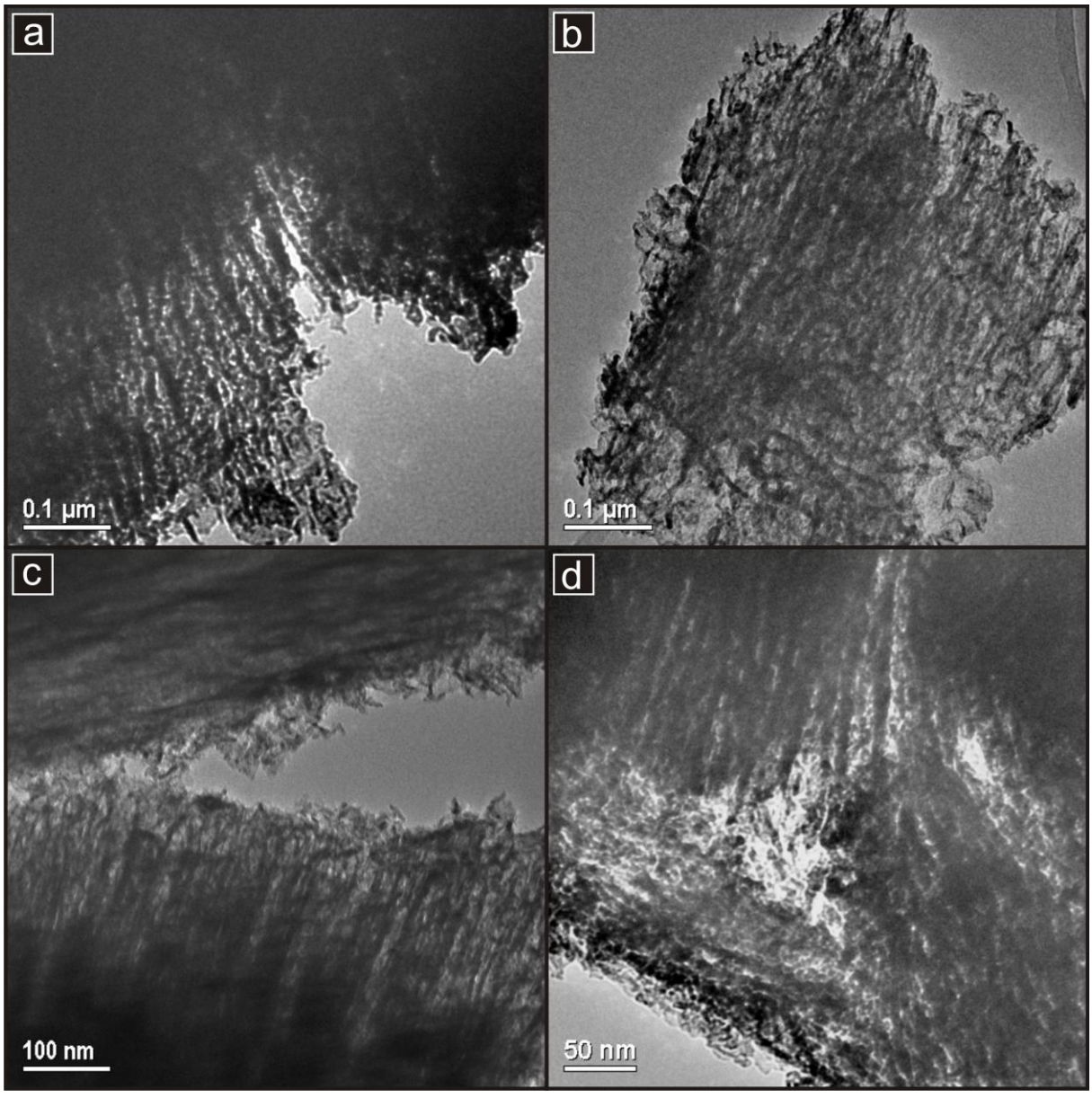

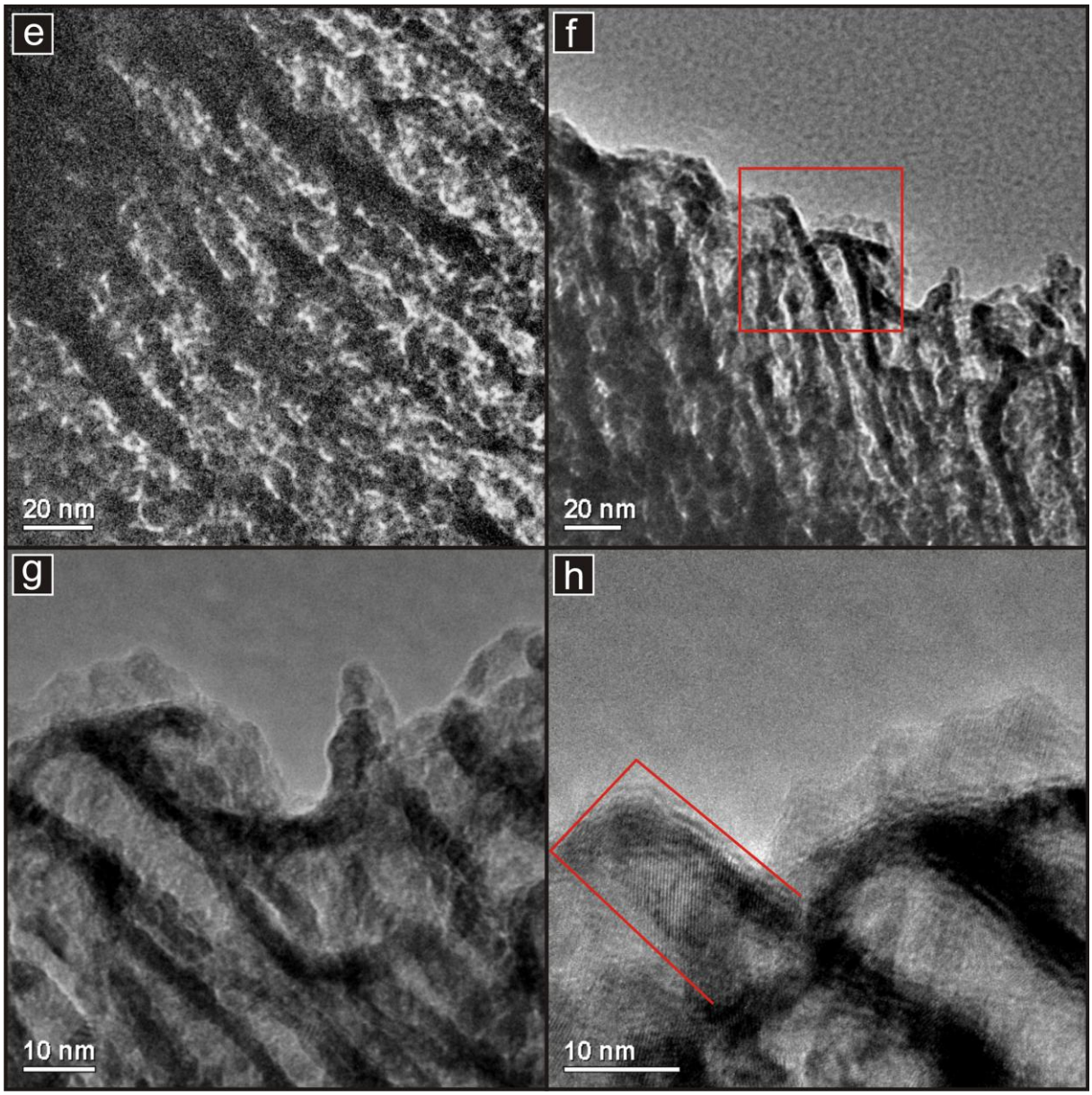

Figure 9-6: TEM images of FDU-15-500A-SDC-FP, (a) and (b) Low magnification images of particles with long range rod ordering, (c) and (d) uni-directional alignment of the rod like structures, (e) and (f) view of the particle formation in the rod like structures (e) and (f) higher magnification of the are in (f) with a zoned area in (h) showing the crystal nature of a rod and its associated lattice planes.

The images presented in Figure 9-7 are representative of the FDU-15-400C-SDC-FP material as viewed using TEM. The material was found to have good long range order Figure 9-7 (a) and (b), with rod like channels that appeared to be well formed. The continuous sequence of rod- pore channel-rod was in good evidence for the majority of the viewed sample Figure 9-7 (c) and (d) although individual articles and discontinuous rod formation was occasionally observed. Typical absences were shown in Figure 9-7 (c) by the indicating arrows and what appears to be an isolated particle in Figure 9-7 (d) was presented as an insert. The Figure 9-7 (e) gives an insight into the rod formation with a sequence of interlinked nodules a common

feature. The continuous interlink between the nodules was viewed in Figure 9-7 (f) with regular porous areas that appeared to be slit like in shape.

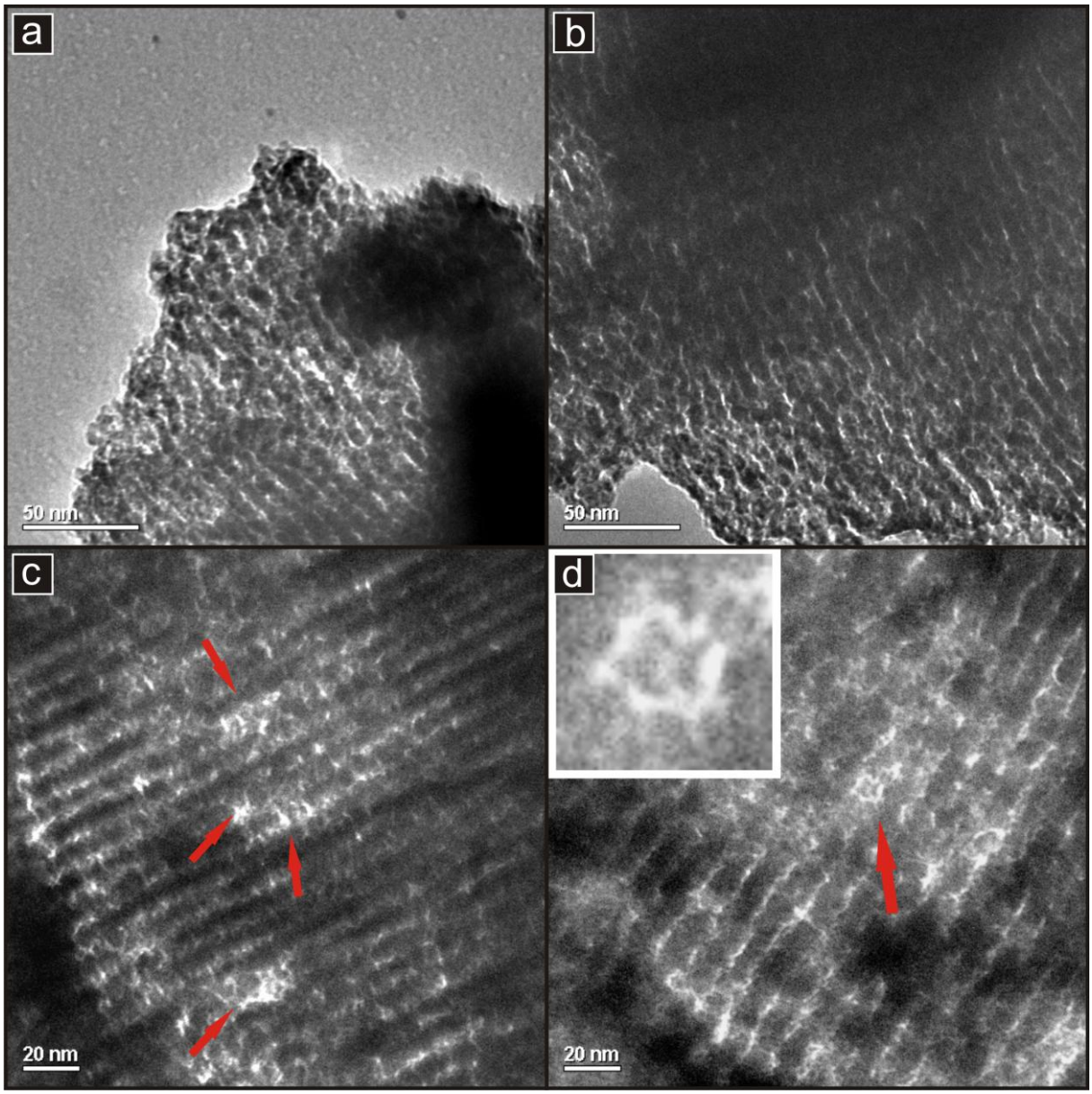

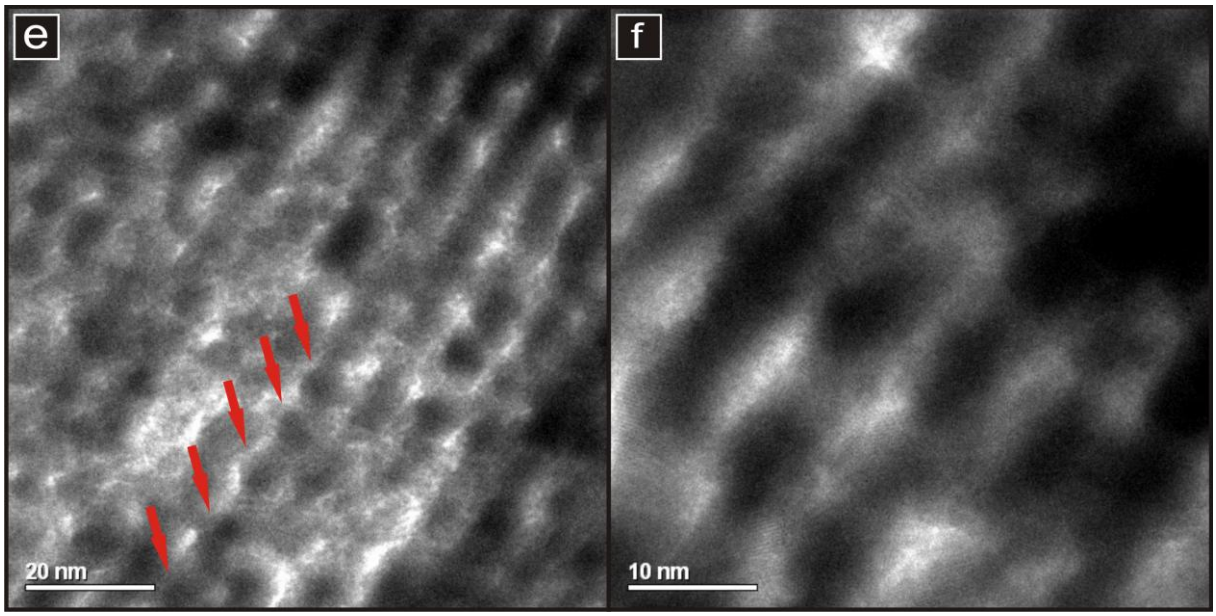

Figure 9-7: TEM images of FDU-15-400C-SDC-FP (a) and (b) low magnification images showing the extensive range of channel order, (c) highlights the discontinuities in rod formation, (d) example of an isolated particle in the matrix of a rod, (e) the repetitive nodules along the formation of the rod as indicated by the red arrows, (f) high resolution image showing the nodules and their fusion along the length of a rod.

Gas physisorption comparison of FDU-15 SDC IT products with associated FDU-15 templates all indicated a level of impregnation. The main mesopore peak and associated maximum mesopore volumes were reported as for FDU-15-350A, FDU-15-500A and FDU-15-400C as being 4.8, 4.8 and 7.8 nm; 1.2, 1.1 and 2.5 cm^3g^{-1} respectively. The main mesopore peak and associated maximum mesopore volumes were reported for FDU-15-350A-SDC-IT, FDU-15-500A-SDC-IT and FDU-15-400C-SDC-IT as being 3.4, 3.3 and 6.2 nm; 0.2, 0.2 and 0.5 cm^3g^{-1} respectively. This indicates that a high level of impregnation was likely and a 1.5 ± 0.1 nm pore shrinkage occurred.

The SDC materials prepared using 350 and 500°C Method A templates showed a significant proportion of inter-particle macroporosity with FDU-15-350A-SDC-FP having approximately double the macropore volume of FDU-15-500A-SDC-FP. The material prepared from Method C showed an insignificant amount of macropore formation indicating that either the change in template synthesis, calcination procedure of the template or combination of both has improved the overall quality of replication. The calcination procedure at the nitrate conversion step can be dismissed as a mitigating factor as it was consistent between all products. The FDU-15-500A-SDC-FP material when imaged using TEM indicated a crystallised structure formed in a rod like fashion in accordance with it being an inverse of the starting template. The rods appeared to be well structured however their alignment in respect to one another appeared to be non-uniform indicating that the material was

partially formed. A possible explanation for this is that the nanobridges required to keep the material in a parallel structure may have failed to form properly.

The initial decision to use 600°C as a calcination temperature was to emulate that used in silica template nanocasting. Further, it was thought probable that the preparation of this material at higher temperatures would see a greater degree of particle fusion towards highly crystalline materials [128]. During the course of research, Sun et al[54] investigated the optimal conditions for metal nitrate conversion and reported that from the use of a pseudo-closed container, crystallisation could be achieved between a temperature range of 200 to 400°C. A major determining variable in the control of crystal growth during nitrate conversion within a template was sample container volume and not temperature. A calcination procedure using key temperatures of 200 and 400°C as previously described was therefore adopted for impregnated FDU-15C to emulate the optimised conditions.

FDU-15-400C-SDC-FP displayed good TEM evidence of rod like structures which were, in contrast to FDU-15-500A-SDC-FP material, parallel and uniform with regular spacing between rods. The associated pore structure between channels appeared to be slit shaped and this is further corroborated with the gas physisorption profile indicating a type 3 hysteresis. TEM images indicated a repetitive nodule crystal growth feature along the length of the rods. A possible growth mechanism has been proposed where individual particles are nucleated along and within the confinement of the template pore channel. These dimensionally hindered individual particles may sinter with neighbouring particles and form bridges along the length of the channel. Alternatively, the formation may be directly related to the shape of the pore channel of the template. High resolution TEM images (Figure 8-9) of the template did not appear to corroborate this as no regular expansions in the pore channel from which an inverse structure could be mirrored was evident.

9.2.3 *SDC Prepared From FDU-16 Template*

SDC material as a final product has been synthesised using FDU-16 template that was prepared in an inert atmosphere at 500°C as outlined in Chapter 8. Final product synthesised from FDU-16 template prepared in an inert gas atmosphere at 350°C did not yield product with any meaningful characterisation and therefore no data is presented. No SDC has been attempted from template prepared using Oxygen. In order to create SDC final product, the template was used in pellet form and vacuum impregnated with nitrate precursor solution using the preparation methods as presented in Chapter 4. The material was then calcined in an inert atmosphere to 600°C and referred to as intermediate product

with the nomenclature FDU-16-500-IT. Final product (FDU-16-500-FP) was prepared from intermediate material by removal of the carbon template and was achieved by heating in atmosphere at 400°C for 3 hours using a ramp rate of 1°C min^{-1}.

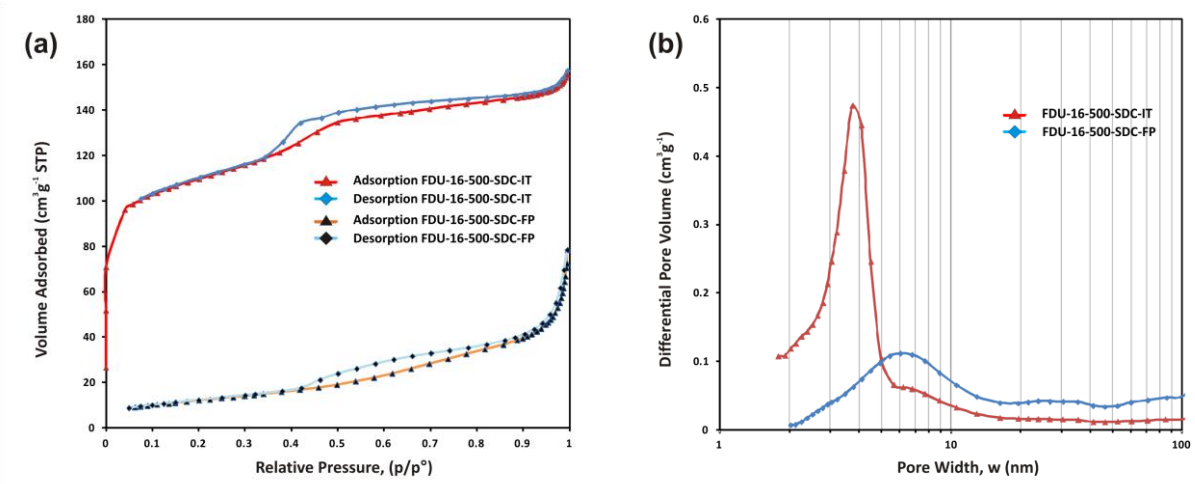

Figure 9-8: Nitrogen physisorption isotherms (a) and Pore size distributions (b) for FDU-16-500-SDC-IT and FDU-16-500-SDC-FP.

Table 9-3 summarises the gas physisorption data obtained using the BET (specific surface area), t-plot (microporosity volume) and BJH (mesopore size distribution and volume) methods.

Table 9-3. Gas physisorption data for FDU-16 template: Values for pore size distribution (w_{BJH}), specific surface area (S_{BET}), mesopore volume (V_{meso}) and micropore volume (V_{micro}).

Sample	w_{BJH} (nm)	S_{BET} (m^2g^{-1})	V_{meso} (m^3g^{-1})	V_{micro} (cm^3g^{-1})
FDU-16-500-SDC-IT	3.8	362	0.10	0.10
FDU-16-500-SDC-FP	6.0	44	0.13	nil

Figure 9-9 presents representative TEM analyses of FDU-16-500-SDC-FP material. A continuous framework structure was viewed Figure 9-9 (a) and (b) and found to be interspersed with regular pores. This porous arrangement appeared to be organised in an array of ordered regular sized pores as presented in Figure 9-9 (c) with a series of red arrows pointing to the pore locations. The image Figure 9-9 (d) indicates the lattice arrangement composed of a crystal wall network that appeared to have several regular branches which were repeating across the width of the particle and stacked into the third dimension. A

higher magnification of this structure as indicated by the red box and viewed in Figure 9-9 (e). A high magnification of two adjoining pores in Figure 9-9 (f) was representative of the regular pore size observed.

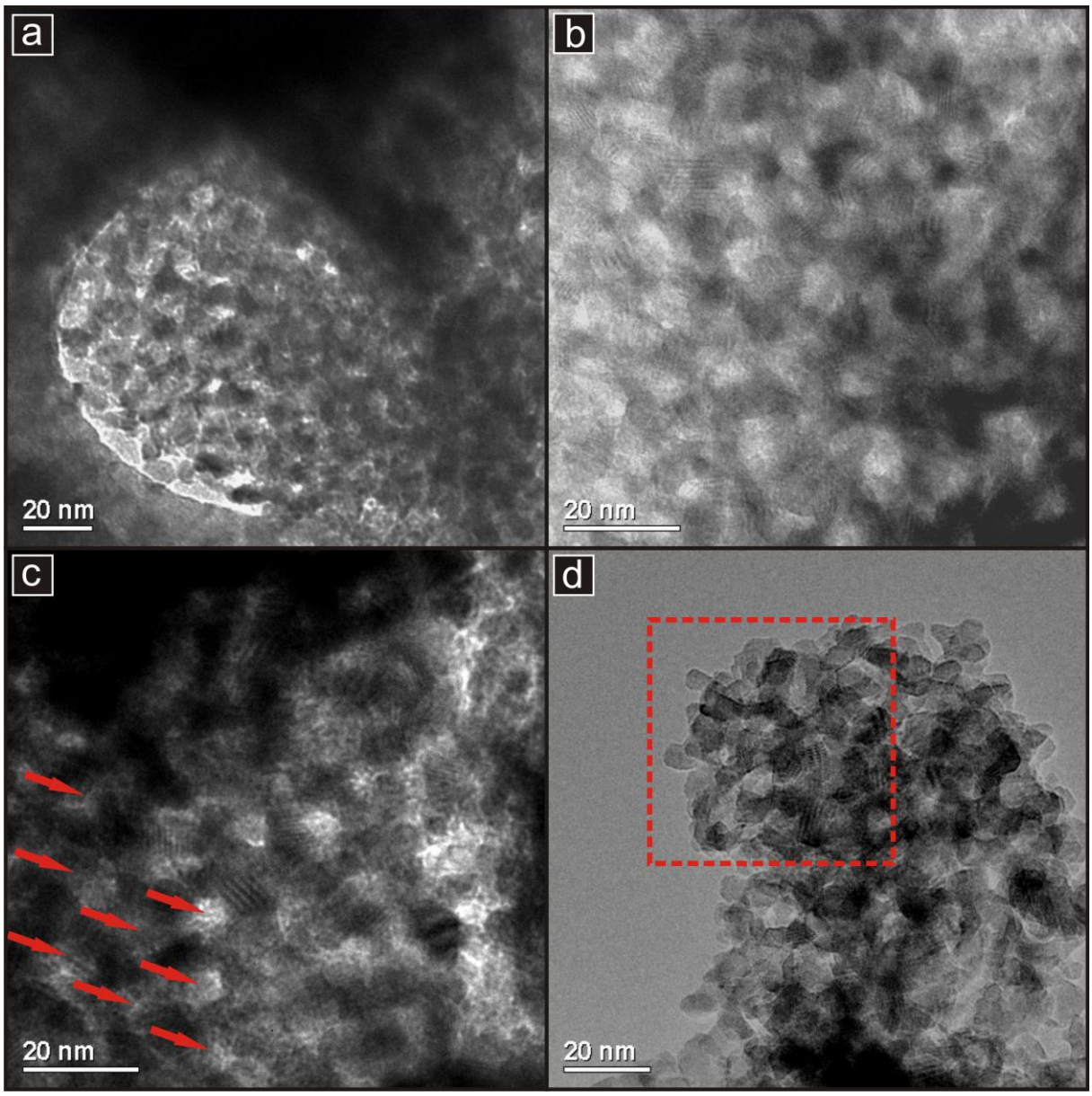

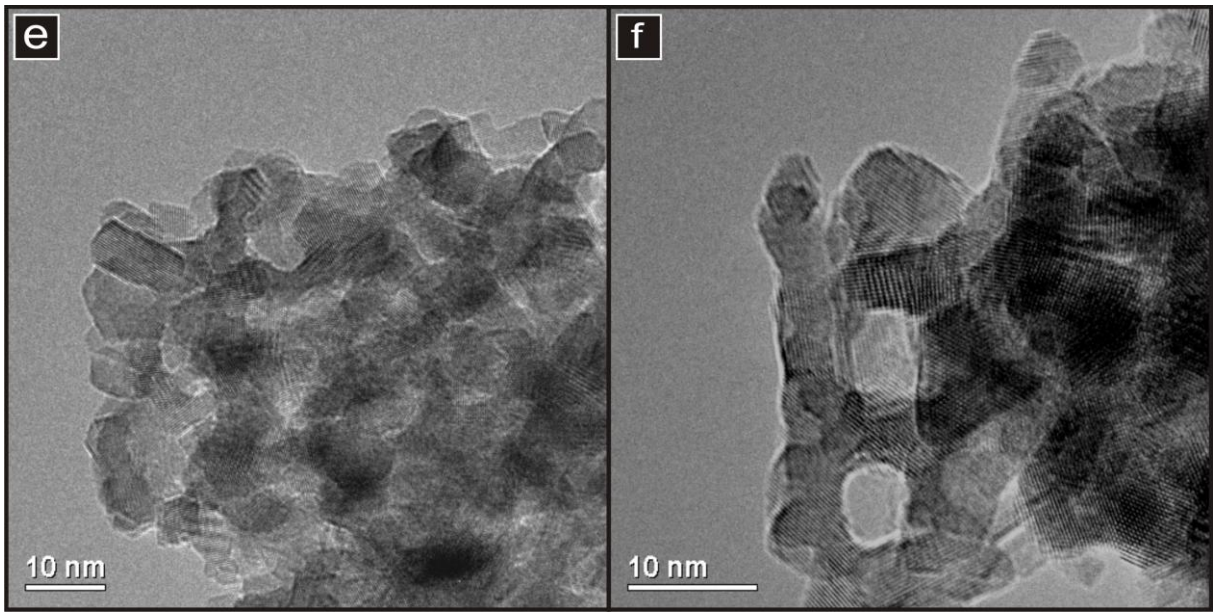

Figure 9-9: TEM images of FDU-16-500-SDC-FP (a) and (b) Images showing the framework interspersed with regular pores, (c) a higher magnification image with red arrows pointing to an array of visible pores, (d) 3-D crystal framework with visible pores, (e) a higher magnification of the red area highlighted in image d, (f) high resolution image showing two pores within the framework.

The pore width w_{TEM} was estimated to be in the 5 nm range and wall thickness d_{TEM} of 5 nm. This is in good agreement with the reported PSD for the material and concurs within 1 nm of the inverse values of PSD for the template.

The impregnation of the FDU-16-500 template was low in comparison to other OMC templates and indicates an approximate change of 25% as a reduction in the pore volume of the main mesopore peak that is centred at 3.8 nm. A broad peak was present across the distribution range of FDU-16-500-SDC-FP including the macropore range which is associated with particulate agglomeration. This would indicate that yield of quality material within the bulk of the sample was low with a reduced specific mesopore peak at the PSD V_{meso} of 6 nm. This would also support the recording of reduced surface area whilst significant mesopore volume was maintained in comparison with other nanocast SDC products. Despite the bulk quality being low, ordered mesoporous material was imaged and reported in the TEM figures accordingly. It appeared that structures with regular arrays of mesopores were present and the crystalline wall structure was cubic in formation.

9.3 Elemental Composition Analysis

In order to verify that all materials were free of carbon template a series of EDX analysis were carried out. Figure 9-10 was a visual indicator of the typical change observed when the carbon template-SDC intermediate material had the template removed. Image (a) was

representative of all the intermediate materials and retains the characteristic black colour of the template. Subsequent removal of the template using a 3 h atmospheric heat treatment at 400°C occurs with an associated colour change from black to yellow indicating that the majority of the template has been removed.

Figure 9-10: Photograph of (a) carbon template with SDC impregnated after calcination but before template removal, (b) the same material after 3 h atmospheric heat treatment at 400°C.

To quantitatively verify the amount of carbon remaining, a series of EDX analysis were performed for all template varieties. Figure 9-11 is a typical representation of the chemical composition change observed going from (a) carbon template, (b) impregnated template - intermediate product- and (c) final product. The strong K_α peak at 0.277 keV associated with carbon is evident in both (a) and (b). This carbon peak was reduced to below 2 wt% and only present at background level in (c). No other elements are present and the material was consistently above 98 wt% samarium, cerium and oxygen and in ratios consistent with $Sm_{0.2}Ce_{0.8}O_{1.9}$. Fig (d) is included as a comparative sample that has been prepared using a solvo-thermal method and is a preparation method that produces similar SDC but devoid of any form of carbon template. The EDX analysis of the sample records an identical carbon background reading of below 2 wt% and high purity SDC material.

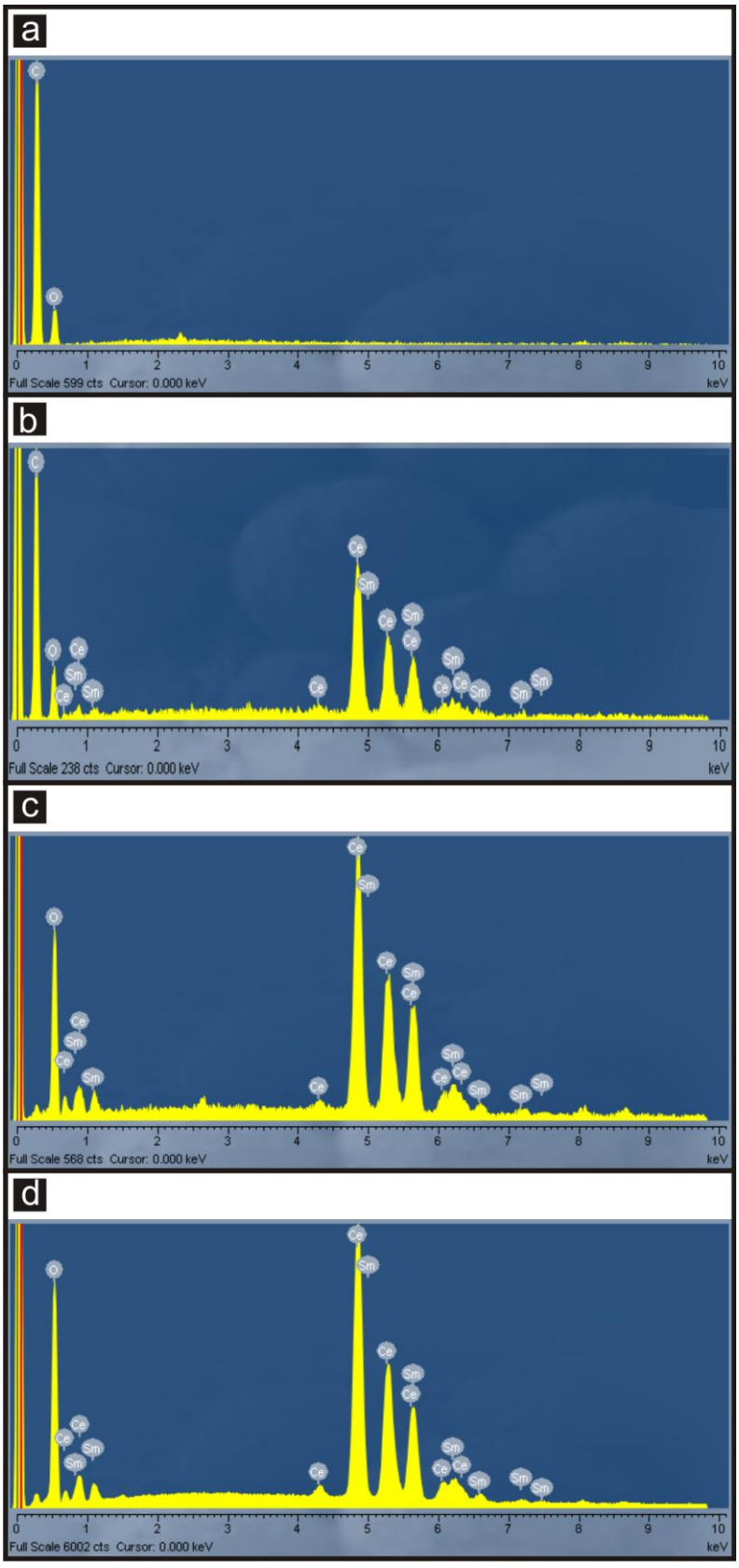

Figure 9-11: EDX analysis of (a) carbon template, (b) impregnated carbon template with $Sm_{0.2}Ce_{0.8}O_{1.9}$ after calcination, (c) final product $Sm_{0.2}Ce_{0.8}O_{1.9}$ after template removal, (d) $Sm_{0.2}Ce_{0.8}O_{1.9}$ prepared using a process not involving carbon (solvo-thermal method).

9.4 X-Ray Diffraction of SDC Materials Prepared From Carbon Templates

In order to verify the crystalline nature of the SDC final products templated from the carbon structures, X-Ray diffraction was performed over a range of 5 to 90° in order to view the crystal lattices and compare with SDC prepared without the use of template but with similar 2/400°C calcinations (400°C calcinations with 1 hour dwell at 200°C). As the first viewable peak is at 28.5°, the range displayed has been curtailed to a starting point of 20°. The diffraction patterns were consistent with the fluorite phase of samarium doped ceria.[149]

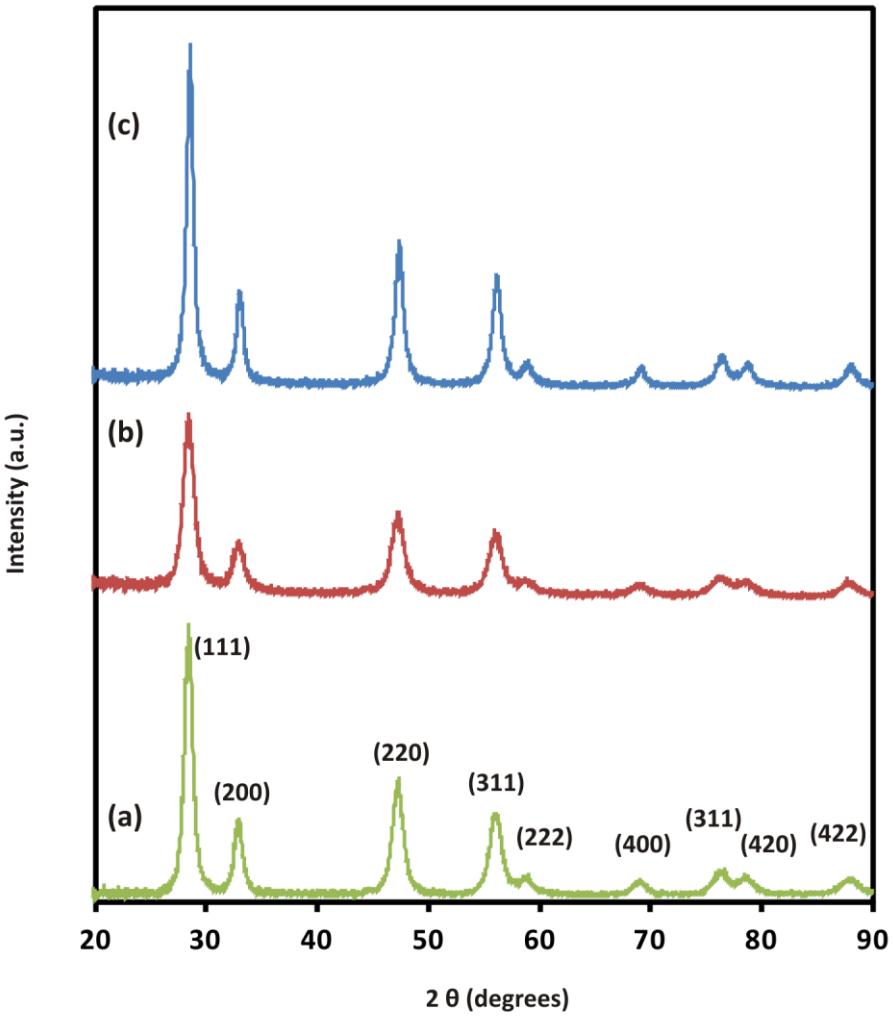

Figure 9-12: XRD Patterns of SDC final product templated from the carbon structures of (b) FDU-15 and (c) FDU-16 and compared to (a) template free 2/400°C SDC product.

9.5 Summary

The use of ordered mesoporous carbon prepared at 500°C and the 350°C polymer derivative was found to be receptive in allowing mixed metal nitrates of samarium and cerium to be impregnated as a saturated ethanol solution. The carbon templates FDU-14, FDU-15 and FDU-16 had a unique effect on the structure and properties of the SDC final product. For

FDU-14, this included increasing the specific pore volume and specific surface area while maintaining a crystal framework around a controlled range of mesopore sizing. FDU-14-500-O2-FP was produced with a specific mesopore size distribution that was confined in an orderly manner around an SDC crystalline framework and reflective of the wall thickness of the FDU-14 template. The properties of high specific surface area and pore volume are comparable to SDC material made from *Ia3d* silica template (KIT-6) material.

The material prepared using FDU-15A at 350°C was indicating partially formed structures. This same template prepared material calcined at 500°C produced a more coherent rod like structure and was comparable to material produced from FDU-15C template. This material FDU-15-400C-FP was produced with a specific mesopore size distribution and wall thickness that is comparable with the inverse structural proportions of its associated template. Impregnation using this template under the calcination 200/400°C profile produced a final product with a framework composed of parallel rods and regular mesoporous spacing. The composition of each rod appeared to be constructed from a series of fused individual particles arranged sequentially along the length of the rods. In between the rod channels, pores have been formed that appear slit like in shape. The properties of high specific surface area and pore volume are comparable to SDC material made from *p6mm* silica template (SBA-15) material.

An SDC final product was produced using an FDU-16 template. The specific surface area was low in comparison to other nanocasted SDC materials although the specific mesopore volume was of a similar value. TEM Images indicated mesopore size distributions that were confined in an orderly manner around an SDC crystalline framework. The wall and pore thickness as measured from the TEM images indicated that the structure was in good agreement with the expected inverse template structure.

Removal of carbon template was achieved efficiently using a thermal method thereby avoiding the use of chemical etching. The amount of carbon remaining was analysed at below 2 wt% with the SDC material showing no other elements present from EDS analysis.

Careful process optimisation of the templates should lead towards better fidelity and higher yields of ordered mesoporous SDC. These techniques should also be transferable into synthesising other mixed metal oxides with the benefits of high purity through the minimal use of inorganic materials in the preparation.

Chapter 10

Preparation of Template Free SDC

10.1 Introduction

The preparation of materials using a combustion synthesis method – also referred to as self-propagating high temperature synthesis – was first reported in the 1970's[136]. It has found favour as a nanomaterials preparation method as the approach is simple, repeatable and scalable making it cost effective. It has also been found to allow intimate mixing of starting reagents such that trace amounts of dopant elements can be homogenously incorporated into the final product in a single step[137]. This has led to a number of publications as well as review articles [136a, 138]. A subset of combustion synthesis is solution combustion synthesis in which the reaction medium is liquid as opposed to a solid or gas (flame combustion) [139]. When the fuel of choice is an alcohol, a nomenclature of alcohothermal synthesis has also been employed [140]. Solution combustion synthesis is a self-sustaining reaction that combines the oxidising agent with a fuel which then combusts when the appropriate ignition temperature is reached. The oxidising agent is often a metal nitrate and is used in combination with urea, glycine or hydrazide as the fuel source. An aqueous solution is normally employed as the solvent medium for both the fuel and metal salts. Literature reports have suggested that the fuel has a duel role; it acting as both a complexing[141] agent or surfactant[142] and as the source of chemical energy. During the combustion process a large amount of gas is evolved which helps in limiting the inter-particle contact with the result that ultrafine powders are formed[143]. Several authors have reported the preparation of doped ceria products using combustion synthesis methods, sometimes with specific surface area (SSA) as high as 200 m^2g^{-1}, but in each instance they are producing an array of individual nanoparticles with no framework structure[144]. Control of the synthesis parameters has generated a variety of novel microstructures ranging from size specific nanoparticles[145] to nanosphere[142] ,nanospindle[146] and nanocube[147] architectures. The value of doped ceria has been recognised for some time given its useful properties of high ionic conductivity and catalytic activity. Much research has focussed on producing ceria-based powders with specific nanoscale properties. For example, the preparation of size-specific crystalline nanoparticles of gadolinium doped ceria by way of a glycine combustion

synthesis was used as a starting material in the manufacture of dense solid oxide fuel cell (SOFC) electrolytes[144a]. However, porous crystalline ceria-based materials are also of considerable interest both for catalysis applications and for catalytic anode materials in SOFCs. The pore structure would allow high specific surface area and good gas phase transport in addition to the other benefits of using doped ceria. For these reasons several manufacturing methods such as the use of soft[148] and hard templating[57d] have been applied to produce doped ceria with porous structures. However, these methods are often procedurally complex with multiple steps which can make them expensive and time-consuming.

An alternative method is presented here that achieves a crystalline doped ceria that has the desired mesoporous structure by using a simple procedure based on a solvo-thermal approach without the aid of template or surfactants. Further, it has been shown that the properties of the pore structure can be controlled by careful selection of the parameters of temperature and container volume during synthesis. The products were characterised using gas adsorption, XRD and electron microscopy (TEM) with elemental analysis (EDX).

10.2 Template Free SDC Nomenclature

In order to achieve an SDC oxide of stoichiometric ratio $Sm_{0.2}Ce_{0.8}O_{1.9}$, The procedure for preparing a saturated solution of the mixed metal nitrates was followed as detailed in Section 4.6. An amount of solution, 1.0 g ± 0.05 g, was placed into a ceramic boat (88 mm in length by 16 mm wide and 8 mm deep) or 1.5 g ± 0.05 g into a boat of size (105 mm in length by 22 mm wide and 15mm deep). This represents a sample ratio of 1:1.5 and a boat volume ratio of 1:3. The larger boat therefore represents an increased closed container volume per g of sample and not simply a doubling of sample preparation. Samples prepared in the small and large boats have been given the nomenclature SB and LB throughout the text. The boats were placed in the muffle furnace and the heating programme started without significant delay (i.e. 15 mins). Heating programmes were performed with either an open container (OC) – the boat had no lid or restriction on top – or a closed (CC) container, strictly a pseudo closure of the boat where ceramic slates were positioned to cap 80 – 90% of the boat opening.

The calcinations were performed in static air in a muffle furnace of 20 L capacity. The conditions of maximum temperature, dwell times, ramp rate and boat size are listed in Table 10-1, which also states the associated nomenclature.

Approximately 0.15 g of product was obtained per gram of saturated nitrate solution. All products had foam-like structures which were easily collapsed to a powder using a spatula. When open container calcination was performed, the material was found to rise just above the ceramic boat whereas in the closed container the product was restricted within the boat. No further treatment – such as centrifuge filtration or milling – was applied.

Table 10-1: Nomenclature and preparation methods for SDC materials synthesised in either open (OC) or pseudo closed containers (CC).

Sample	Preparation Method
SDC-400-OC	1°C min^{-1} heating rate to 400°C, with no dwell in a small boat open container.
SDC-600A-OC	1°C min^{-1} heating rate to 600°C, with no dwell in a small boat open container.
SDC-600B-OC	2°C min^{-1} heating rate to 600°C, with no dwell in a small boat open container.
SDC-800-OC	1°C min^{-1} heating rate to 800°C, with no dwell in a small boat open container.
SDC-2/400-CC-SB	1°C min^{-1} heating rate to 200°C with 1 hour dwell then 400°C with 1 hour dwell in a small boat pseudo closed container.
SDC-400-CC-SB	1°C min^{-1} heating rate to 400°C with no dwell in a small boat pseudo closed container.
SDC-400-CC-LB	1°C min^{-1} heating rate to 400°C with no dwell in a large boat pseudo closed container.
SDC-600-CC-SB	1°C min^{-1} heating rate to 600°C with no dwell in a small boat pseudo closed container.
SDC-600-CC-LB	1°C min^{-1} heating rate to 600°C with no dwell in a large boat pseudo closed container.
SDC-800-CC-SB	1°C min^{-1} heating rate to 800°C with no dwell in a small boat pseudo closed container.
SDC-800-CC-LB	1°C min^{-1} heating rate to 800°C with no dwell in a large boat pseudo closed container.

10.3 Results

10.3.1 *Gas Physisorption*

The gas sorption isotherms presented in Figure 10-1 are typical of Type IV mesoporous solids with hysteresis best defined as H1 for both the open (OC) and closed (CC) container methods.

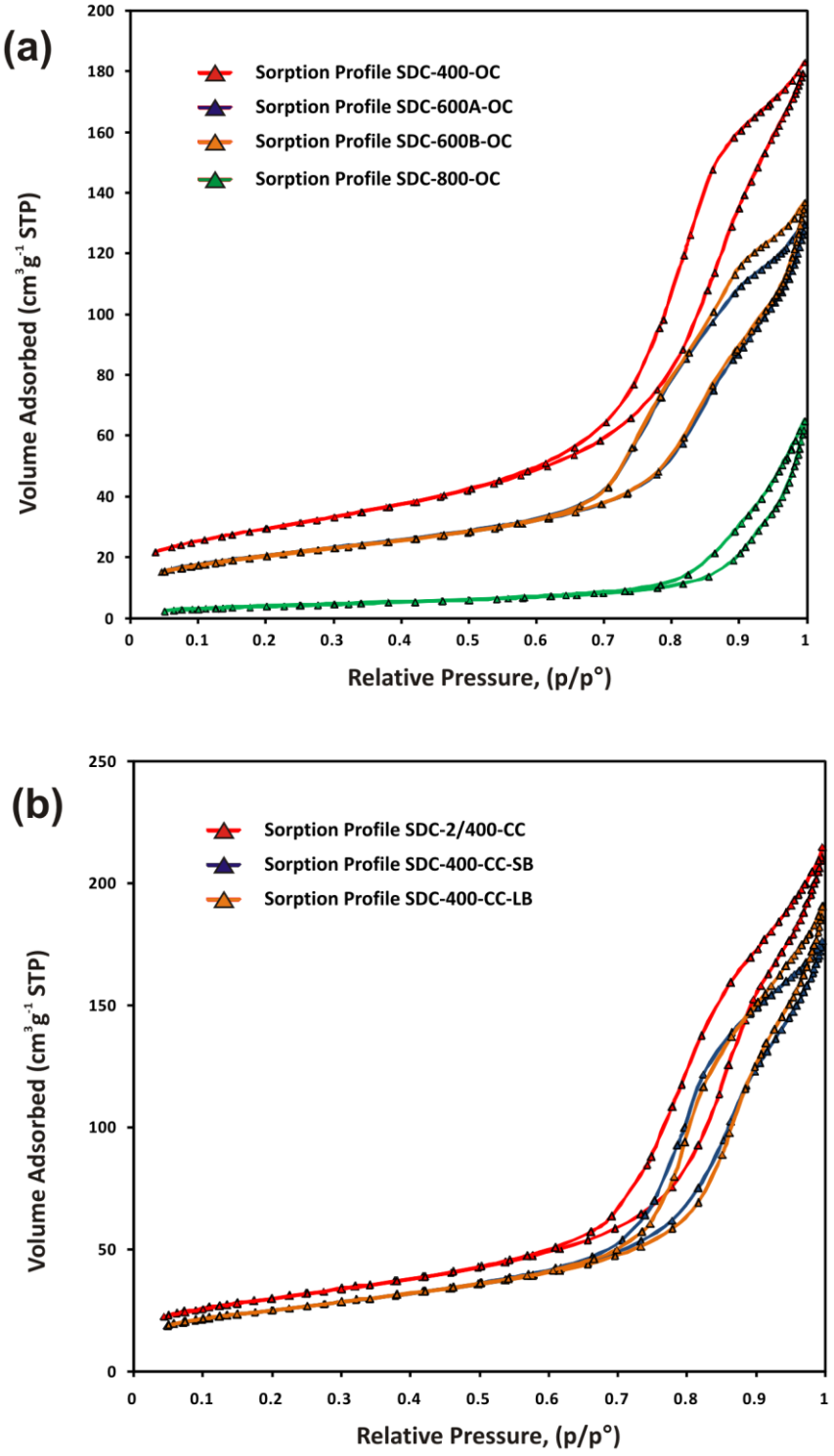

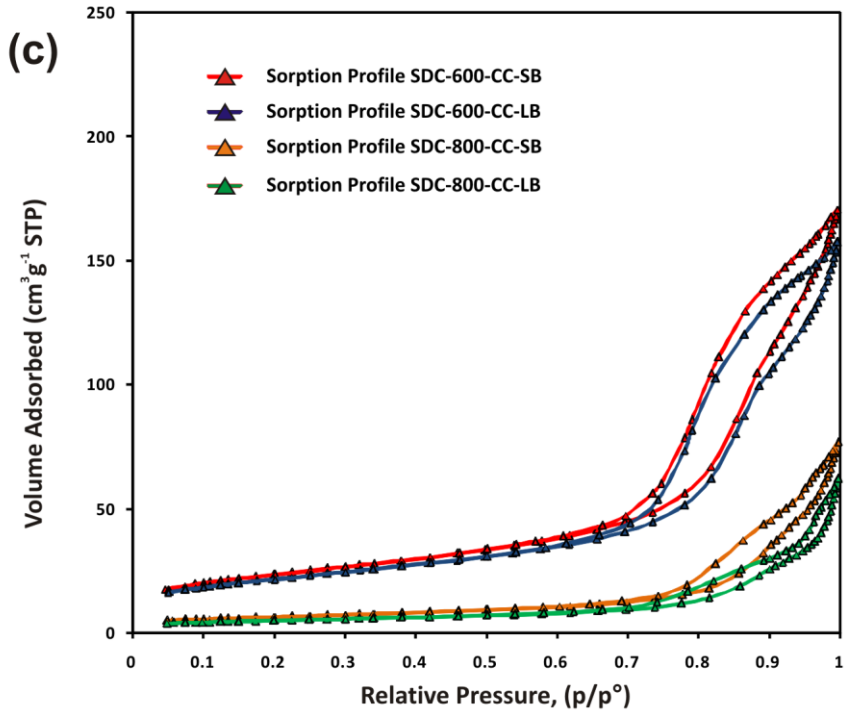

Figure 10-1: Gas physisorption isotherms of SDC products manufactured using (a) open container (b,c) closed container methods. Isotherms are typical of mesoporous solids with IUPAC defined type IV profile and H1 hysteresis. The closed container isotherms have been split for purposes of clarity.

Using the Brunauer-Emmett-Teller (BET) approach, the specific surface area ($\mathbf{S_{BET}}$, m^2g^{-1}) of the products was obtained. Barrett-Joiner-Halenda (BJH) algorithms were utilised to obtain the pore size distribution (PSD) and mesopore volume ($\mathbf{V_{meso}}$, cm^3g^{-1}) for each product. Representative values for pore size, w_{BJH}, were obtained from the maximum in differential pore volume in the PSDs. The t-plot method was utilised to obtain micropore volume ($\mathbf{V_{micro}}$, cm^3g^{-1}). These data values are tabulated in Table 10-2 and PSDs are presented in Figure 10-1 (a) and (b).

Table 10-2: Representative pore size (w_{BJH}), specific meso (V_{meso}) and micro (V_{micro}) pore volume and specific surface area (S_{BET}) of SDC material prepared using open container (OC) and closed container (CC) methods.

Sample	w_{BJH} (nm)	V_{meso} (cm^3g^{-1})	V_{micro} (cm^3g^{-1})	S_{BET} (m^2g^{-1})
SDC-400-OC	12.9	0.30	0.001	103
SDC-600A-OC	12.9	0.21	0.003	72
SDC-600B-OC	13.0	0.23	0.003	71
SDC-800-OC	24	0.11	nil	15
SDC-2/400-CC-SB	15	0.36	0.007	105
SDC-400-CC-SB	16	0.29	0.003	89
SDC-400-CC-LB	17	0.31	0.003	89
SDC-600-CC-SB	16	0.28	0.005	83
SDC-600-CC-LB	15	0.26	0.004	77
SDC-800-CC-SB	20	0.13	0.002	23
SDC-800-CC-LB	16	0.10	0.002	17

Considering first the PSDs for the products made using the OC method, the pore size is seen to have increased significantly as treatment temperature increased from 400 to 600 then to 800°C. The PSD for SDC-400-OC shows a single peak at a pore size of 6.5 nm while that for SDC-600-OC displays both a main peak at 12.9 nm and a shoulder at around 25 nm and SDC-800-OC exhibits only a small peak at 23.7 nm. Mesopore volume, $\mathbf{V}_{meso}$, increased from SDC-400-OC to SDC-600-OC and then decreased sharply for SDC-800-OC. Micropore volumes are extremely small for all samples. SSA decreased with increasing preparation temperature, showing a sharp decrease between samples prepared at 600 and 800 °C. Comparing the PSDs and data from Table 10-2 for SDC-600A-OC and SDC-600B-OC shows that increasing the ramp rate had little effect, causing a small increase in pore volume ($\mathbf{V}_{meso}$), but no change in pore size or SSA.

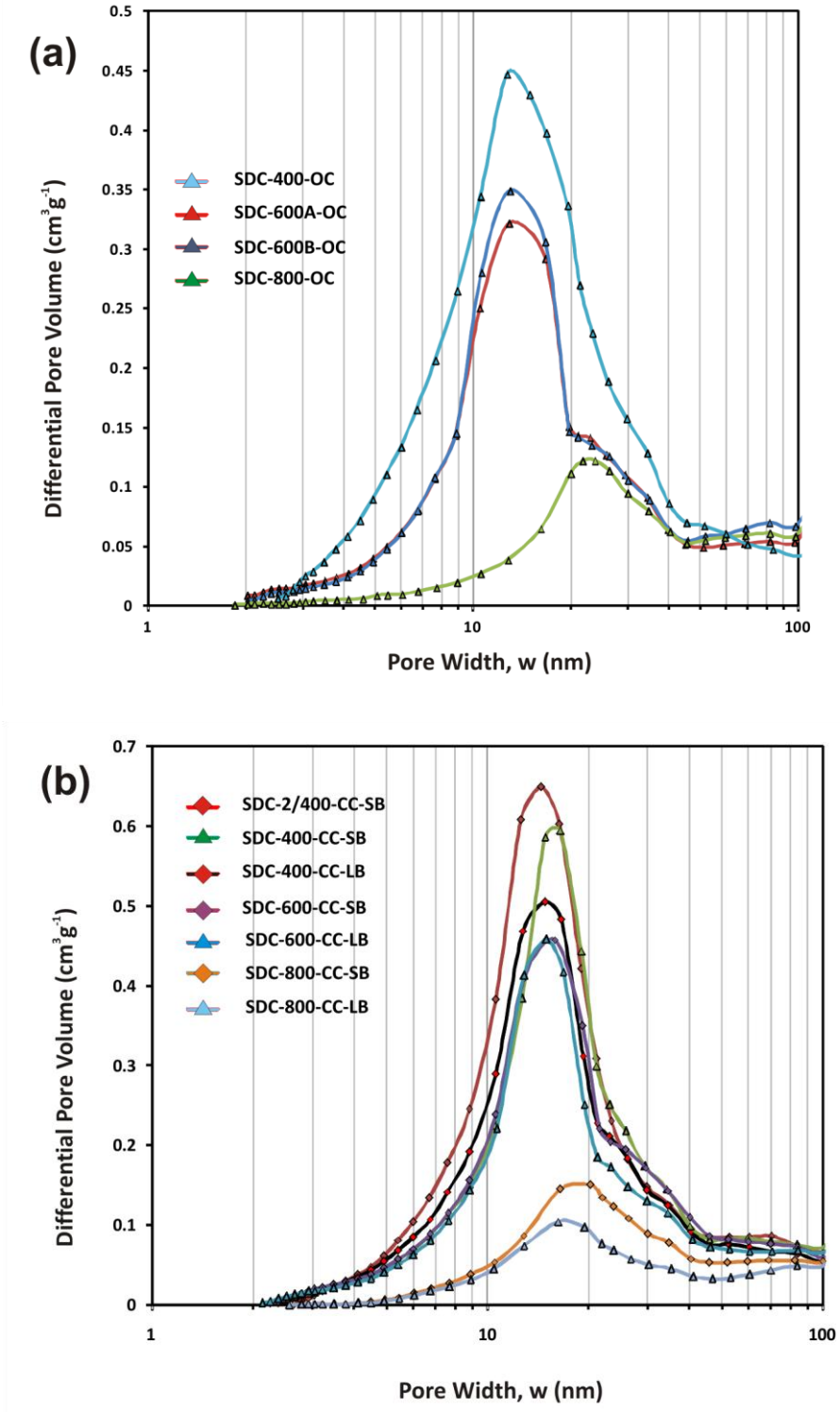

Figure 10-2: Pore Size Distribution of SDC products manufactured from (a) open container (b) closed container.

Turning to the samples prepared by the CC method, the changes in pore size with treatment temperature are much less marked than that for the OC samples. Values of w_{BJH} for samples prepared at 400 and 600 °C are very similar (15-16 nm, with small shoulders at higher values) and, although there is an increase for preparation at 800 °C (20 and 16 nm), it is smaller than for the OC case. Pore volume (V_{meso}) is largest for preparations at 400 °C, falls

slightly for samples made at 600 °C and then drops sharply for the 800 °C cases. $\mathbf{V}_{meso}$ is consistently slightly higher for CC samples than for corresponding OC samples. In Figure 10-2(b), peaks for CC samples are generally much sharper than those for the OC samples, implying a narrower pore size distribution in the former. Values for SSA deceased with increasing temperature in a similar way as for the OC samples but have consistently higher values. Use of a small container (SB) rather than a large one gives rise to slightly smaller pores, lower $\mathbf{V}_{meso}$ but similar SSAs at 400 °C but larger pores and higher $\mathbf{V}_{meso}$ and SSA at the higher preparation temperatures.

10.3.2 *Transmission Electron Microscopy*

To further investigate the porous nature of the samples indicated by the gas sorption results, a representative selection of samples were imaged using TEM. Figure 10-3 presents images of the sample SDC-600-OC. At low magnifications, a structure of randomly arranged mesopores is observed consistently throughout the sample (Figure 10-3(a)). At higher magnifications, the crystalline nature of the particles comprising the porous structure is confirmed by the observation of lattice planes (Figure 10-3(b-d)). At these higher magnifications, the sample appears to consist of crystalline walls surrounding pores. One such structure is highlighted in Figure 10-3(c) and (d) by a red line and clearly shows parallel lattice planes in the material surrounding a central area of approximately 5 nm where no observable lattice planes exist. The interconnecting crystalline walls appear to be between 5 and 8 nm in thickness.

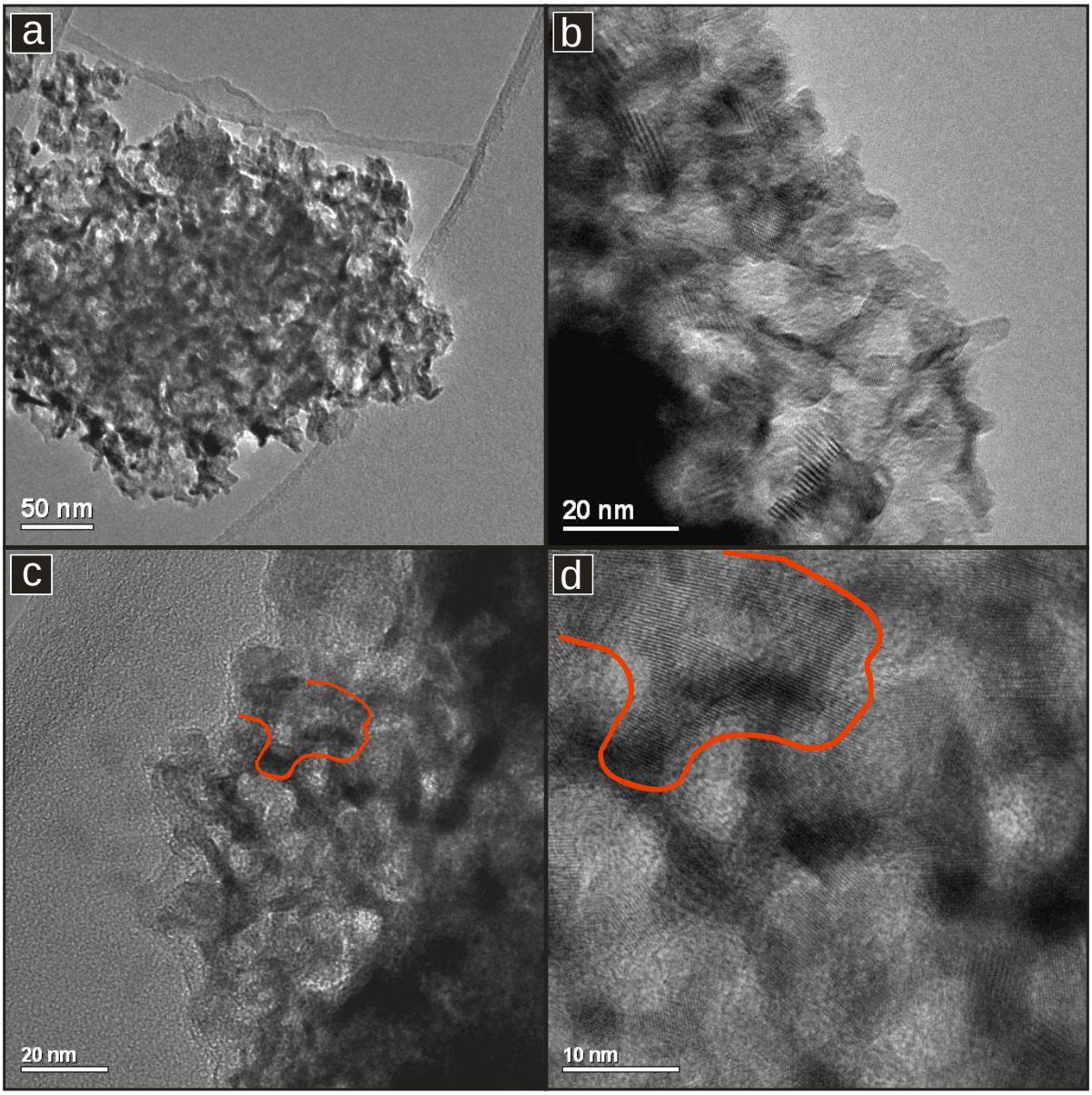

Figure 10-3: TEM images of SDC-600-OC showing its disordered mesoporous nature: (a,b) the disordered porous framework across the entirety of the particle; (c) pore surrounded by crystalline walls; (d) greater magnification of a crystalline wall surrounding a pore (indicated by the red line) showing lattice planes.

Figure 10-4 show TEM images of the SDC-2/400-CC-SB sample, prepared by the CC method. A disordered structure of mesopores is seen throughout the sample and is very similar to that seen in Figure 10-3. Again, crystalline walls of thickness 5 – 8 nm are seen to surround pores. An example – with a 15 nm diameter pore – is presented in Figure 10-4 (c) and (d). The alignments of the SDC lattice planes in the wall surrounding the pore are clearly seen.

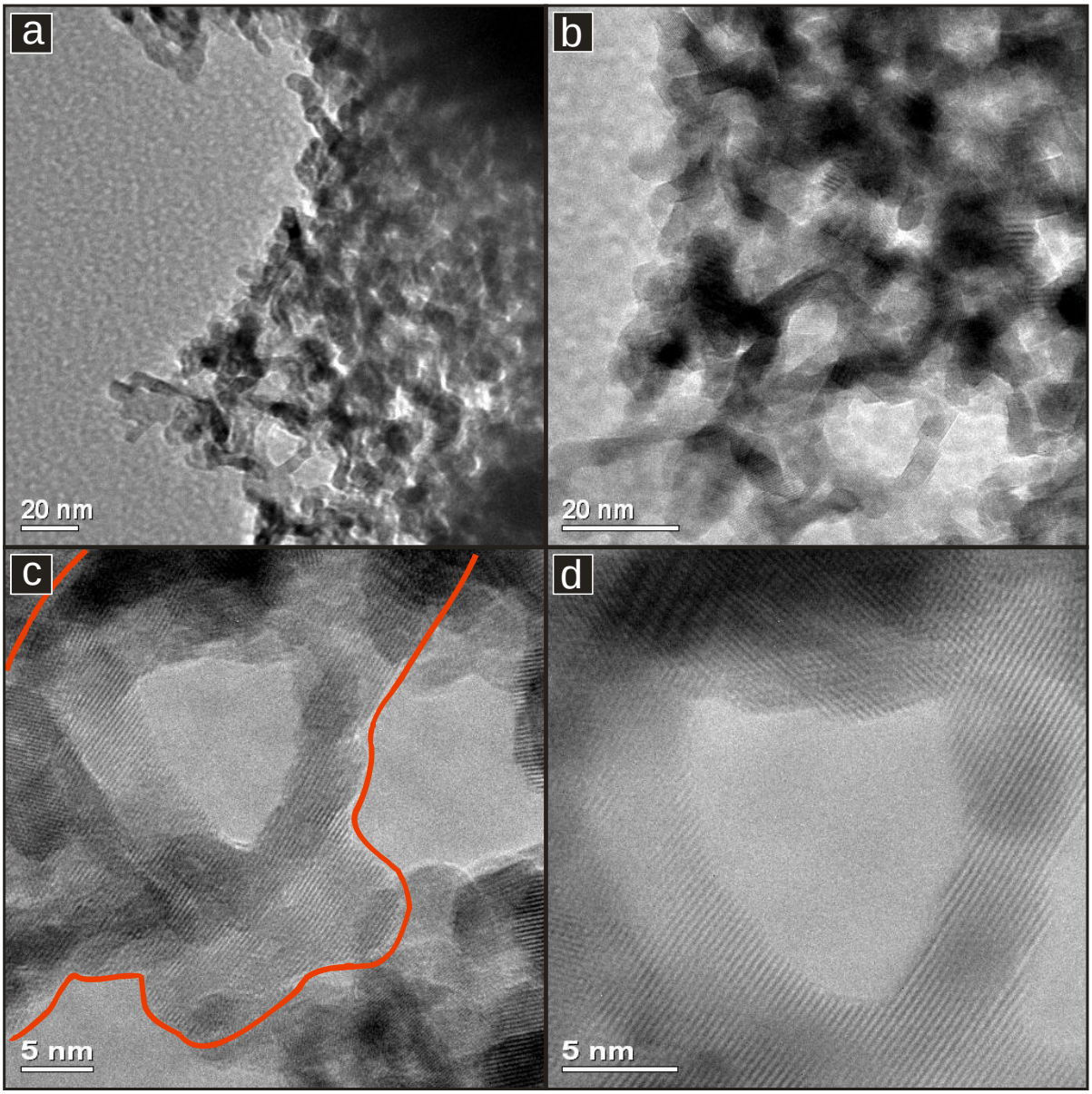

Figure 10-4: TEM images of SDC-2/400-CC-SB: (a,b) disordered mesoporous structure; (c) crystalline walls surrounding a pore within the PSD range reported, indicated by the red line; (d) High magnification image of the wall structure surrounding a pore with the aligned lattice planes in evidence.

Figure 10-5 presents images of the sample SDC-800-CC-SB. The mesopores seen in samples prepared at lower temperatures is not observed here. The only pores being those between randomly distributed SDC crystallites. It is clear also that these crystallites are much larger than in the other samples images (SDC-600-OC and SDC-2/400-CC-SB), with diameters of around 20 nm.

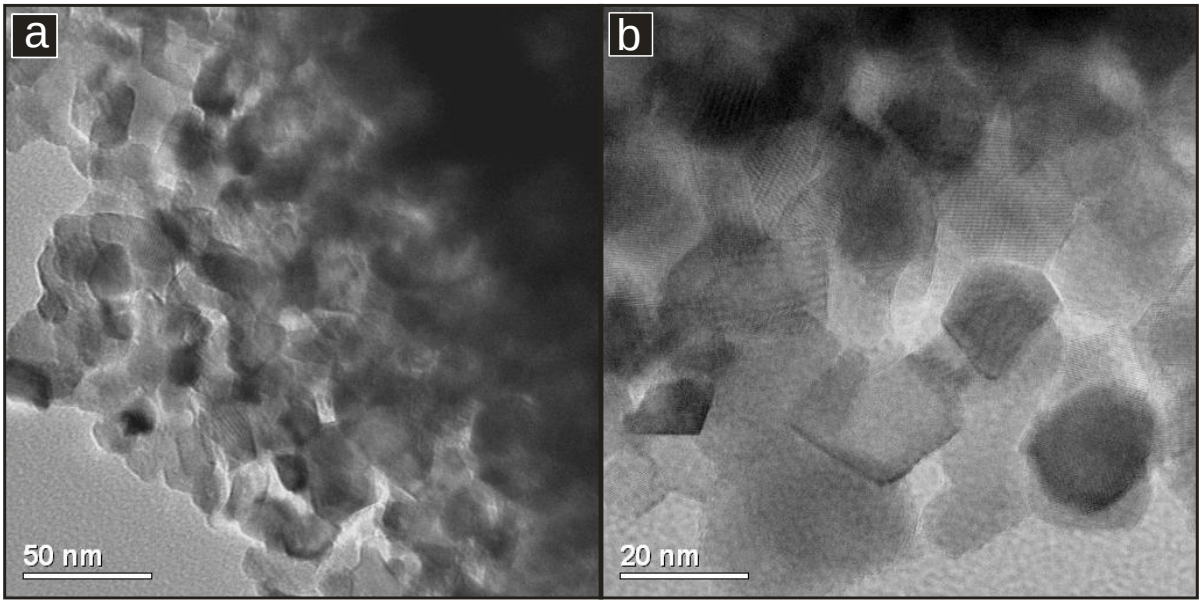

Figure 10-5: TEM images of SDC-800-CC-SB showing: (a) the apparently random agglomeration of particles without the mesopores seen after lower temperature preparations (b) the crystalline particles.

10.3.3 *X-Ray Diffraction*

Diffraction patterns for all samples were consistent with the cubic fluorite phase of samarium doped cerium oxide[149] and are presented in Figure 10-6. There is a noticeable change from broad, less intense peaks to sharper peaks of higher intensity as the calcination temperature was increased for both OC and CC series. The Scherrer equation (Eqn. 14) was used to estimate average crystallite size, $\boldsymbol{D_{xrd}}$.

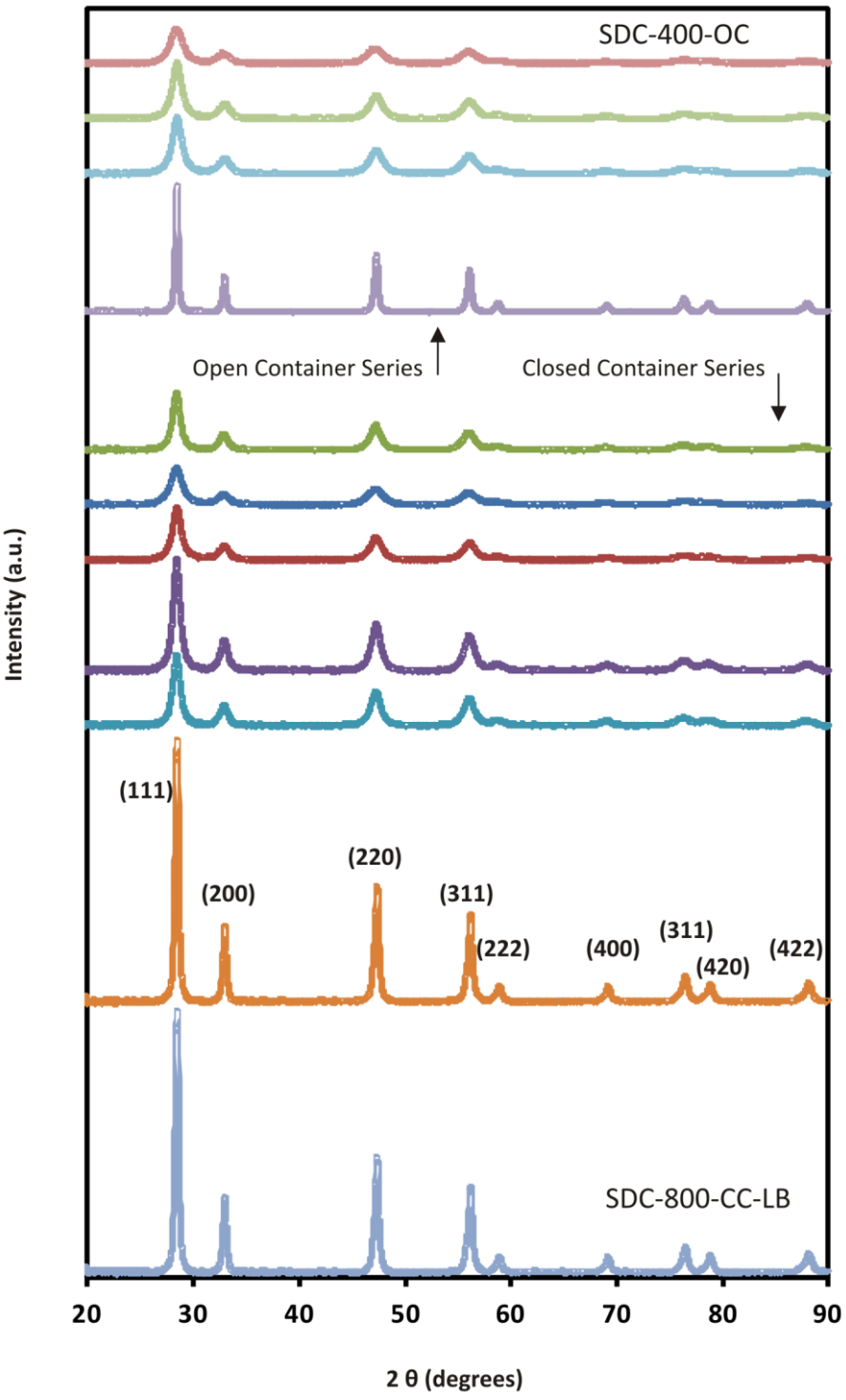

Figure 10-6: XRD patterns of the SDC series displayed from top (SDC-400-OC) to bottom (SDC-800-CC-LB) as listed in **Table 10-1**.

Lattice parameter (***a***) and associated unit cell volume (***V***) was also calculated from the XRD patterns and summarised, together with D_{xrd} values, in Table 10-3. The D_{xrd} values indicate crystal growth as calcination temperature was increased. Extending calcination time also

caused crystallite size to increase in SDC-2/400-CC-SB compared to SDC-400-CC-SB. Larger crystallite sizes were observed in CC samples than in the corresponding samples prepared by the OC method. However, as mentioned above, SSA values were generally higher for the CC samples than for the corresponding OC samples.

Table 10-3: Lattice parameter (***a***), unit cell volume (***V***)and crystallite size (D_{XRD}) of SDC material prepared using open container (OC) and closed container (CC) methods.

Sample	a *(Å)* (± 0.0005)	V *(Å^3)*	D_{XRD} *(nm)*
SDC-400-OC	5.4396	160.95	6.1
SDC-400-OC-R	5.4358	160.62	5.4
SDC-600A-OC	5.4349	160.54	8.1
SDC-600B-OC	5.4347	160.52	8.0
SDC-800-OC	5.4306	160.16	31.0
SDC-2/400-CC	5.4349	160.54	8.7
SDC-400-CC-SB	5.4359	160.63	5.6
SDC-400-CC-LB	5.4298	160.09	7.2
SDC-600-CC-SB	5.4350	160.55	11.1
SDC-600-CC-LB	5.4353	160.57	10.7
SDC-800-CC-SB	5.4286	159.98	33.6
SDC-800-CC-LB	5.4289	160.01	33.3

10.3.4 *EDX Mapping*

Figure 10-7 presents an image of the sample SDC-600-CC-SB together with corresponding elemental maps obtained using EDX for O, Ce and Sm. These maps show that these elements have a coincident distribution across the agglomeration imaged. This indicates that the material contained no segregated phases and was chemically homogenous.

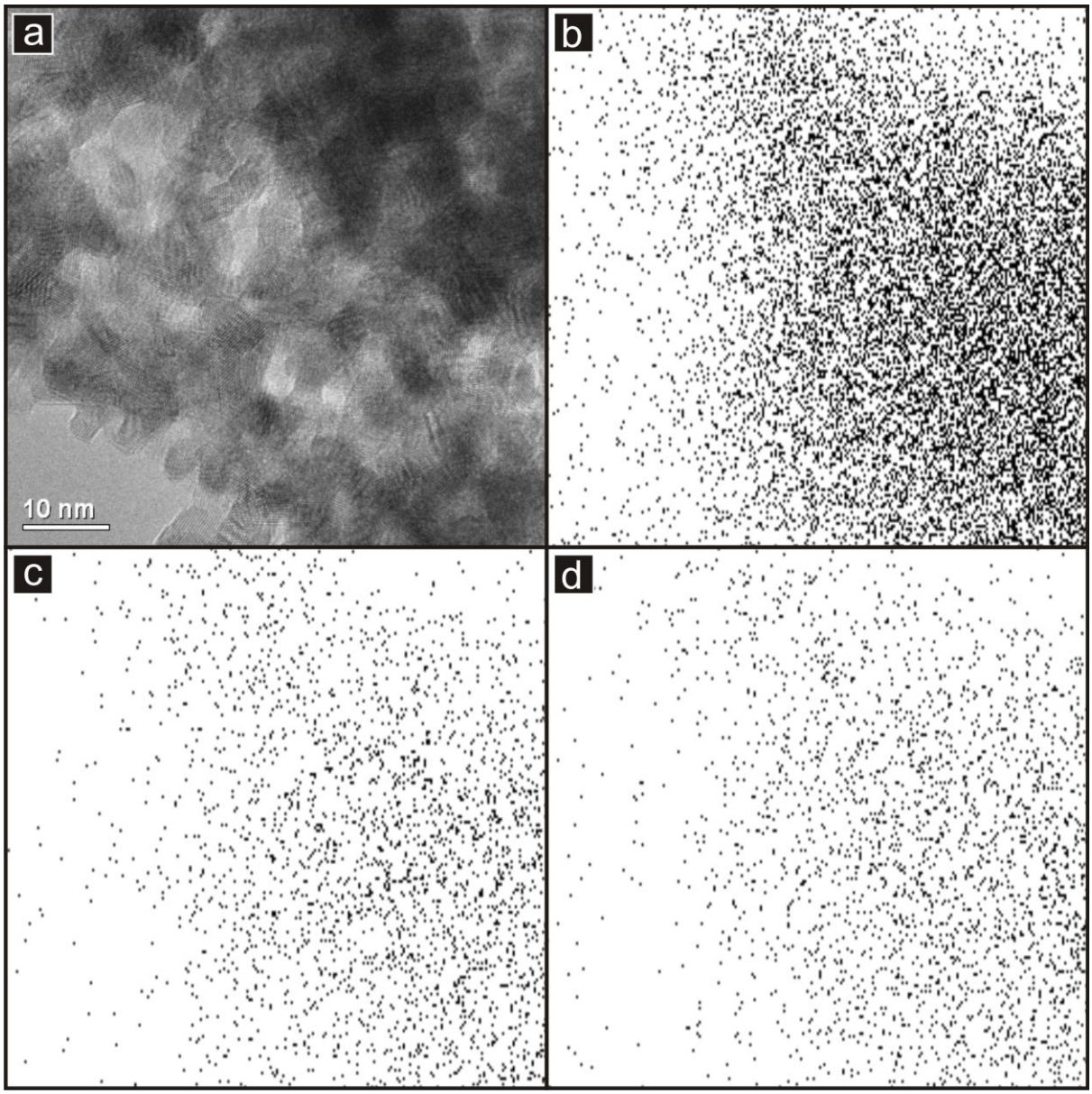

Figure 10-7: (a) TEM image of SDC-600-CC-SB and corresponding EDX elemental maps of (b) Oxygen ($K\alpha_1$) (c) Cerium ($L\alpha_1$) (d) Samarium ($L\alpha_1$). The image is rotated anticlockwise in relation to the maps due to difference in geometries between the EDX detector and TEM digital camera.

A chemical analysis of the material was found to report the ratios as presented in Table 10-4. The atomic % of samarium and cerium was in good agreement with the expected ratio for a material composed as $Sm_{0.2}Ce_{0.8}O_{1.9.}$ A typical EDX spectrum from the range of OC and CC prepared materials can be viewed in Figure 10-8.

Table 10-4: Reported chemical composition from SEM-EDX spectroscopy.

Element	Weight %	Atomic %
cerium	79.62	80.74
samarium	20.38	19.26

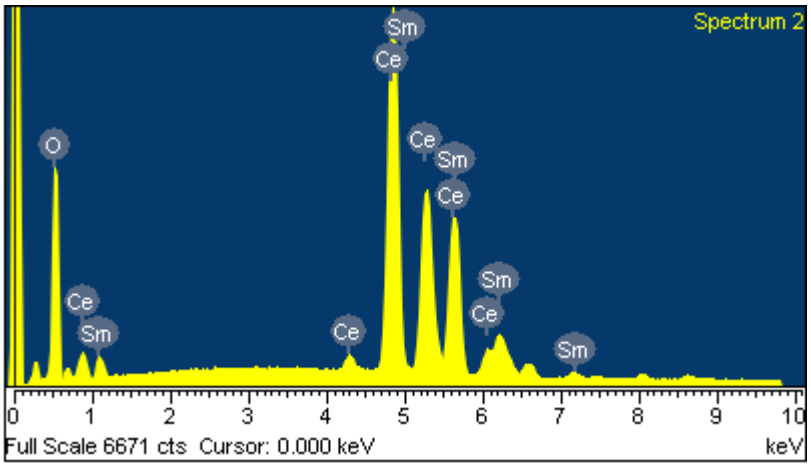

Figure 10-8: EDX analysis of template free prepared SDC material.

10.4 Discussion

Two mechanisms of ignition have been reported which are dependent on the experimental method chosen – one where self-propagation occurs with the exothermic reaction travelling from a local reaction point throughout the material in a wave like fashion[150] often induced deliberately by an external thermal source. The second is described as volumetric combustion where the ignition temperature is reached by way of uniform heating[151]. It is the latter of these mechanisms that is likely to be driving the reaction to proceed given the slow heating rate and specific boat size employed in the synthesis of the materials being studied. The use of ethanol is critical to the manufacture of the SDC product as it acts both as a solvent and as a fuel in the combustion synthesis. If the saturated solution is added to the furnace with significant delay (i.e. left to dry overnight) then the final product is not realised as the limited 'foam like' expansion of the material does not occur. As the ignition mechanism to initiate the reaction should be uniform and consistent between OC and CC method, the main influencing variable is likely attributable to the pseudo-closure of the container. From the research by Sun and co-workers[54], the difference between the OC and CC materials with all other variables equal could be attributable to the closed container effect. The research highlighted the critical closure of the sample during calcination in order to delay water evaporation and maximise crystal growth. The data presented for CC prepared materials appear to be positively influenced when compared against similarly prepared OC materials as physical characteristics of SSA and pore volume have all increased. The use of a closed container appears to have a similar effect on the PSD of the materials with the materials reporting a tighter distribution in the main mesopore range.

The values of SSA in temperatures at or below 600°C indicate a structural stability however with the 800°C calcination it appears that either collapsing of the structure or a detrimental influence on the synthesis mechanism is occurring given the loss of SSA in combination with loss of PSD. Generation of an even higher SSA is achievable using the CC method with an associated increase in mesopore volume (V_{meso}) which is double that achieved from the 400°C OC method.

The crystallite sizes observed in the TEM images is in agreement with those estimated from the XRD patterns using the Scherrer equation. Also, both techniques indicate that the wall structure became thicker as preparation temperature increased in both OC and CC samples until eventually at 800°C the uniformly-sized mesopores were lost and only large nanoparticles of approximately 20 to 30 nm in size are seen.

The data in Table 10-3 show small increases in crystallite size with calcination temperature from 400 to 600°C and then a sharp increase to 800°C. Referring also to the TEM images, this large jump in crystallite size can be explained as a change in the structure of the samples from one of walls surrounding pores to one of larger individual particles. The crystallite sizes obtained from the XRD patterns are also a good indication that the mesoporous structure observed by TEM is a bulk rather than only a localised characteristic.

The use of a different temperature programme in the synthesis of SDC-2/400-CC-SB gave rise to the largest values of mesopore volume (V_{meso}), micropore volume (V_{micro}) and SSA of all samples. It would appear that the influencing variables in this instance are the 200°C temperature step with dwell time which is allowing for controlled crystal formation. The temperature range between 150 and 200°C is thought critical in the CC method as it is the temperature at which the nitrate decomposes but before water vaporisation[54]. The additional dwell time of 2 h is likely to be the reason for the crystallites being larger in this sample than in the others prepared at 400°C. The influence of heating rate in the preparation of SDC-600A-OC and SDC-600B-OC was also considered. Analysis of these materials indicated that changing the heating rate had only a minor effect on sample structure. To investigate the effect of container volume two boat volumes referred to as small boat (SB) and large boat (LB) were used with a solution ratio of 1:2 and volume ratio of 1:3. Boat size had a negligible effect on crystallite size except at 400°C, where it was smaller for the SB sample. Pore size, mesopore and micropore volumes and SSA were higher for the SB samples prepared at 600 or 800°C but these trends were reversed for samples made at 400°C. This indicates that the container volume is a control variable as expected but its effect is reversed as a function of temperature.

The lattice parameter for ceria and SDC nanoparticles has been reported to decrease as crystallite size also decreased[152] which was explained as an effect of increasing lattice strain with decreasing crystallite size[153]. In this study the lattice parameter was found to increase for both OC and CC series as a function of decreasing crystallite size. This may be because of the tendency for smaller particles – with more low coordination Ce sites – to contain a higher proportion of reduced Ce and so to allow lattice expansion.

Previous studies by Kosinski and Baker[149] have shown that SDC material synthesised by a citrate method had a stable lattice parameter across a range of calcination temperatures and that the lattice parameter changed with changing samarium content. Interestingly in this study, the lattice parameter was found to vary in response to the synthesis conditions applied while the samarium level as confirmed by EDX analysis has remained constant. Typically, to prepare and SDC material with repeatable physical and chemical properties and with a homogenous dispersion of samarium, a citrate method was employed. Material prepared by the citrate method as per section 4.7.4 has been found to have gas physisorption values relating to a mesopore volume of ($\boldsymbol{V_{meso}}$) 0.10 cm^3g^{-1} and zero micropore volume ($\boldsymbol{V_{micro}}$). The specific surface area ($\mathbf{S_{BET}}$) of 22 m^2g^{-1} was reported. The physical properties can be refined by ball milling leading to an increase in reported ($\mathbf{S_{BET}}$) of 59 m^2g^{-1} and no significant change in pore volumes.

As the preparatory method started with a solution of nitrates, it was expected that the SDC material would be a homogenously doped ceria of composition $Sm_{0.2}Ce_{0.8}O_{1.9}$. The EDX maps presented in Figure 10-7 indicated a coincident distribution of oxygen, cerium and samarium and therefore a homogeneous chemical composition.

10.5 Summary

A method to produce samarium-doped ceria that is simple and inherently cost effective compared to nanocasting or self-assembly strategy is presented. The SDC material was synthesised using nothing more than samarium and cerium nitrates in ethanol followed by calcination in air to facilitate the chemical reaction. By controlling temperature and container volume during calcination, a high specific surface area crystalline doped ceria can be synthesised with a range of mesopore structures of uniform wall thickness and pore size. The products were high purity, homogenously doped, bulk powders that required no post synthesis treatment.

Chapter 11

Conclusions

This chapter is divided into three sections, which cover the preparation and analysis of OMS templates and their associated nanocast samarium-doped ceria (SDC) products, preparation and analysis of OMC templates and their associated nanocast SDC products and finally template free prepared SDC materials.

11.1 OMS Template and Nanocast Material

- Three ordered mesoporous silica templates (OMS), SBA-15, KIT-6 and FDU-12 were prepared with good yield and reproducibility in accordance with literature procedures. Their structures were verified using techniques of TEM, gas physisorption and low angle PXRD.
- An SBA-15 modified using swelling agents to produce a structure with enlarged pores of 25 nm while maintaining a 5nm wall thickness (comparable with non-modified SBA-15) was successfully synthesised.
- An extensive and systematic study of the thermal degradation of silica templates up to a temperature of 900°C concluded that pore structures remained stable for SBA-15 and KIT-6 up to 600°C and 500°C for FDU-12.
- The mode of structural collapse in the OMS templates was found to be influenced by framework structure.
- The pore structure of FDU-12 was found to collapse at the point of connection between adjacent pores leading to encapsulated and isolated pores.
- Using ^{29}Si MAS-NMR it was concluded that the surface silanol groups in the OMS materials were related as a function of temperature. As temperature increased there was a decrease in surface silanols from increased condensation.
- Attempts at functionalising the surface of SBA-15 using 1,1,3,3-tetramethyldisilazane (TMDS) and (3-Aminopropyl)trimethoxysilane (APTS) were made. The use of TMDS appeared to be unsuccessful as no significant gas sorption change occurred. APTMS

was also unsuccessful but for the different reason that complete pore closure occurred as observed in gas sorption analysis.

- An attempt at functionalising the surface of ultra-large pore SBA-15 (UL-SBA-15) using (TMDS) and (APTS) was made. The use of TMDS appears to be ineffectual at functionalising the surface of the UL-SBA-15 as no significant gas sorption change was observed. APTMS did affect the pore size distribution (PSD) of the UL- SBA-15 by shifting the main PSD peak from 25 nm to 15 nm. This change occurred along with almost a halving of the total mesopore volume. This suggested that surface grafting may have occurred physically expanding the surface thickness and correspondingly narrowing the pore channels.
- Microtomy was used as a sample preparation method for TEM analysis. This technique proved to be very useful in viewing mesopore materials in cross –section orientations that are normally difficult to observe. It was useful for viewing impregnated templates, helping to establish the degree to which pore channels were filled.
- OMS template in the form of pellets were successfully prepared and found to be a good alternative to loose powder when impregnating under vacuum. The ingress of precursor into the bulk of the pellet could be followed visually. Excess addition of precursor was reduced in comparison to the use of a powder. As the pellet was compacted in its bulk property, there were minimal large voids which would only serve to create large particulate agglomerations.
- Mesoporous SDC was nanocast from an SBA-15 template. The material displayed physical properties of high specific surface area of 140 m^2g^{-1}, mesopore volume of 0.42 cm^3g^{-1} and a regular repeating crystalline framework composed of rods and ordered mesoporous channels after removal of the OMS template.
- Mesoporous SDC was nanocast from KIT-6 template. Evidence for the crystal growth mechanisms were observed in that bridging between nanorods and alignment of the crystal planes of adjacent rods was evident. The material displayed physical properties that were unique for this material such as high specific surface area of 195 m^2g^{-1} and a mesopore volume of 0.34 cm^3g^{-1}. This SSA is higher than expected (Appendix 4) possibly explained by the incomplete removal of silica template.
- Mesoporous SDC was nanocast from FDU-12 template. A crystalline framework was not apparent but individual nanoparticles were shown to exist that appeared to be

spherical with spatially arranged nodules. The shape and position of the sphere-nodules correlate as a nanocast as to where interconnecting pore channels would have joined the pores in the FDU-12 template. The material displayed physical properties that were unique for this material such as high specific surface area of 150 m^2g^{-1} and a mesopore volume of 0.18 cm^3g^{-1}. This SSA is marginally higher than expected (Appendix 4) possibly explained by the incomplete removal of silica template.

- Mesoporous SDC was nanocast from ultra large pore SBA-15 template. A change in PSD to a reduced mesopore size was noticed. The range of the mesopore PSD was between 2 and 20nm with large associated pore volume. Solvo-thermal effects could not be completely discounted without further research despite 24 h drying. The pore range and sorption profile was very similar for the functionalised material indicating that a direct relationship exists between the porosity of the nanocast material and the ultra-large pores of the template.
- The use of functionalised silica templates for producing ordered mesoporous SDC material was found to be unsuccessful.
- An extensive study into removal of silica from OMS nanocast SDC products concluded that a standard wash procedure using NaOH removed the bulk of the silica template but a high percentage remained. The dissolution rate of silica using NaOH was determined using UV-vis spectroscopy.
- Removal of silica was not achieved using TMAH as an alternative to NaOH.
- Complete removal of silica using ammonium bifluoride occurred only at the expense of the chemical composition of the SDC material with silicon and oxygen being substituted by fluorine.
- Removal of silica was greatly improved using catechol but residual silicon was still evident in the chemical composition of SDC.

11.2 OMC Template and Nanocast Material

- The synthesis of FDU-14 carbon template was successful although the method was protracted with yield of ordered mesoporous product low. It was found that in order to make an open pore structure, an amount of oxygen (2 %) was necessary to

remove tri-block copolymer during calcination. The pores sizes for the material were found to be mainly in the 1-2 nm (micropore) range.

- The synthesis of FDU-15 carbon template was successful with synthetic pathways based on an aqueous one-pot and on a two phase method. The methods proved to be suitable for producing material with desired nanostructure throughout the bulk of the material and in good yield. It was found that in order to make an open pore structure, unlike FDU-14 or FDU-16, no additional oxygen was necessary to remove tri-block copolymer during calcination. The two synthesis methods produced templates with ordered mesopores but with differing pore size distributions. A third method using an evaporative induced self-assembly technique produced the desired template but the yield of ordered mesoporous material was low.
- The synthesis of the FDU-16 carbon template was successful although the method was protracted and yield of ordered mesoporous material low. It was found that in order to make an open pore structure, an amount of oxygen (2 %) was necessary to remove tri-block copolymer during calcination.
- Concerns regarding the template being composed of mixed phase structures of *p6mm* and *Im3m* exist. Small fluctuations in synthesis conditions especially the control of temperature during micelle and polymer framework formation would affect the type of self-assembled structure obtained.
- OMC templates in the form of pellets were successfully prepared and found to be a good alternative to powder when impregnating using vacuum. Unlike OMS pellets, ingress of precursor into the bulk of the pellet could not be followed visually. As with OMS pellets, excess addition of precursor was reduced in comparison to the use of a powder. As the pellet was compacted in its bulk property, there were minimal large voids which would only serve to create large particulate agglomerations. As FDU-15 synthesised by the two-phase method produced a monolith, this could be moulded in the gel phase just before thermopolymerisation to a desired shape and size.
- To function as a nanocasting template, it was fundamental that carbon based OMP and OMC materials had to be impregnated with nitrate precursors dissolved in polar solvents. It can be concluded through characterisation of the sequence: template – intermediate – final product, that successful impregnation occurred in both OMP and OMC templates prepared at 350 and 500°C respectively.

- SDC Materials were successfully nanocast from 350 and 500°C prepared FDU-14. Material from the 350°C template displayed physical properties of low specific surface area of 49 m^2g^{-1} and mesopore volume of 0.11 cm^3g^{-1}. Material from the 500°C template displayed physical properties of high specific surface area of 142 m^2g^{-1} and mesopore volume of 0.18 cm^3g^{-1} which were in good agreement with the expected values for material nanocast from an *Ia3d* structure. Gas physisorption analysis also reported specific mesopore size distributions were distinct between the SDC materials prepared from the 350°C template or 500°C template indicating that the temperature in template formation had a direct influence on the nanocast SDC product. The physical characteristics of the material prepared from 500°C template were much superior to that from 350C°.
- SDC materials synthesised from aqueous one-pot FDU-15 (Method A) produced materials with distinct mesopore size distributions depending on whether the template was produced at 350 or 500°C. These materials were an inverse rod like structure of the starting template with high specific surface area and mesopore volume.
- SDC materials synthesised from two-phase prepared FDU-15 (Method C) template produced material with distinct mesopore size distributions. This material was an inverse rod like structure of the starting template with high specific surface area and mesopore volume.
- SDC materials synthesised from FDU-16 template had low specific surface area. A broad range of meso-macropores was reported indicating significant mesopore volume remained as inter-particle agglomeration. Impregnation of the material occurred but was comparatively lower than that achieved with other OMC templates. The yield of quality material within the bulk of the sample was therefore low. A proportion of the material was imaged however that was characteristic of the inverse structure of the starting template.
- Removal of OMC template by pyrolysis was effective and produced materials of high purity which were free of carbon.

11.3 Template-Free SDC Prepared Material

- A facile method for producing SDC material without the use of a template was developed. It introduced calcination of a saturated nitrate solution in ethanol at a range of temperatures up to and including 800°C.
- Gram quantities (2-3 g) of the material were produced in a timeframe of less than 24 h. The procedure would be very amenable to large scale bulk production.
- The material after calcination was found to have a crystalline structure composed of a consistent wall thickness interspersed with a disordered arrangement of mesopores. It had physical attributes of high specific surface area and high pore volume in comparison to materials prepared by other bulk methods of preparation. These specific physical properties could be controlled to some extent by using variables of temperature of reaction and volume of reaction chamber.
- These materials were found to be of high purity using EDX spectroscopy.

Chapter 12

Future Work

12.1 SDC Material Prepared From OMS Template

Further work to understand the relationship between calcination temperature and the growth of the material while within the confines of the template would be desirable. In conjunction with further studies of the closed container method and ultra-microtomy sample preparation a deeper understanding of the growth mechanism may be possible.

12.2 Material Characterisation

To further understand where silica resides after template removal, future work using TEM or SEM with high resolution EDX mapping may provide valuable information.

The further use of ultra-microtomy would be valuable for examining cross-sectioned mesoporous particles. A detailed study of precursor impregnation using this method could be undertaken.

12.3 Carbon Templates

It has been reported that the thermo-polymerisation procedure in the preparation of OMPs and OMCs which normally extends to 24 h can be dramatically shortened with careful selection of heating protocols[154]. Although the two-phase method has proven to be faster than other methods and reliable in the product synthesised, it should be possible to shorten process time significantly from 2 days into a few hours.

Altering the final properties of the OMC material might be useful in its application as a nanocast template and this could be achieved through the changing of reagents. One particular alteration to FDU-15 would involve replacing the hydrochloric acid in the framework synthesis step with nitric acid in order to remove the potential for chlorine to exist in any final product which may be undesirable for certain catalytic applications. Alternatively, sulphuric acid has been shown to encourage pore loading. Phosphoric acid

influences the surface properties of the OMC thereby increasing the hydrophilic nature of the pore walls. Phosphoric acid has also been reported to give rise to larger pores, thicker walls and higher pore volume and specific surface area[155].

Synthesis of the cubic (*Im3m*) FDU-16 structure was successful at 500°C with and without the use of oxygen in the calcination gas stream and represented a dramatic improvement from the template prepared at 350°C. It would be of interest to prepare the material at 400°C using the oxygen amendment to the procedure and investigate a longer dwell time. When the template changes from 350 through to 500°C, there is a shrinkage associated with decomposition of the polymer framework. For this reason selection of 400°C might be expected to give rise to a material with a high percentage of surface functional groups. To investigate this, a similar thermal deformation study as performed with the silica templates could be performed. It would also be interesting to know if the use of oxygen in the gas stream prevents elemental oxygen from the framework being consumed, thereby protecting the functional groups.

12.4 SDC Material Prepared From OMP and OMC Template

As an understanding now exists for the successful preparation of carbon templates, further studies into the preparation of template SDC and other mixed metal oxides could be performed. Of particular interest is the growth mechanism of the rod-like structures from FDU-15-400 template. Using the closed container method at temperatures above and below 400°C or altering the dwell times may alter the rate of fusion of the material within the confines of the carbon structure, perhaps leading to improved replication of the template.

12.5 Catalytic Performance

The preparation of SDC materials with high purity, specific surface area, crystallinity and controlled mesoporosity should allow it to be used in various catalytic applications. One of the aims in producing this material with such characteristics was to fulfil the requirements of the anode component of an intermediate temperature solid oxide fuel cell. Future work would aim towards evaluating the material with and cross comparing the performance with commercially available alternatives.

Appendix 1

The two figures presented below are summaries of the gas physisorption data for silica based products (Figure A-1) and carbon based products (Figure A-2). Each individual graph is an overlay of (1) the template used for impregnation, (2) the template at an intermediate stage having had samarium doped cerium nitrate impregnated and subsequently converted to SDC, (3) the final product produced after the template has been removed.

Gas Physisorption Data for Silica Template Products

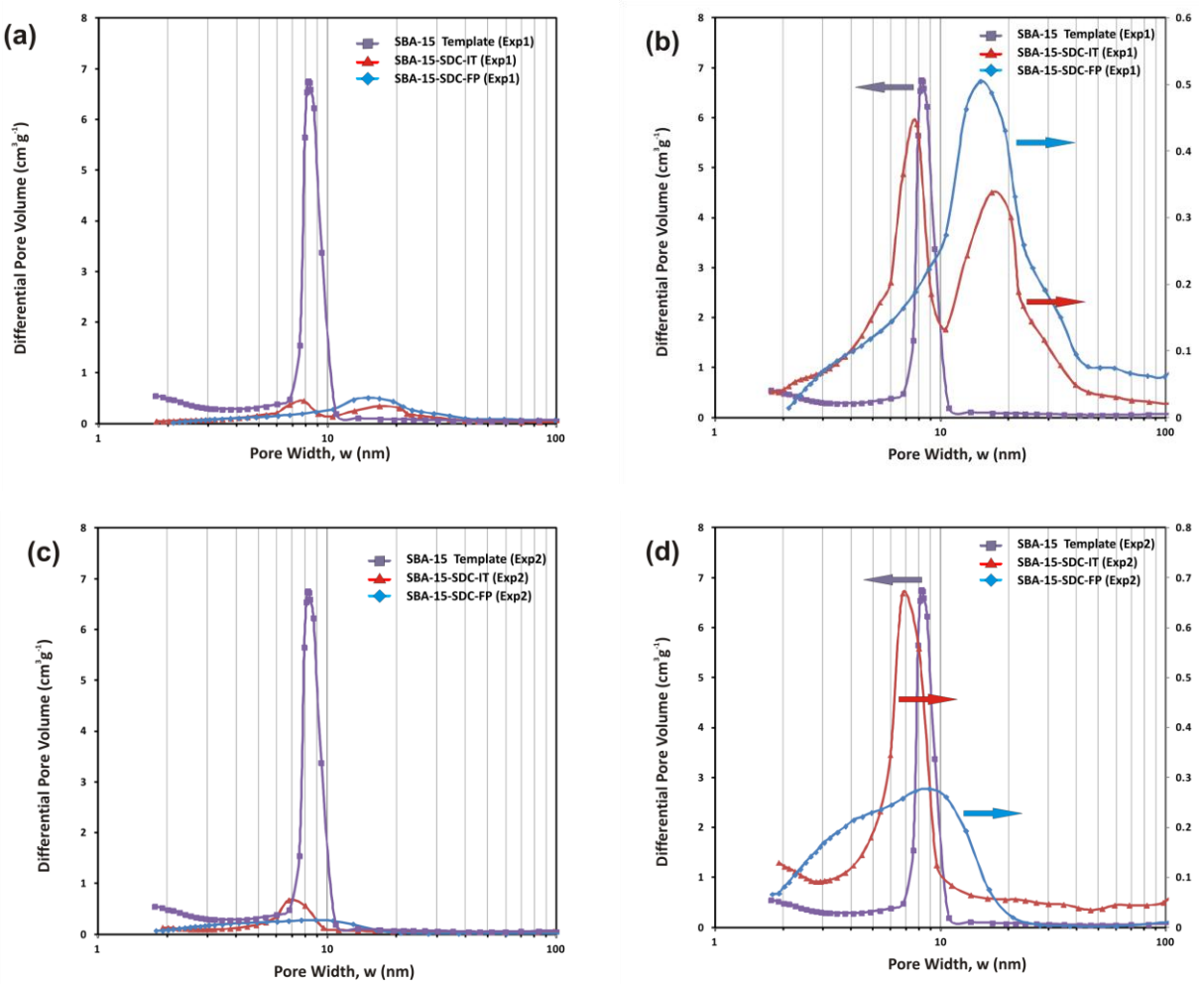

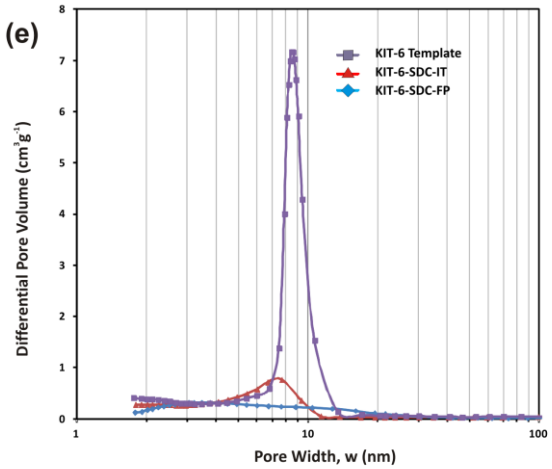
(e)
KIT-6 Template
KIT-6-SDC-IT
KIT-6-SDC-FP
Differential Pore Volume (cm³g⁻¹)
Pore Width, w (nm)

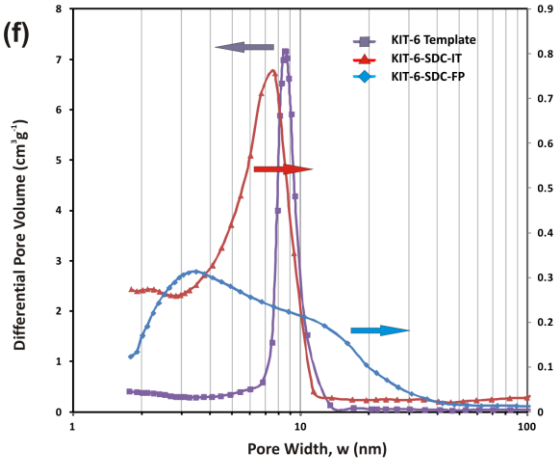
(f)
KIT-6 Template
KIT-6-SDC-IT
KIT-6-SDC-FP
Differential Pore Volume (cm³g⁻¹)
Pore Width, w (nm)

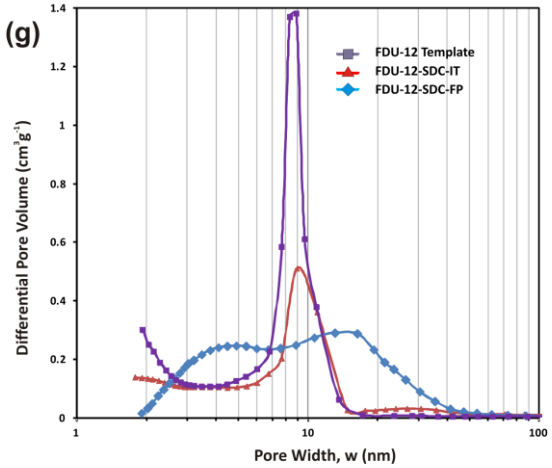
(g)
FDU-12 Template
FDU-12-SDC-IT
FDU-12-SDC-FP
Differential Pore Volume (cm³g⁻¹)
Pore Width, w (nm)

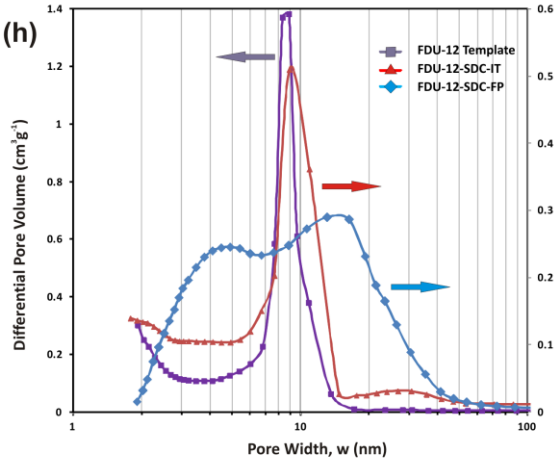
(h)
FDU-12 Template
FDU-12-SDC-IT
FDU-12-SDC-FP
Differential Pore Volume (cm³g⁻¹)
Pore Width, w (nm)

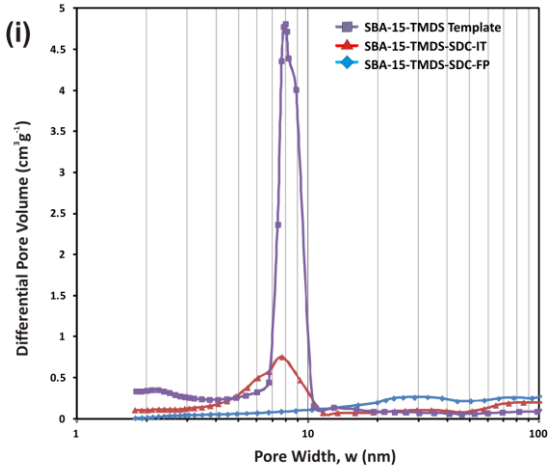
(i)
SBA-15-TMDS Template
SBA-15-TMDS-SDC-IT
SBA-15-TMDS-SDC-FP
Differential Pore Volume (cm³g⁻¹)
Pore Width, w (nm)

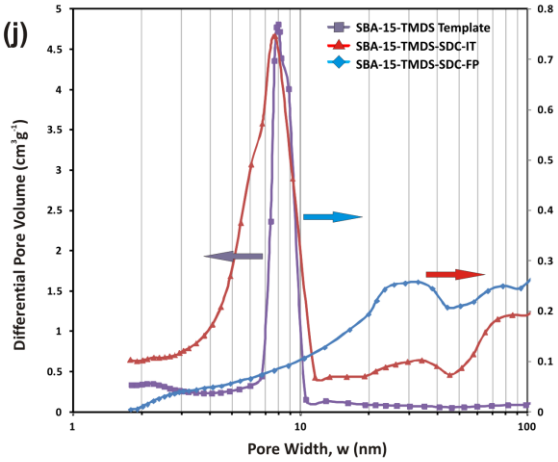
(j)
SBA-15-TMDS Template
SBA-15-TMDS-SDC-IT
SBA-15-TMDS-SDC-FP
Differential Pore Volume (cm³g⁻¹)
Pore Width, w (nm)

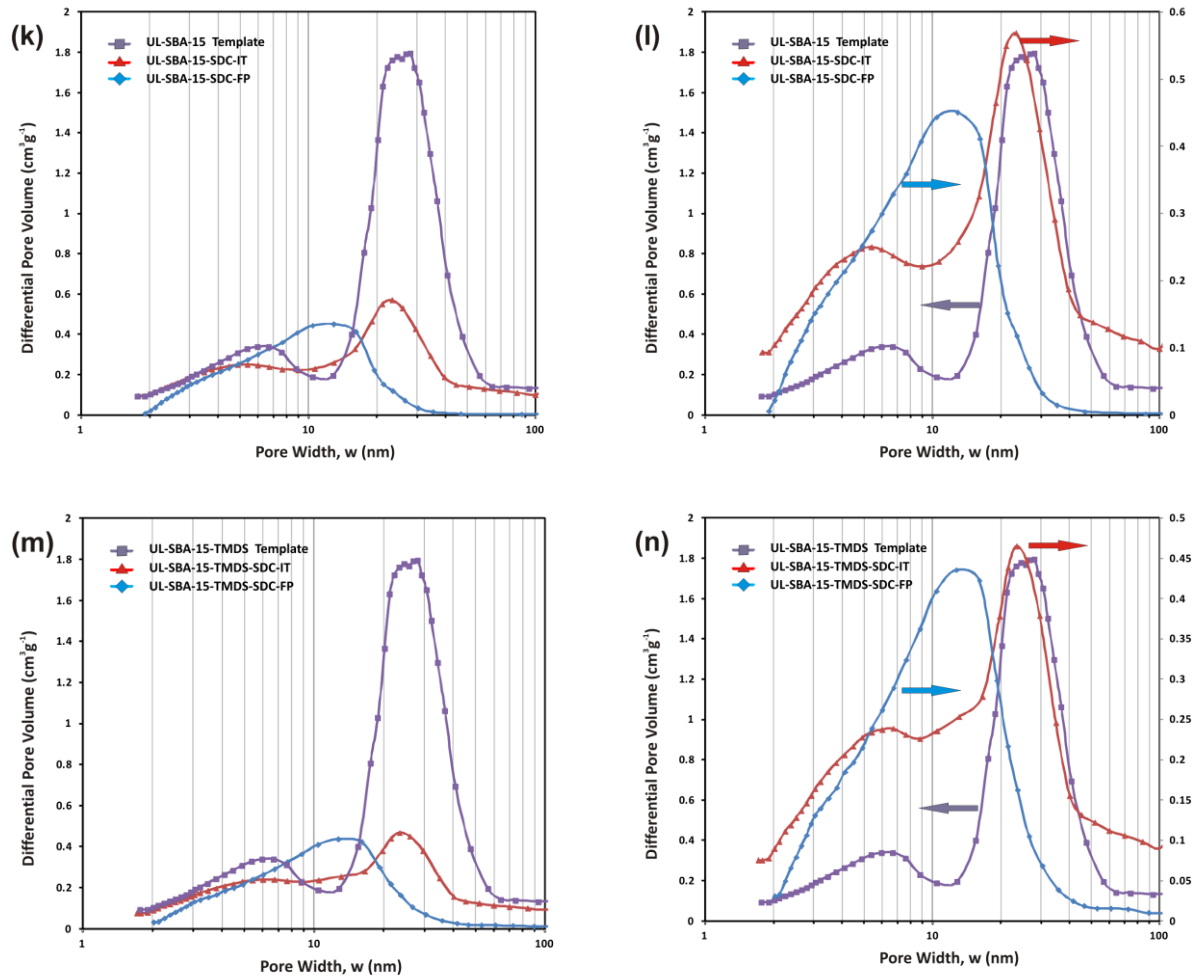

Figure A-1: Nitrogen physisorption pore size distributions (PSD) for silica based products. Each graph displays template, the intermediate product (IT) composed of template and *insitu* calcined SDC, Final product (FP) SDC which is the recovered product after template removal. Where appropriate the IT and FP material has been shown on a secondary axis to allow PSD shifts to be viewed easier and offsets for the change in differential pore volume due to the change in density between template and SDC. (a),(b) SBA-15-Experiment 1; (c),(d) SBA-15-Experiment 2; (e),(f) KIT-6; (g),(h) FDU-12; (i),(j) SBA-15-TMDS; (k),(l) UL-SBA-15; (m),(n) UL-SBA-15-TMDS.

Gas Physisorption Data for Carbon Template Products

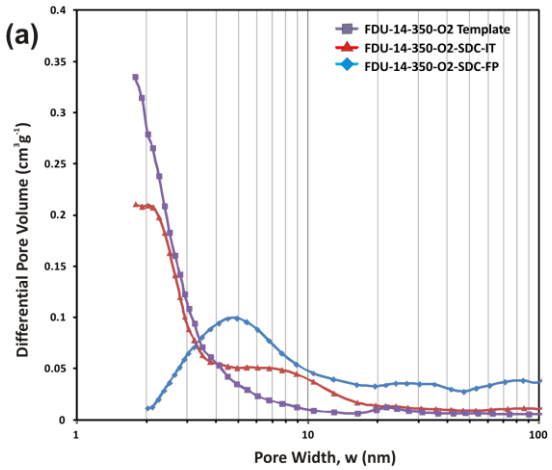

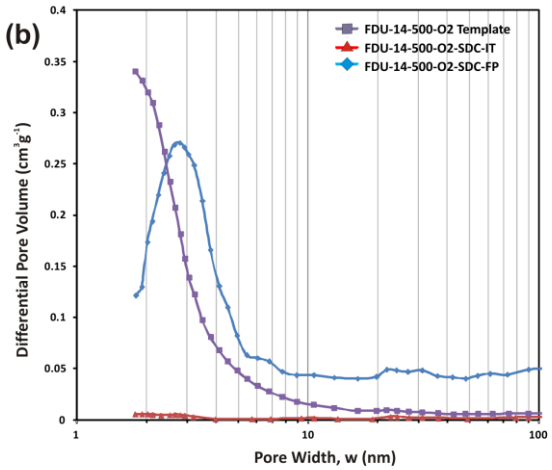

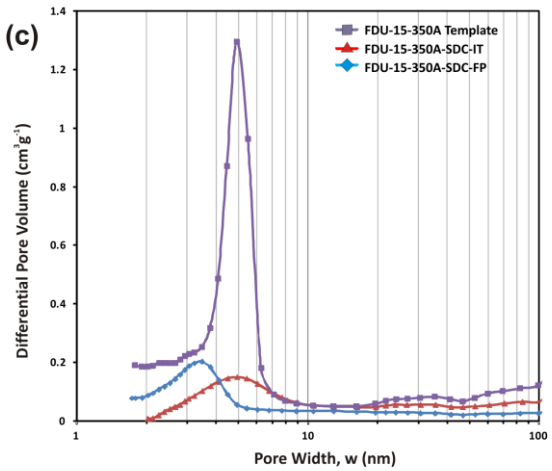

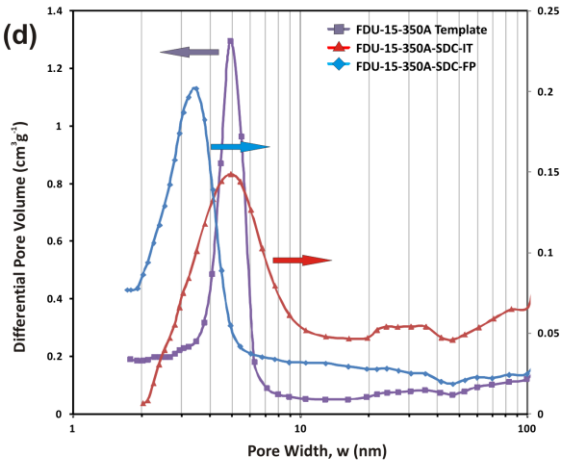

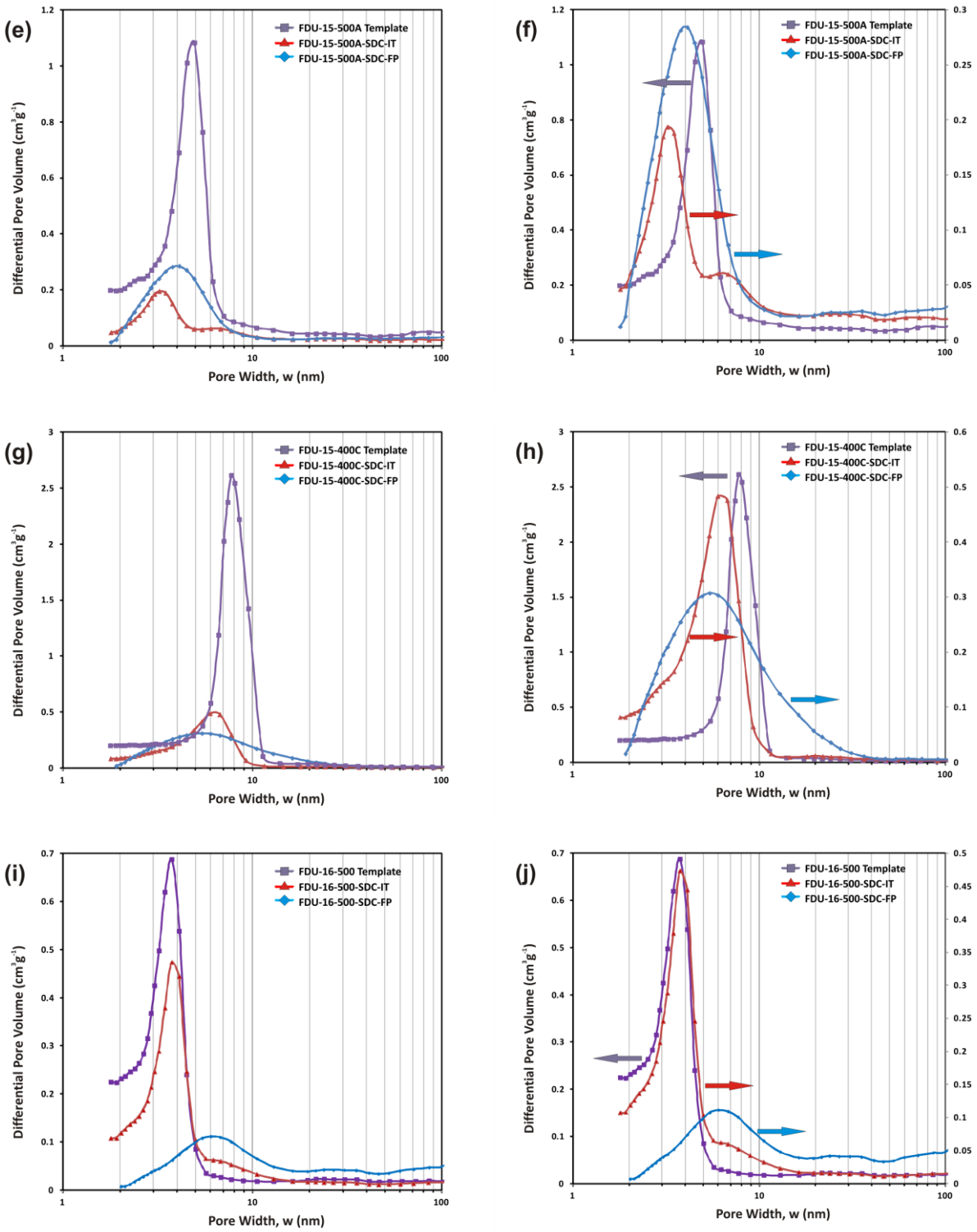

Figure A-2: Nitrogen physisorption pore size distributions (PSD) for carbon based products. Each graph displays template, the intermediate product (IT) composed of template and *insitu* calcined SDC, Final product (FP) SDC which is the recovered product after template removal. Where appropriate the IT and FP material has been shown on a secondary axis to allow PSD shifts to be viewed easier and offsets for the change in differential pore volume due to the change in density between template and SDC. (a) FDU-14-350-O2; (b) FDU-14-500-O2; (c),(d) FDU-15-350A; (e),(f) FDU-15-500A; (g),(h) FDU-15-400C and (i),(j) FDU-16-500.

Appendix 2

Unit cell parameter formulae

Eqn. 20 is the formula used to calculate the unit cell parameter (***a***) for a face-centered cubic structure.

$$a = (\sqrt{(h^2+k^2+l^2)})\, d_{hkl} \qquad \textit{Eqn. 20}$$

a = Unit cell parameter (nm)

d = ***d***-spacing (nm)

h,k,l = Miller indices

Eqn. 21 is the formula used to calculate the unit cell parameter (***a***) for a tetragonal structure.

$$a = d_{100}/\sin 60° \qquad \textit{Eqn. 21}$$

$$a = d_{110}/\cos 60° \qquad \textit{Eqn. 21b}$$

$$a = 2d_{200}/\sin 60° \qquad \textit{Eqn. 21c}$$

a = Unit cell parameter (nm)

d = ***d***- spacing (nm) for the Miller indices

Appendix 3

Table Appendix 3-0-1 is a comprehensive review of syntheses where carbon templates have been prepared directly using self-assembly techniques. Each ID number is specific to an individual process of synthesis. Table Appendix 3-0-2 lists details of the key data values for each ID numbered material. Where appropriate, the same material prepared using specific temperatures of calcination are also given.

Table Appendix 3-0-3: Values for unit cell parameters (***a_o1 – a_o3***), interplanar spacings (***d***), pore width (***w***) and pore wall thickness (***t***) obtained using the method indicated (BJH, SAXS, TEM). All values are in nm. Values of ***a_o*** are calculated from the corresponding ***d_{SAXS}*** value. Miller indices are given in italics below each value of ***d***.

ID	Reagents	Structure	Designation	Type of Reaction
1[125]	RF-F127	Hexagonal	COU-1	2 phase
2[125]	RF-F127 (x2)	Hexagonal	COU-1	2 phase
3[125]	RF-F127 (x3)	Worm Like	COU-2	2 phase
4[125]	RF-F127 or P123	Hexagonal	COU-1	2 phase
5[125]	RF-P123	Worm Like	COU-2	2 phase
6[75]	RF-F127	Cubic	none	1 pot aqueous
7[75]	RF-F127	Hexagonal	none	1 pot aqueous
8[74]	RF-F127	Hexagonal	FDU-15	1 pot aqueous
9[74]	PF-F127	Cubic	FDU-16	1 pot aqueous
10[74]	PF-P123 (s1)	Hexagonal	FDU-15	1 pot aqueous
11[74]	PF-P123 (s2)	Hexagonal	FDU-15	1 pot aqueous
12[74]	PF-P123	Bicontinuous Cubic	FDU-14	1 pot aqueous
13[78]	RF-F127	Hexagonal	FDU-15	2- Phase
14[73]	PF-P123	Bicontinuous Cubic	FDU-14	1 pot aqueous
15[156]	H-RF-F127	Hexagonal	none	hydrothermal
16[76]	PF-P123	Bicontinuous Cubic	FDU-14	EISA
17[76]	PF-F127 or P123	Hexagonal	FDU-15	EISA
18[76]	PF-F127 or P123	Cubic	FDU-16	EISA
19[77b]	RF-F127	Hexagonal	OMC1	2-Phase
20[77b]	RF-F127	Hexagonal	OMC2	2-Phase
21[77b]	RF-F127	Hexagonal	OMC3	2-Phase
22[77b]	RF-F127	Hexagonal	OMC4	2-Phase

23[77a]	RF-F127	Hexagonal	OMC	2-Phase
24[118]	PF-F127	Hexagonal	C-ORNL-1	2-Phase

(x2 and x3 represent increasing F127 to Resol ratios); (s1 and s2 represent hexadecane and decane swelling agents respectively), F: formaldehyde, H-Hexamine, R: Resorcinol, P: Phenol

Table Appendix 3-0-4: Values for unit cell parameters (***a_o1 - a_o3***), interplanar spacings (***d***), pore width (***w***) and pore wall thickness (***t***) obtained using the method indicated (BJH, SAXS, TEM). All values are in nm. Values of ***a_o*** are calculated from the corresponding ***d_{SAXS}*** value. Miller indices are given in italics below each value of ***d***.

ID	*Structure*	*Calcination (°C)*	*Pore Volume*	*s.d.*	*d-spacing*	*Unit Cell Parameter*	w_{TEM}	t_{TEM}
1	Hexagonal	800	0.43	602	9.6	-	4.7	6.4
2	Hexagonal	800	0.49	651	10.1	-	5.8	5.9
3	Worm Like	800	0.61	716	9.8	-	4.8	-
4	Hexagonal	800	0.58	611	11.3	-	6.8	6.3
5	Worm Like	800	0.51	708	10.5		4.4	-
6a	Cubic	350	nil	5	-	15.4	nil	nil
6b		500	0.33	747	-	13.3	3.4	8.1
6c		900	0.37	870	-	12.1	3.1	7.4
7a	Hexagonal	350	0.39	496	-	15.0	6.7	8.3
7b		500	0.42	659	-	13.4	6.1	7.3
7c		900	0.49	853	-	11.3	5.2	6.1
8a	Hexagonal	500	0.34	670	-	12.7	3.5	7.5
8b		800	0.50	1030	-	11.6	3.2	6.8
9a	Cubic	350	0.41	460	-	11.3	5.0	6.3
9b		800	0.55	1040	-	8.6	3.8	4.8
10a	Hexagonal	350	0.40	500	-	13.6	6.8	6.8
10b		800	0.40	750	-	10.9	4.1	6.8
11a	Hexagonal	350	0.40	550	-	19.6	3.8	4.4
11b		800	0.50	1000	-	15.4	2.8	3.6
12a	Bicontinuous Cubic	350	0.68	626	-	12.3	7.7	-
12b		600	0.69	770	-	11.9	6.5	-
12c		800	0.68	758	-	11.3	5.6	-
13a	Hexagonal	350	0.40	550		19.0	3.8	4.2
13b		700	0.57	1150		15.4	2.7	3.6
14a	Bicontinuous Cubic	350	0.57	633	11.9	13.7	5.30	-

14b		900	0.96	1483	9.9	11.4	4.74	-
15a	Hexagonal	As made	-	-		30.0	-	-
15b		350	0.10	130		23.5	3.1	6.1
15c		350N	0.23	280		24.0	3.9	5.8
15d		600	0.32	630		20.0	2.3	5.4
15e		800	0.34	690		20.0	2.0	5.5
16a	Bicontinuous Cubic	As made	0.34	-		19.0	-	-
16b		350N	-	460		16.9	6.6	8.0
16c		400N	0.47	670		16.1	6.1	7.8
16d		500	0.42	660		14.6	4.9	7.7
16e		600	0.36	580		13.9	4.3	7.7
16f		600N	0.44	690		14.5	4.9	7.6
16g		700	0.37	690		13.0	3.8	7.5
16h		800	0.47	820		13.0	3.8	7.5
16i		800N	0.43	760		13.1	3.8	7.5
16j		900	0.41	740		12.9	3.8	7.4
16k		1200	0.54	990		12.7	3.8	7.2
16l		1200N	0.85	1490		12.8	3.8	7.3
16m		1400	0.54	990		12.6	3.5	7.4
17a	Hexagonal	As made	-	-		15.9	-	-
17b		350	0.40	430		13.1	5.4	7.7
17c		350N	0.65	640		14.0	7.1	6.9
17d		400	0.41	510		12.2	4.9	7.3
17e		400N	0.59	630		13.4	6.6	6.8
17f		500	0.42	670		11.1	3.8	7.3
17g		600	0.34	590		10.4	3.1	7.3
17h		600N	0.55	750		11.2	4.9	6.3
17i		700	0.42	750		10.0	3.1	6.9
17j		800	0.40	720		9.9	3.1	6.8
17k		800N	0.66	900		10.6	4.3	6.3
17l		900	0.37	650		9.7	3.1	6.6
17m		1200	0.42	730		9.8	2.8	7.0
17n		1200N	0.59	1060		9.8	3.1	6.7
17o		1400	0.61	690		10.1	2.8	7.3
18a	Cubic	350	0.10	130		23.5	3.1	6.1
18b		350N	0.23	280		24.0	3.9	5.8
18c		600	0.32	630		20.0	2.3	5.4
18d		800	0.34	690		20.0	2.0	5.5

19	Hexagonal	800	0.66	734	10.1	-	4.5	6.9
20	Hexagonal	800	0.65	751	9.7	-	4.2	5.7
21	Disordered	800	0.52	674	-	-	3.8	-
22	Hexagonal	800	0.72	781	-	-	4.6	7.5
23	Hexagonal	800	0.66	734	9.9	-	4.5	-
24a	Hexagonal	850	0.58	607		12.24	-	-
24b		1800	0.46	390		12.20	-	-
24c		2200	0.47	371		-	-	-
24d		2400	0.37	288		-	-	-
24e		2600	0.30	230		-	-	-

x2 and x3 represent increasing F127 to Resol ratios, N represents Nitrogen atmosphere.

Appendix 4

Ce	A.M.U.	= 140.12
$Ce(NO_3)_3.6H_2O$	M.W.	= 434.22
CeO_2	Density (ρ)	= 7.22 g/cm^{-3}
Sm	A.M.U.	= 150.4
$Sm(NO_3)_3.6H_2O$	M.W.	= 444.46
$(SmO_{1.5})_{0.2}(CeO_2)_{0.8}$	Density (ρ)	= 7.14 g/cm^{-3}
Silica framework[102, 157]	Density (ρ)	= 2.2 g/cm^{-3}
Carbon framework (FDU-15)[76, 158]	Density (ρ)	= 1.1-1.3 g/cm^{-3}
Carbon framework (FDU-14/16)[76, 159]	Density (ρ)	= 1.8-2.1g/cm^{-3}

General Formula of SDC

$Sm_xCe_{1-x}O_{2-(x/2)}$

Density Calculations

$(SmO_{1.5})_{0.2}(CeO_2)_{0.8}$ ***Eqn. 22***

Unit Cell M.W. = (150.4+(16.00*1.5)*0.2)+(140.12+(16.00*2)*0.8)

= 172.6 a.m.u.

Unit Cell Volume[1] = $(5.4351)^3$ Å^3

Density (ρ) = $m/V * N_A$

= [172.6 / (1.6055 x 10^{--22}cm^3)*6.023 x 10^{23}] F.C.C.

= 7.14 g/cm^3

[1]Average unit cell volume from Table 10-3, Section 10.3.3

Preparation of $Sm_{0.2}Ce_{0.8}O_{1.9}$ Saturated Solution

Ratio of n (no. of moles) of 1 Sm to 4 of Ce required

Therefore m (mass) ratio required

Where $Ce_n = 0.8$ then Ce_m is given by 434.22 x 8 = 3473.8

And $Sm_n = 0.2$ then Sm_m is given by 444.46 x 2 = 888.9

Or 6.94g to 1.78g as a working value (dissolved in 5g ethanol)

Theoretical Specific Surface Area of SDC inverse structure from an OMS template.

$$SSA_{SDC} = SSA_{Template} * (\rho_{Template} / \rho\ Sm_{0.2}Ce_{0.8}O_{1.9}) \qquad Eqn.\ 23$$

SSA_{SDC} Calculation for Inverse SBA-15 structure using Eqn. 23

[$\rho_{SBA\text{-}15} = \rho_{Silica}$ –Total Pore Volume $_{SBA\text{-}15}$]

[$\rho_{SBA\text{-}15}$ = 2.2 – 0.8]

[$\rho_{SBA\text{-}15}$ = 1.4]

$SSA_{SDC} = 831 * (\rho_{SBA\text{-}15} / 7.14)$

$SSA_{SDC} = 163\ m^2g^{-1}$

SSA_{SDC} Calculation for Inverse KIT-6 structure using Eqn. 23

[$\rho_{KIT\text{-}6} = \rho_{Silica}$ –Total Pore Volume $_{KIT\text{-}6}$]

[$\rho_{KIT\text{-}6}$ = 2.2 – 0.9]

[$\rho_{KIT\text{-}6}$ = 1.4]

$SSA_{SDC} = 770 * (\rho_{KIT\text{-}6} / 7.14)$

$SSA_{SDC} = 151\ m^2g^{-1}$

SSA_{SDC} Calculation for Inverse FDU-12 structure using Eqn. 23

[$\rho_{FDU\text{-}12} = \rho_{Silica}$ –Total Pore Volume $_{FDU\text{-}12}$]

[$\rho_{FDU\text{-}12}$ = 2.2 – 0.3]

[$\rho_{FDU\text{-}12}$ = 1.9]

$SSA_{SDC} = 490 * (\rho_{FDU\text{-}12} / 7.14)$

$SSA_{SDC} = 130\ m^2g^{-1}$

References

[1] G. P. Peters, R. M. Andrew, T. Boden, J. G. Canadell, P. Ciais, C. Le Quere, G. Marland, M. R. Raupach and C. Wilson, *Nature Climate Change* **2013**, *3*, 4-6.
[2] V. E. Fortov and O. S. Popel', *Thermal Engineering* **2014**, *61*, 389-398.
[3] S. P. S. Badwal, S. Giddey, C. Munnings and A. Kulkarni, *Journal of the Australian Ceramic Society* **2014**, *50*, 23-37.
[4] A. Kirubakaran, S. Jain and R. K. Nema, *Renewable & Sustainable Energy Reviews* **2009**, *13*, 2430-2440.
[5] http://www.nrel.gov/hydrogen/proj_fuelcells.html in *Vol.* FTEC, **US Dept. of Energy, access date: 2014 May**.
[6] E. Franceschini and H. Corti in *Applications and Durability of Direct Methanol Fuel Cells*, *Vol.* Eds.: H. R. Corti and E. R. Gonzalez), Springer Netherlands, **2014**, pp. 321-355.
[7] S. Q. Yang, T. Chen, Y. Wang, Z. B. Peng and W. G. Wang, *International Journal of Electrochemical Science* **2013**, *8*, 2330-2344.
[8] S. Singhal in *Solid Oxide Fuel Cells: Past, Present and Future*, *Vol.* Eds.: J. T. S. Irvine and P. Connor), Springer London, **2013**, pp. 1-23.
[9] S. D. Vora, *Solid Oxide Fuel Cells 13 (Sofc-Xiii)* **2013**, *57*, 11-19.
[10] J. Thijssen in *Solid Oxide Fuel Cells and Critical Materials: A Review of Implications*, *Vol.* **2011**.
[11] D. Shekhawat, J. J. Spivey and D. A. Berry, *Fuel cells : technologies for fuel processing*, Elsevier Science, Amsterdam ; London, **2011**, p. xii, 555 p.
[12] A. Tarancón, *Energies* **2009**, *2*, 1130-1150.
[13] J. H. J. S. Thijssen, *NETL* **2007**.
[14] K. Ahn, S. Jung, J. M. Vohs and R. J. Gorte, *Ceramics International* **2007**, *33*, 1065-1070.
[15] M. Tsuchiya, B. K. Lai and S. Ramanathan, *Nature Nanotechnology* **2011**, *6*, 282-286.
[16] S. J. Skinner and A. Lashtabeg, *Journal of Materials Chemistry* **2006**, *16*, 3161-3170.
[17] M. Hans-heinrich, Bernd, Rohland in *Method of producing fuel cells with solid electrolytes and ceramic oxide electrode layers*, *Vol.* Univ, Ernst Moritz Arndt, United States, **1968**.
[18] H. Kurokawa, T. Z. Sholklapper, C. P. Jacobson, L. C. D. Jonghe and S. J. Visco, *Electrochemical and Solid-State Letters* **2007**, *10*, B135-B138.
[19] a) O. A. Marina, C. Bagger, S. Primdahl and M. Mogensen, *Solid State Ionics* **1999**, *123*, 199-208; b) J. B. Wang, J.-C. Jang and T.-J. Huang, *Journal of Power Sources* **2003**, *122*, 122-131.
[20] K. Eguchi, T. Setoguchi, T. Inoue and H. Arai, *Solid State Ionics* **1992**, *52*, 165-172.
[21] K. M. Dooley, A. K. Bhat, C. P. Plaisance and A. D. Roy, *Applied Catalysis A: General* **2007**, *320*, 122-133.
[22] a) E. P. Brandt, W. Yanying and J. W. Grizzle, *Control Systems Technology, IEEE Transactions on* **2000**, *8*, 767-776; b) M. Shelef and R. W. McCabe, *Catalysis Today* **2000**, *62*, 35-50.
[23] H. C. Yao and Y. F. Y. Yao, *Journal of Catalysis* **1984**, *86*, 254-265.
[24] A. Trovarelli, *Catalysis Reviews* **1996**, *38*, 439-520.
[25] M. Bowker, *The basis and applications of heterogeneous catalysis*, Oxford University Press, Oxford, **1998**, p. 90p.
[26] A. Trovarelli, *Catalysis by ceria and related materials*, Imperial College Press, London, **2002**, p. xvii, 508 p.
[27] J. N. Kondo and K. Domen, *Chemistry of Materials* **2008**, *20*, 835-847.
[28] D. Y. Zhao, J. L. Feng, Q. S. Huo, N. Melosh, G. H. Fredrickson, B. F. Chmelka and G. D. Stucky, *Science* **1998**, *279*, 548-552.
[29] M. Jaroniec, J. R. Matos, M. Kruk, L. P. Mercuri, L. Zhao, T. Kamiyama, O. Terasaki, T. J. Pinnavaia and Y. Liu, *Journal of the American Chemical Society* **2003**, *125*, 821-829.
[30] M. Jaroniec, P. F. Fulvio and S. Pikus, *Journal of Colloid and Interface Science* **2005**, *287*, 717-720.

[31] a) H. Tüysüz, C. W. Lehmann, H. Bongard, B. Tesche, R. Schmidt and F. Schüth, *Journal of the American Chemical Society* **2008**, *130*, 11510-11517; b) F. Kleitz, S. H. Choi and R. Ryoo, *Chemical Communications* **2003**, 2136-2137.
[32] M. Kruk and C. M. Hui, *Microporous and Mesoporous Materials* **2008**, *114*, 64-73.
[33] D. Zhao, Q. Huo, J. Feng, B. F. Chmelka and G. D. Stucky, *Journal of the American Chemical Society* **1998**, *120*, 6024-6036.
[34] A. Galarneau, H. Cambon, F. Di Renzo and F. Fajula, *Langmuir* **2001**, *17*, 8328-8335.
[35] C. T. Kresge, M. E. Leonowicz, W. J. Roth, J. C. Vartuli and J. S. Beck, *Nature* **1992**, *359*, 710-712.
[36] Q. S. Huo, D. I. Margolese and G. D. Stucky, *Chemistry of Materials* **1996**, *8*, 1147-1160.
[37] J. S. Beck, J. C. Vartuli, W. J. Roth, M. E. Leonowicz, C. T. Kresge, K. D. Schmitt, C. T. W. Chu, D. H. Olson, E. W. Sheppard, S. B. Mccullen, J. B. Higgins and J. L. Schlenker, *Journal of the American Chemical Society* **1992**, *114*, 10834-10843.
[38] X. Y. Liu, B. Z. Tian, C. Z. Yu, F. Gao, S. H. Xie, B. Tu, R. C. Che, L. M. Peng and D. Y. Zhao, *Angewandte Chemie-International Edition* **2002**, *41*, 3876-3878.
[39] D. Y. Zhao, Q. S. Huo, J. L. Feng, B. F. Chmelka and G. D. Stucky, *Journal of the American Chemical Society* **1998**, *120*, 6024-6036.
[40] J. Fan, C. Z. Yu, T. Gao, J. Lei, B. Z. Tian, L. M. Wang, Q. Luo, B. Tu, W. Z. Zhou and D. Y. Zhao, *Angewandte Chemie-International Edition* **2003**, *42*, 3146-3150.
[41] M. W. Anderson, *Zeolites* **1997**, *19*, 220-227.
[42] a) H. Tuysuz and F. Schuth, *Advances in Catalysis, Vol 55* **2012**, *55*, 127-239; b) Y. Ren, Z. Ma and P. G. Bruce, *Chemical Society Reviews* **2012**, *41*, 4909-4927; c) K. P. d. Jong, *Synthesis of solid catalysts*, Wiley-VCH, Weinheim, **2009**, p; d) Y. H. Ren, B. Yue, M. Gu and H. Y. He, *Materials* **2010**, *3*, 764-785.
[43] H. Y. Huang, R. T. Yang, D. Chinn and C. L. Munson, *Industrial & Engineering Chemistry Research* **2003**, *42*, 2427-2433.
[44] S. Y. Zheng, F. Fang, G. Y. Zhou, G. R. Chen, L. Z. Ouyang, M. Zhu and D. L. Sun, *Chemistry of Materials* **2008**, *20*, 3954-3958.
[45] a) T. Asefa and Z. M. Tao, *Canadian Journal of Chemistry-Revue Canadienne De Chimie* **2012**, *90*, 1015-1031; b) S. W. Song, K. Hidajat and S. Kawi, *Langmuir* **2005**, *21*, 9568-9575.
[46] Z. A. ALOthman, *Materials* **2012**, *5*, 2874-2902.
[47] O. Y. Gutierrez, G. A. Fuentes, C. Salcedo and T. Klimova, *Catalysis Today* **2006**, *116*, 485-497.
[48] a) D. Y. Zhao and H. F. Yang, *Journal of Materials Chemistry* **2005**, *15*, 1217-1231; b) A. H. Lu and F. Schuth, *Advanced Materials* **2006**, *18*, 1793-1805; c) J. S. Lee, S. H. Joo and R. Ryoo, *Journal of the American Chemical Society* **2002**, *124*, 1156-1157.
[49] a) R. T. Baker and B. Liu, *Journal of Materials Chemistry* **2008**, *18*, 5200-5207; b) A. G. Kong, H. Y. Zhu, W. J. Wang, Q. Y. Zhang, F. Yang and Y. K. Shan, *Journal of Porous Materials* **2011**, *18*, 107-112.
[50] F. Gao, Q. Y. Lu, X. Y. Liu, Y. S. Yan and D. Y. Zhao, *Nano Letters* **2001**, *1*, 743-748.
[51] S. A. Johnson, P. J. Ollivier and T. E. Mallouk, *Science* **1999**, *283*, 963-965.
[52] C. T. Yang and M. H. Huang, *Journal of Physical Chemistry B* **2005**, *109*, 17842-17847.
[53] X. Deng, W. N. Schmidt and H. Tüysüz, *Chemistry of Materials* **2014**, *26*, 6127-6134.
[54] X. H. Sun, Y. F. Shi, P. Zhang, C. M. Zheng, X. Y. Zheng, F. Zhang, Y. C. Zhang, N. J. Guan, D. Y. Zhao and G. D. Stucky, *Journal of the American Chemical Society* **2011**, *133*, 14542-14545.
[55] D. Y. Zhao, B. Z. Tian, X. Y. Liu, H. F. Yang, S. H. Xie, C. Z. Yu and B. Tu, *Advanced Materials* **2003**, *15*, 1370-+.
[56] B. Liu and R. T. Baker, *Journal of Materials Chemistry* **2008**, *18*, 5200-5207.
[57] a) L. Almar, T. Andreu, A. Morata, M. Torrell, L. Yedra, S. Estrade, F. Peiro and A. Tarancon, *Journal of Materials Chemistry A* **2014**, *2*, 3134-3141; b) W. H. Shen, X. P. Dong, Y. F. Zhu, H. R. Chen and J. L. Shi, *Microporous and Mesoporous Materials* **2005**, *85*, 157-162; c) H. Yen, Y. Seo, R. Guillet-Nicolas, S. Kaliaguine and F. Kleitz, *Chemical Communications* **2011**, *47*, 10473-10475; d) P. F. Ji, J. L. Zhang, F. Chen and M. Anpo, *Journal of Physical Chemistry C* **2008**, *112*, 17809-17813; e) B. Puertolas, B. Solsona, S. Agouram, R. Murillo, A. M. Mastral, A. Aranda, S. H. Taylor and T. Garcia, *Applied Catalysis B-Environmental* **2010**, *93*, 395-405; f) E. Rossinyol, E. Pellicer, A. Prim, S. Estrade, J. Arbiol, F. Peiro, A. Cornet and J. R. Morante, *Journal of Nanoparticle Research* **2008**, *10*, 369-375.

[58] a) X. D. Zhou, W. Huebner, I. Kosacki and H. U. Anderson, *Journal of the American Ceramic Society* **2002**, *85*, 1757-1762; b) D. K. Kim, P. S. Cho, J. H. Lee, D. Y. Kim, H. M. Park, G. Auchterlonie and J. Drennan, *Electrochemical and Solid State Letters* **2007**, *10*, B91-B95.
[59] M. Knoll and E. Ruska, *Zeitschrift Fur Physik* **1932**, *78*, 318-339.
[60] M. C. Scott, C. C. Chen, M. Mecklenburg, C. Zhu, R. Xu, P. Ercius, U. Dahmen, B. C. Regan and J. W. Miao, *Nature* **2012**, *483*, 444-U491.
[61] A. D. McNaught, A. Wilkinson, A. D. Jenkins and International Union of Pure and Applied Chemistry. in *IUPAC compendium of chemical terminology the gold book*, *Vol.* International Union of Pure and Applied Chemistry, Research Triangle Park, N.C., **2006**.
[62] P. Kusgens, M. Rose, I. Senkovska, H. Frode, A. Henschel, S. Siegle and S. Kaskel, *Microporous and Mesoporous Materials* **2009**, *120*, 325-330.
[63] K. S. W. Sing, D. H. Everett, R. A. W. Haul, L. Moscou, R. A. Pierotti, J. Rouquerol and T. Siemieniewska, *Pure and Applied Chemistry* **1985**, *57*, 603-619.
[64] J. C. Groen, L. A. A. Peffer and J. Perez-Ramirez, *Microporous and Mesoporous Materials* **2003**, *60*, 1-17.
[65] A. R. Lim, G. T. Schueneman and B. M. Novak, *Solid State Communications* **1999**, *110*, 333-338.
[66] D. H. Hall, E. Hartwieg and K. C. Q. Nguyen, *Caenorhabditis Elegans: Cell Biology and Physiology, Second Edition* **2012**, *107*, 93-149.
[67] A. A. Mironov, R. S. Polishchuk and G. V. Beznoussenko, *Introduction to Electron Microscopy for Biologists* **2008**, *88*, 83-+.
[68] P. Webb and C. Orr, *Analytical methods in fine particle technology*, Micromeritics Instrument Corporation, Norcross, Ga., **1997**, p. xvii,301p.
[69] L. Cao, T. Man and M. Kruk, *Chemistry of Materials* **2009**, *21*, 1144-1153.
[70] P. Schmidt-Winkel, P. D. Yang, D. I. Margolese, B. F. Chmelka and G. D. Stucky, *Advanced Materials* **1999**, *11*, 303-307.
[71] R. Anwander, I. Nagl, M. Widenmeyer, G. Engelhardt, O. Groeger, C. Palm and T. Roser, *Journal of Physical Chemistry B* **2000**, *104*, 3532-3544.
[72] Y. H. Liu, H. P. Lin and C. Y. Mou, *Langmuir* **2004**, *20*, 3231-3239.
[73] F. Q. Zhang, Y. Meng, D. Gu, Y. Yan, C. Z. Yu, B. Tu and D. Y. Zhao, *Journal of the American Chemical Society* **2005**, *127*, 13508-13509.
[74] F. Q. Zhang, Y. Meng, D. Gu, Y. Yan, Z. X. Chen, B. Tu and D. Y. Zhao, *Chemistry of Materials* **2006**, *18*, 5279-5288.
[75] D. Liu, J. H. Lei, L. P. Guo, D. Y. Qu, Y. Li and B. L. Su, *Carbon* **2012**, *50*, 476-487.
[76] Y. Meng, D. Gu, F. Q. Zhang, Y. F. Shi, L. Cheng, D. Feng, Z. X. Wu, Z. X. Chen, Y. Wan, A. Stein and D. Y. Zhao, *Chemistry of Materials* **2006**, *18*, 4447-4464.
[77] a) P. Gao, A. W. Wang, X. D. Wang and T. Zhang, *Catalysis Letters* **2008**, *125*, 289-295; b) P. Gao, A. Wang, X. Wang and T. Zhang, *Chemistry of Materials* **2008**, *20*, 1881-1888.
[78] J. M. Xu, A. Q. Wang and T. Zhang, *Carbon* **2012**, *50*, 1807-1816.
[79] T. A. Dougherty in *Synthesis and Characterisation of Ordered Mesoporous Materials*, *Vol. PhD* St. Andrews, St. Andrews, **2009**, p. 230.
[80] A. Taguchi and F. Schuth, *Microporous and Mesoporous Materials* **2005**, *77*, 1-45.
[81] C. M. Yang, B. Zibrowius, W. Schmidt and F. Schuth, *Chemistry of Materials* **2004**, *16*, 2918-2925.
[82] B. Z. Tian, X. Y. Liu, C. Z. Yu, F. Gao, Q. Luo, S. H. Xie, B. Tu and D. Y. Zhao, *Chemical Communications* **2002**, 1186-1187.
[83] B. L. Newalkar and S. Komarneni, *Chemical Communications* **2002**, 1774-1775.
[84] a) M. Colilla, F. Balas, M. Manzano and M. Vallet-Regi, *Chemistry of Materials* **2007**, *19*, 3099-+; b) M. Jaroniec, P. F. Fulvio and S. Pikus, *Journal of Materials Chemistry* **2005**, *15*, 5049-5053.
[85] a) M. Kruk and L. Cao, *Langmuir* **2007**, *23*, 7247-7254; b) X. F. Zhou, S. Z. Qiao, N. Hao, X. L. Wang, C. Z. Yu, L. Z. Wang, D. Y. Zhao and G. Q. Lu, *Chemistry of Materials* **2007**, *19*, 1870-1876; c) M. Luechinger, G. D. Pirngruber, B. Lindlar, P. Laggner and R. Prins, *Microporous and Mesoporous Materials* **2005**, *79*, 41-52; d) J. Fan, C. Z. Yu, J. Lei, Q. Zhang, T. C. Li, B. Tu, W. Z. Zhou and D. Y. Zhao, *Journal of the American Chemical Society* **2005**, *127*, 10794-10795.
[86] a) Y. C. Liang and R. Anwander, *Journal of Materials Chemistry* **2007**, *17*, 2506-2516; b) J. W. Park, Y. J. Park and C. H. Jun, *Chemical Communications* **2011**, *47*, 4860-4871; c) M. Ostwal, R. P. Singh, S. F. Dec, M. T. Lusk and J. D. Way, *Journal of Membrane Science* **2011**, *369*, 139-147; d) X. G.

Wang, K. S. K. Lin, J. C. C. Chan and S. F. Cheng, *Journal of Physical Chemistry B* **2005**, *109*, 1763-1769.
[87] M. R. Hill, S. J. Pas, S. T. Mudie, D. F. Kennedy and A. J. Hill, *Journal of Materials Chemistry* **2009**, *19*, 2215-2225.
[88] T. Yu, H. Zhang, X. W. Yan, Z. X. Chen, X. D. Zou, P. Oleynikov and D. Y. Zhao, *Journal of Physical Chemistry B* **2006**, *110*, 21467-21472.
[89] K. Morishige and K. Yoshida, *Journal of Physical Chemistry C* **2010**, *114*, 7095-7101.
[90] F. Kleitz, W. Schmidt and F. Schuth, *Microporous and Mesoporous Materials* **2003**, *65*, 1-29.
[91] R. Ryoo, C. H. Ko, M. Kruk, V. Antochshuk and M. Jaroniec, *Journal of Physical Chemistry B* **2000**, *104*, 11465-11471.
[92] P. Shah and V. Ramaswamy, *Microporous and Mesoporous Materials* **2008**, *114*, 270-280.
[93] L. A. Huang, X. W. Yan and M. Krut, *Langmuir* **2010**, *26*, 14871-14878.
[94] M. Kruk and C. M. Hui, *Journal of the American Chemical Society* **2008**, *130*, 1528-+.
[95] M. Mandal and M. Kruk, *Chemistry of Materials* **2012**, *24*, 149-154.
[96] H. Tuysuz, C. W. Lehmann, H. Bongard, B. Tesche, R. Schmidt and F. Schuth, *Journal of the American Chemical Society* **2008**, *130*, 11510-11517.
[97] M. Luhmer, J. B. dEspinose, H. Hommel and A. P. Legrand, *Magnetic Resonance Imaging* **1996**, *14*, 911-913.
[98] X. S. Zhao, G. Q. Lu, A. K. Whittaker, G. J. Millar and H. Y. Zhu, *Journal of Physical Chemistry B* **1997**, *101*, 6525-6531.
[99] R. T. Baker and M. R. Kosinski, *Journal of Power Sources* **2011**, *196*, 2498-2512.
[100] R. T. Baker, L. M. Gomez-Sainero and I. S. Metcalfe, *Journal of Physical Chemistry C* **2009**, *113*, 12465-12475.
[101] J. B. Lowe and R. T. Baker, *Journal of Nanomaterials* **2014**, *2014*, 13.
[102] R. K. Iler, *The chemistry of silica : solubility, polymerization, colloid and surface properties, and biochemistry*, Wiley, New York ; Chichester, **1979**, p. 40 - 46.
[103] J. Schwartzentruber, W. Fürst and H. Renon, *Geochimica et Cosmochimica Acta* **1987**, *51*, 1867-1874.
[104] D.-T. Liang and D. W. Readey, *Journal of the American Ceramic Society* **1987**, *70*, 570-577.
[105] W. StÖBer in *Formation of Silicic Acid in Aqueous Suspensions of Different Silica Modifications*, *Vol. 67* AMERICAN CHEMICAL SOCIETY, **1967**, pp. 161-182.
[106] G. M. Anderson, *Amercian Journal of Science* **1967**, *265*, 12.
[107] L. L. Hench in *Gel-Silica Optics*, *Vol.* William Andrew Publishing, Westwood, NJ, **1998**, pp. 80-96.
[108] M. Prigogine and J. J. Fripiat, *Journal De Chimie Physique Et De Physico-Chimie Biologique* **1979**, *76*, 26-34.
[109] a) M. A. Rosa, N. Q. Ngo, D. Sweatman, S. Dimitrijev and H. B. Harrison, *Ieee Journal of Selected Topics in Quantum Electronics* **1999**, *5*, 1249-1254; b) K. W. Park, H. G. Kang, M. Kanemoto, J. G. Park and U. Paik, *Journal of the Korean Physical Society* **2007**, *51*, 214-223.
[110] D. W. Barnum, *Inorganic Chemistry* **1972**, *11*, 1424-&.
[111] O. Terasaki, *Mesoporous crystals and related nano-structured materials : proceedings of the Meeting on Mesoporous Crystals and Related Nano-Structured Materials, Stockholm, Sweden, 1-5 June 2004*, Elsevier, Amsterdam ; Oxford, **2004**, p.
[112] I. Muylaert, A. Verberckmoes, J. De Decker and P. Van der Voort, *Advances in Colloid and Interface Science* **2012**, *175*, 39-51.
[113] C. D. Liang, K. L. Hong, G. A. Guiochon, J. W. Mays and S. Dai, *Angewandte Chemie-International Edition* **2004**, *43*, 5785-5789.
[114] P. P. Chu and H. D. Wu, *Polymer* **2000**, *41*, 101-109.
[115] P. Van der Voort, C. Vercaemst, D. Schaubroeck and F. Verpoort, *Physical Chemistry Chemical Physics* **2008**, *10*, 347-360.
[116] C. D. Liang and S. Dai, *Journal of the American Chemical Society* **2006**, *128*, 5316-5317.
[117] Y. Meng, D. Gu, F. Q. Zhang, Y. F. Shi, H. F. Yang, Z. Li, C. Z. Yu, B. Tu and D. Y. Zhao, *Angewandte Chemie-International Edition* **2005**, *44*, 7053-7059.
[118] X. Q. Wang, C. D. Liang and S. Dai, *Langmuir* **2008**, *24*, 7500-7505.
[119] C. Y. Liu, L. X. Li, H. H. Song and X. H. Chen, *Chemical Communications* **2007**, 757-759.

[120] N. B. McKeown, B. S. Ghanem, K. J. Msayib, M. Carta, P. M. Budd and J. D. Selbie, *Abstracts of Papers of the American Chemical Society* **2007**, *234*.
[121] S. A. El-Safty, T. Hanaoka and F. Mizukami, *Advanced Materials* **2005**, *17*, 392-392.
[122] K. Mortensen and J. S. Pedersen, *Macromolecules* **1993**, *26*, 805-812.
[123] D. Lof, A. Niemiec, K. Schillen, W. Loh and G. Olofsson, *Journal of Physical Chemistry B* **2007**, *111*, 5911-5920.
[124] S. Manet, A. Lecchi, M. Imperor-Clerc, V. Zholobenko, D. Durand, C. L. P. Oliveira, J. S. Pedersen, I. Grillo, F. Meneau and C. Rochas, *Journal of Physical Chemistry B* **2011**, *115*, 11318-11329.
[125] J. Jin, N. Nishiyama, Y. Egashira and K. Ueyama, *Microporous and Mesoporous Materials* **2009**, *118*, 218-223.
[126] M. Klingstedt, K. Miyasaka, K. Kimura, D. Gu, Y. Wan, D. Y. Zhao and O. Terasaki, *Journal of Materials Chemistry* **2011**, *21*, 13664-13671.
[127] M. Kang, D. Kim, S. H. Yi, J. U. Han, J. E. Yie and J. M. Kim, *Catalysis Today* **2004**, *93-5*, 695-699.
[128] J. Lee, M. C. Orilall, S. C. Warren, M. Kamperman, F. J. Disalvo and U. Wiesner, *Nature Materials* **2008**, *7*, 222-228.
[129] M. C. Orilall and U. Wiesner, *Chemical Society Reviews* **2011**, *40*, 520-535.
[130] M. U. A. Prathap and R. Srivastava, *Journal of Colloid and Interface Science* **2011**, *358*, 399-408.
[131] a) W. C. Li, A. H. Lu, C. Weidenthaler and F. Schuth, *Chemistry of Materials* **2004**, *16*, 5676-5681; b) J. Tang, J. Liu, N. L. Torad, T. Kimura and Y. Yamauchi, *Nano Today* **2014**, *9*, 305-323.
[132] Z. X. Wu, P. A. Webley and D. Y. Zhao, *Langmuir* **2010**, *26*, 10277-10286.
[133] K. A. Trick and T. E. Saliba, *Carbon* **1995**, *33*, 1509-1515.
[134] a) F. Jiao, A. H. Hill, A. Harrison, A. Berko, A. V. Chadwick and P. G. Bruce, *Journal of the American Chemical Society* **2008**, *130*, 5262-5266; b) H. Tuysuz, E. L. Salabas, E. Bill, H. Bongard, B. Spliethoff, C. W. Lehmann and F. Schuth, *Chemistry of Materials* **2012**, *24*, 2493-2500.
[135] D. Gu and F. Schuth, *Chemical Society Reviews* **2014**, *43*, 313-344.
[136] a) S. T. Aruna and A. S. Mukasyan, *Current Opinion in Solid State & Materials Science* **2008**, *12*, 44-50; b) Merzhano.Ag and Borovins.Ip, *Doklady Akademii Nauk Sssr* **1972**, *204*, 366-&.
[137] a) K. C. Patil, S. T. Aruna and T. Mimani, *Current Opinion in Solid State & Materials Science* **2002**, *6*, 507-512; b) D. G. Lamas, R. E. Juarez, G. E. Lascalea and N. E. W. De Reca, *Journal of Materials Science Letters* **2001**, *20*, 1447-1449.
[138] a) K. Morsi, *Journal of Materials Science* **2012**, *47*, 68-92; b) G. H. Liu, J. T. Li and K. X. Chen, *International Journal of Refractory Metals & Hard Materials* **2013**, *39*, 90-102; c) H. C. Yi and J. J. Moore, *Journal of Materials Science* **1990**, *25*, 1159-1168; d) A. G. Merzhanov, *Ceramics International* **1995**, *21*, 371-379; e) H. Birol, C. R. Rambo, M. Guiotoku and D. Hotza, *Rsc Advances* **2013**, *3*, 2873-2884.
[139] L. Madler, W. J. Stark and S. E. Pratsinis, *Journal of Materials Research* **2002**, *17*, 1356-1362.
[140] Y. W. Zhang, R. Si, C. S. Liao and C. H. Yan, *Journal of Physical Chemistry B* **2003**, *107*, 10159-10167.
[141] R. D. Purohit, B. P. Sharma, K. T. Pillai and A. K. Tyagi, *Materials Research Bulletin* **2001**, *36*, 2711-2721.
[142] B. Liu, B. B. Liu, Q. J. Li, Z. P. Li, R. Liu, X. Zou, W. Wu, W. Cui, Z. D. Liu, D. M. Li, B. Zou, T. A. Cui and G. T. Zou, *Journal of Alloys and Compounds* **2010**, *503*, 519-524.
[143] I. Mahata, G. Das, R. K. Mishra and B. P. Sharma, *Journal of Alloys and Compounds* **2005**, *391*, 129-135.
[144] a) L. D. Jadhav, M. G. Chourashiya, K. M. Subhedar, A. K. Tyagi and J. Y. Patil, *Journal of Alloys and Compounds* **2009**, *470*, 383-386; b) D. H. Prasad, J. W. Son, B. K. Kim, H. W. Lee and J. H. Lee, *Journal of the European Ceramic Society* **2008**, *28*, 3107-3112.
[145] a) S. Hosokawa, K. Shimamura and M. Inoue, *Materials Research Bulletin* **2011**, *46*, 1928-1932; b) M. Zawadzki, *Journal of Alloys and Compounds* **2008**, *454*, 347-351.
[146] D. S. Zhang, F. H. Niu, T. T. Yan, L. Y. Shi, X. J. Du and J. H. Fang, *Applied Surface Science* **2011**, *257*, 10161-10167.
[147] H. X. Mai, L. D. Sun, Y. W. Zhang, R. Si, W. Feng, H. P. Zhang, H. C. Liu and C. H. Yan, *Journal of Physical Chemistry B* **2005**, *109*, 24380-24385.
[148] D. M. Lyons, K. M. Ryan and M. A. Morris, *Journal of Materials Chemistry* **2002**, *12*, 1207-1212.

[149] M. R. Kosinski and R. T. Baker, *Journal of Power Sources* **2011**, *196*, 2498-2512.
[150] A. G. Merzhanov, *Journal of Materials Processing Technology* **1996**, *56*, 222-241.
[151] A. S. Mukasyan and P. Dinka, *International Journal of Self-Propagating High-Temperature Synthesis* **2007**, *16*, 23-35.
[152] V. N. Morris, R. A. Farrell, A. M. Sexton and M. A. Morris, *EMAG-NANO 2005: Imaging, Analysis and Fabrication on the Nanoscale* **2006**, *26*, 119-122.
[153] S. Deshpande, S. Patil, S. V. N. T. Kuchibhatla and S. Seal, *Applied Physics Letters* **2005**, *87*.
[154] Y. Zhang, Z. Qiang and B. D. Vogt, *Rsc Advances* **2014**, *4*, 44858-44867.
[155] K. K. Hou, A. F. Zhang, M. Liu and X. W. Guo, *Rsc Advances* **2013**, *3*, 25050-25057.
[156] D. Liu, J. H. Lei, L. P. Guo and K. J. Deng, *Carbon* **2011**, *49*, 2113-2119.
[157] M. Kruk, M. Jaroniec and A. Sayari, *Chemistry of Materials* **1999**, *11*, 492-500.
[158] T. H. Ko, W. S. Kuo and Y. H. Chang, *Journal of Applied Polymer Science* **2001**, *81*, 1084-1089.
[159] J. Roggenbuck and M. Tiemann, *Journal of the American Chemical Society* **2005**, *127*, 1096-1097.